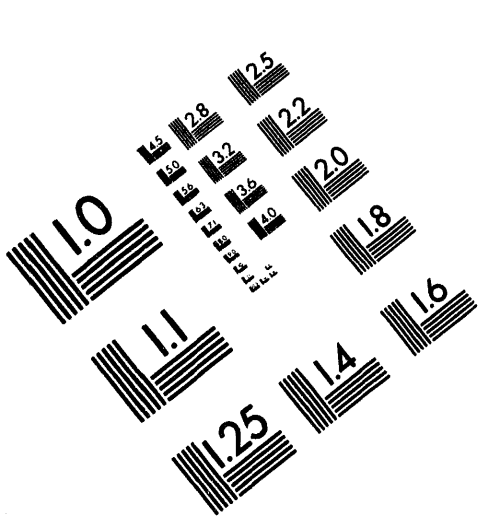

Association for Information and Image Management
1100 Wayne Avenue, Suite 1100
Silver Spring, Maryland 20910
301/587-8202

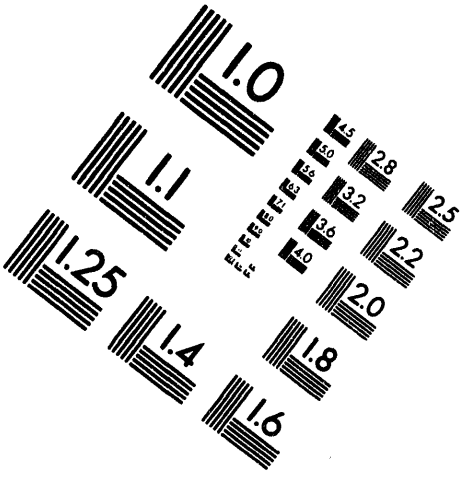

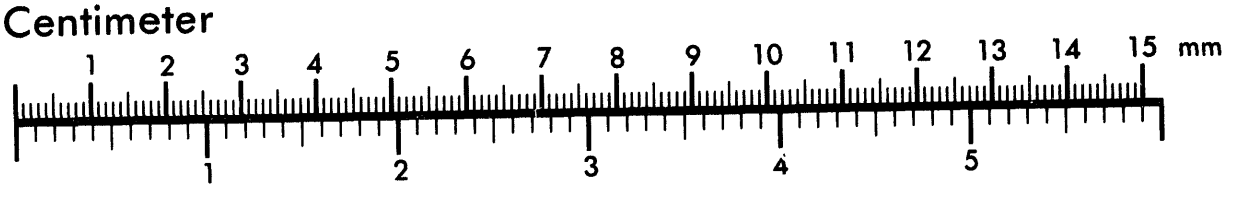

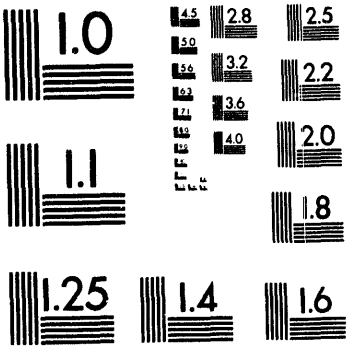

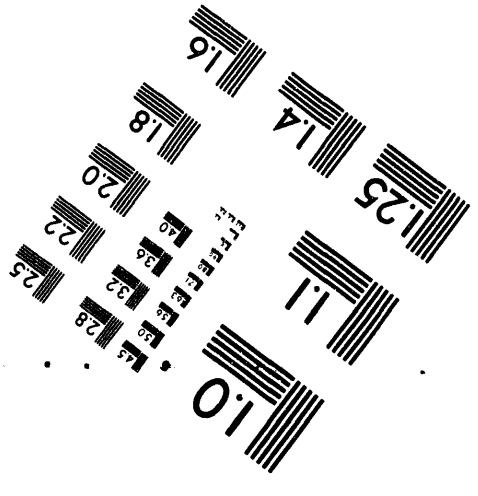

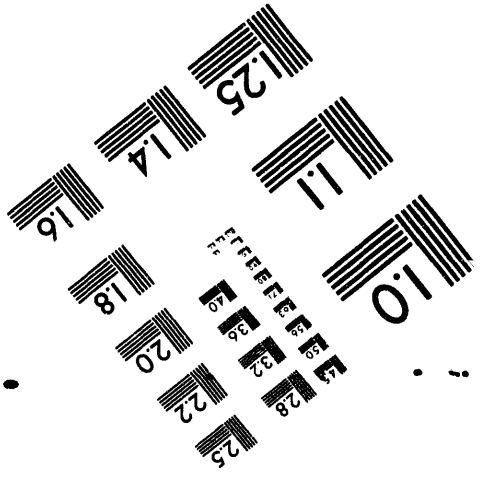

MANUFACTURED TO AIIM STANDARDS
BY APPLIED IMAGE, INC.

1 of 3

ORNL-6812

Fossil Energy Program

Fossil Energy Program Annual Progress Report for April 1993 Through March 1994

R. R. Judkins
Program Manager

Date: June 1994

Prepared for the
DOE Office of Fossil Energy
(AA, AB, AC, AW, AZ, SA)

Prepared by the
OAK RIDGE NATIONAL LABORATORY
Oak Ridge, Tennessee 37831-6285
managed by
MARTIN MARIETTA ENERGY SYSTEMS, INC.
for the
U.S. DEPARTMENT OF ENERGY
under Contract DE-AC05-84OR21400

CONTENTS

FOSSIL ENERGY PROGRAM ANNUAL PROGRESS REPORT FOR APRIL 1993 THROUGH MARCH 1994[1]

R. R. Judkins, Program Manager

ABSTRACT

This report covers progress made during the period April 1, 1993, through March 31, 1994, for research and development projects that contribute to the advancement of various fossil energy technologies. Projects on the Fossil Energy Program are supported by the DOE Office of Fossil Energy, the DOE Morgantown Energy Technology Center, the DOE Pittsburgh Energy Technology Center, the DOE Fossil Energy Clean Coal Technology Program, the DOE Bartlesville Project Office, the DOE Fossil Energy Office of Petroleum Reserves, and the U.S. Agency for International Development.

---

1. INTRODUCTION

P. T. Carlson

The Oak Ridge National Laboratory (ORNL) Fossil Energy Program research and development activities, performed for the Department of Energy (DOE) Assistant Secretary for Fossil Energy, cover the areas of coal, clean coal technology, and support to the Strategic Petroleum Reserve. The coal activities include materials research and development; environmental analysis support; bioprocessing of coal to produce liquid or gaseous fuels; and coal combustion research.

The Fossil Energy Program has projects in several ORNL divisions. Included as part of the Fossil Energy Program is the technical management of all activities on the DOE Fossil Energy Advanced Research and Technology Development (AR&TD) Materials Program. The AR&TD Materials Program includes research at six other DOE laboratories, at universities, and at industrial organizations.

---

[1]Research sponsored by the U.S. Department of Energy, Office of Fossil Energy, under contract DE-AC05-84OR21400 with Martin Marietta Energy Systems, Inc.

1.1 MATERIALS RESEARCH AND DEVELOPMENT

Materials research and development activities at Oak Ridge National Laboratory include development of ceramic composites for high temperature applications; new metal alloys with unique mechanical properties for advanced fossil energy systems; development of functional materials, such as ceramic filters, ceramic membranes, and carbon materials; and corrosion research to understand the behavior of materials in coal processing environments. The transfer of technology developed on this program is enhanced through interactions with industry and joint research programs with those interested in using the technology. Transfer to industry of the technology developed on the program has been an important activity this year, and this commitment to technology transfer is reflected in an active CRADA involvement. Materials technical support and failure analyses are provided to projects on the Clean Coal Technology Program.

1.2 ENVIRONMENTAL ANALYSIS SUPPORT

Activities in environmental analysis support included assistance to the Morgantown and Pittsburgh Energy Technology Centers (METC and PETC) in reviewing and preparing documents required by the National Environmental Policy Act (NEPA) for several projects selected for the Clean Coal Technology (CCT) Program. A key milestone was the completion for PETC of the final Environmental Impact Statement (EIS) for the Healy Clean Coal Project (HCCP) in Healy, Alaska. This work is notable because it is the first site-specific EIS completed for the CCT Program. Another important activity was the preparation for METC of a draft Environmental Assessment (EA) for the Externally Fired Combined Cycle (EFCC) Project in Warren, Pennsylvania. Also, the final EA was completed for the Gasification Product Improvement Facility (GPIF), a proposed project near Morgantown, West Virginia, which is part of METC's R&D Program. In addition, ORNL staff members published a Technical Memorandum entitled "Potential Effects of Clean Coal Technologies on Acid Precipitation, Greenhouse Gases, and Solid Waste Disposal" which documents the findings of three "white papers" prepared for DOE/FE.

The Fossil Energy Program provides assistance to PETC in satisfying the NEPA requirements for the retirement and dismantling of the Advanced Coal Liquefaction Research and Development Facility in Wilsonville, Alabama.

1.3 BIOPROCESSING RESEARCH

Fundamental bioprocessing research has concentrated on the use of biocatalysts in organic media and on advanced bioreactor systems. Coal conversion research has continued on the biological solubilization of coal using chemically-modified enzymes in organic solvents. Biophotolysis is being studied for the production of hydrogen.

1.4 COAL COMBUSTION RESEARCH

It is known that fossil energy combustion devices, such as fluidized beds and pulsed combustors, can exhibit characteristic features of deterministic chaos. The ability to measure and describe chaotic components will contribute to greatly improved methods for characterizing, modeling, designing, and controlling commercial fossil energy processes such as combustion, coal gasification, hot-gas cleanup, and oil retorting. The Fossil Energy Program is involved in the evaluation of chaotic components in data from fluidized beds and other coal combustion processes. ORNL provided technical assistance in the implementation of collaborative coal projects under the U.S. Agency for International Development (USAID)/Government of India Phase II, Alternative Energy Resources Development (AERD) Project.

1.5 FOSSIL FUEL SUPPLIES MODELING AND RESEARCH

The Strategic Petroleum Reserve (SPR) is a government-owned stockpile of crude oil intended to serve as a buffer against possible oil market disruptions. The overall purpose of this project is to develop and apply improved models for SPR long-run planning. Current project efforts emphasize developing new modeling tools to explicitly and flexibly portray oil market uncertainty and SPR planning risk.

2. MATERIALS RESEARCH AND DEVELOPMENT

N. C. Cole

This section describes research and development activities performed for the Fossil Energy Materials Program. Work on the Fossil Energy Materials Program includes the fabrication and characterization of fiber-reinforced ceramic composites, development of ceramic fiber-ceramic matrix hot-gas filters, development of ceramic membranes for the separation of gases, microwave-assisted chemical vapor infiltration, development of iron aluminides, studies of environmental effects on iron aluminides, development of advanced alloys, fundamental studies of corrosion, and materials technical support and evaluations.

2.1 FABRICATION OF FIBER-REINFORCED COMPOSITES BY CHEMICAL INFILTRATION AND DEPOSITION (CVID)

D. P. Stinton

INTRODUCTION

The recent production of very high strength ceramic (SiC) fibers has spurred the development of ceramic composite materials. Reinforcement of typical ceramic materials with high strength fibers has the potential to greatly increase the fracture toughness of the material and yet retain the properties of strength, refractoriness, and chemical inertness. High strengths result because loads can be transferred from the matrix to the fibers, taking advantage of the high strengths of the fibers. High fracture toughness values for ceramic composites occur because energy is absorbed as the fibers pull out of the matrix causing crack deflection or blunting. High toughness and high strengths have already been reported for certain fiber-reinforced ceramic composite systems; however, most ceramic fabrication processes tend to mechanically, thermally, or chemically damage the fibers.

The purpose of this task is to form the matrix of the composite by a comparatively low stress, low-temperature chemical vapor infiltration (CVI) process which will avoid the difficulties associated with conventional ceramic processing. CVI has been utilized extensively in the past for the fabrication of various composites; however, processing times required for infiltration were extremely long (weeks to months). Infiltration times were long because the isothermal or thermal gradient processes used relied on diffusion for transport of the reactant gases to the center of the preform. The ORNL-patented infiltration process utilized in this work combines a thermal gradient and a pressure gradient approach to force CVI gases to the center of the preform and reduce the processing times from weeks to hours, significantly reducing production costs and making the materials practical for many industrial applications.

The goal of this project is to demonstrate that composite materials of high interest to the fossil energy community can be fabricated by CVI. Earlier work demonstrated that composites could be fabricated in simple geometries (thick-walled plates). However, more complex geometries were identified as important in a recent Continuous Fiber Ceramic Composite (CFCC) Initiative

report. Potential applications for CFCC's include air heaters or recuperators, heat exchangers, catathermal or porous combustors, components for filtration systems, gas turbine components (primarily combustors), and radiant burner tubes. Nearly all of these applications require tubular composites; therefore, the process will be developed for the fabrication of tubular shapes.

DISCUSSION OF CURRENT ACTIVITIES

No contribution was received for work performed during this reporting period.

2.2 DEVELOPMENT OF OXIDATION/CORROSION-RESISTANT COMPOSITE MATERIALS AND INTERFACES

D. P. Stinton

INTRODUCTION

The mechanical properties of composites are strongly influenced by the nature of interfacial bonding between the fiber and the matrix. Very strong bonds result in brittle fracture because cracks propagate undisturbed through both the matrix and the fiber. Conversely, very weak bonds between matrix and fiber fail to transfer the load from the matrix to the fiber, and thus fail to effectively utilize the high strength of the fibers. Composites with both high strength and adequate toughness can only be obtained by permitting the fibers to debond and slip during fracture. If debonding at the fiber-matrix interface occurs as cracks propagate through a composite, the cracks are deflected around the fibers and the fibers remain intact and able to sustain the load. Selection of a material that produces appropriate debonding is challenging because debonding must occur at all temperatures and not be affected by extended service at elevated temperatures.

Pyrolytic carbon or boron nitride coatings applied to the Nicalon® fibers prior to infiltration with SiC produce appropriate fiber debonding, sliding, and pull out, and result in the desired mechanical properties at room and elevated temperatures. Unfortunately, the commercialization of Nicalon/SiC composites is severely limited because the mechanical properties deteriorate drastically during stressed oxidation. Upon matrix cracking, oxygen penetrates the cracks and oxidizes the carbon interlayer, and thus destroys the mechanical properties of the composite. Current solutions to this problem include protective overcoats such as glassy coatings that flow at elevated temperatures and seal cracks, or modifications to the matrix that seal cracks after they form. Unfortunately, scenarios always exist in which the overcoats or inhibited matrices are insufficient to prevent oxidation of the interface. To enhance the use of fiber-reinforced composites in fossil energy environments, oxidation resistant materials will be developed for use as interfacial coatings.

DISCUSSION OF CURRENT ACTIVITIES

No contribution was received for work performed during this reporting period.

2.3 Microwave-Assisted Chemical Vapor Deposition

Mark A. Janney
Oak Ridge National Laboratory
Oak Ridge, Tennessee 37831-6087

Overview

The purpose of this research is to explore the feasibility of using microwave heating to enhance the chemical vapor infiltration (CVI) process developed under FEMP sponsorship. The goal is to achieve faster deposition rates, greater control over deposition conditions and resulting microstructures, and perhaps lower temperature infiltration.

Introduction

Forced flow chemical vapor infiltration has been demonstrated at ORNL to be an excellent technology for the fabrication of continuous filament composites. Silicon carbide is the preferred matrix and both silicon carbide and oxide fibers have been used successfully as the reinforcing phase. Combining CVI with microwave processing may result in an improved CVI process through better control of heating and enhanced reaction rates associated with the microwaves.

It is proposed that there will be specific benefits to be derived from combining the current CVI technology with microwave processing to form MW-CVI. First, from a purely physical perspective, microwave heating of the substrate may give more control to the heating pattern in the sample. This would be especially true for the combination of oxide fibers with an SiC matrix. The oxide fibers are transparent to the microwaves and the SiC is a good microwave absorber. Therefore, only the SiC phase will be heated. This will establish a natural gradient in temperature with the SiC being the hottest part of the sample. This gradient will be similar to that established by external cooling in the current forced flow CVI process. Second, there may be microwave-enhanced reactions that occur during deposition. In work at ORNL on the reaction of silicon with nitrogen gas, it has been demonstrated that the rate of reaction to form silicon nitride is much higher for microwave processing than for conventional processing. Similar rate increases have been demonstrated by other researchers in a variety of organic reactions in both the liquid and vapor phases. Therefore, CVI reactions might be accelerated by the use of microwave processing.

Technical Progress

An existing 700W microwave furnace was modified to accommodate the CVI experiment. Modifications were made to the furnace so that a bell jar could be installed inside the microwave furnace to contain reactive gases such as methyltrichlorosilane (MTS). Appropriate gas handling equipment was constructed outside the furnace. The entire experiment was sited inside a fume hood. Non-contact methods of temperature measurement (2-color IR pyrometry) were developed to monitor the temperature of the preforms during deposition of the SiC into the fiber lay-up.

One of the most important areas to be determined at the beginning of this study was the particular experimental setup to be used. From other microwave processing studies, we had determined that experimental setup was a vital component of a successful project.

The first set of experiments focused on our ability to heat a Nicalon® preform to the coating temperature of 1200°C. A statistically-designed set of experiments was performed based on the Taguchi-style design of experiments. A reduced factorial design was used that allows one to investigate the effects of several factors using a limited number of experiments.

The following factors were selected as being most important to study:

(1) the number of layers of Nicalon® cloth - It has been demonstrated in many earlier studies of microwave heating of ceramic materials that the volume of material being heated is an essential element in how efficiently it heats. For many materials, the efficiency of microwave heating increases markedly with increasing mass up to a plateau value.

(2) the composition of the insulation - The two main insulations used in microwave processing are alumina and zirconia fiberboard. Alumina insulation is essentially transparent to microwave radiation for most applications and therefore acts only as a thermal insulator. Zirconia insulation is a reasonably good absorber of microwave radiation, especially at higher temperatures, and therefore may increase the highest temperature achievable during microwave irradiation.

(3) the amount of insulation - For conventional heating, a more efficient insulating arrangement would be expected to lead to better heating. However, in microwave processing, the unexpected happens more often than the expected.

(4) the atmosphere - The atmosphere may be expected to affect how efficiently the sample could be heated based on heat transfer considerations.

The Factor Table for the experiment, Table 1, shows the particular test conditions that were run in this study. Figure 1 shows the physical arrangement of the experiment.

The results of the experiments are summarized in the Response Table, Table 2. Two sets of experiments are reported in Table 2. In the first set, the three atmosphere test conditions were: (1) in air, (2) in air in the bell jar, and (3) in hydrogen at 0.5 atm pressure in the bell jar. In the second set, nitrogen at 1 atm pressure replaced hydrogen. The most important factor was determined to be the use of hydrogen at 1 atm. In this case, it was demonstrated that effective heating was not possible in the existing 700W microwave furnace. That is, temperatures above 800°C could not be generated because the hydrogen was highly effective in convecting heat away from the sample to the bell jar. In addition, it was demonstrated that samples could not be effectively heated at vacuum levels achievable with a mechanical vacuum pump (~50 mTorr). A plasma formed inside the bell jar which absorbed virtually all of the microwave power. Essentially no heating of the Nicalon® sample occurred.

The second most important factor was the use of the bell jar, which markedly reduced the heating efficiency. The reason for the drop in heating effectiveness with the bell jar is as follows. The base of the bell jar is made of aluminum, which shields the sample from the microwave radiation. It therefore effectively reduces the power available for heating the sample.

Similar in importance to the use of the bell jar was the use of zirconia instead of alumina insulation. As was mentioned above, zirconia insulation absorbs microwaves quite effectively at elevated temperatures. It therefore acts like an "electric blanket" in helping to heat the sample it is surrounding.

Table 1. A Taguchi-Style Reduced Factorial Design Was Used to Study the Heating of Nicalon® Preforms in the Microwave Furnace.

Experiment Number	Insulation Arrangement (# Layers)	Preform Size	Atmosphere	Insulation Composition
1	Top & Bottom	10	air-no jar	alumina
2	Top & Bottom	20	air-jar	zirconia
3	Top & Bottom	15	H2-jar	zirconia
4	T&B + Ring	10	air-jar	zirconia
5	T&B + Ring	20	H2-jar	alumina
6	T&B + Ring	15	air-no jar	zirconia
7	T&B, Ring, T&B-2	10	H2-jar	zirconia
8	T&B, Ring, T&B-2	20	air-no jar	zirconia
9	T&B, Ring, T&B-2	15	air-jar	alumina

Table 2. Response Table for Nicalon® Heating Experiments

Factor	Temperature @ 415W (°C) (H_2 @ 0.5 atm)	Temperature @ 470W (°C) (N_2 @ 1 atm)
Insulation configuration		
Top & Bottom	906	1195
T&B plus Ring	906	1246
T&B, Ring, 2nd T&B	933	1285
Layers of Nicalon® cloth		
10	938	1256
15	890	1232
20	916	1239
Atmosphere		
Air - no bell jar	1095	1357
Air - bell jar	999	1206
H_2 / N_2 - bell jar	650	1163
Insulation composition		
Alumina	873	1138
Zirconia	936	1294

Another important factor was the total amount of insulation. The more insulation, the better the heating efficiency. This suggests that conventional heat transfer considerations are important for this application of microwave heating.

The least important factor investigated was the number of layers of Nicalon® cloth used for the sample. The highest temperatures were achieved using the smallest number of layers of cloth. However, the effect of increaseing the number of layers of cloth from 10 to 20 was small.

Based on what has been learned so far, we have decided that more power is required to conduct the CVI experiments on the current scale (nominal 10 to 20 grams of Nicalon® cloth) or on larger scales in the future. Therefore, the entire experiment is being transferred to a larger microwave furnace, which has 12 kW of microwave power available.

In the coming months, the MW-CVI process will be investigated in terms of the kinetics of deposition and microstructural evolution, and compared to the baseline conventional processing. A set of statistically-designed experiments (Taguchi-style) will be conducted to determine the key aspects that control the process. The parameters that will be studied will include the temperature of the substrate, size of the substrate, flow rates of the reactant gases, gas pressure, type of reactant gas e.g., (MTS vs $SiCl_4$ - CH_4), type of insulation system, microwave power levels and so on. We have been contacted by two industrial firms who are interested in working with us in the future on MW-CVI projects.

2.4 CARBON-FIBER COMPOSITE MOLECULAR SIEVES

T. D. Burchell

INTRODUCTION

Hydrogen recovery technologies are required to allow the upgrading of heavy hydrocarbons to transport fuels, thus reducing the amount of carbon rejected during the conversion of fossil resources into hydrocarbon products. The purpose of this work is to develop carbon molecular sieves (CMS) starting with porous Carbon Fiber Composites (CFC) manufactured from petroleum pitch derived carbon fibers. The Carbon Fiber Composite Molecular Sieves (CFCMS) will be utilized in Pressure Swing Adsorption (PSA) units for the efficient recovery of hydrogen from refinery purge gases, and for other gas separation operations associated with petroleum refining.

DISCUSSION OF CURRENT ACTIVITIES

No contribution was received for work performed during this reporting period.

2.5 CARBON FIBER COMPOSITE MOLECULAR SIEVES FROM SOLVENT-EXTRACTED COAL TAR PITCH CARBON FIBERS

T. D. Burchell

INTRODUCTION

The manufacture of carbon-carbon composites for use in the aerospace industry has been heavily reliant on petroleum and coal tar pitches as matrix precursors. It is of great importance to strategic materials production for the Department of Defense that a stable, long-lived source of pitch be developed. As an integral part of the work on the development of carbon-fiber composite molecular sieves, a series of industrial subcontracts will be initiated to develop carbon-carbon composite materials from pitches derived from coal via a solvent extraction process. The objectives of this project are twofold. First, solvent-extracted pitch will be used to develop carbon-carbon composites with similar or improved properties over those currently manufactured from petroleum pitches. Second, improved, lower-cost composites will be developed.

The manufacture of graphite utilizes cokes and pitches derived from petroleum refining by-products and by-product coke ovens. These include isotropic and anisotropic cokes, binder, and impregnant pitches. Assuring feedstock quality is of great importance to the graphite industry. Therefore, a stable long-lived source of feedstock pitch (and hence coke) would be of considerable benefit to the industry. Another aspect of this task will be to develop suitable precursor pitches, binders, impregnants, and cokes for the production of graphites and other carbon products.

DISCUSSION OF CURRENT ACTIVITIES

No contribution was received for work performed during this reporting period.

2.6 HYDROGEN PRODUCTION USING INORGANIC MEMBRANES

D. E. Fain and G. E. Roettger
Oak Ridge K-25 Site*
Martin Marietta Energy Systems, Inc.
Oak Ridge, TN 37831-7271

INTRODUCTION

The purpose of this task is to develop a ceramic membrane that will efficiently separate hydrogen from gasified coal at temperatures of 1000°F or higher. Very high separation factors should be achievable with a ceramic membrane that has pores sufficiently small to separate gas molecules on the basis of molecular size, i.e., by molecular sieving. Ceramic gas separation membranes are receiving much attention today because of their potential for providing a high separation factor and a long service life in demanding applications involving high temperatures or corrosive environments.

The development approach for this task is focused on fabricating and testing membranes with progressively smaller pores, and on studying and understanding the transport mechanisms for gas transport through these membranes so that membranes can be designed to achieve maximum separation factors at any temperature. A key objective for FY 1994 is to reduce the membrane pore size sufficiently to provide a separation factor of 50 or higher at temperatures greater than 1000°F.

A high temperature flow test system is being used with good success to determine separation factors of the experimental membranes using helium, carbon dioxide, and carbon tetrafluoride as test gases. Preparations are being made for using hydrogen as an additional test gas since hydrogen separation is a main goal of the task. Methods have been developed (using the gas transport model to interpret data from the high temperature flow test system) for determining pore radii smaller than 10 Å, which are of importance to this task but could not be measured accurately by the Dynamic Pore Size Test.

---

*The Oak Ridge K-25 Site is managed by Martin Marietta Energy Systems, Inc. for the U.S. Department of Energy under contract No. DE-AC05-84OR21400.

A mathematical model for gas transport that was developed earlier was capable of predicting separation factors as a function of membrane pore size for room temperature operation and at a "high temperature limit" where adsorption and surface flow effects should not be present (Fig. 1). A current objective of the task is to expand the model to include the temperature dependencies of gas transport mechanisms. This objective should be achievable using available gas transport data from the high temperature flow test in conjunction with independently determined gas adsorption data. An adsorption measurement system has been upgraded for operation at elevated temperatures and is being used to provide the needed adsorption data.

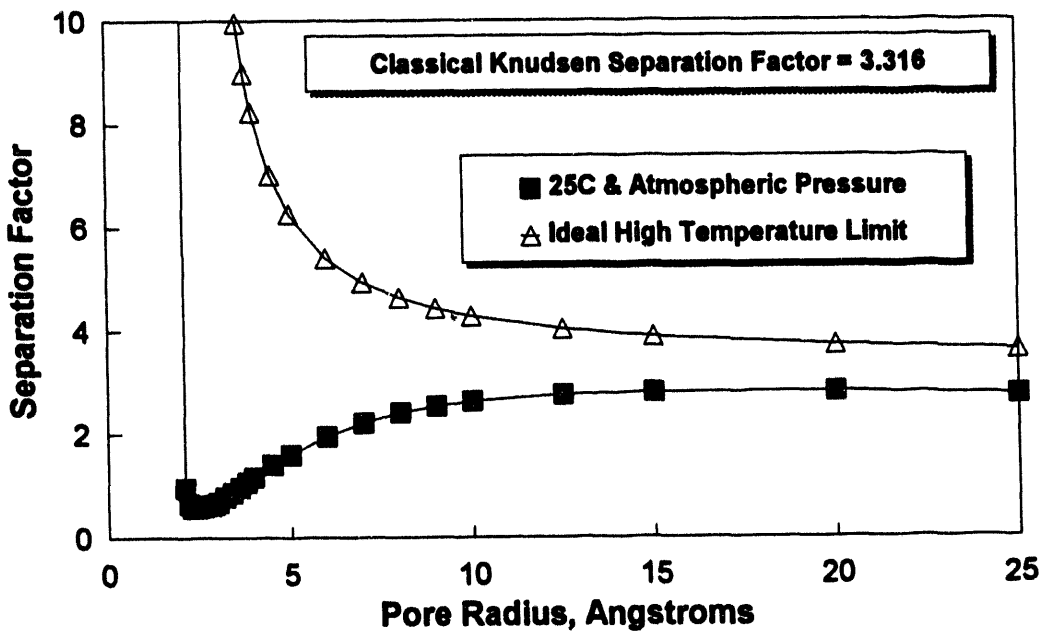

Fig. 1. Transport model calculations for He-CO_2 separation factors at room temperature and at the ideal high temperature limit.

DISCUSSION OF CURRENT ACTIVITIES

The membrane fabrication techniques that are currently being developed are showing good progress in producing ceramic membranes having smaller pores. Experimental alumina

membranes have been produced that have mean pore radii smaller than 5 Å and high temperature separation factors as high as 13 for the helium/carbon tetrafluoride gas pair. The techniques that are under development have potential for producing pore radii as small as 2 to 3 Å, which should provide separation factors of 100 or higher.

The ceramic membranes are being tested in our high temperature flow test system using helium, carbon dioxide, and carbon tetrafluoride as test gases. High precision flow measurements are made with each of the test gases at several temperatures between 20°C and 275°C and over a pressure range of approximately 85 to 185 cm Hg. Examples of the flow data obtained on a recent alumina membrane having a mean pore radius of approximately 5 Å are shown in Figs. 2, 3, and 4 for helium, carbon tetrafluoride, and carbon dioxide, respectively. The flow data are plotted as a permeance (sccm/sq cm/cm Hg) versus average pressure (average of the forepressure and backpressure). A linear (least squares) fit is included in the plots for data taken at each temperature. For comparison purposes, similar data are shown in Figs. 5, 6, and 7 for an alumina membrane having a mean pore radius of 30 Å.

The ideal separation factor for a binary gas mixture is the ratio of the zero pressure permeances of the two gases (normally the ratio of light gas to heavy gas). The zero pressure permeance is obtained from the flow data as plotted in Figs. 2 through 7 by extrapolating the least squares fit of the data to zero pressure as shown. Separation factors for the gas pairs may, thus, be determined from the flow data measured at room temperature, 100°C, 200°C, 250°C, and 275°C. An Arrhenius-type plot (ln separation factor plotted against the reciprocal of the absolute temperature, 1/T) provides an excellent fit of the separation factors determined at various temperatures. The helium/carbon tetrafluoride separation factors determined for a recent alumina membrane and plotted in this manner are shown in Fig. 8. The pore size of this membrane was too small to measure with our Dynamic Pore Size Test.

Extrapolation of the least squares fit (Fig. 8) to a zero value of I/T provides an estimate of the separation factor at the high temperature limit where adsorption and surface flow effects would be eliminated. The high temperature separation factor of 12.99 can be interpreted using the hard sphere model to provide an estimate of the mean pore size of the membrane. Those calculations indicate that a membrane mean pore radius of 4.98 Å is required to provide a high temperature separation factor of 12.99 for the helium/carbon tetrafluoride gas pair.

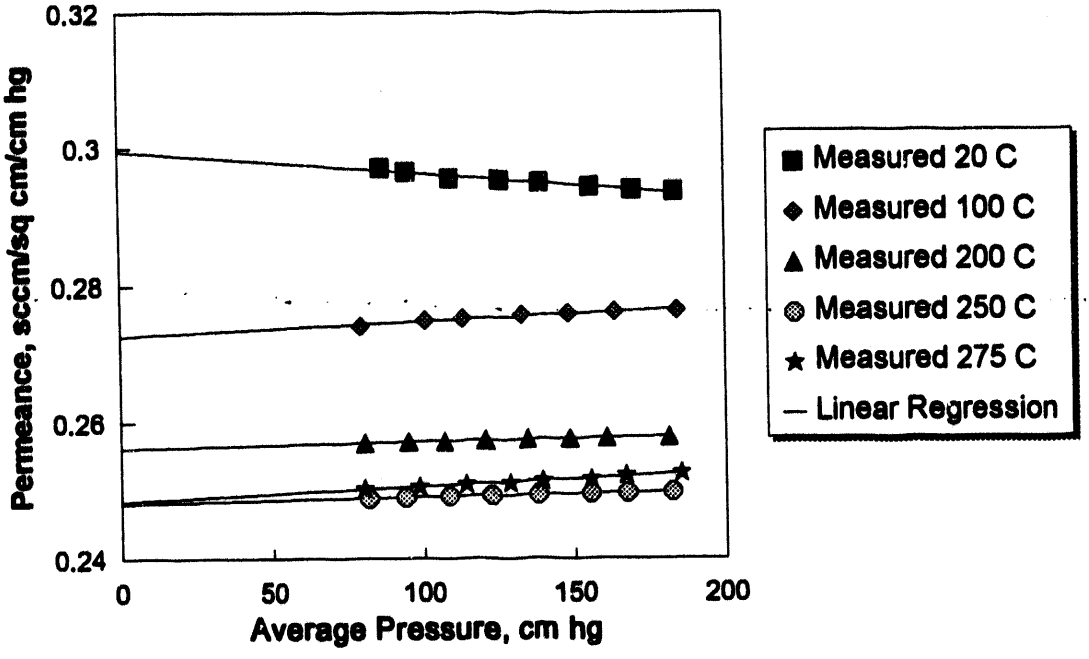

Fig. 2. Helium flow data measured at several temperatures through alumina membrane having 5 Å mean pore radius.

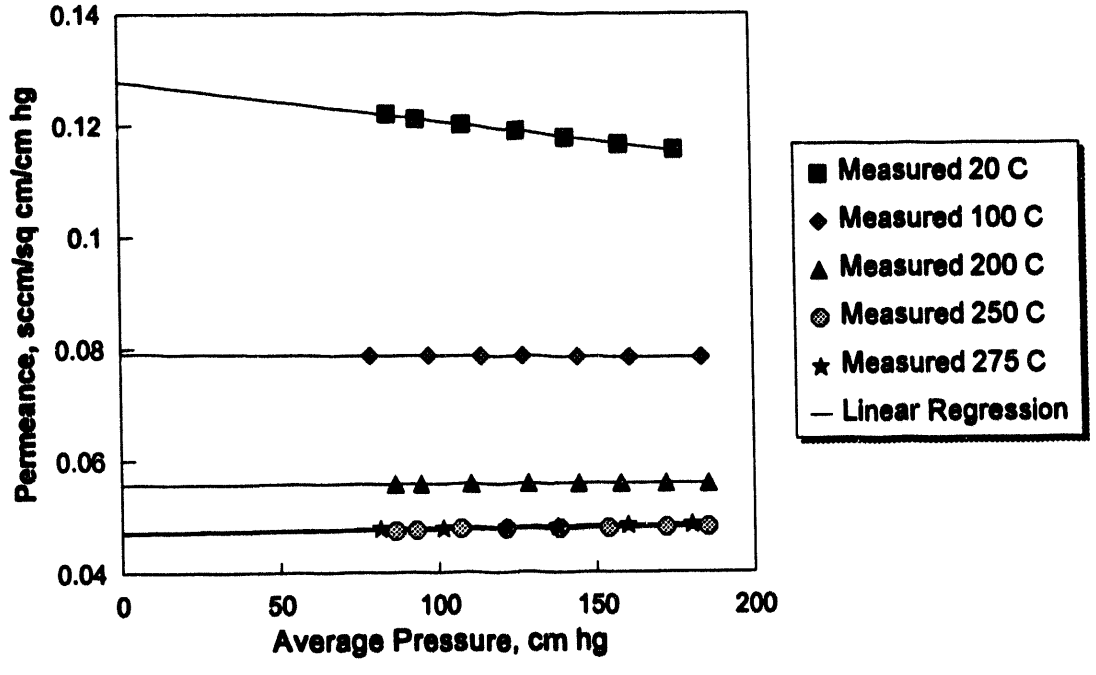

Fig. 3. Carbon tetrafluoride flow data measured at several temperatures through alumina membrane having 5 Å mean pore radius.

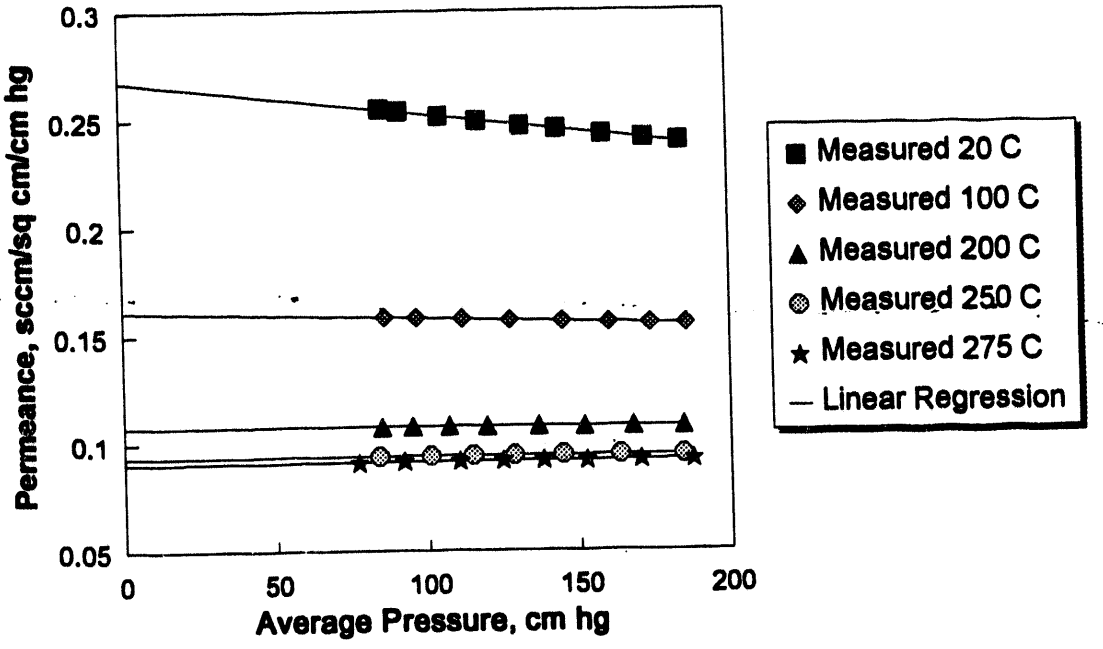

Fig. 4. Carbon dioxide flow data measured at several temperatures through alumina membrane having 5 Å mean pore radius.

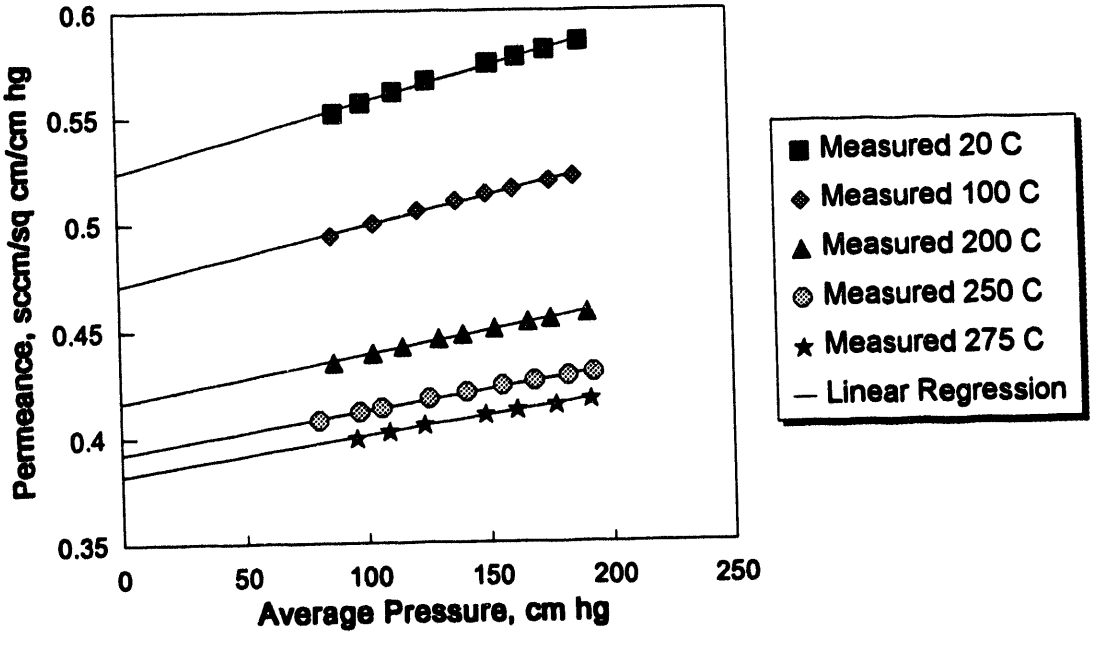

Fig. 5. Helium flow data measured at several temperatures through alumina membrane having 30 Å mean pore radius.

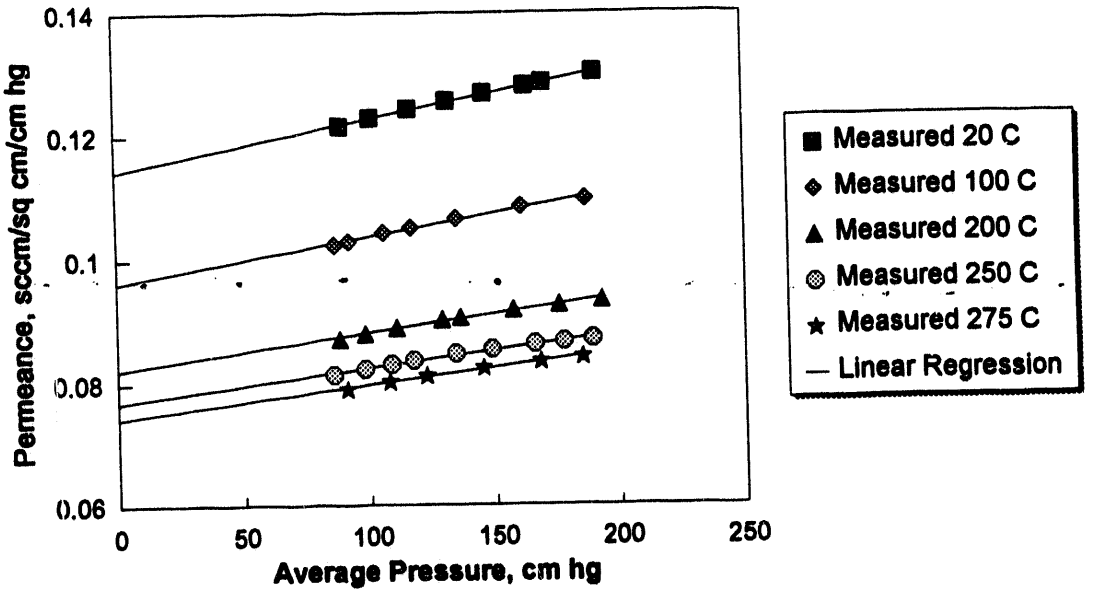

Fig. 6. Carbon tetrafluoride flow data measured at several temperatures through alumina membrane having 30 Å mean pore radius.

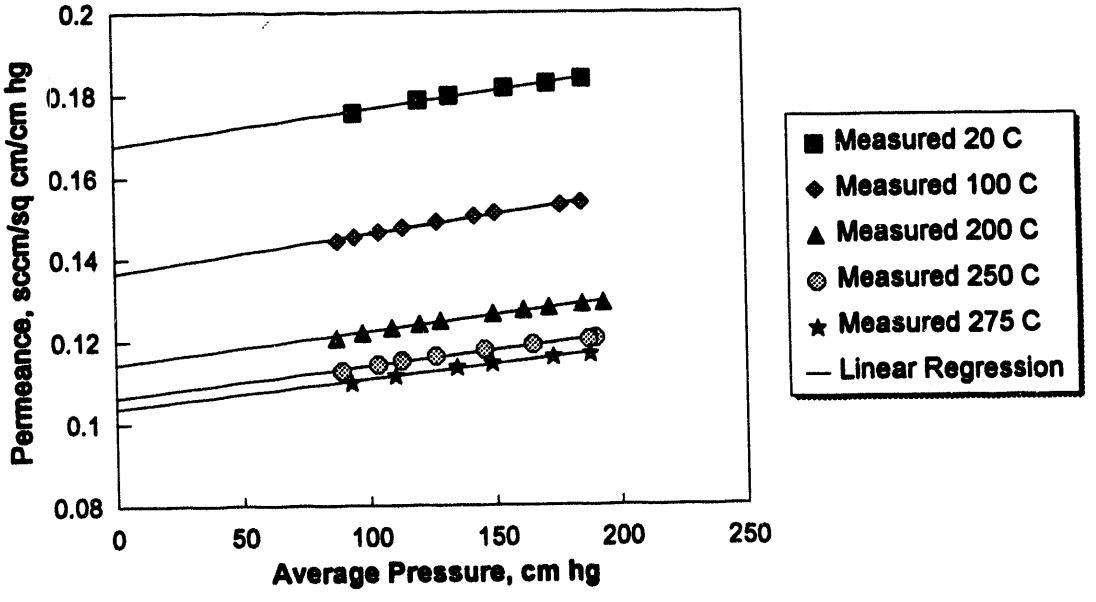

Fig. 7. Carbon dioxide flow data measured at several temperatures through alumina membrane having 30 Å mean pore radius.

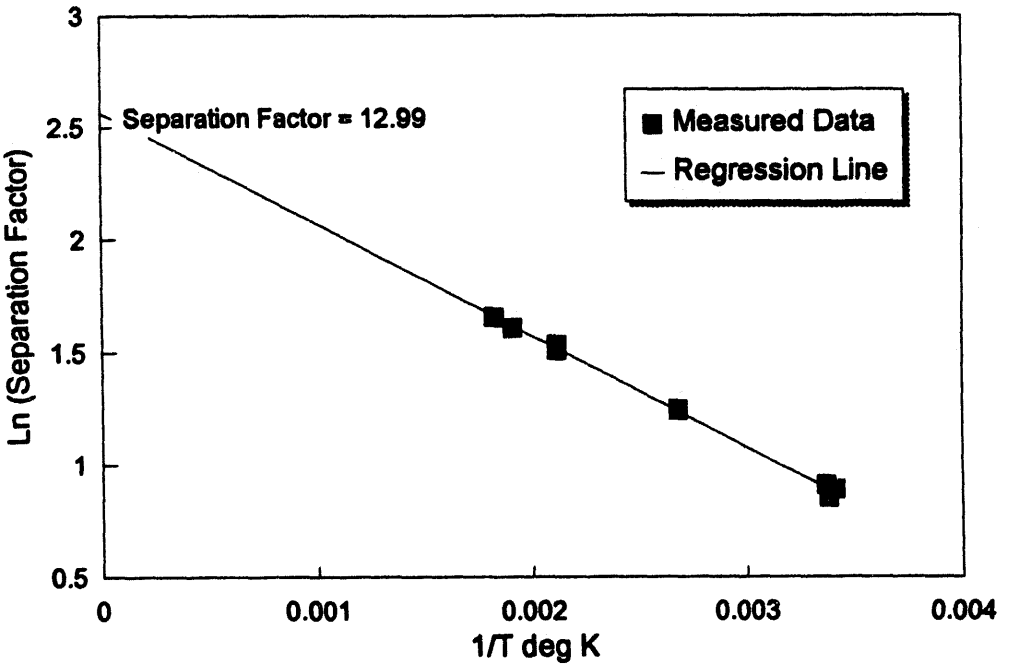

Fig. 8. He/CF_4 separation factors measured at various temperatures on alumina membrane having 5 Å mean pore radius.

The effects of membrane pore size on the separation factor/temperature data are shown in Fig. 9, which contrasts data measured on two alumina membranes having mean pore radii of 30 Å and 8.9 Å (as determined by the Dynamic Pore Size Test). For the 30 Å membrane at room temperature, the data show a separation factor of 4.60 (approximately the Knudsen value), and the separation factors increase only slightly at higher temperatures. Separation factors determined at room temperature for the 8.9 Å membrane are considerably lower than for the 30 Å membrane due to increased surface flow of the heavier gas in the small pores. The separation factors of the 8.9 Å membrane increase with temperature at a relatively high rate as adsorption and surface flow are reduced and the benefits of smaller pore size are realized.

A total of 14 alumina membranes have been tested in the high temperature flow test system. The mean pore radii of these membranes ranged from 30 Å to less than 5 Å. The separation factors determined for these membranes at room temperature and at the high temperature limit are plotted against the membrane mean pore size in Fig. 10. These empirical values show good agreement with the trends predicted by the transport model and shown earlier in Fig. 1.

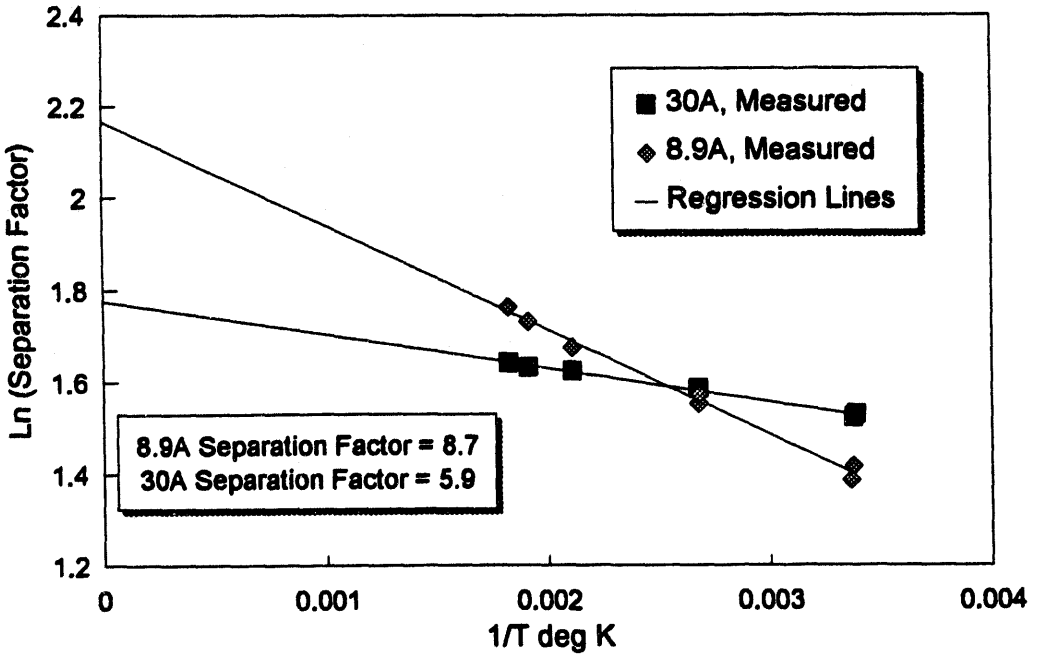

Fig. 9. He/CF_4 separation factors measured on alumina membranes having mean pore radii of 30 Å and 8.9 Å.

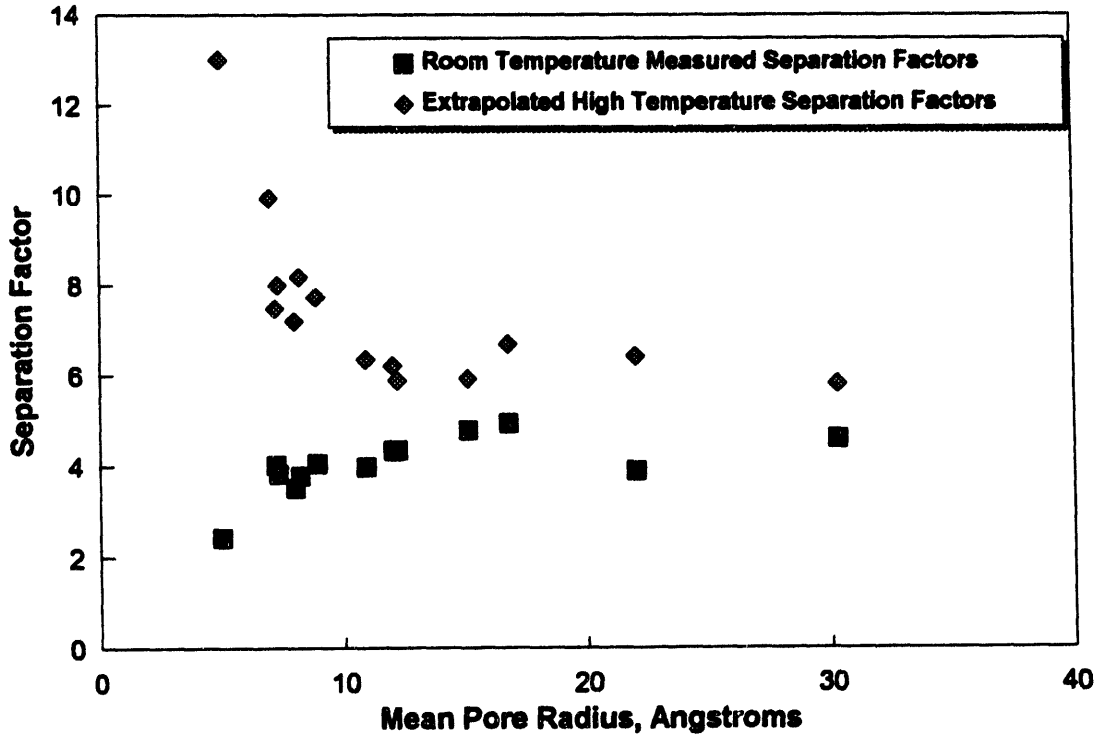

Fig. 10. Summary of He/CF_4 separation factors at room temperature and at the high temperature limit determined from flow data.

The flow tests that have been performed on 14 membranes to date have provided a large database of gas transport data at several temperatures up to 275°C. These data, used in conjunction with independently determined gas adsorption data, will permit the temperature dependencies of gas transport mechanisms to be determined and incorporated into the gas transport model. A variable volume adsorption measurement system has been upgraded to permit gas adsorption to be measured on membrane materials at temperatures up to 275°C. The variable volume consists of a cylinder and a piston. The pressure and temperature of the gas in the cylinder are measured by a calibrated pressure transducer and thermocouple as the volume of the cylinder is changed. A fixed amount of gas is introduced into the cylinder. A sample holder of predefined volume is connected to the variable volume. The holder is enclosed in a heated chamber that provides temperatures up to 275°C. Using the volume, pressure, and temperature determinations, the mass of gas present in the gas phase can be accurately determined over a range of pressures. The difference between the initial mass of gas introduced and the amount in the gas phase is the amount adsorbed.

The variable volume adsorption measurement system is being used to measure the adsorption of gases on alumina membrane material over a range of pressures and at various temperatures up to 275°C. The test gases being used include helium, carbon dioxide, and carbon tetrafluoride, i.e., the same gases used to evaluate membranes in the high temperature flow test system. These adsorption data will be used with the existing analytical expression (and others if needed) for the various transport mechanisms to regression fit the permeability data as shown in Figs. 2 through 7. With these regression equations, separation factors at different temperatures can be calculated (as in Fig. 1).

REFERENCES

(None)

2.7 ENVIRONMENTAL EFFECTS ON IRON ALUMINIDE

J. H. DeVan, P. F. Tortorelli, and M. J. Bennett*

Oak Ridge National Laboratory
P. O. Box 2008
Oak Ridge, Tennessee 37831-6156

Consultant, South Moreton, England, OX11 9AH

ABSTRACT

Air oxidation tests of iron-aluminum alloys containing 16 and 28 atom % Al, respectively, were conducted at 1300°C to determine the effect of alloy composition and section thickness on the time to breakdown of oxidation resistance. The oxidation rates of the 16% Al alloy were significantly higher than for 28% Al (Fe_3Al) alloys. The times over which the oxide scales remained protective correlated with the extent of aluminum depletion of the alloy matrix and were therefore a direct function of the initial aluminum content of the alloy, the section thickness, and the oxidation rate. The oxidation rate of the Fe_3Al alloys was significantly reduced by the addition of 0.1% Zr, which improved the adherence of the scale during thermal cycling to room temperature. However, the oxidation rates of the Fe_3Al alloys were higher at 1300°C than those reported for oxide-dispersion-strengthened (ODS) Fe-18%Cr-10%Al alloys containing Y_2O_3. Times to the onset of breakaway oxidation were similar for zirconium-containing Fe_3Al and the ODS alloys, the lower oxidation rate of the latter offsetting the higher initial aluminum of the former.

Studies of the effects of chlorine (HCl) on the oxidation/sulfidation resistance of Fe_3Al-based alloys were conducted using test facilities at the National Physical Laboratory (NPL) in the United Kingdom. Alloys were exposed to a test gas composed of CO_2, H_2, H_2O, and H_2S plus 1000-5000 ppm HCl at 450 and 550°C for 1000 h. Weight gains were relatively low and were generally less than companion specimens of Fe-Cr-Al alloys.

INTRODUCTION

The corrosion behavior of iron-aluminum alloys is being studied in high temperature mixed-oxidant atmospheres typical of coal combustion and gasification environments. The alloys are of two general types: Fe_3Al-based alloys containing 28 atom % Al with variable additions of Cr, Nb, Mo, and Zr, and iron-aluminum alloys containing 16% Al, 5% Cr, 1% Mo, 0.1% Zr, and 0.5%Y (compositions in atom %). The corrosion studies are intended to establish the operating performance limits of these alloys as a function of temperature and oxidant species (oxygen-sulfur-chlorine).

The effects of alloy composition on the oxidation and scaling resistance in air are being evaluated in laboratory tests under isothermal and cyclic temperature conditions. As reported earlier[1,2], the oxidation resistance of the 16% Al alloy was shown to approach that of the 28% Al alloys under isothermal conditions between 900 and 1000°C and under cyclic conditions at 1000 and 1150°C. The extent of oxide scale spallation in cyclic oxidation tests at 1000 and 1150°C was significantly reduced by the incorporation of 0.1% Zr in the alloys. Protection derived from the formation of a coherent and adherent α-Al_2O_3 scale.

More recent studies have been undertaken to assess the effect of both the aluminum and the zirconium contents upon the oxidation behavior of Fe_3Al alloys in air at 1300°C, and to compare their oxidation properties with other alumina-forming alloys. Recent work[3,4] on long term cyclic oxidation behavior of some of the best commercial alloys currently available (the alumina forming oxide dispersion strengthened [ODS] Fe+16-20% Cr+10% Al+0.1% Y_2O_3 ferritic alloys-MA956, ODM 751 and PM 2000), has demonstrated that for typical plant component thicknesses, life-time service conditions will be determined not by component section loss but by the time to onset of breakaway oxidation. This resulted from the aluminum content of the alloy falling (due to consumption by oxidation) below a critical value needed to sustain the protective alumina scale. At this juncture breakaway attack ensued, with the rapid formation of non-protective iron-rich oxides. The other principal parameter controlling the time to breakaway was the aluminum reservoir available within the alloy, which was determined by the alloy aluminum content and the component thickness. The aluminum concentration in these FeCrAl + Y_2O_3 ODS alloys is nominally 10%, whereas that of the Fe_3Al alloys can be up to 28%, thereby affording a much greater reservoir of aluminum.

The sulfidation resistance of iron aluminide alloys also makes them promising candidates as heat exchanger materials for coal gasifiers. Such an application requires the alloy to resist product gases containing small concentrations of H_2S and HCl at relatively low oxygen partial pressures ($<10^{-14}$ Pa) at temperatures up to 500°C. Laboratory tests of the 28% Al alloys in a H_2S-H_2-H_2O mixed gas with reference gasifier sulfur and oxygen activities showed the alloy to have considerably better resistance to H_2S than currently-used heat exchanger alloys. More recent tests have examined the corrosion of the iron aluminides in similar mixed gases containing small concentrations of HCl.

DISCUSSION OF CURRENT ACTIVITIES

High Temperature Oxidation Studies

Experimental

Four iron aluminum alloys, designated FAP, FA129, FA180 and FAL, were included in the test program. Compositions of the alloys are given in Table 1. Specimens, typically 1 x 1 cm or 2 x 1 cm, were cut from sheet having thicknesses between 0.23-0.70 mm. The specimens were contained in alumina crucibles and oxidized in either air or oxygen for successive periods ranging from 6-200 h, but usually 80 h, with intervening furnace cooling to room temperature. The oxidation temperature was 1300°C, but in addition FAP was oxidized at 1250°C. The extent of attack and of oxide spallation were measured gravimetrically. The specimens were also photographed to provide information on dimensional changes. Following the completion of the exposures, the chemical and physical nature of the attack was characterized by a range of surface analytical procedures, including X-ray diffraction (XRD), optical microscopy, scanning electron and transmission electron microscopy, energy dispersive X-ray analysis (EDAX) and electron microprobe analysis (EPMA).

Table 1. Alloy Composition

Alloy	Composition (atom %)					
	Fe	Al	Cr	Zr	Nb/Mo	Non-metals
FAP	72.9	16.1	5.0	0.1	1.1 Mo	0.1 C
FA129	65.7	28.0	5.0		1.0 Nb	0.2 C
FAL	66.9	28.0	5.0	0.1		
FA180	65.6	28.0	5.0	0.025	0.5 Nb 0.8 Mo	0.05 C 0.05 B
FAS	70.0	28.0	5.0			0.05 B

Results and Discussion

All the alloys tested contained 5% Cr but differed with respect to aluminum and zirconium contents. FA129, FA180 and FAL all contained 28% aluminum but had different zirconium levels. FA129 contained no zirconium, and FA180 and FA129 contained 0.025% and

0.1%, respectively. FAP contained a lower aluminum content (16%) and the higher zirconium level (0.1%). Therefore, comparison of FAP and FAL provides insight into the role of aluminum content, and the other alloys allow an assessment of the role of zirconium content.

The oxidation behavior of these alloys was characterized by four main features, namely, a protective oxidation regime, oxide spallation, oxidation-induced dimensional growth and breakaway attack. The increases in weight gain (i.e. the overall extent of attack) with time for the individual FA129, FA180, and FAL specimens are shown in Figure 1. Initially the FAL oxidation kinetics were essentially parabolic, indicative of a protective oxidation regime, which X-ray diffraction and microscopic examination showed to have resulted from the formation of an α-Al_2O_3 scale. At a critical weight gain, which increased with specimen thickness, the oxidation rate abruptly increased rapidly, resulting from the transformation from protective type oxidation to breakaway attack. Although the exact time to onset of breakaway could not be pinpointed exactly, it lay in the time interval between the last measurement in the protective regime and the first measurement following breakaway, which is the range of times quoted subsequently.

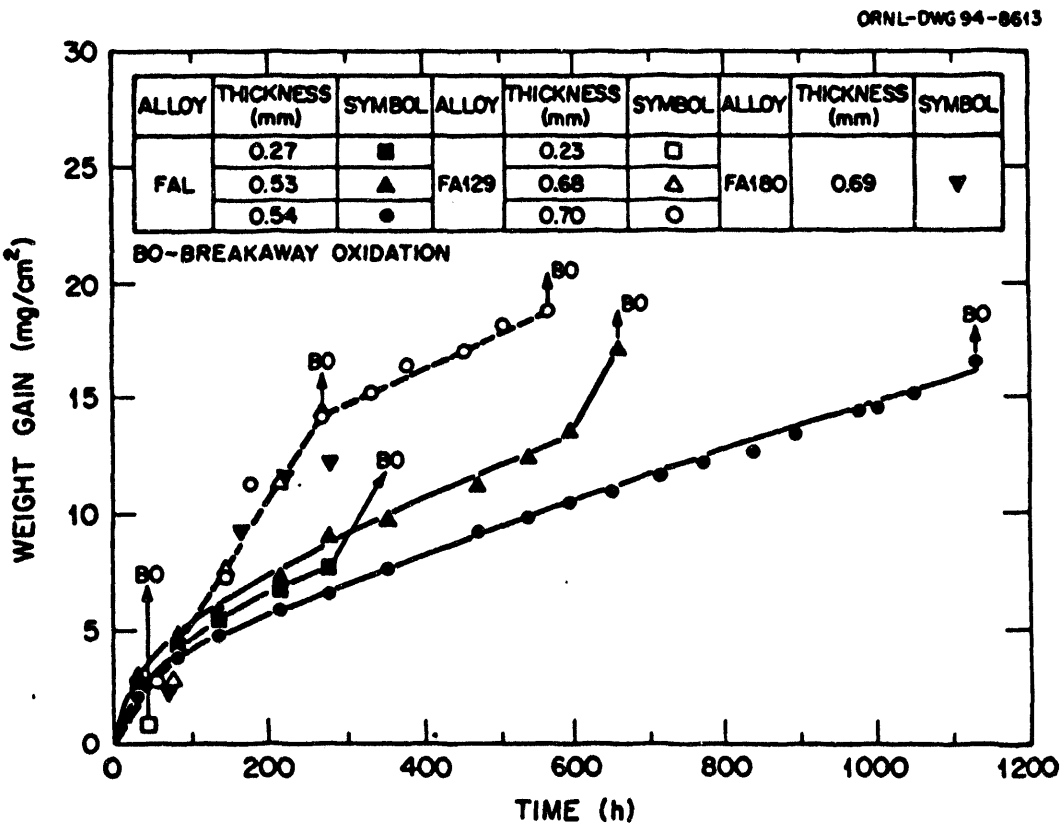

Figure 1. Comparison between the oxidation kinetics of FA129, FA180 and FAL in air at 1300°C.

Up to ~50 h the extent of oxidation of FA129, and also FA180, was comparable to that of FAL. At longer times the oxidation kinetics of FA129 and FA180 increased over that of FAL and became effectively linear (Figure 1). For comparable specimen thicknesses, the times to breakaway for FAL at 1300°C significantly exceeded those for FA129. On exposure at 1300°C the FAP alloy, with 16% aluminum, went immediately into breakaway oxidation; however, at 1250°C breakaway followed an initial period of parabolic oxidation behavior.

Although oxide spalled from all the alloys on cooling to room temperature, there was a major difference between the behavior of FA129 and FA180 and of FAL. With FA129 and FA180 most of the oxide formed spalled, such that the weight of spalled oxide increased linearly with exposure time. In contrast, with FAL most of the scale remained completely adherent throughout oxidation, and only a small fraction of the outermost layer of the scale spalled, primarily following the first thermal cycle. Although scale delamination was optically visible, the extent of spallation was often less than the gravimetric measurement limits. After 500 h of oxidation, the weight of spalled oxide from FA129 was 26 mg/cm^2 compared to only 0.5 mg/cm^2 from FAL.

Oxidation caused an increase in both the length and width of the FAL specimens. The kinetics of area extension followed that of oxidation, in that they were faster initially and continued at a rate which decreased progressively with time. For the 0.5 mm thick specimens the area had grown by ~35% prior to breakaway. FA129 specimens also grew in area as a result of oxidation with similar kinetics but by a smaller extent, with a ~16% extension prior to breakaway.

These results clearly indicate that both the zirconium and aluminum contents have a significant effect on the high temperature oxidation behavior of iron-aluminum alloys. Mechanistic understanding of the role of zirconium was revealed by detailed characterization of the oxide scale formed on FA129 and FAL and how this related to current understanding of the development and failure of protective alumina scales.[5,6,7] The alumina scale on FA129 was similar to that formed on FeCrAl alloys[5] in that it was convoluted and generally detached from the alloy with only localized areas of attachment. In contrast, the corresponding scales on FAL were both compact and adherent. The FAL scales were shown by EPMA to be enriched in zirconium, whose concentration was highest near the gas interface and decreased with scale depth. Various surface analytical techniques (SEM, TEM with EDAX, and XRD) established that zirconium was present as discrete 0.5-1.2 mm diameter ZrO_2 (monoclinic) particles. On the basis of studies on related systems[6], it would also be expected that zirconium would be segregated at the oxide grain boundaries, although this has yet to be established for FAL.

Based on reference 9, the alumina scale on FA129 can be assumed to have developed by the transport both of cations outward and oxidant inward. At 1300°C convoluted scale formation is indicative of rapid aluminum surface diffusion. This scale cracked and spalled readily on cooling. However, on re-exposure of the alloy, scale regeneration was facilitated by the relatively high aluminum level in the alloy (until it fell below the critical level for onset of breakaway). The linear oxidation kinetics were consistent with successive scale thickening and breakdown, with oxidation being controlled by transport through a thin, surface oxide barrier layer.

Zirconium is one of the so called reactive elements known to improve the protection afforded by alumina scales, and indeed it acted in this role on FAL. As a result of ZrO_2 particle formation and the resultant oxide grain boundary segregation of zirconium by Ostwald ripening, outward cation transport was inhibited, such that the scale on FAL would have developed primarily by inward anion transport.[6,7] Zirconium also dramatically improved scale adherence, probably largely due to the change in oxide growth mechanism. A further contributing factor was that the stresses resulting from oxidation were relieved by deformation of the underlying alloy, which like all ferritic alloys had a low creep strength at 1300°C. As a consequence the resultant strain on the alumina scale on cooling was considerably lower than would have been experienced by a comparable scale on the significantly stronger ODS alloys, which in certain circumstances is known to cause scale spallation.[3,4] It should be added that the lower deformation of FA129 compared with FAL was entirely consistent with the poorer adhesion and thinner scales on the FA129 alloy. Finally, it should be noted that whereas a zirconium concentration of 0.1% proved to be effective in improving oxidation resistance, a factor of four lower level (0.025%) was not.

In this series of iron-aluminum alloys, in which the chromium content was limited to 5%, the concentration of 16% aluminum in FAP was insufficient for protective alumina scale formation at 1300°C, even though the alloy also contained 0.1% zirconium. However, a protective type oxidation regime was established on the alloy at lower temperatures. At 1300°C the higher aluminum content (28%) afforded by the Fe_3Al alloy proved to be essential. In the case of the FeCrAl alloys, the presence of 10% aluminum in combination with 18-20% chromium provides better oxidation resistance at 1300°C than observed for the FAL alloy and demonstrates a synergistic interaction between chromium and aluminum that promotes the formation of protective alumina scales at lower aluminum levels.

The overall mechanism leading to breakaway oxidation of these alloys appears to be similar to that already modelled for the alumina forming FeCrAl-Y_2O_3 ODS alloys.[3,4] Non-protective oxidation occurred when the alloy aluminum content was reduced, by scale formation,

to a value below that needed to sustain continuing growth of a protective alumina scale. Breakaway was dependent, therefore, on four critical parameters. These included the extent of aluminum available (i.e. the alloy aluminum content and specimen thickness), the rate of aluminum consumption through oxidation (including effects of spallation), and the rate of aluminum diffusion from within the alloy to the oxidizing surface. As observed with the ODS alloys[4], the rate of aluminum diffusion was relatively rapid; i.e., there was no perceptible aluminum concentration gradient across oxidized FAL specimens based on EPMA analyses. The fourth parameter was the value of the residual alloy aluminum content leading to breakaway attack. This could be determined from the last weight gains prior to breakaway and also from EPMA measurements on metallographically mounted specimens taken from alloy regions beneath protective oxide scales that adjoined regions which had oxidized completely following breakaway. For FAL the values calculated from weight changes ranged between 3.1-5.8 weight %, while the EPMA values were between 1.8 and 2.4 weight %. These were slightly higher than the corresponding calculated residual aluminum contents for FeCrAl+Y_2O_3 (reference 4) for which the average of fifteen values, ranging between 0.3 and 3.5 weight %, was 1.8%. For FA129 the calculated and EPMA residual aluminum values, respectively, were higher than the FAL values.

The measured times to breakaway for the three Fe_3Al alloys have been superimposed in Figure 2 upon the corresponding plot of weight change vs specimen thickness derived for the ODS FeCrAl+Y_2O_3 alloys[3,4] in air and oxygen. The data are generally consistent for all alloys-the time to breakaway increased with specimen thickness, FAP exhibited the worst behavior, while FA129 was inferior to FAL. That the FAL values fell on or slightly above the best estimate line through the ODS results is entirely coincidental, but it does demonstrate that the behavior of this alloy is at least as good as the best commercially available ODS ferritic alloys. It also suggests that the potential offered by the increased aluminum content of FAL compared to the FeCrAl alloys is not being fully exploited. Two factors limiting the performance of FAL compared with the ODS alloys were, first, the slightly higher residual aluminum level where breakaway occurred, and, second and more significantly, the higher oxidation rate of FAL. As an indication, at 1300°C the FAL parabolic rate constant (40×10^{-2} $mg^2 \cdot cm^{-4} \cdot h^{-1}$) was over an order of magnitude greater than that for the ODS alloy ODM 751 (2.5×10^{-2} $mg^2 \cdot cm^{-4} \cdot h^{-1}$). If the Fe_3Al oxidation rate could be reduced to the lower value, then the time to breakaway would be significantly increased; e.g., for a 0.5 mm thick component this time would be in excess of 9000 h rather than 600 h as at present.

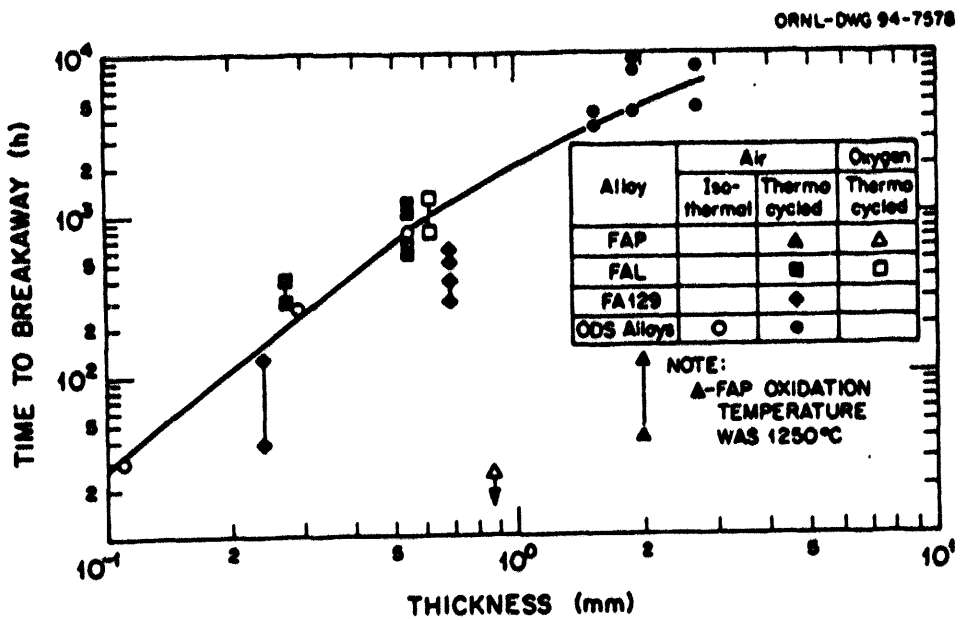

Figure 2. Influence of alloy thickness on the time to breakaway oxidation of FAL, FA129, and FAL and of ODS FeCrAl+Y_2O_3 alloys in air and oxygen at 1300°C.

Reducing the oxidation rate of Fe_3Al alloys to at least that of commercial ODS alloys appears to be a feasible objective. It should be achievable by optimizing not only the concentration, but also the nature of the reactive element. There are strong arguments for incorporating the reactive element as an oxide dispersoid and also for gaining synergistic effects from multiple reactive element additions. Both aspects are being researched as part of our overall iron aluminide development program.

Effect of HCl on Sulfidation of Fe_3Al by H_2S-Containing Mixed Gases

Experimental

Test specimens of the iron-aluminum alloys FAS, FA129, and FAP were supplied to National Physical Laboratory (NPL) for exposure to a CO-H_2-H_2O-CO_2 mixed gas containing small concentrations of both H_2S and HCl. Nominal compositions of the alloys are given in

Table 1. The specimen size was 10 mm x 10 mm x 3 mm. The major faces of the specimens were precision machined so that the 3 mm cross section was flat and parallel to within 2.5 μm. This was required to accommodate the automated measuring technique that NPL uses to monitor thickness changes due to corrosion, which has a precision of ± 3μm. The test gas was composed of 24.8% CO, 20.4% H_2, 3.93% CO_2, 6.3% H_2O, 0.123% H_2S, bal. N_2 (by volume). HCl was added to a concentration of 1000 ppm by passing the gas mixture over a dilute solution of hydrogen chloride heated to achieve the appropriate HCl and H_2S vapor pressures. Duplicate specimens of each material were exposed to the flowing test gas at 450°C, and single specimens, at 550°C. Analyses of the gas leaving the specimen retorts indicated that the oxygen-containing species had not equilibrated at the test temperatures, so the $p(O_2)$ was assumed to be fixed by the H_2/H_2O ratio.[8] The sulfur and oxygen activities of the gas at the respective test temperatures are recorded in Table 2. Exposures were conducted for a total duration of 1000 h with six weighings during the first 320 h and five weighings thereafter. A FeCrAl alloy containing 20% Cr, 8% Al, 0.1% Y, bal. Fe (provided by NPL) was exposed concomitantly with the iron-aluminum specimens and served as a reference against which to evaluate the relative corrosion resistance of the various alloys.

Table 2. Fugacities of S_2 and O_2 in the NPL Test Atmosphere

Temperature °C	O_2 Fugacity*	S_2 Fugacity
450	9.7×10^{-27}	5.1×10^{-8}
550	2.0×10^{-22}	1.9×10^{-6}

* Based on $p(H_2):p(H_2O)$ ratio

Results and Discussion

Figure 3 compares the weight changes for the Fe_3Al alloys (28% Al) at 450°C with those for the FeCrAl alloy. The weights increased for the first 600 h and then became constant or decreased slightly. Except for one of the FAS specimens, all the iron aluminides showed lower weight gains than the FeCrAl alloy. The FAP alloy (16% Al) at 450°C showed relatively high initial weight losses (>8 mg/cm^2) followed by still larger weight gains (≤75 mg/cm^2) after 600 h. As shown in Figure 4, at 550°C weight gains of the Fe_3Al alloys increased uniformly with test time, although the gains were initially less than those for corresponding times at 450°C. After

1000 h the gains at 550°C were approximately the same as at 450°C and were approximately half the weight gains of FeCrAl at 550°C. The FAP alloy at 550°C showed a relatively high weight gain after only 20 h, but after 1000 h the weight gain was somewhat less than at 450°C.

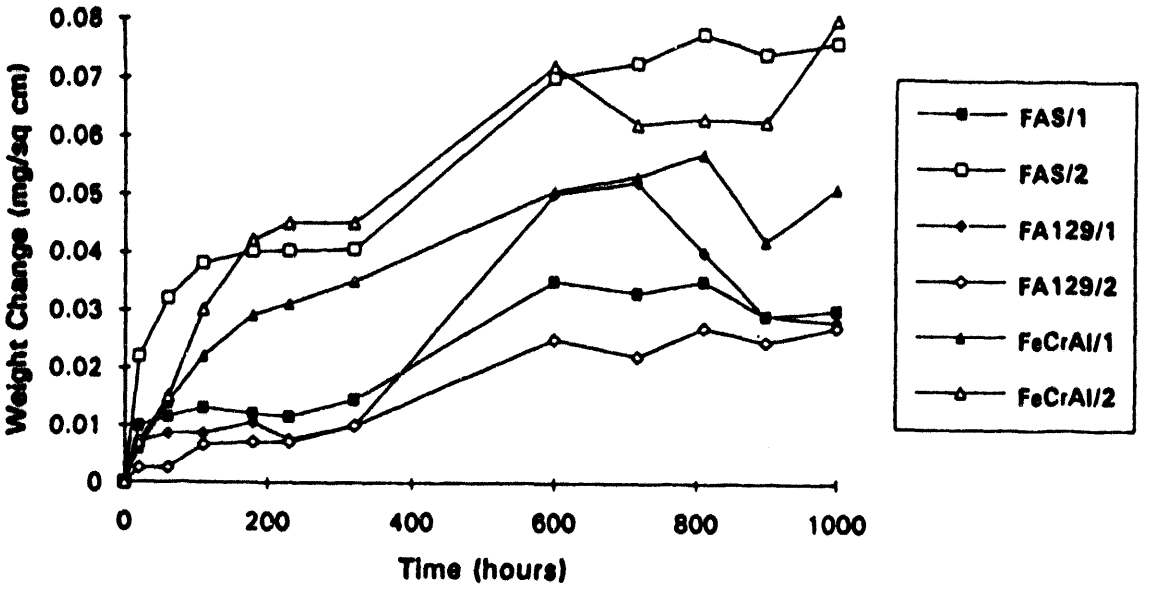

Figure 3. Comparative weight changes of Fe_3Al-based alloys and FeCrAl at 450°C in simulated coal gas atmosphere containing 1000 ppm HCl.

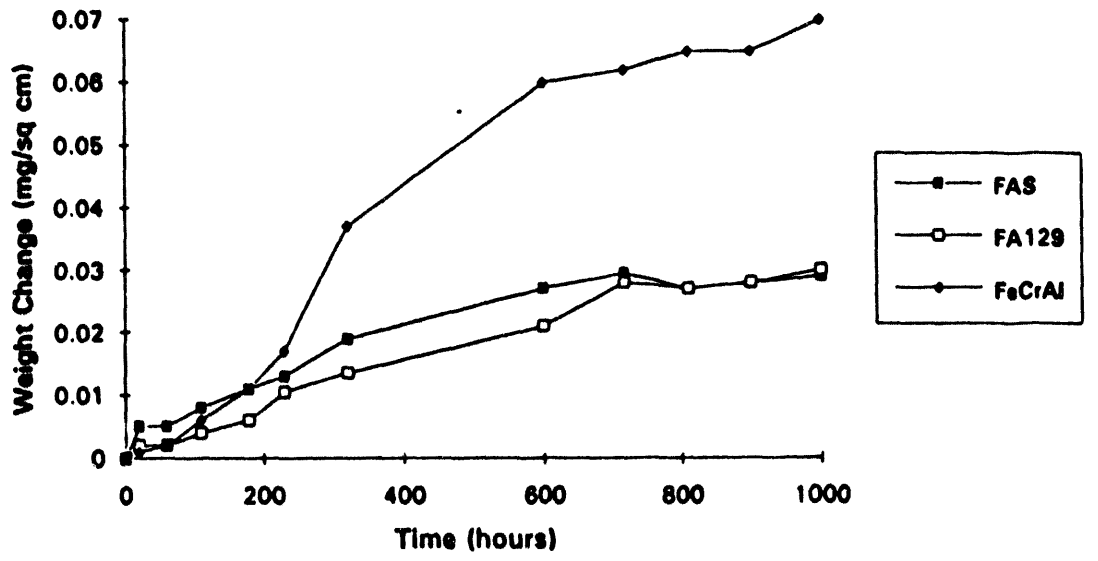

Figure 4. Comparative weight changes of Fe_3Al-based alloys and FeCrAl at 550°C in simulated coal gas atmosphere containing 1000 ppm HCl.

The relatively low weight changes observed for the Fe_3Al alloys in these tests are in accord with results from laboratory tests conducted at higher temperatures (700-800° C) in H_2S-containing gas mixtures without HCl.[9] However, the FAP alloy was much less resistant to attack in the NPL test environment than in the higher temperature laboratory tests in mixed gas with H_2S and no HCl. Furthermore, in the latter laboratory tests, the sulfidation resistance of the FAP alloy, though less than that of the Fe_3Al alloys, was significantly better that of the FeCrAl alloy.[10] The higher chromium content of the FeCrAl alloys and the lower aluminum content both contributed to the poorer performance of this material under purely sulfidizing conditions at ≥700° C. In the case of the NPL tests, where the exposure temperatures are lower and HCl is present, chromium at the 20% level no longer had a detrimental effect on corrosion resistance, particularly compared to the FAP alloy containing 16% aluminum and 5% chromium. Furthermore, the addition of 5% chromium to the Fe_3Al base composition (FA129), which markedly reduces the sulfidation resistance against H_2S at higher temperatures,[10] either did not change or slightly improved the corrosion resistance in the NPL tests. To what extent this result is due to the lower temperature or to the influence of HCl is not clear from the present test results. However, the absence of any significant effect of the HCl on the corrosion resistance of the Fe_3Al-based alloys suggests that the lower temperature may be the more important factor.

REFERENCES

1. J. H. DeVan and P. F. Tortorelli "Environmental Effects on Iron Aluminides", *Proceedings of the Seventh Annual Conference Fossil Energy Materials*, ORNL/FMP-93/1, 277-288, Oak Ridge National Laboratory, Oak Ridge, TN (1993).

2. P. F. Tortorelli, J. H. DeVan and E. K. Abdali, "Cyclic Oxidation of Iron Aluminides:, *CORROSION 93*, paper 258/9, National Association of Corrosion Engineers, Houston (1993).

3. W. J. Quadakkers and M. J. Bennett, "Oxidation Induced Lifetime Limits of Thin Walled, Iron Based, Alumina Forming Oxide Dispersion Strengthened Alloy Components", to be published in *Materials Science and Technology*, 1994.

4. M. J. Bennett, R. Perkins, J. B. Price and J. A. Desport, "The Oxidation Behavior of Alumina Forming Ferritic Oxide Dispersion Strengthened alloys", to be published in the *Proceedings of the First Mexican Symposium on Metallic Corrosion*, held at Merida, Yucatan, Mexico, March 7-12, 1994.

5. F. A. Golghtly, F. H. Stott and G. C. Wood, "The Influence of Yttrium Additions on the Oxide Scale Adhesion on a Fe-Cr-Al Alloy", *Oxid. Met.*, 10, 163-187 (1976).

6. B. A.Pint, J. R. Martin, and L. W. Hobbs, "^{18}O/SIMS Characterization of the Growth Mechanism of Doped and Undoped α-Al_2O_3", *Oxid. Met.* 39, 167-195 (1993).

7. R. Prescott and M. J. Graham, "The Formation of Aluminum Oxide Scales on High Temperature Alloys", *Oxid. Met.*, 38, 233-255 (1992).

8. W. T. Bakker, "Effect of Gasifier Environment on Materials Performance", *Materials at High Temperatures*, 11 (1-4), 81-93 (1993).

9. J. H. DeVan and P. F. Tortorelli, "Oxidation/Sulfidation of Iron-Aluminum Alloys", *Materials at High Temperatures*, 11 (1-4), 30-35 (1993).

10. J. H. DeVan and P. F. Tortorelli, "The Oxidation Behavior of Iron Alloys Containing 16-40 at % Aluminum", *Corrosion Science*, 35 (5-8) 1065-1071 (1993).

2.8 Cr_2Nb-BASED ALLOY DEVELOPMENT

C. T. Liu, J. A. Horton, and C. A. Carmichael

Oak Ridge National Laboratory
Metals and Ceramics Division
P. O. Box 2008
Oak Ridge, TN 37831-6115

ABSTRACT

This paper summarizes recent progress in developing Cr_2Nb/Cr(Nb) alloys for structural use in advanced fossil energy conversion systems. Alloy additions were added to control the microstructure and mechanical properties. Two beneficial elements have been identified among all alloying additions added to the alloys. One element is effective in refining the coarse eutectic structure and thus substantially improves the compressive strength and ductility of the alloys. The other element enhances oxidation resistance without sacrificing the ductility. The tensile properties are sensitive to cast defects, which can not be effectively reduced by HIPping at 1450-1580°C and/or directionally solidifying via a floating zone remelting method.

INTRODUCTION

The objective of this task is to develop new-generation structural materials based on intermetallic alloys for use as critical hot components in advanced fossil energy conversion systems. The intermetallic phase, Cr_2Nb, with a C-15 complex cubic structure,[1] has been selected for this development effort because of its high-melting point (1770°C),[2-3] relatively low density (7.7 g/cm^2),[4] and potential resistance to oxidation and corrosion.[2] This intermetallic phase, like many other Laves phases, has a wide range of compositional homogeneity,[3] suggesting the possibility of improving its mechanical and metallurgical properties by alloy additions.

The major concern with Cr_2Nb and other A_2B Laves phases is their poor toughness and fracture resistance at ambient temperatures.[2,5,6] The single-phase Cr_2Nb is very hard (~800 DPH) and brittle at room temperature. Because of the brittleness, our development effort has been concentrated on two-phase structures containing the intermetallic phase Cr_2Nb (hard phase) and the Cr-rich solid-solution phase (ductile phase). Previous studies

indicated that the two-phase alloys exhibited plastic deformation under compression tests at room temperature, with strength much superior to nickel-base superalloys at and above 1000°C.[5,7,8] Bhandarker[9,10] has demonstrated that a dispersion of Fe_2Ta Laves-phase particles dispersed within grains of a ferritic steel produced good elevated-temperature strength without causing low-temperature embrittlement. Recently, considerable effort has been devoted to the development of new superalloys containing Laves phases for high-temperature structural use.[5-8, 10-16]

Our results obtained so far indicate that the two-phase Cr_2Nb/Cr(Nb) alloys have excellent strength for structural use at ultrahigh temperatures (e.g., 1000-1200°C).[5-8] Potential applications include hot components in advanced energy conversion systems, advanced heat engines, and high-temperature cutting and grinding tools. Current studies are focused on enhancement of fracture resistance and oxidation resistance. This report summarizes our recent progress on controlling microstructure and improving mechanical properties of Cr_2Nb/Cr(Nb) alloys through alloying additions and material processing. A detailed study of the corrosion behavior of these alloys has been reported separately by Tortorelli et al.[17-19]

ALLOY PREPARATION AND PROCESSING

Cr_2Nb/Cr(Nb) alloys weighing 300 g were prepared by arc melting and drop casting in copper molds (1" diam. x 3" long). In order to minimize the interstitial content (e.g., oxygen) in these alloys, high-purity niobium and chromium metal chips were used as charge materials, and the alloys were melted in a high vacuum (10^{-5} Pa) furnace. Cast molds were pre-heated to 100-300°C in order to control solidification and to reduce thermal shock during drop casting.

Oxide slags in cracked pieces were observed on the top of alloy buttons and ingots. Sometimes, these oxides were found to be trapped inside alloy ingots. Careful x-ray fluorescence studies indicate that these oxide slags contain mainly zirconium and aluminum. Removal of zirconium and aluminum from the alloys dramatically reduces the slag amount. The drop-cast behavior of the alloys is also sensitive to alloy additions. The drop castability can be substantially improved by certain alloying elements; however, these elements can only be identified by melting and casting practice.

The cast alloy ingots generally contain cast cavities, which vary in size from a few to several hundred μm. The existing phase diagram of the Cr-Nb system indicates an eutectic temperature of 1620°C for the Cr_2Nb and Cr-rich phases.[3] Accordingly, the Cr_2Nb/Cr(Nb) alloys were HIPped at 1450 and 1580°C at a maximum stress of 207 MPa

(30 ksi) in order to reduce or eliminate the cavities. Metallographic examination of the ingot interior indicates only marginal reduction in cast porosities by these HIPpings. This observation indicates extremely high strength at these temperatures and/or a higher melting point of these alloys. Thus, we re-examined the incipient melting point of the chromium niobium (CN) alloys. In this study, alloy specimens were rapidly heated from 1200°C to a preset temperature and kept at that temperature for 6 min., followed by turning off the power. Our studies indicate that the melting point of CN alloys is ~1670 ± 20°C, which is about 50°C above the reported eutectic temperature for the Cr-Nb system. Based on the determined melting point, we plan to HIP the alloys again at a temperature close to 1650°C.

Two alloys, CN-67 and -65, were processed by floating-zone remelting at a velocity of 1.9 - 2.4 cm/hr in high-purity inert gas at the University of Tennessee, using drop-cast ingots as a starting material. Figure 1 shows the rough ingot surfaces, which resulted from evaporation of chromium and formation of surface oxides during crystal growth. Metallographic examination of sectioned ingots shows large holes formed near the ingot surfaces (probably due to chromium evaporation) and cast micro-cavities away from the surface region. This observation indicates that cast cavities in these alloys cannot be completely eliminated by directional solidification through a floating-zone remelting method.

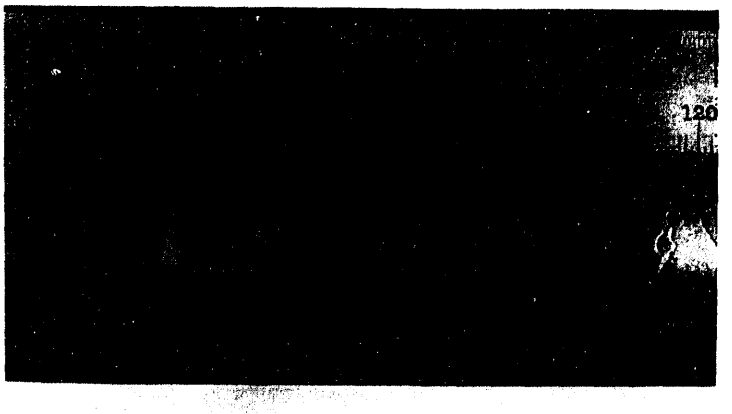

Fig. 1 CN-65 alloy ingot prepared by levitation-zone remelting.

EFFECT OF ALLOYING ADDITIONS ON MICROSTRUCTURE AND PHASE COMPOSITION

During this year, a total of 25 new alloys were prepared. A partial list of the alloy compositions is shown in Table 1. The alloys with 5.6 to 12 at. % Nb basically contain primary Cr-rich solid solution surrounded by the eutectic structure (Fig. 2a), a mixture of Cr_2Nb-type and the Cr-rich phases. The supersaturated Cr-rich solid solution (bright-contrast phase) precipitates out Cr_2Nb-type particles when annealed above 1000°C. The brittle, coarse Cr_2Nb particles in the eutectic structure are, in most cases, interconnected into a skeleton (dark-contrast phase in Fig. 2a) which is believed to be one of the major causes of poor fracture resistance of the CN alloys.

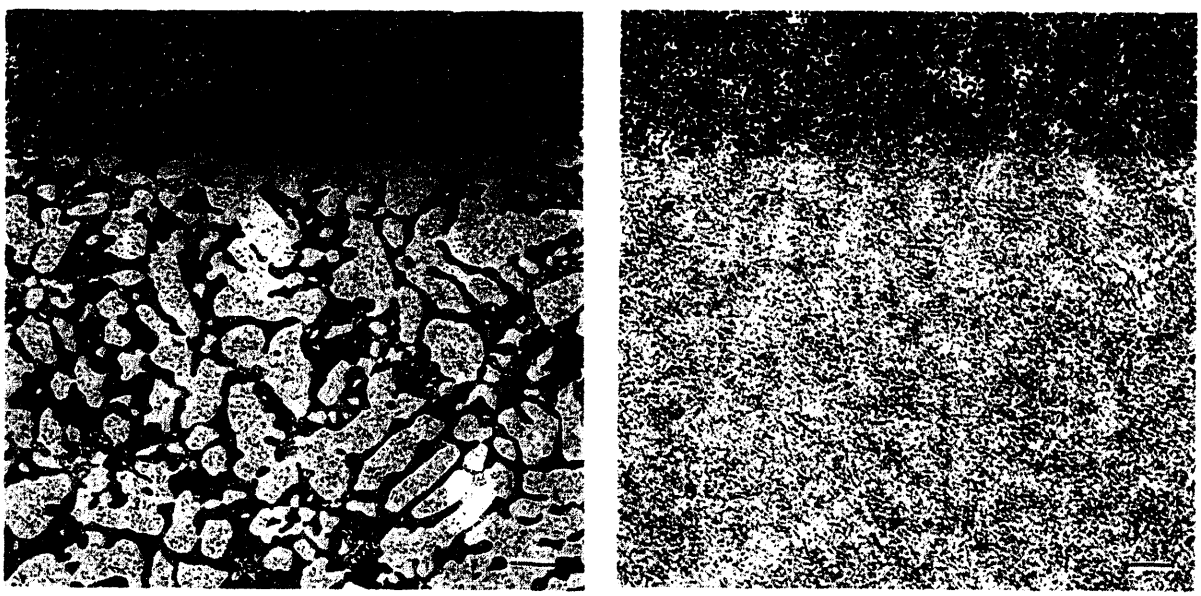

(a) (b)

Fig. 2 Optical micrographs of (a) CN-61 and (b) CN-60 annealed for 3 d at 1100°C. (Scale marker is 10 μm).

Alloying additions were added to refine the coarse Cr_2Nb eutectic structure in the CN alloys. Among all elements added to the alloys, the element referred to as XM is most effective in refining the interconnected eutectic structure (Fig. 2b). As shown in Fig. 3, the eutectic skeleton is broken into blocky Cr_2Nb-type particles in the alloy containing 6% XM. Another element, referred to as XO, is found to be most effective to date in improving oxidation resistance of the CN alloys. Because of their beneficial effects, a series of alloys containing these two elements were prepared as shown in Table 1. Our

studies of the mechanical properties and oxidation resistance[19] suggest the optimum amount of XM and XO in the same alloy to be 6 and 4%, respectively.

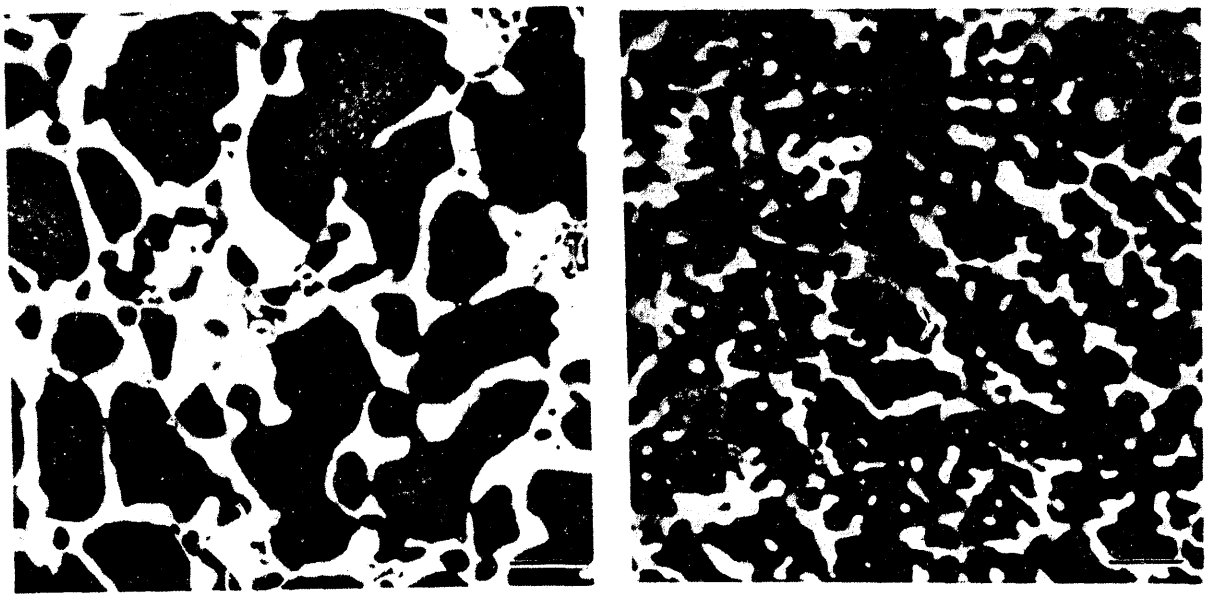

(a) (b)

Fig. 3 Backscattered electron images of (a) CN-61 and (b) CN-60 annealed for 3 d at 1100°C. (Scale marker is 10 μm).

Table 1. Nominal Alloy Compositions of Selected CN Alloys

Alloy Number	Composition (at. %)
CN-60	Cr-12.0Nb-4.0Re-2.0Al-6.0XM
CN-80	Cr-12.0Nb-1.5Al-6.0XM
CN-72	Cr-12.0Nb-1.5Al-0.1Zr-6.0XM
CN-61	Cr-12.0Nb-4.0Re-2.0Al-4.0XO
CN-81	Cr-10.0Nb-1.5Al-6.0XM-4.0XO
CN-67	Cr-8.0Nb-1.5Al-0.1Zr-6.0XM
CN-64	Cr-5.6Nb-1.5Al-0.1Zr-4.0XM
CN-65	Cr-5.6Nb-1.5Al-0.1Zr-6.0XM
CN-69	Cr-5.6Nb-1.5Al-6.0XM
CN-70	Cr-5.6Nb-1.5Al-0.1B-6.0XM
CN-68	Cr-5.6Nb-1.5Al-0.1Zr-4.0Re-6.0XM
CN-66	Cr-5.6Nb-1.5Al-0.1Zr-10.0XM
CN-71	Cr-5.6Nb-1.5Al-0.1Zr-15.0XM
CN-74	Cr-5.6Nb-1.5Al-0.1Zr-6.0XM-4.0XO
CN-75	Cr-5.6Nb-1.5Al-0.1Zr-6.0XM-6.0XO
CN-76	Cr-5.6Nb-1.5Al-0.1Zr-6.0XM-8.0XO

Figure 4 shows the effect of heat treatment on the microstructures of the CN-65 alloy containing 5.6% Nb. Fine precipitates distribute uniformly across grains and some coarse Cr_2Nb particles are observed at grain boundaries in the specimen (Fig. 4a) annealed at 1100°C for 3 days. HIPping at 1450°C apparently dissolved a major part of the fine precipitates within grains but did not remove the coarse Cr_2Nb particles at grain boundaries (Fig. 4b). A few cavities are visible in the HIPped specimen. Figure 5 shows the microstructure of the alloy containing 6% XM and 6% XO, where the eutectic structure can be easily identified. Comparison of Fig. 5 with Figs. 3b and 4a suggests that XO additions stabilize the classic eutectic structure.

The composition of phases in CN alloys was determined by electron microprobe analyses. Table 2 summarizes the composition of the phases determined by wavelength-dispersive spectrometry (WDS). The Cr-rich solid solution, the matrix phase, contains a low level of niobium, ~1%. The Cr_2Nb-type phase, on the other hand, contains more than 20% Nb, and the exact amount of niobium in the Cr_2Nb-type phase depends on the partitioning of alloying additions in the CN alloys. The element XM partitions more or less equally in the Cr_2Nb and the Cr-rich phases. The analysis of the composition of Cr_2Nb-type phase in CN-65 indicates that XM essentially occupies the niobium sites. The element XO in CN-75 partitions strongly in the Cr_2Nb-type phase, as indicated in Table 2. The partitioning ratio of XO in the Cr_2Nb-type and Cr-rich phases is 5.6 to 1. Unlike XM,

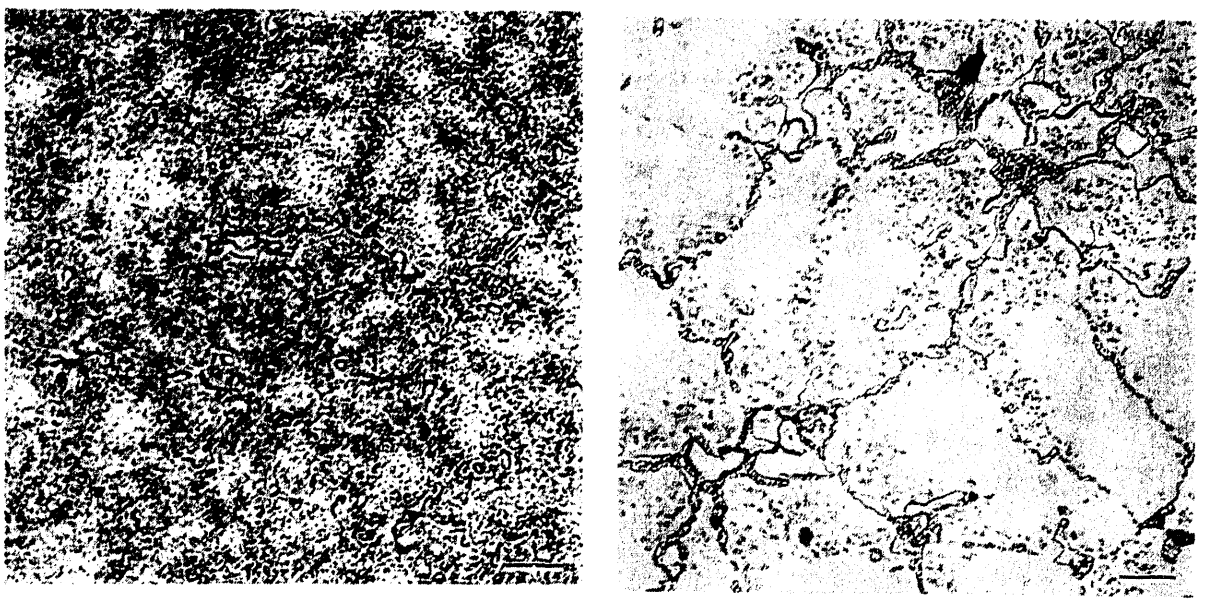

(a) (b)

Fig. 4 Optical micrographs of CN-65 (a) annealed for 3 d at 1100°C, and (b) HIPped for 2 h at 1450°C. (Scale marker is 10 μm).

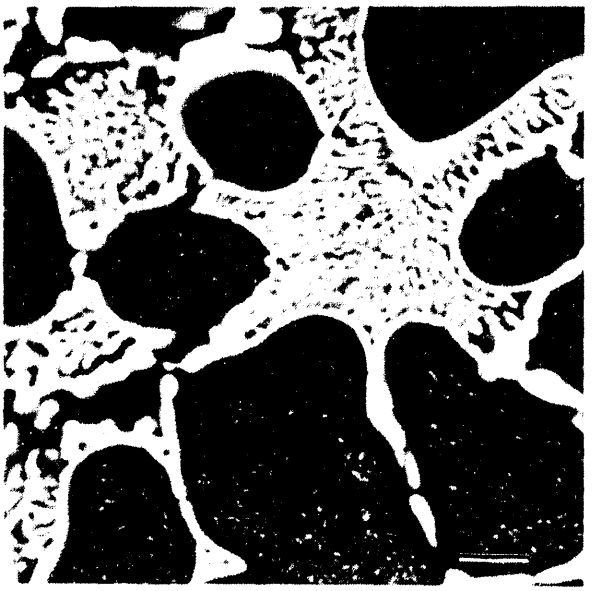

Fig. 5 Backscattered electron image of CN-75 annealed for 3 d at 1200°C. (Scale marker is 10 μm).

Table 2. WDS Compositional Analysis of CN Alloys*

Alloy Number	Cr_2Nb-type Phase (at.%)	Cr-rich Matrix Without Fine Cr_2Nb Precipitates (at.%)	Cr-rich Matrix With Fine Cr_2Nb Precipitates (at.%)
CN-65	Cr = 67.0 Nb = 25.8 XM = 5.4 Al = 1.8 Zr = 0.0	Cr = 90.9 Nb = 1.2 XM = 6.7 Al = 1.2 Zr = 0.0	Cr = 88.2 Nb = 4.4 XM = 6.2 Al = 1.2 Zr = 0.0
CN-60	Cr = 63.4 Nb = 25.4 XM = 5.0 Re = 4.2 Al = 2.0		Cr = 79.0 Nb = 7.6 XM = 6.8 Re = 5.1 Al = 1.5
CN-75	Cr = 55.0 Nb = 22.3 XM = 7.9 XO = 14.0 Al = 0.8 Zr = 0.0	Cr = 90.2 Nb = 0.6 XM = 5.2 XO = 2.5 Al = 1.5 Zr = 0.0	Cr = 86.8 Nb = 3.0 XM = 5.5 XO = 3.4 Al = 1.3 Zr = 0.0

*Specimens annealed for 3 d at 1100°C or 1200°C.

XO mainly occupies the Cr sites instead of the niobium sites. The elements rhenium and aluminum partition approximately equally in the two phases. Zirconium was not detected in the CN alloys, and was probably lost due to its formation of ZrO_2 slags during melting.

The alloys CN-60 and CN-61 were examined by transmission electron microscopy (TEM). Both alloy specimens were annealed for 3 d at 1100°C, and then cut into 3 mm disks and ground to a thickness of approximately 50 μm, followed by ion milling at 6 kV. The specimens were examined in a Philips CM30 at 300 kV. Energy dispersive spectroscopy (EDS) was performed with an EDAX 9100 spectrometer. The EDS analyses were made on precipitates that intersected the ion milling perforations, thereby minimizing the contributions from surrounding matrix material.

Both alloys showed a mixture of the Cr-rich solid solution and Cr_2Nb-type phases. The small precipitates in the Cr-rich matrix ranged up to 0.4 μm in diameter. Figure 6a shows the eutectic structure (dark areas) in CN-61 (containing 4% XO) with only a few secondary precipitates visible. Figure 6b shows a region in CN-60 (containing 6% XM) with an extensive secondary precipitation. EDS analyses of the matrix versus the precipitates were made along the edge of the specimen as shown in Fig. 6b. Figure 6c shows dislocations in the Cr-rich matrix in CN-60. While many of the dislocations appeared to have interacted with small precipitates by bowing between them, many other dislocations have formed low-angle network structures.

EDS results were averaged and are shown in Table 3. Basically, the data in Table 3 agree well with those in Table 2 determined by electron microscopic analysis. In CN-60, the XM and rhenium additions did not preferentially partition to Cr_2Nb particles. Only about 1% of niobium remained in solution, with the rest precipitating out. In CN-61, the XO additions did preferentially precipitate out with the niobium in Cr_2Nb-type particles, while again the rhenium levels were similar in both matrix and in the Cr_2Nb-type phase. Apparently, no zirconium was retained by the alloy.

MECHANICAL BEHAVIOR

Compressive Properties

Because the cast CN alloys, even in the HIPped conditions, contain defects such as cavities, the compressive properties are much less sensitive to these defects.

Therefore, the compressive properties of the CN alloys were determined at temperatures to 1200°C. Alloy specimens were annealed for 3 d at 1100°C prior to testing at room temperature in air and at elevated temperatures in vacuum. Tables 4 and 5 summarize the results at different temperatures. For the alloys containing 12 at.% Nb, the yield strength at room temperature increases significantly by alloying with XM, rhenium, and XO. However, only XM improves the room-temperature ductility. XM is also very

Fig. 6 TEM micrographs of (a) the eutectic Cr_2Nb structure in CN-61, (b) block particles in CN-60, and (c) dislocations in CN-60. All specimens were annealed for 3 d at 1100°C.

Table 3. EDS/TEM Compositional Analysis of CN-60 and CN-61

Alloy No.	Concentrations (at.%) Cr	Nb	Re	Al	XM	XO
CN-60						
nominal	76	12	4	2	6	
matrix	86	1	5	0	7	
secondary precipitation	52	39	5	0	3	
large precipitates	63	28	4	0	5	
CN-61						
nominal	78	12	4	2		4
matrix	91	1	3	1		5
large precipitates	53	28	4	1		13
secondary precipitates	57	29	5	0		15

Table 4. Compressive Properties of CN Alloys Tested at Room Temperature in Air

Alloy No.	Concentration of Key Elements (at.%)	Strength, MPa (ksi) Yield	Ultimate	Ductility (%)
CN-4	12Nb	960 (139)	1760 (255)	5.4
CN-44	12Nb-4Re	1230 (179)	2050 (298)	4.3
CN-60	12Nb-4Re-6XM	1793 (260)	2546 (369)	8.5
CN-61	12Nb-4Re-4XO	1395 (202)	1946 (282)	5.2
CN-7	6Nb	702 (102)	1261 (183)	9.5
CN-65	5.6Nb-6XM	1116 (161)	2228 (323)	16.0
CN-65*	5.6Nb-6XM	1097 (159)	2116 (307)	18.5
CN-68	5.6Nb-4Re-6XM	1111 (161)	2023 (293)	17.7
CN-70*	5.6Nb-0.1B-6XM	1047 (152)	2059 (297)	16.3
CN-75	5.6Nb-6XM-6XO	1300 (189)	2080 (302)	16.2

*HIPped at 1450°C and annealed 3 d/1100°C.

effective in improving both the strength and ductility of the CN alloys containing 5.6-6% Nb at room temperature (Table 4). The alloy CN-65 containing 5.6% Nb and 6% XM showed a yield strength of 1097 MPa and a ductility of 18.5% at room temperature.

Alloying with 6% XO together with 6% XM appears not to lower the room-temperature ductility of the 5.6% Nb alloy.

At 1000 and 1200°C, both XM and rhenium effectively increase the compressive strength of the CN alloys containing 5.6 and 12% Nb (Table 5). The ductility of the alloys is not sensitive to alloying additions, and all the alloys showed ductility of more than 23%. HIPping at 1450°C appears not to affect the ductility at either room or elevated temperatures. The CN alloys are much stronger than Ni-base superalloys, whose strength drops to about zero at 1200°C.

Table 5. Compressive Properties of CN Alloys Tested at 1000 and 1200°C in Vacuum

Alloy No.	Concentration of Key Elements (at.%)	Strength, MPa (ksi) Yield	Ultimate	Ductility (%)
		1000°C		
CN-4	12Nb	685 (99)	856 (124)	22.8
CN-44	12Nb-4Re	855 (124)	1061 (154)	26.2
CN-60	12Nb-4Re-6XM	896 (130)	1632 (237)	29.2
CN-61	12Nb-4Re-4XO	741 (107)	1257 (182)	28.5
CN-7	6.0Nb	436 (63)	738 (107)	32.7
CN-65	5.6Nb-6XM	634 (92)	1203 (174)	33.8
CN-68	5.6Nb-4Re-6XM	675 (98)	1118 (162)	26.5
CN-70*	5.6Nb-0.1B-6XM	778 (113)	1394 (202)	23.1
CN-75	5.6Nb-6XM-6XO	710 (103)	1302 (189)	32.4
		1200°C		
CN-4		363 (53)	487 (71)	>31.5
CN-44		432 (63)	566 (82)	> 4.1
CN-60		535 (78)	664 (96)	> 5.6
CN-7		258 (37)	309 (45)	31.4
CN-65		404 (59)	547 (79)	30.4

*HIPped at 1450°C.

Tensile Properties

Tensile properties of HIPped and/or directionally solidified specimens were determined at room temperature and 1000°C. As mentioned before, these specimens contain cast defects (even after HIPping), and only the highest fracture strength for each alloy are reported in Table 6. The alloys showed a fracture strength at a level of 200-500

MPa, which appears to be independent of alloy composition. There is no apparent difference in fracture strength at room temperature and 1000°C, suggesting that the fracture process is dominated by cast defects in the alloys. Further studies are required to reduce cast defects by either HIPping at higher temperature (>1580°C) or hot extruding the CN alloys. A recent study of two-phase alloys based on Nb and Nb_5Si_3 indicates that their tensile ductility and strength can be dramatically improved by hot extrusion of the alloys at 1426°C.

Table 6. Tensile Properties of CN Alloys Tested at Room Temperature in Air and 1000°C in Vacuum

Alloy No.	Alloy Composition (at.%)	Treatment Condition*	Fracture Stress, MPa (ksi)
	Room Temperature		
CN-70	Cr-5.6Nb-1.5Al-0.1B-6XM	HIP/1450°C	326 (47.3)
CN-65	Cr-5.6Nb-1.5Al-0.1Zr-6XM	HIP/1580°C	266 (38.6)
CN-65	Cr-5.6Nb-1.5Al-0.1Zr-6XM	DS	367 (53.3)
CN-67	Cr-8Nb-1.5Al-0.1Zr-6XM	DS/HIP/1580°C	207 (30.1)
CN-74	Cr-5.6Nb-1.5Al-0.1Zr-6XM-4XO	HIP/1580°C	416 (60.4)
	1000°C		
CN-70	Cr-5.6Nb-1.5Al-0.1B-6XM	HIP/1450°C	478 (69.4)
CN-65	Cr-5.6Nb-1.5Al-0.1Zr-6XM	HIP/1580°C	360 (52.2)
CN-67	Cr-8Nb-1.5Al-0.1Zr-6XM	DS/HIP/1580°C	382 (55.5)
CN-74	Cr-5.6Nb-1.5Al-0.1Zr-6XM-4XO	HIP/1580°C	248 (36.0)

HIP = hot isostatically pressing
DS = directional solidification by levitation zone remelting

Fracture surfaces of the tensile specimens tested at room temperature and 1000°C were examined using a scanning electron microscope operated at 10 kV. The CN alloys showed mainly cleavage fracture at both temperatures with a more ductile appearance at 1000°C. Cast defects are visible on the fracture surfaces.

Creep Resistance

We recently initiated creep tests of CN alloys containing XM. The alloy CN-70 showed no measurable creep deformation at 1200°C at a stress of 55 MPa (8 ksi), indicating excellent creep resistance. The alloy exhibited a creep rate of 1.5×10^{-7} h^{-1} at

1000°C at a stress of 345 MPa (50 ksi). The alloy is much more creep resistant than Ni-base superalloys.

ACKNOWLEDGMENTS

The authors are grateful to Ben Oliver (University of Tennessee) for processing of the alloys by levitation-zone remelting, Tommy Henson for electron microprobe analyses, Dewey Easton for x-ray fluorescence analyses, and Joe Wright and Elmer Lee for metallography. Thanks are also due to Sharon Kneé for preparation of the manuscript.

REFERENCES

1. F. Laves, in *Theory of Alloy Phases*, American Society for Metals, Metals Park, OH, 1956, p. 124.

2. H. J. Goldschmidt and J. A. Brand, J. *Less-Common Met.* **3**, 44 (1961).

3. T. B. Massalski, J. L. Murray, L. H. Bennett, and H. Baker (eds.), *Binary Alloy Phase Diagram*, American Soceity for Metals, Metals Park, OH, 1986.

4. A. I. Taub and R. L. Fleischer, *Science* **243**, 616 (1989).

5. M. Takeyama and C. T. Liu, *Mat. Sci. and Eng.* **A132**, 61 (1991).

6. J. D. Livingston, *Phys. Stat. Sol.* (a)**131**, 415 (1992).

7. C. T. Liu, pp. 375-383 in *Proc. 6th Annual Conf. on Fossil Energy Materials*, ORNL/FMP-9211, Oak Ridge National Laboratory, July 1992.

8. C. T. Liu, J. A. Horton, and C. A. Carmichael, pp. 297-307, in *Proc. 7th Annual Conf. on Fossil Energy Materials*, ORNL/FMP-93/1, Oak Ridge National Laboratory, July 1993.

9. M. D. Bhandarkar, M. S. Bhat, V. F. Zackay, and E. R. Parker, *Metall. Trans.* **6A**, 1281 (1975).

10. M. D. Bhandarkar, M. S. Bhat, E. R. Parker, and V. F. Zackay, *Metall. Trans.* **7A**, 753 (1976).

11. Y. Liu, J. D. Livingston, and S. M. Allen, *Metall. Trans. A*, **23A**, 3303 (1992).

12. K. C. Chen, S. M. Allen, J. D. Livingston, p. 373 in MRS Proc. Vol. 288, ed. Baker et al. (1993).

13. Y. Liu, S. M. Allen, and J. D. Livingston, p. 203 in MRS Proc. Vol. 288, ed. Baker et al. (1993).

14. R. L. Fleischer, *Scr. Metall.* **27**, 1799 (1992).

15. D. L. Anton and D. M. Shah, p. 733 in MRS Proc. Vol. 213, ed. Johnson et al. (1991).

16. G. E. Vignoul, J. M. Sanchez, and J. K. Tien, p. 739 in MRS Proc. Vol. 213, ed. Johnston et al. (1991).

17. P. F. Tortorelli and J. D. DeVan, pp. 229-236 in Proc. Symp. on *Oxide Films on Metals and Alloys*, B. R. MacDougall, R. S. Alwitt, and T. A. Ramanarayanan (eds.), Proceedings Vol. 92-22, The Electrochemical Society, 1992.

18. P. F. Tortorelli, L. J. Carsen, and J. H. DeVan, pp. 309-318 in *Proc. 7th Annual Conf. on Fossil Energy Materials*, ORNL/FMP-93/1, Oak Ridge National Laboratory, July 1993.

19. P. F. Tortorelli and J. H. DeVan in this procs.

20. M. G. Mendiratta and D. M. Dimiduk, *Metall. Trans. A.* **24A**, 501 (1993).

21. M. G. Mendiratta, J. J. Lewandowski, and D. M. Dimiduk, *Metall. Trans. A* **22A**, 1573 (1991).

2.9 DEVELOPMENT OF IRON ALUMINIDES

C. G. McKamey, S. Viswanathan, G. M. Goodwin, and V. K. Sikka

INTRODUCTION

Recent studies have demonstrated that improved engineering ductility (to 10-15% in Fe_3Al) can be achieved in wrought Fe_3Al-based iron aluminide alloys through control of composition and microstructure.[1-4] Accompanying this improvement has been an increased understanding of the causes for ambient temperature embrittlement in this system.[5-6] Because of these advances, iron aluminide alloys are being considered for many structural uses, especially for applications where their excellent corrosion resistance is needed. Several alloy compositions developed at ORNL have been licensed to commercial vendors for development of scale-up procedures. With the licensees and other vendors, several applications for iron aluminides are being pursued.

The understanding and control of cast structures are important steps in making iron-aluminide alloys viable engineering materials. This includes understanding the various components of cast structure, their evolution, their properties, their behavior during further processing, and, finally, their effect on mechanical properties. The first phase of our study of cast Fe_3Al-based alloys characterized the various components of the cast structure in the FA-129 alloy,[7,8] while the current phase of the research involves characterizing the as-cast mechanical properties of Fe_3Al-based alloys. Room temperature mechanical properties in air for the cast and cast-plus-homogenized condition have been reported previously.[7,8] In this reporting period, we have continued the investigation of the room temperature mechanical properties of as-cast Fe_3Al, including tensile tests in air, oxygen, and water vapor environments. We have also begun studies to refine the grain size of the cast structure. An investigation of the effect of environmental hydrogen embrittlement on the weldability of wrought alloys was also initiated during this period with the aim of understanding the role of environment in the cold-cracking of iron aluminides.

DISCUSSION OF CURRENT ACTIVITIES

Tensile Properties of As-Cast Iron Aluminide Alloys

Vacuum induction melts of Fe_3Al-based FA-129 alloy (Fe-28% Al-5% Cr-0.5%Nb-0.2%C, at.%) were prepared and cast in a mold of dimensions 32 × 180 × 110 mm.

Undersized tensile specimens (6.4 mm diam., 25.4 mm gauge length) were machined from the ingot. Two specimens were tested in each of three test environments: water vapor (75 torr and 400 torr pressure), oxygen (500 torr pressure), and laboratory air (approximately 30% humidity).

Figure 1 compares the tensile strength for tests conducted in air, oxygen, and water vapor environments. The alloy exhibited similar strength values in air and water vapor environments, approximately 200 MPa for yield strength and 300 MPa for ultimate tensile strength. Ductility values as measured by total elongation (Fig. 2) were also similar and comparatively low (about 1.5%) for the air and water vapor tests, although values in water vapor environments were marginally lower than those in air. In the oxygen environment, the alloy exhibited a yield strength very similar to that measured in air and water vapor. However, both ultimate tensile strength (400 MPa) and total elongation (3%) measured in the oxygen environment were significantly higher than values measured in air or water vapor. These results point to the existence of an environmental effect (embrittlement due to the hydrogen in water vapor) and parallel those obtained earlier for wrought materials.[5,6]

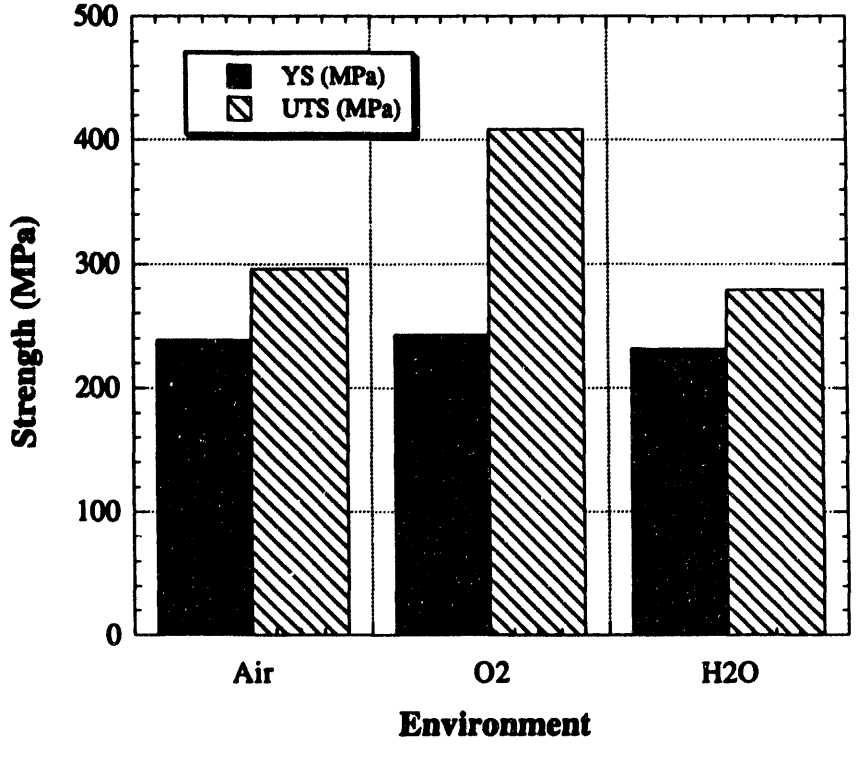

Figure 1. Room temperature tensile strength of as-cast FA-129 alloy tested in air (30% humidity), oxygen (500 torr), and water vapor (400 torr).

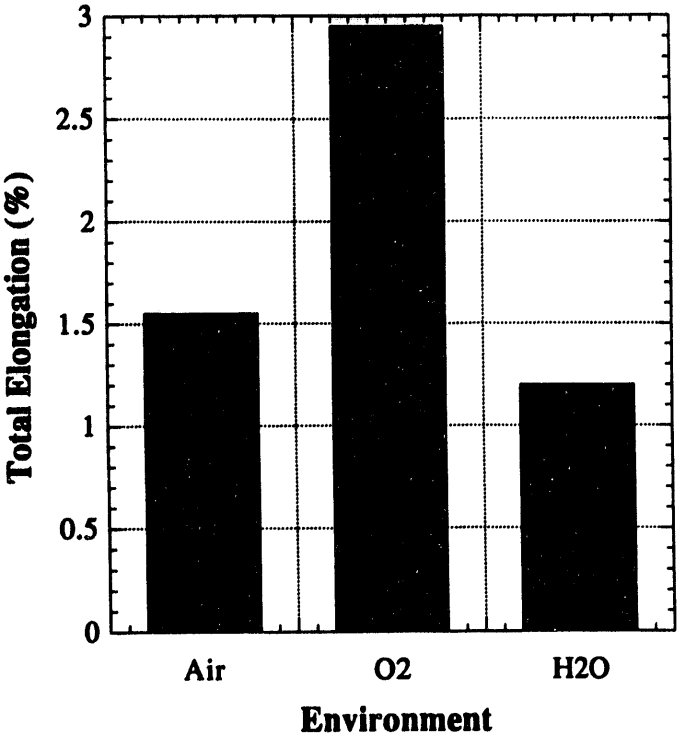

Figure 2. Room temperature tensile elongation of as-cast FA-129 alloy tested in air (30% humidity), oxygen (500 torr), and water vapor (400 torr).

Weldability

Corrosion-resistant, weldable iron aluminide alloys with improved high temperature strength are being developed for structural applications and as weld overlay cladding for conventional structural steels and alloys. Weldability of Fe_3Al is a priority of the Fossil Energy Materials Program, but alloying effects noted in other programs involving higher aluminum contents often provide helpful input.[9]

The iron aluminides are susceptible to two general types of cracking; hot cracking which occurs during solidification, and cold cracking which is hydrogen-related and happens during cooling or some hours or days after welding. Prior work on this program[10] found that iron aluminide alloys have a highly variable susceptibility to weld hot cracking, but that by appropriate compositional control, hot cracking resistance equivalent to commercial austenitic stainless steels can be achieved. Subsequent work has therefore emphasized the study of hydrogen-related cold cracking.

To reduce the number of variables involved, a single heat of Fe_3Al alloy (FA-185, heat #15479) has been used for essentially all of the recent cold cracking studies. This alloy contains 28% Al, 5% Cr, and 0.1% C (all in at. %). Testing has been performed using the Sigmajig fixture in a variety of controlled atmospheres. Although the Sigmajig test was designed to study hot cracking, it has also shown itself to be useful for evaluating cold cracking by several techniques, as will be described.

Heat #15479 has a hot cracking threshold stress of 19 ksi (131 MPa), indicating very good resistance to hot cracking. Its resistance to cold cracking is probably also better than average, based on the fact that transverse cold cracking is not observed during hot crack testing, as it is with most Fe_3Al compositions. The hot cracking threshold stress was also found to be 19 ksi (131 MPa) in the high purity glove box environment (<50 ppm oxygen plus water vapor), indicating no effect of atmospheric contamination on hot cracking. As far as cold cracking is concerned, however, the glove box environment was found to have a profound effect.

A series of tests was performed where welds were produced at a very low preapplied stress (5 ksi, 34 MPa), followed by the application of load after welding at a linear rate of 1 ksi (7 MPa) per minute until specimen separation occurred. Welds produced using normal shielding techniques in the ambient environment would withstand stresses of approximately yield strength magnitude (60 ksi, 414 MPa) unless liquid water was present on the specimen surface, in which case brittle failure occurred at 30 ksi (207 MPa), less than half of the yield strength.

Tests in the glove box were performed in pure argon (<50 ppm oxygen plus water vapor) and with intentional additions of hydrogen or water vapor, using both preapplied stress and the post-weld load application technique.

With preapplied stress, no cracking occurred in pure argon after welding at the threshold stress for hot cracking, 19 ksi (131 MPa). Welding in a mixture of 98% argon-2% hydrogen still did not result in cracking at preapplied stresses less than 19 ksi (131 MPa). Similar tests in 98% Ar-2% H_2O, however, gave complete specimen fracture at any preapplied stresses in excess of 6 ksi (41 MPa). This result strongly corroborates the mechanism cited by Liu et al.[5] for Fe_3Al. Further, with the assumption that both molecular hydrogen and water vapor would be ionized by the welding arc in roughly equal amounts, thus charging the

weld puddle with dissolved hydrogen, these results indicate that hydrogen from moisture in the environment has a much greater effect on cracking than dissolved hydrogen.

Ramp tests in the glove box atmospheres confirmed the preapplied stress results. Welds produced in 98% Ar-2% H_2 mixtures would withstand post-weld stresses of up to 16 ksi (110 MPa), whereas welds made in 98% Ar-2% H_2O consistently failed at 8 ksi (55 MPa).

The results of these thin sheet experiments suggest that structural welds in these materials will need to be stress relieved after welding, that design stresses will need to be restricted, and that weld overlay clad specimens should be subjected to environmental testing under stress.

Industrial Interactions on Fe_3Al-Based Alloys

In this reporting period there have been strong interaction with four industrial partners on Fe_3Al-based alloys. Each is briefly described below.

Rapid Technologies, Inc., Newnan, GA

The Fe_3Al-based alloy FA-129 with added zirconium has been identified as a material for rails in walking beam furnaces. The major advantages of the material are its high melting point and good high-temperature oxidation resistance up to 1375°C. The oxidation resistance data are based on two-week-long isothermal oxidation tests at 1375°C conducted at ORNL. Based on these properties, Rapid Technologies, Inc. has placed an order to procure over 20 rails from Manufacturing Sciences Corp. in Oak Ridge, TN. The rails are expected to go in service during the month of April. ORNL has worked very closely with Rapid Technologies, Inc. in alloy selection, the proposed method of manufacturing, chemical analyses, and generation of property data.

Manufacturing Sciences Corp, Oak Ridge, TN

ORNL scientists have worked closely with Manufacturing Sciences Corp. in identifying the manufacturing steps for iron aluminide rails. The selected steps include: vacuum melting of 182-kg (400-lb) heats, casting them into 102-mm-thick (4-in.) slabs, hot rolling them into 19-mm-thick (0.75 in.) plate, hot shearing into rough dimensions, surface cleaning by acid bath and/or sand blasting, and machining into final shape. A joint effort between ORNL and

Manufacturing Science Corp. is currently underway to identify inexpensive methods of machining the rails out of iron aluminide plate.

Babcock & Wilcox (B&W)

The B&W company has identified Fe_3Al-based alloys as shielding material for applications in boiler plants and incinerators. The shields are typically 3.2 mm (0.125 in.) thick and in the shape of a half tube. One prototype shield has already been supplied and several others are currently being fabricated. The shields are expected to go into service by the middle of June 1994.

PALL Corp.

Efforts continued during this period in support of PALL Corp. to resolve issues related to manufacturing of porous sintered metal gas filters. The support to PALL has been a joint effort between Ametek and ORNL. Most recently, Ametek has produced water-atomized powder and has supplied it to PALL and ORNL. Pall is developing the sintering techniques for this powder, while ORNL is consolidating, evaluating its microstructure and properties, and comparing it to the gas-atomized powder produced earlier by Ametek.

REFERENCES

1. R. G. Bordeau, *Development of Iron Aluminides*, AFWAL-TR-87-4009 (Air Force Wright Aeronautical Laboratories, Wright-Patterson Air Force Base, OH, May 1987).
2. G. Culbertson and C. S. Kortovich, *Development of Iron Aluminides*, AFWAL-TR-85-4155 (Air Force Wright Aero. Laboratories, Wright-Patterson Air Force Base, OH, March 1986).
3. C. G. McKamey, et al., J. Mater. Res. 6(8), 1779 (1991).
4. V. K. Sikka, SAMPE Qrt. 22(4), 2 (1991).
5. C. T. Liu, C. G. McKamey, an E. H. Lee, Scripta Metall. 24, 385 (1990).
6. C. G. McKamey and C. T. Liu, in *Proceedings of NACE Meeting on Environmental Effects on Advanced Materials*, edited by R. D. Kane (NACE, Houston, TX, 1992).
7. S. Viswanathan, P. J. Maziasz, and V. K. Sikka, p. 283 in *Proceedings of the Sixth Annual Conference on Fossil Energy Materials*, ORNL/FMP-92/1, Oak Ridge National Laboratory, July 1992.
8. S. Viswanathan, P. J. Maziasz, and V. K. Sikka, p. 293 in *Semiannual Progress Report, Fossil Energy AR&TD Materials Program*, ORNL/FMP-92/2, Oak Ridge National Laboratory, Oak Ridge, TN, December 1992.
9. P. J. Maziasz and G. M. Goodwin, Ann. Prog. Report for FY 1990, Advanced Industrial Materials Program, Advanced Industrial Concepts Division, U.S. Department of Energy (June 1991).
10. G. M. Goodwin, C. G. McKamey, P. J. Maziasz, and V. K. Sikka, pp. 181-88 in *Proceedings of the Seventh Annual Conference on Fossil Energy Materials*, ORNL/FMP-93/1 (July 1993).

2.10 HIGH-STRENGTH IRON ALUMINIDE ALLOYS

C. G. McKamey and P. J. Maziasz

INTRODUCTION

Past studies have shown that binary Fe_3Al possesses low creep-rupture strength compared to many other alloys, with creep-rupture lives of less than 5 h being reported for tests conducted at 593°C and 207 MPa (ref. 1). The combination of poor creep resistance and low room-temperature tensile ductility due to a susceptibility to environmentally-induced dynamic hydrogen embrittlement[2,3] has resulted in limited use of these alloys for structural applications even though their excellent corrosion properties could be very beneficial. Improvements in tensile ductility have been realized through the use of alloying and thermomechanical processing techniques to control alloy chemistry, microstructure, and surface condition,[4] and ductilities of 10-20% and tensile yield strengths as high as 500 MPa have been attained.[5,6] In terms of creep-rupture strength, small additions of Mo, Nb, and Zr have produced improvements, but at the expense of room temperature tensile ductility and weldability.[1,7-9] Further efforts are therefore necessary to produce a Fe_3Al-based composition with an acceptable combination of tensile and creep-rupture properties.

This report presents the results of efforts conducted during this reporting period to improve the creep-rupture strength of Fe_3Al-based alloy compositions through control of the microstructure. One composition containing small additions of Nb, Mo, Zr, B, and C was chosen as the base alloy and the effect of heat treatment temperature on the microstructure and creep-rupture properties was investigated.

DISCUSSION OF CURRENT ACTIVITIES

The alloy composition used in this study was Fe-28 at.% Al with 0.5% Nb, 0.8% Mo, 0.025% Zr, 0.05% C, and 0.005% B (Oak Ridge National Laboratory designation FA-180). It was prepared by arc-melting and drop casting into a chilled copper mold. Fabrication to 0.8-mm-thick sheet was accomplished by hot-rolling, beginning at 1000°C and finishing at 600-650°C, with the final sheet material containing approximately 70% warm work. After a stress relief heat treatment of 1 h at 700°C, flat tensile specimens (0.8 × 3.18 × 12.7 mm) were mechanically punched from the rolled sheet. Before testing, the tensile specimens were further annealed for 1 h at temperatures between 1100 and 1250°C. The results were

compared to specimens which were heat treated at 750°C, a temperature which has been shown to result in predominantly a B2 ordered structure and to produce a maximum in the room temperature tensile ductility.[5,5,10,11] Creep-rupture tests were performed in air at 593°C and a stress of 207 MPa (30 ksi). Creep ductilities were determined from measurements of the lengths of the specimens before and after testing. Minimum creep rates were measured as the slope of the linear portion of the test curve. Optical metallography and scanning electron microscopy (SEM) were used to study the microstructures and fracture modes. Analytical electron microscopy (AEM) using a Philips CM30 (300 kV) or JEOL 2000FX (200 kV) electron microscope was performed on samples cut from the gage portion of selected test specimens.

The 750°C heat treatment temperature was used as the base for comparison and resulted in an average creep life of approximately 100 h for two tests (see Table I). Preliminary results on slightly different compositions had indicated that only limited increases in creep life could be expected for heat treatments below approximately 1000°C (refs. 12,13). Therefore, for this series of tests, heat treatments were performed between 1100 and 1250°C. The temperatures chosen and the results of creep-rupture tests at 593°C are shown in Table I and Fig. 1. Creep-rupture life is plotted as a function of heat treatment temperature in Fig. 2, where the dashed line represents the 100-h average creep life for the 750°C heat treatment. The results show a dramatic increase in creep-rupture resistance with a heat treatment of 1150°C.

Optical microscopy of the unstressed ends of the fractured creep specimens (from areas where no strain occurred) was used to determine the starting microstructure; it was assumed that in the unstrained regions no grain growth resulted from exposure to 593°C for the length of the tests. The 750°C heat treatment resulted in primarily a banded structure typical of rolled sheet. However, recrystallized grains no larger than about 20 μm were visible predominantly near the surfaces and suggested that the sheet was about 20% recrystallized. Grain sizes for the 1100 and 1225°C heat treatments were equiaxed and ranged from 60-80 μm. These grain sizes are smaller than those reported earlier for binary Fe_3Al heat treated at 850°C (ref. 1), indicating that the alloying additions in FA-180 have provided some measure of grain refinement and have minimized grain coarsening. The starting grain size was also determined for a specimen heat treated at 1175°C which had lasted 840 h in creep. Grain size measurements from six different fields through the cross section indicated a

Table I. Effect of 1-h heat treatment on creep-rupture properties of alloy FA-180[a]

Heat treatment temperature (°C)	Grain size (μm)	Life (h)	Elongation (%)	MCR (%/h)
750	b	91	79	0.3
		103	75	0.3
1100	62	187	44	0.03
		235	36	0.03
1125		349	42	0.04
		222	20	0.01
		602	12	0.004
1150		2732	9	0.0005
		1530	7	0.001
1175		985	31	0.002
	122,350[c]	840	10	0.0001
1200		343	36	0.02
		285	31	0.05
		181	26	0.06
1225		135	17	0.09
	78	109	25	0.09

[a]Composition = Fe-28Al-5Cr-0.5Nb-0.8Mo-0.025Zr-0.05C-0.005B (at.%).
[b]Rolled microstructure, ≈10-20% recrystallized, with ≈20 μm grains.
[c]Duplex microstructure, see text for discussion.

bimodal microstructure. Most of the specimen showed an average grain size of approximately 120-125 μm. However in two of the fields measured, several grains as large as 500-700 μm were observed. These grains contributed to an average grain size of approximately 350 μm in those fields. The presence of large grains at 1175°C suggests the absense of precipitates to pin grain boundaries and prevent grain growth. The particular precipitates that were present at 1100°C have possibly either dissolved completely at 1175°C and stayed in solution (unlikely given the low solubility of Nb or Zr in Fe_3Al at room temperature) or have dissolved and reprecipitated as particles too fine to provide grain boundary pinning. At temperatures above 1175°C, other mechanisms, such as precipitate coarsening or reprecipitation of higher-melting-temperature phases, are evidently being activated, resulting in a smaller uniform grain size, similar to that measured for the specimen heat treated at 1100°C. These initial grain

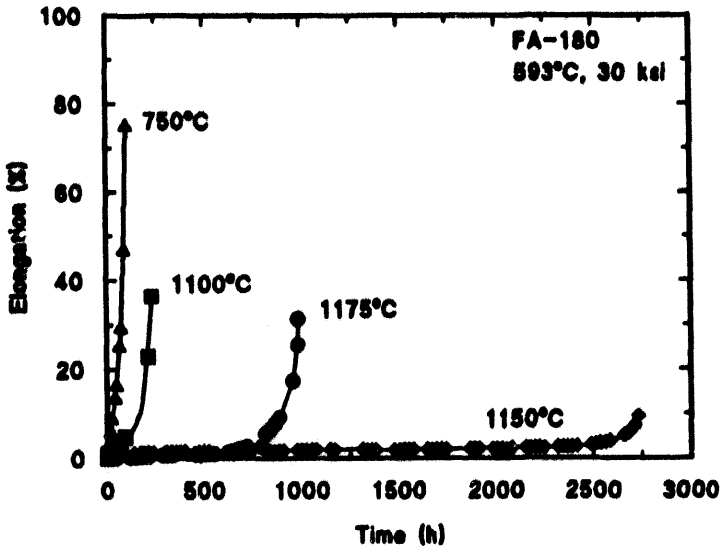

Fig. 1. Creep-rupture curves of alloy FA-180 heat treated at temperatures of 750, 1100, 1150, and 1175°C. Tests were conducted at 593°C and 207 MPa.

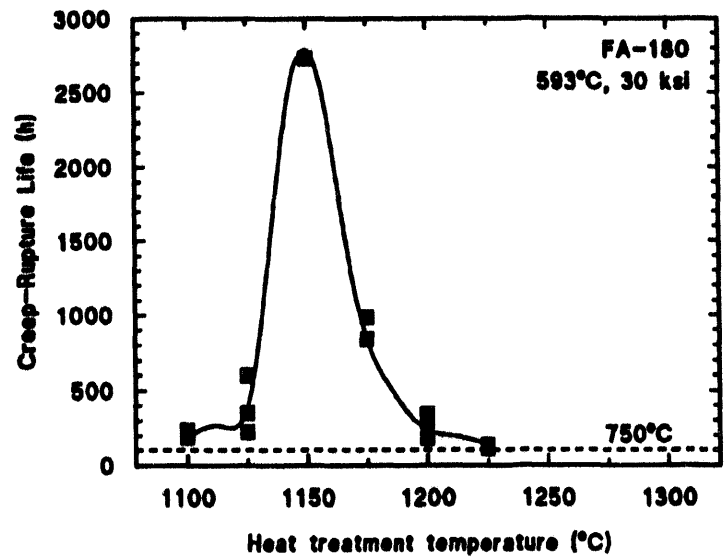

Fig. 2. Creep-rupture life as a function of heat treatment temperature for tests conducted on alloy FA-180 at 593°C and 207 MPa.

sizes correlate well with the creep life data shown in Fig. 2; the large-grained bimodal microstructure produced by the 1175°C heat treatment resulted in the longest life compared to the uniform smaller-grained microstructures produced by the 1100 or 1225°C heat treatments.

The fracture microstructures and morphologies were studied using optical and scanning electron microscopy. SEM of fracture surfaces showed that with all heat treatment temperatures, including 750°C, a ductile dimple type of fracture occurred with many large creep cavities [Fig. 3(a)]. Particles were observed at the bottom of most of the dimples [Fig. 3(b)]. The composition of these particles have yet to be confirmed but are assumed to be Mo- or Nb-based carbides.[1] Optical metallography was performed on the fractured specimens which had received the 750, 1100, 1175, and 1225°C heat treatments. None of these specimens showed the gross grain boundary separation that was observed for the binary specimen.[1] However there were some differences in grain morphology among the failed specimens. The specimen heat treated at 1100°C retained its uniform grain size of 60-80 μm during testing at 593°C for 187 h, but the grains were elongated slightly by the 44% tensile strain that it sustained. By contrast, the specimen heat treated at 1225°C, which had a uniform grain size of approximately 78 μm before testing, after testing for only 109 h showed a bimodel grain morphology with small areas of 100-150 μm diameter grains and larger areas of grains which filled the thickness of the specimen (~700 μm). Inbetween, the specimen heat treated at 1175°C, which had a bimodel morphology before testing, maintained that bimodel morphology through 840 h of testing at 593°C. The grains in this specimen also remained fairly equiaxed, which might be expected for a specimen that failed with only 10% elongation. These results show a complex interaction between composition, annealing temperature, and test conditions which have not yet been fully explained.

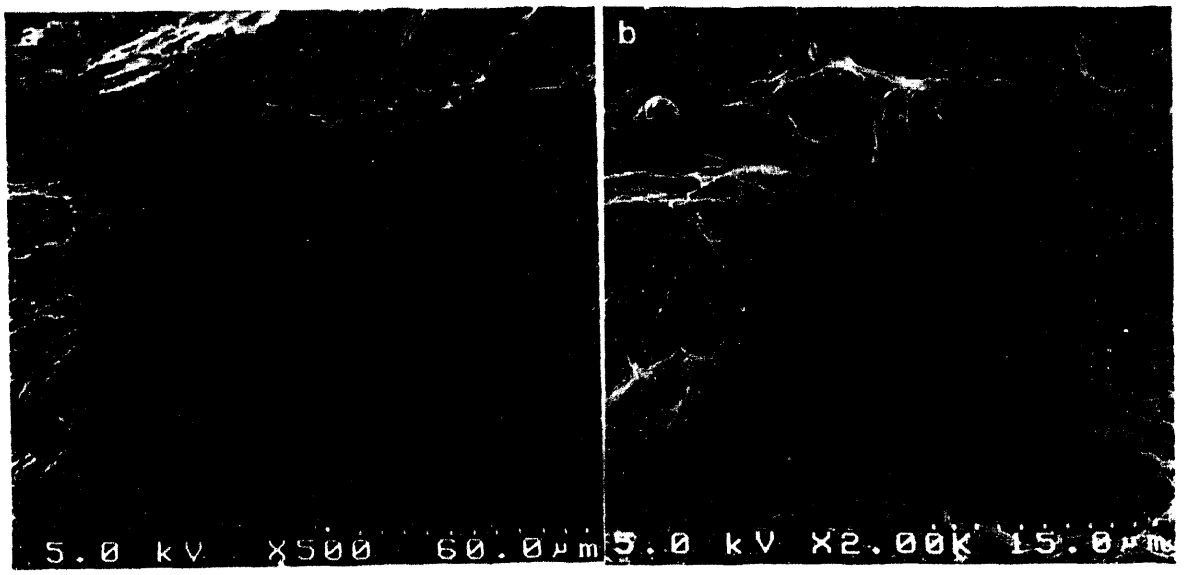

Fig. 3. Scanning electron fractographs showing (a) ductile dimple fracture of creep-ruptured specimen and (b) particles at the bottom of dimples.

Transmission electron microscopy was used to compare the pre- and post-test microstructures of specimens heat treated at 750 and 1150° C.[14] The pre-test microstructure of the specimen heat treated at 750° C was characterized by numerous dislocation arrays typical of a cold- or warm-rolled structure, recovered islands enclosed by dislocation networks which had formed into subgrain boundaries, and a few small newly-recrystallized grains along grain boundaries. Most of the dislocations appeared to be two-fold B2 superdislocations. No fine precipitation could be detected, although large (1-3 μm) inclusions, presumably niobium- and molybdenum-based carbides as determined in an earlier study,[1] were observed. These large inclusions are assumed to be those observed on the fracture surfaces in Fig. 3(b). In comparison, the creep-tested specimen showed shorter, loose, recovered dislocations, with few subgrain boundaries, suggesting that the the processes of strain and recovery had occurred simultaneously. The large amount of strain in both the pre- and post-test specimens made it difficult to determine the kind of order (B2 or DO_3) present, but the presence of two-fold dislocations suggests that both contained the B2 ordered structure.

The pre-test microstructure of the specimen heat treated at 1150° C was almost devoid of dislocations, and the grain boundaries were sharp and clean. The use of the proper diffraction conditions[15] resulted in the observation of B2 domains enclosing much finer DO_3 domains. This structure was expected considering the annealing temperature and the fact that the specimens were quenched in air. Adjustment of the diffraction conditions revealed extremely fine precipitates distributed throughout the matrix. After testing for 1530 h, a specimen heat treated at 1150° C was observed to contain many tangled networks consisting of two-fold dislocations of various lengths. [Due to a furnace failure this specimen failed prematurely with about 7% strain and was judged to be useful for TEM. The other specimen of this pair finally ruptured after 2732 h (see Table I).] Higher magnification again revealed the presence of fine precipitates and suggested that the precipitates may be pinning the dislocations, thereby producing increased creep-rupture life. Slip traces were also observed, suggesting the pinning of the partials which make up the B2 superdislocation. Additionally, small precipitates were judged to have formed on grain boundaries during the test. These precipitates are believed to be contributing to grain boundary strengthening or pinning.

In summary, the results of creep-rupture tests on an Fe_3Al-based alloy containing additions of Nb, Mo, Zr, B, and C showed that significantly-increased creep lives can be produced by controlling the microstructure. A heat treatment at 1150° C resulted in over

2700 h of creep life in a specimen tested at 593°C under a stress of 207 MPa. Although the mechanisms of this strengthening have not been completely explained, the results of this study indicate that the strengthening is probably associated with the dissolution and reprecipitation of fine particles which serve to pin dislocations and possibly strengthen or pin grain boundaries. Grain growth during creep-rupture testing was indicated for a specimen heat treated at a higher temperature of 1225°C which had exhibited a much lower creep life. Transmission electron microscopy of that specimen and analysis of precipitate compositions produced by the various annealing temperatures (to be conducted during the next reporting period) should add to our understanding of the the creep-rupture test results presented here and the strenthening mechanisms involved.

REFERENCES

1. C. G. McKamey, P. J. Maziasz, and J. W. Jones, J. Mater. Res. 7(8), 2089 (1992).
2. C. T. Liu, C. G. McKamey, and E. H. Lee, Scr. Metall. Mater 24(2), 385 (1990).
3. C. T. Liu and C. G. McKamey, pp. 133-151 in *High Temperature Aluminides and Intermetallics*, edited by S. H. Whang, C. T. Liu, D. P. Pope, and J. O. Stiegler (TMS, Warrendale, PA, 1990).
4. C. G. McKamey and C. T. Liu, paper No. 17-1 in *Proceedings of ADVMAT/91, First International Symposium on Environmental Effects on Advanced Materials*, edited by R. D. Kane (NACE, Houston, TX, 1992).
5. V. K. Sikka, SAMPE Quart. 22(4), 2 (1991).
6. V. K. Sikka, S. Viswanathan, and C. G. McKamey, pp. 483-91 in *Structural Intermetallics*, edited by R. Darolia, J. J. Lewandowski, C. T. Liu, P. L. Martin, D. B. Miracle, and M. V. Nathal, (TMS, Warrendale, PA, 1993).
7. C. G. McKamey, J. H. DeVan, P. F. Tortorelli, and V. K. Sikka, J. Mater. Res. 6(8), 1779 (1991).
8. P. J. Maziasz and C. G. McKamey, Mater. Sci. & Eng. A152, 322 (1992).
9. D. M. Dimiduk, M. G. Mendiratta, D. Banerjee, and H. A. Lipsitt, Acta Metall. 36, 2947 (1988).
10. J. R. Knibloe, R. N. Wright, and V. K. Sikka, pp. 219-31 in *1990 Advances in Powder Metallurgy*, Vol. 2 (Metal Powder Industries Federation, Princeton, NJ, 1990).
11. P. J. Maziasz, C. G. McKamey, and C. R. Hubbard, p. 349 *Alloy Phase Stability and Design*, edited by G. M. Stocks, D. P. Pope, and A. F. Giamei (MRS, Pittsburgh, 1990).
12. C. G. McKamey, P. J. Maziasz, G. M. Goodwin, and T. Zacharia, accepted by Mat. Sci. & Eng. (1994).
13. C. G. McKamey, unpublished results.
14. C. G. McKamey and P. J. Maziasz, to be published in *Processing, Properties, and Applications of Iron Aluminides*, eds. J. H. Schneibel and M. Crimp (TMS, Warrendale, PA, 1994).
15. M. J. Marcinkowski and N. Brown, J. Appl. Phys. 33(2), 537 (1962).

2.11 LOW-ALUMINUM CONTENT IRON-ALUMINUM ALLOYS

V. K. Sikka

INTRODUCTION

The purpose of this task is to develop a conventionally fabricable, low-cost, and lower-density iron-aluminum-base alloy with a good combination of strength, ductility, weldability, and corrosion resistance for use as components in advanced fossil energy conversion systems. Initial emphasis is on the development of iron-aluminum alloys for heat-recovery applications in coal gasification systems. Many nonfossil energy applications have also been identified so that the FAPY alloy will become available commercially when needed for fossil energy applications.

Discussion of Current Activities

Alloys

The FAP and FAPY are the designations of two low-aluminum content iron-aluminum alloys. The alloy compositions are given in Table 1. Both alloys are disordered α-alloy with the only difference being that FAPY contains yttrium. The FAP and FAPY alloy compositions were designed[1] after a systematic study[2] of alloy compositions listed in Table 2. Each element of the alloy has a specific role which is described below:

Aluminum: The aluminum content is controlled to eliminate the environmental effect through minimization or elimination of the aluminum reaction with moisture to generate hydrogen.

Chromium: The chromium addition to the alloy is made to gain resistance to aqueous corrosion.

Molybdenum: Molybdenum is added to the alloy to protect against pitting corrosion.

Zirconium and Carbon: These elements are added to form high-melting-point zirconium-carbon particles to provide grain refinement during solidification.

Yttrium: Small additions of yttrium are made to enhance high-temperature oxidation resistance.

Tensile properties of FAP and FAPY alloys in the wrought condition are given in Table 3 which shows that the FAP and FAPY alloys have over 20% ductility at room temperature and are not sensitive to environmental effects, Fig. 1, unlike the ordered alloy. The FAP and FAPY

Table 1. Chemical composition of two low-aluminum-content iron-aluminum alloys (FAP and FAPY)

Element	Alloy, (%)			
	FAP		FAPY	
	(at.)	(wt)	(at.)	(wt)
Al	16.12	8.46	16.12	8.46
Cr	5.44	5.50	5.44	5.50
Zr	0.11	0.20	0.11	0.20
C	0.13	0.03	0.13	0.03
Mo	1.07	2.00	1.07	2.00
Y	---	---	0.06	0.10
Fe	77.13	83.81	77.07	83.71

Table 2. Chemical analysis of various alloys

Alloy	Atomic percent					
	Iron	Aluminum	Chromium	Carbon	Zirconium	Molybdenum
FAL-B8	84	16	---	---	---	---
FAL-B12	78	22	---	---	---	---
FAL-B16	72	28	---	---	---	---
FAL-T8	79	16	5	---	---	---
FAL-T12	73	22	5	---	---	---
FAL-T16	67	28	5	---	---	---
FAL-TC8	78.80	16	5	0.2	---	---
FAL-TC16	66.80	28	5	0.2	---	---
FAL-TCZ8	78.78	16	5	0.11	0.11	---
FAL-TCZ12	72.78	22	5	0.11	0.11	---
FAL-TCZ16	66.78	28	5	0.11	0.11	---
FAP	77.21	16.1	5.4	0.11	0.11	1.07

Table 3. Tensile properties of FAP and FAPY alloys

Temperature		Strength				Ductility, (%)	
		0.2% Yield		Ultimate			
°F	(°C)	(ksi)	(MPa)	(ksi)	(MPa)	Total elongation	Reduction of area
				FAP (Sheet, Wrought Material)[a]			
RT[b]	25	73.0	503	94.0	648	27	45
200	93	60.5	417	87.0	600	26	44
400	204	48.0	331	85.0	586	22	37
600	316	45.0	310	85.0	586	23	32
800	427	44.5	307	83.0	572	24	30
1000	538	43.0	297	64.0	441	35	43
1100	593	44.5	307	55.0	379	51	50
1200	649	30.0	207	38.0	262	64	65
1300	704	20.0	138	20.0	138	78	75
1400	760	3.0	21	---	---	---	---
1500	816	---	---	---	---	---	---

[a]Sheet annealed at 800°C for 1 h followed by air cooling prior to testing.
[b]RT = Room temperature.

Table 3. Tensile properties of FAP and FAPY alloys
(Continued)

Temperature		Strength				Ductility, (%)	
		0.2% Yield		Ultimate			
°F	(°C)	(ksi)	(MPa)	(ksi)	(MPa)	Total elongation	Reduction of area
				FAPY (Cast), Vacuum-Induction Melt[c]			
RT[b]	25	68.0	469	74.0	510	1.5	1.5
200	93	58.0	400	79.0	545	13	9
400	204	46.0	317	80.0	552	24	32
600	316	41.5	286	76.0	524	32	44
800	427	37.5	259	67.5	465	39	52
1000	538	35.0	241	54.0	372	47	60
1100	593	32.5	224	45.0	310	53	65
1200	649	30.0	207	40.0	276	59	69
1300	704	25.5	176	30.0	207	68	74
1400	760	20.0	138	22.0	152	77	77
1500	816	13.5	93	14.0	97	89	80

[b]RT = Room temperature.
[c]Vacuum-induction melted and cast into a 76-mm-diam ingot.

Table 3. Tensile properties of FAP and FAPY alloys
(Continued)

Temperature		Strength				Ductility, (%)	
		0.2% Yield		Ultimate		Total elongation	Reduction of area
°F	(°C)	(ksi)	(MPa)	(ksi)	(MPa)		
				FAPY (Cast) Air Melt[d]			
RT[b]	25	59.0	407	60.0	414	1.0	1.0
200	93	50.0	345	62.0	427	6	4
400	204	37.5	259	65.0	448	13	13
600	316	37.0	255	65.0	448	13	14
800	427	37.0	255	63.0	434	14	16
1000	538	36.0	248	54.0	372	15	31
1100	593	35.0	241	45.0	310	16	44
1200	649	33.0	228	40.0	276	17	56
1300	704	28.0	193	30.0	207	17	65
1400	760	23.0	159	23.0	159	17	70
1500	816	12.0	83	14.0	97	17	74

[b]RT = Room temperature.
[d]Air melted and cast into three step castings by Cast Masters (Bowling Green, Ohio).

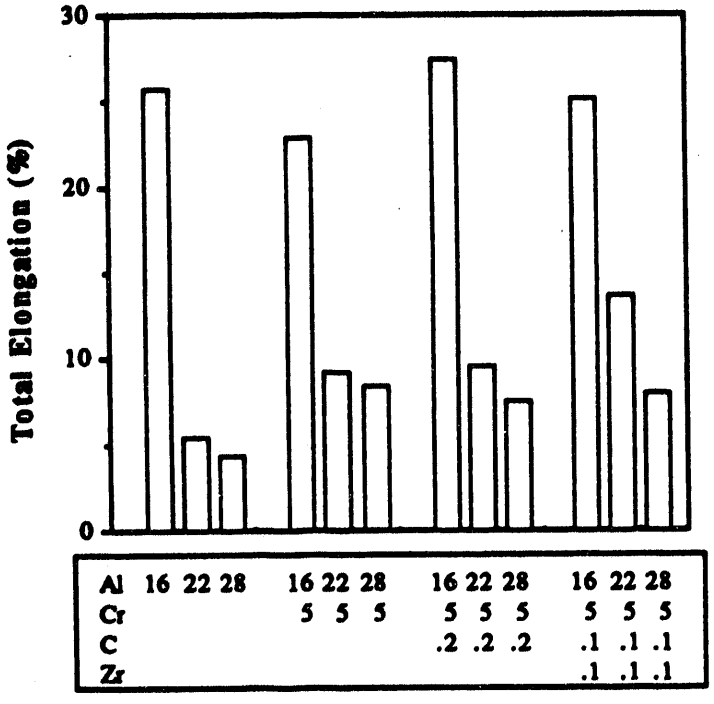

Fig. 1. Effect of alloying additions in atomic percent to reduce the environmental effect of Fe-Al alloys. All of the specimens were tested in air after a 1-h heat treatment at 700°C followed by air cooling.

alloys are also free from various phase transformations, unlike Fe_3Al alloys (FA-129) which goes from DO_3 to B2 to α at temperatures of 543 and 924°C, respectively. The transformation temperatures are functions of chemistry and may vary from the numbers given here for other alloys.

Melting

Once the alloy compositions are finalized, it is important to have technology for their commercial melting and processing. Figure 2 (ref. 3) shows that as aluminum is added to iron, the formation of the intermetallic FeAl is exothermic. Similarly, the formation of NiAl is even more exothermic. It is suggested that the melting of FAP and FAPY alloys be carried out to take advantage of the exotherm. The proper utilization of the exotherm saves energy, controls chemistry, reduces melting time, and minimizes scale formation. The furnace loading to take advantage of the exotherm during FAP and FAPY melting is shown in Fig. 3. The iron content of the alloy is divided between the top and the bottom of the melt crucible. The ratio of iron to aluminum on the top is chosen to equal 50:50 at (%). The remaining iron is put at the bottom,

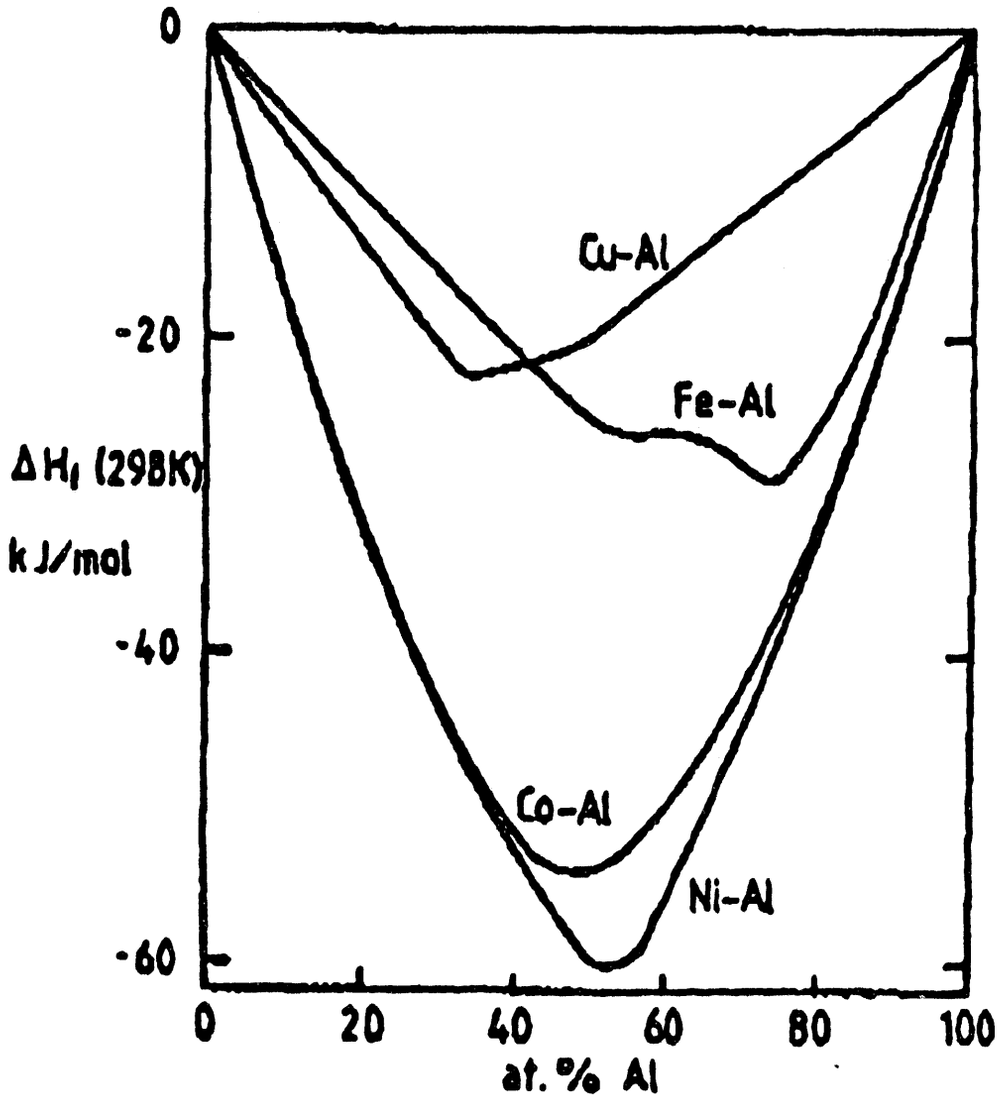

Fig. 2. Extent of exothermic reaction in aluminum binary systems with transition metals including: iron, cobalt, nickel, and copper [German (2)].

and the alloying elements are sandwiched between the top and the bottom. When the entire furnace load is heated to nearly 660°C, the aluminum melts and reacts with the iron setting next to the molten aluminum at the crucible top. The reaction is exothermic and produces a liquid at furnace load is heated to nearly approximately 1500°C. As this liquid travels down, it dissolves the alloying elements on the way, and further heats up the iron at the bottom. With additional energy supplied to the furnace, the entire melt is brought to the desired temperature for pouring. This scheme has been successfully used commercially by Sandusky International for melting 2500-kg heats of nickel-aluminide alloy containing approximately the same amount of aluminum as present in the FAP and FAPY alloys.

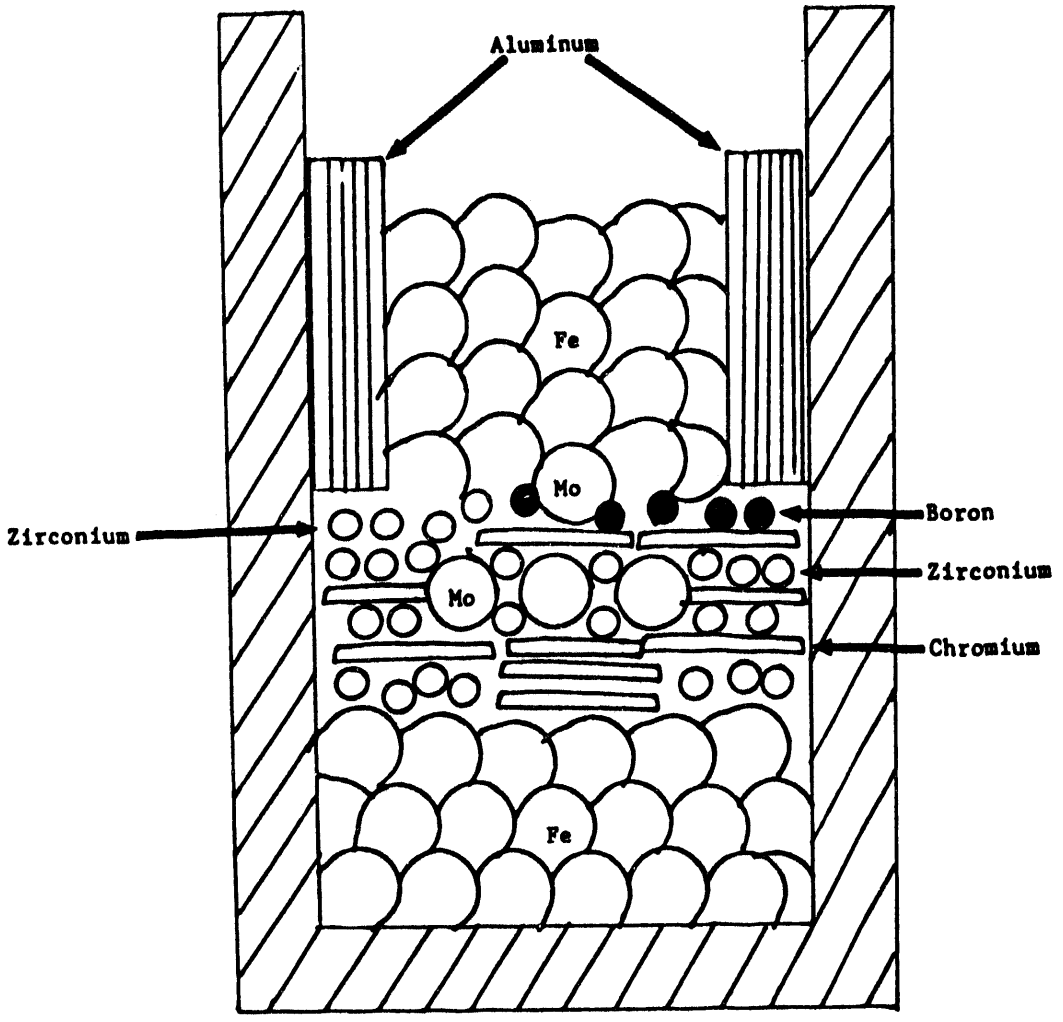

Fig. 3. Furnace-loading sequence to take advantage of heat of formation of FeAl during the melting of FAP and FAPY alloys.

The crucible selection for melting of high-aluminum alloys is also important. Figure 4 shows the free energy of formation for Al_2O_3 and MgO as a function of temperature. Based on this figure, the aluminum in the FAP and FAPY alloys will reduce MgO of the magnesia crucible at temperatures ≥1600°C. This type of reduction of MgO will promote magnesium pickup by the alloy and erosion of the crucible. The effects of magnesium on properties of FAP and FAPY alloys are not yet known. However, given the choice, the Al_2O_3 crucible should be preferred over the magnesia crucible.

The most effective method of adding yttrium to the melt is to use an Al-Y eutectic ⇒ which melts at approximately 600°C and is commercially available.

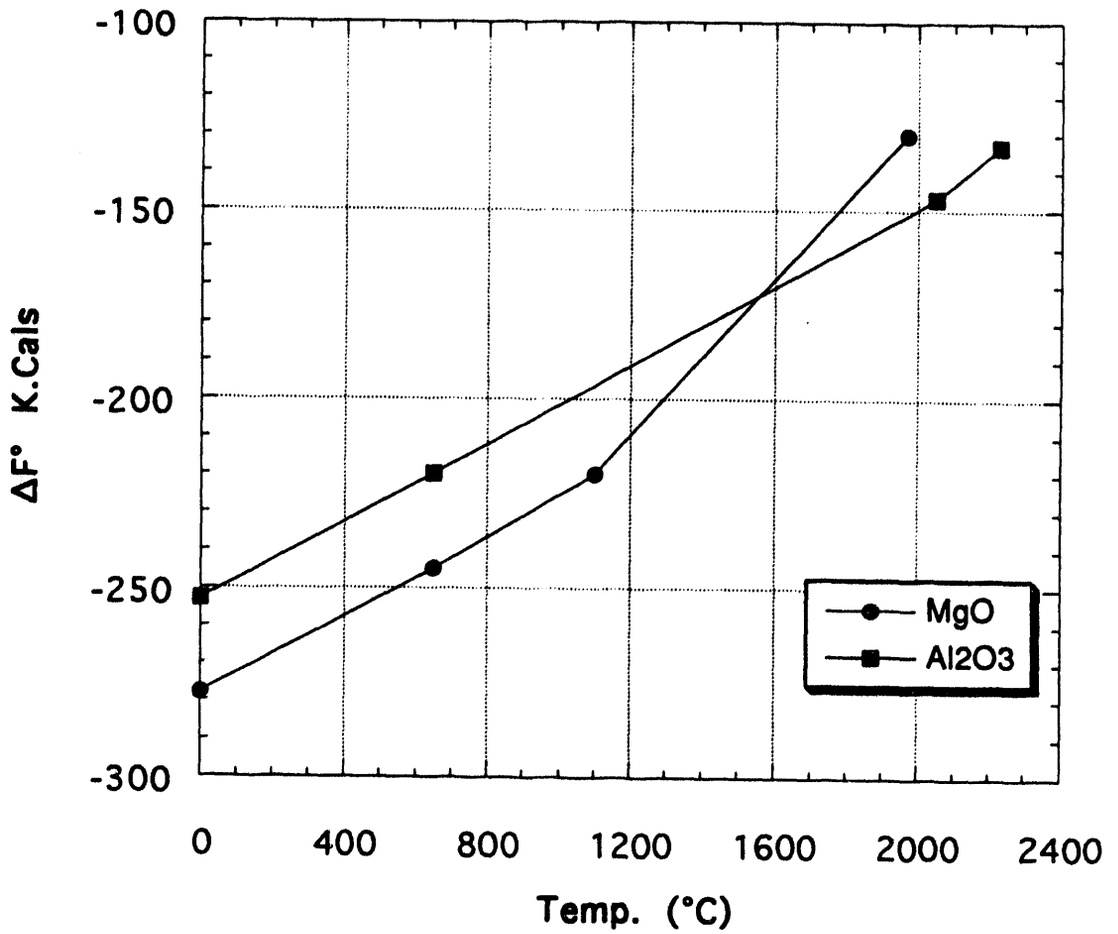

Fig. 4. Comparison of standard free energy of formation as a function of temperature to reveal the relative stability of Mgo and Al_2O_3 during melting of the alloys.

Processing

The FAP and FAPY ingots (round or flat) can be hot worked rather easily. The hot-working processes include: extrusion, forging, and rolling (bar and flat). All of the hot-working processes can be used in the temperature range of 1000 to 1200°C. In fact, one 2000-lb, arc-melted commercial heat of FAPY alloy has been bloomed and hot-bar rolled to 1/4-in.-diam bar coils on production equipment. The slabs have been hot rolled at 1050°C with a reduction per pass of 50% at the Oak Ridge National Laboratory and Manufacturing Sciences Corporation (Oak Ridge, Tennessee).

The ductility of the FAPY alloy in the cast and wrought conditions are compared in Fig. 5. At room temperature, the cast ductility is ≤2%. However, these values approach those of the wrought condition at ≥200°C. Figure 6 shows that the ductility value of the air-melted and

cast ingot is generally lower than the vacuum-melted and cast ingot. Based on ductility values in Figs. 5 and 6, it is obvious that the cast ingots cannot be cold rolled. However, once the cast grain structure is broken up by the hot-working process, cold-working operations are possible. The successful cold-working operation carried out on the FAPY material include: swaging of extruded bar, wire drawing, and flat rolling.

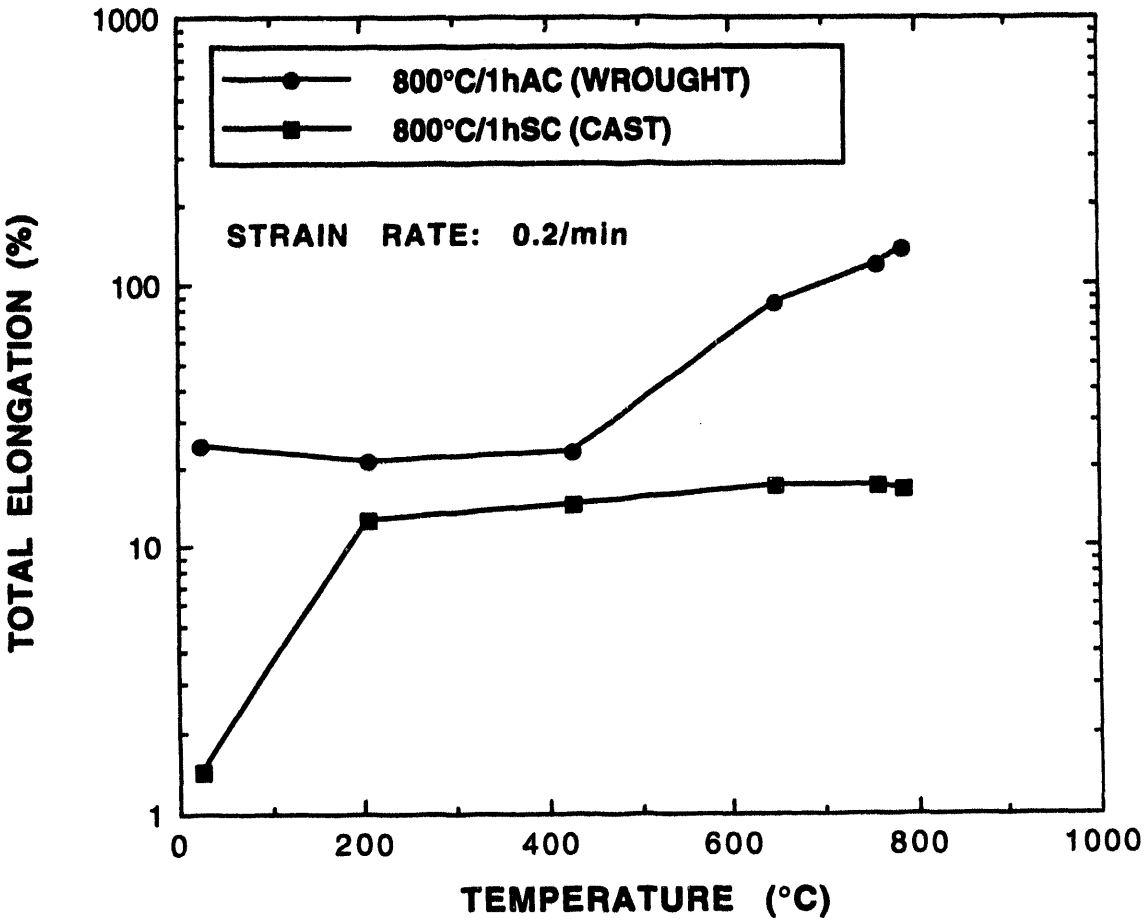

Fig. 5. Comparison of ductility of FAPY alloy in the cast and wrought conditions. The wrought sheet specimens were air cooled, whereas the cast specimens were slow cooled.

Weld Wire

One 15-lb heat of FAPY alloy, prepared by vacuum-induction melting, was converted into 1/8-in. diam weld wire by a combination of hot extrusion and drawing. The wire has been successfully used in making gas tungsten arc weld overlays on 2-1/4 Cr-1 Mo steel. The 1/8-in.-diam weld wire is also currently being used for flux coating to develop the shielded metal-arc

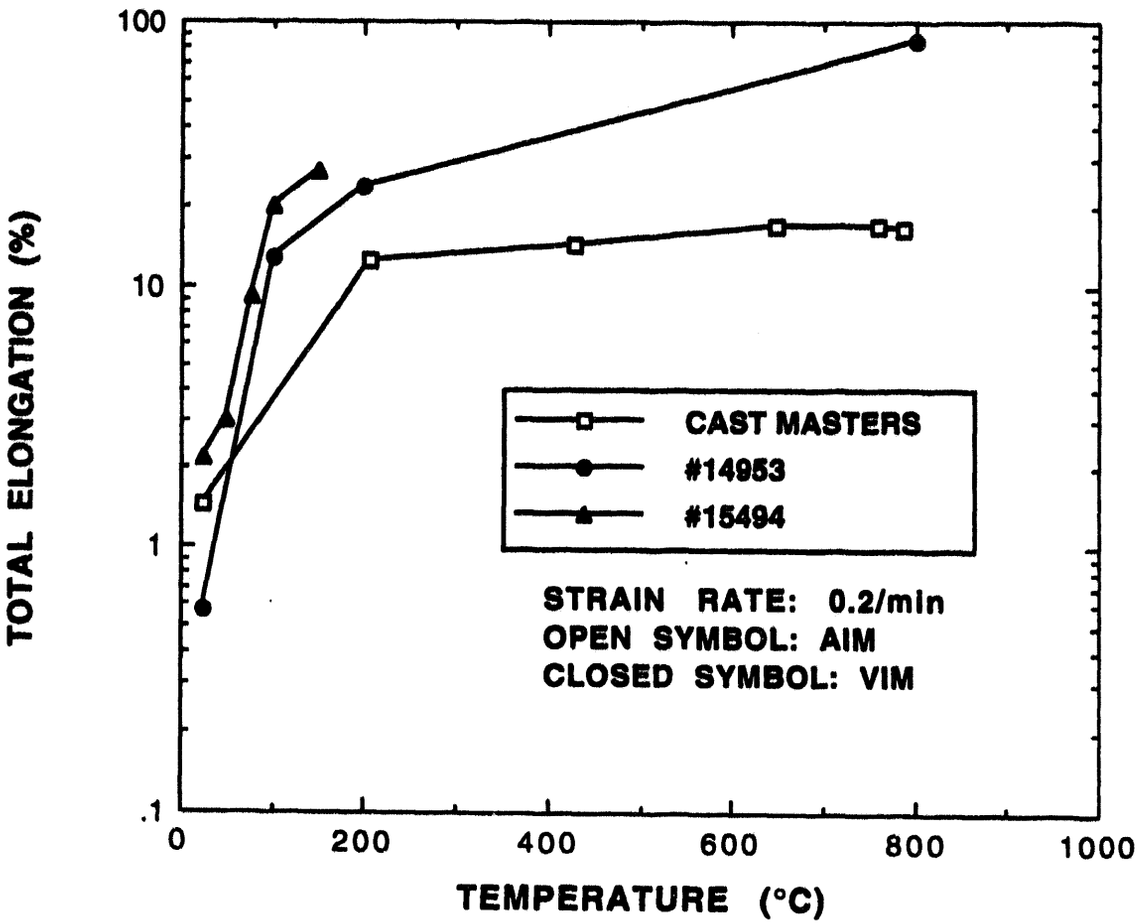

Fig. 6. Effect of melting practice on ductility of FAPY alloy in the as-cast condition.

electrodes. The FAPY wire with 16 at. % (8.5 wt %) Al is being considered as a core wire to develop the higher aluminum alloy (Fe_3Al and FeAl) weld wires.

Future Work

The tensile brittle-to-ductile transition temperature (BDTT) for FAPY alloys is around 150°C. The BDTT is the same for the Charpy notched specimens of the wrought material. Efforts are required to bring the BDTT below room temperature. Possibilities for such a reduction in BDTT include: (1) improvement of melting technique to reduce any possible contamination, (2) produce fine-grain cast structures, and (3) further modification of the alloy composition.

REFERENCES

1. Vinod K. Sikka and Claudette G. McKamey, "Iron-Aluminum Alloys Having High Room-Temperature and Method for Making Same," Patent No. 5,238,645 (August 24, 1993).
2. V. K. Sikka, S. Viswanathan, and S. Vyas, "Acceptable Aluminum Additions for Minimal Environmental Effect in Iron-Aluminum Alloys, " pp. 971-976 in *High Temperature Ordered Intermetallic Alloys V*, ed. L. A. Johnson, D. P. Pope, and J. O. Stiegler, Materials Research Society symposium (Mater. Res. Soc. Proc. 288), Pittsburgh, PA, 1993.
3. R. M. German, pp. 205-231 in *Thermal Analysis in Metallurgy*, ed. R. D. Shull and A. Joshi, The Minerals, Metals and Materials Society, Warrendale, PA, 1992.

2.12 DEVELOPMENT OF A MODIFIED 310 STAINLESS STEEL

R. W. Swindeman

Oak Ridge National Laboratory
P. O. Box 2008
Oak Ridge, Tennessee, 37830

ABSTRACT

Structural materials performance requirements were re-evaluated for use in emerging fossil energy applications. Concepts included low emission boilers, advanced steam cycle, and combined-cycle technologies. Both pressure-bearing and non-pressure-bearing applications were considered. The adequacies of martensitic and austenitic steels were examined, and comparisons of the potential of various alloy selections were undertaken. Both austenitic and martensitic steels were judged to have applicability for boilers operating at 600°C while fine-grained austenitic alloys were judged to be best for service to 650°C. For applications in the range 650 to 760°C, modified 310 stainless steels were judged to be good choices. Above 760°C, the alloys being considered for pressurized fluidized bed combustors (PFBCs) included oxidation-resistant stainless steels. For carbonizers and gasifiers operating below 900°C, cobalt-bearing alloys and modified 310 stainless steels were of interest. Iron-aluminide cladding was also considered, and experimental studies were begun to examine compatibility with pressure boundary materials. The data base for modified 310 stainless steels was expanded to 1038°C, and testing times ranged to beyond 10,000 h. The performance of weldments in modified 310 stainless steel was examined and found to be adequate to enable the use of the material at 871°C. Exploratory work on fatigue was undertaken. For service above 900°C, exploratory evaluations of cast high alloys (HP) and alloy 160

were begun. Creep, fatigue and crack growth testing was initiated on alloy 160. Interactions and collaboration with industry were maintained.

INTRODUCTION

The need for more efficient coal combustion was identified ten years ago, when research on advanced steam cycle concepts was begun by the Electric Power Research Institute (EPRI) to improve the performance of pulverized coal power plants (1). The initial thrust of the FE/AR&TD alloy development research was to evaluate austenitic alloys that could be used for superheater tubing in the boiler of the EPRI Phase 2 conceptual plant (2). Such a plant, producing steam at 650°C and 35 MPa (1200°F and 5000 psi), was expected to be more efficient than existing plants and have lower emissions. The EPRI Phase 2 effort received very little support by the U.S. utility industry. Rather, state-of-the-art combined-cycle concepts and second-generation combined cycle concepts received increased attention from a few enterprising utilities, the EPRI, and the DOE energy technology centers (3). Recognizing that issues remained regarding the use of materials for second-generation combined-cycle systems, efforts undertaken in the last year to collaborate with the fossil power industry in various areas of structural materials technology. Topics that are covered included structural alloys for low emission boilers, advanced steam cycle, and second-generation combined cycle applications that incorporated gasifiers, carbonizers, fluidized bed combustors, and indirect heaters.

LOW EMISSION BOILERS

Low emission boilers (LEB) are being designed with steam temperatures in the range of 593 to 649°C (1100 to 1200°F), and pressures could be as high as 35 MPa (5000 psi) (4). Choices must be made regarding the materials of construction. Both ferritic and austenitic alloys are being considered. Main steam line piping, reheat piping, and headers will be thick-wall components.

Candidate materials include martensitic steels such as Gr91, NF616, and MCM12 and austenitic steels such as 316N and 347H stainless steels. Although base metal properties of these alloys appear to meet the needs for the expected service, issues remain regarding the performance of weldments. A small research effort at ORNL has been directed at examining the performance of weldments under creep rupture and fatigue loadings. Collaboration with utilities and component manufacturers has been part of this effort. Exploratory creep-rupture and fatigue testing of cross welds taken from heavy wall pipe of Gr 91 revealed much reduced life as a result of weakness in the heat affected zone of the welds. The reduced life is expected to be less significant at lower stresses, but long-time testing has yet to be performed. More severe losses are expected in NF616 and MCM12 weldments because of high strength levels in the base metal and their tendency to form a brittle Laves phase.

Recuperator temperatures in some LEB designs are as high as 649°C (1200°F). Some recuperator designs call for thin-section oxidation-resistant steels alloys. Candidates include modified 300 series stainless steels, modified alloy 800H, and nickel base alloys. Research undertaken to support the advanced steam cycle may be applicable to such LEB recuperators, and a small effort is underway to address this issue. An understanding of weld metal and weldment behavior at long times is essential for reliable design of LEB components, so research on weldments that was related to the advanced steam cycle has continued with this new application in mind. Cross-weld tests on modified alloy 800H have been underway, and creep testing times exceeding 25,000 h have been achieved at temperatures in the range of 600 to 700°C (1112 to 1292°). Both fine grain and medium grain size materials are being examined.

SECOND-GENERATION COMBINED-CYCLE

Materials and design methods for second-generation combined-cycle (SGCC) plants were examined. However, many different concepts for SGCC

exist, and materials performance requirements differ greatly from one concept to another. Fluidized bed combustors, carbonizers, gasifiers, and slagging combustors are all being considered in the coal combustion or conversion processes. Heat recovery and gas cleanup systems also vary. In spite of heavy usage of refractories and structural ceramics, it seems likely that metals will be needed for pressure retention, cyclones, gas stream piping liners, expansion bellows, filter supports, blowback systems, and heat recovery tubing. The material selection for these components will depend on the temperature, composition, and alkali corrosion potential of the gas stream.

Materials and design methods for SGCC systems were examined, and, in a collaborative effort with industry, criteria for design at high temperatures were studied (5). Concomitant with the study of criteria, exploratory mechanical testing was undertaken of candidate materials. Some alloys were provided by industry. Materials included alloy 800H, alloy 333, alloy 556, HR-160, modified HP, and stainless steels such as 309S, 310S, and 253MA. Also, the potential of modified type 310 stainless steel for fossil energy applications at temperatures above 815°C was assessed, and it was concluded that a 25Cr-20Ni steel having a strength comparable to alloy 800H would be of commercial interest. Two commercial heats of 310HCbN stainless steel tubing for testing. One experimental heat of a Ta-modified 310 stainless steel (310TaN) was procured as plate and included in the experimental investigations.

In Fig. 1, a comparison is shown of the creep curves for a few alloys of interest at 927°C and 25 MPa (1700°F and 3.63 ksi). It may be seen that the 310TaN stainless steel is substantially more creep resistant than 309 and 253MA stainless steels. Improved creep resistance over alloy 800H is also noted. Further comparisons are provided in Figs. 2a and 2b. Here, the strength to produced rupture in 10,000 h is compared for temperatures in the range of 760 to 982°C (1400 to 1800°F). The 310TaN stainless steel has more than twice the strength of 310 stainless steel and is substantially stronger that 253MA and RA85H over the entire temperature range (Fig. 2a). Depending on

the temperature, the 310TaN stainless steel is equivalent to or stronger than RA333 and alloy 811 and approaches the strength of alloy 556 above 900°C. Testing of 310TaN has been extended to beyond 10,000 h, and data for a number of temperatures and stresses have been correlated on the basis of the Larson Miller parameter. Such a correlation is shown in Fig. 3 where a parametric constant of 15 has been used to collapse the data to a single curve for all temperatures. A few tests on specimen from welds in 12.5-mm plate were also tested under creep conditions. These data are compared to base metal data in Fig. 4, which plots log stress versus the Larson Miller parameter. All specimens were cross welds, but two types of welds are represented. Alloy 556 filler metal was used to produce gas tungsten arc welds, and alloy 117 electrodes were used to produce shielded metal arc welds. Weldment rupture lives fell near the parametric curve for base metal. An autogenous weld was produced in sheet of the material and tested for formability. Small radius bends

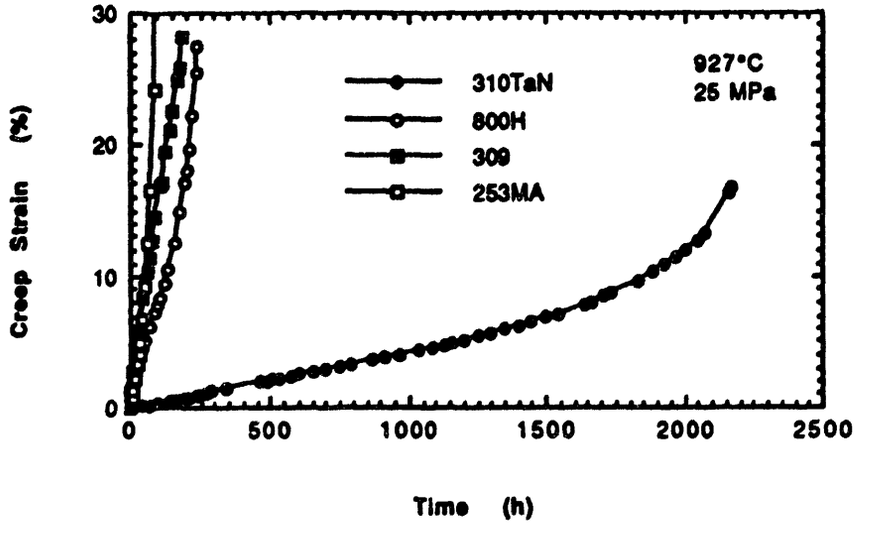

Fig. 1. Comparison of the creep curve for 310TaN stainless steel with curves for three structural alloys at 927°C and 25 MPa.

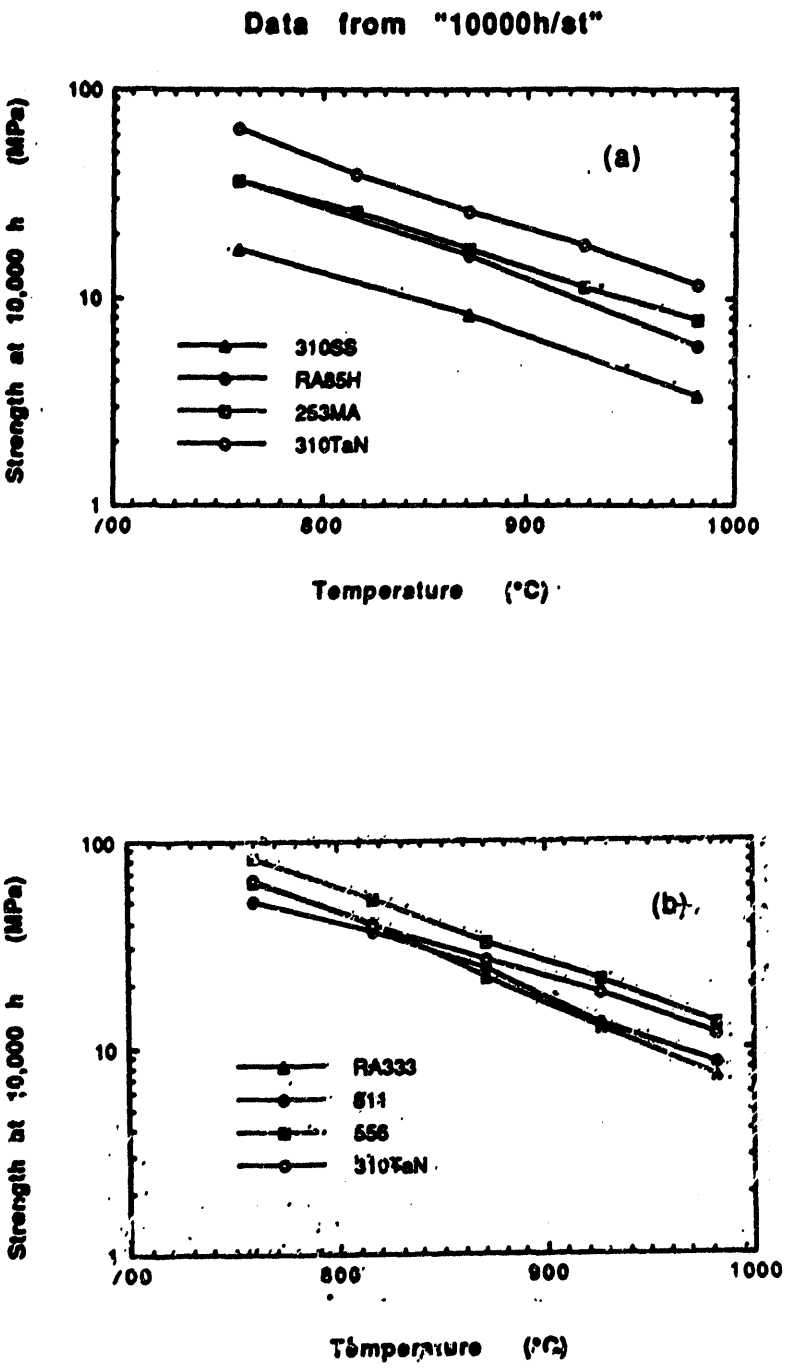

Fig. 2. Comparison of the strength at 10,000 h versus temperature for 310TaN stainless steel with (a) other stainless steels and (b) alloys 333, 556, and 811.

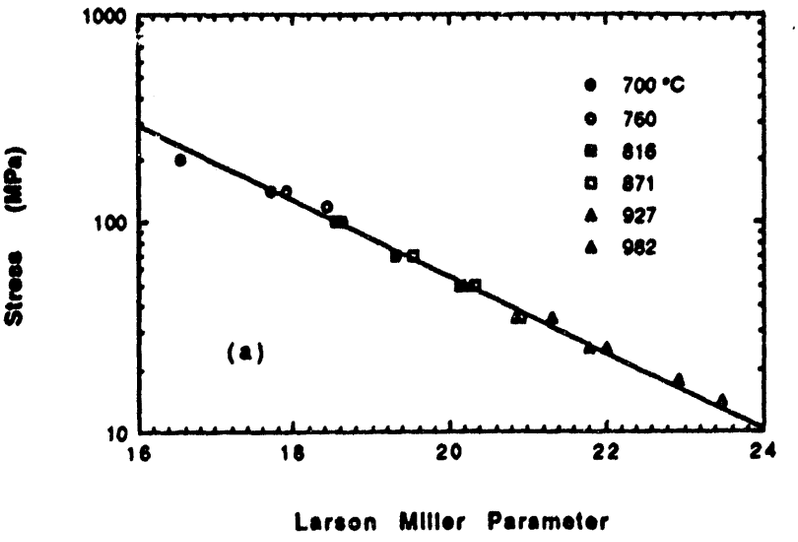

Fig. 3. Stress versus the Larson Miller parameter for rupture of 310TaN stainless steel.

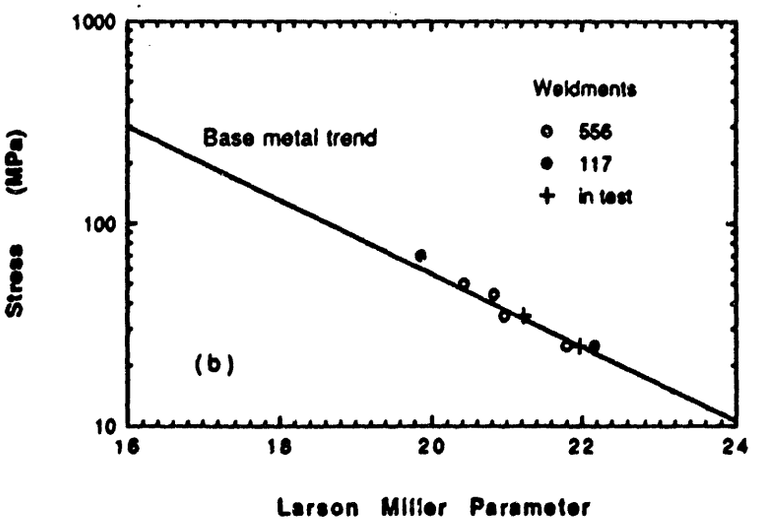

Fig. 4. Stress versus the Larson Miller parameter for rupture of cross welds in 310TaN stainless steel plate using alloys 556 and 117 as filler metal.

were made with no evidence of cracking. A few fatigue tests were performed around 816°C. Data indicated fatigue resistance was similar to other stainless steels. A few tensile tests were performed on aged samples. These tests reveal some loss in ductility, but room temperature elongation remained around 20%. Additional aging studies are in progress. A few oxidation studies were undertaken and results indicated that the oxidation rates for 310TaN stainless steel were similar to 310 and 310HCbH stainless steels at 870°C.

For protection against sulfidizing environments, an examination of the potential of iron-aluminide as a cladding material was explored (6). Coextrusion were made with iron-aluminide on type 310 and 310 stainless steels. Samples from these extrusions are being exposed to thermal cycling and aging.

An evaluation of the design and analysis of structural components in hot-gas cleanup systems was undertaken several years ago. Emphasis at that time was on the tubesheet that supported ceramic filters. Because of the low yield strengths of commercially available high temperature structural alloys, tubesheet alloys were judged to be susceptible to low-cycle fatigue failures under restrained thermal cycling conditions. A nickel-chrome-aluminide intermetallic alloy (cast IC 396M) with a very high yield strength was selected as an alternative material for tube sheet construction. A database was gathered on IC 396M sufficient for an elastic-plastic-creep analysis, and a re-analysis of the critical region of the tubesheet was performed (7). It was found that the high-strength intermetallic alloy would not be an improvement over commercial wrought alloy in regard to thermal fatigue resistance.

SUMMARY

Progress has been made on the evaluation of structural materials for a number of fossil energy applications, and most of the research involves collaborative efforts with industry. The materials and research thrusts were selected to meet the needs of industrial participants in advanced fossil energy projects. For low emmision boilers, most materials of interest are either

commercial or near-commercial in regard to fabrication technology. For construction of components in second- generation combined cycle applications were examined, and emphasis was placed on gathering data needed for establishing design methods and analysis procedures.

REFERENCES

1. S. B. Bennett, *Engineering Assessment of an Advanced Pulverized Coal Power Plant,* EPRI CS-2555, Electric Power Research Institute, Palo Alto, CA, August 1982.

2. R. W. Swindeman, et al., *Alloy Design Criteria and Evaluation Methods for Advanced Austenitic Alloys in Steam Service*, ORNL-6274, Oak Ridge National Laboratory, Oak Ridge, TN, 1986.

3. R. A. Bajura and H. A. Webb, "The Marriage of the Gas Turbines and Coal," *Mechanical Engineering*, pp. 58-63, September, 1991.

4. L. A. Ruth, "Combustion 2000, Clean, Efficient Power for the Future," paper presented at the *International Symposium on Improved Technology for Fossil Power Plants-New & Retrofit Applications*, Washington, D.C., 1993.

5. R. W. Swindeman and D. L. Marriott, "Criteria for Design with Structural Materials in Combined-Cycle Applications Above 815°C," paper 93-GT-203, International Gas Turbine and Aeroengine Congress and Exposition, Cincinnati, OH, May 24-27, 1993.

6. R. W. Swindeman, Summary of Work on Coatings and Claddings for Fossil Energy Applications, ORNL/TM-12367, Oak Ridge National Laboratory, Oak Ridge, TN, May 1993.

7. R. H. Mallett, *Creep-Fatigue Damage Analysis for a Hot Fluegas Vessel Tubesheet of Nickel-Chromium Aluminde Material*, MSTI-TR-756, Mallett Technology, Inc., August, 1993.

2. 13 ALLOYING EFFECTS ON THE HIGH-TEMPERATURE OXIDATION RESISTANCE OF Cr-Cr_2Nb

P. F. Tortorelli and J. H. DeVan

Oak Ridge National Laboratory
Metals and Ceramics Division
P. O. Box 2008
Oak Ridge, Tennessee 37831-6156

INTRODUCTION

Chromium-based alloys incorporating the Cr_2Nb Laves-phase are potential new materials for use in hostile environments of advanced heat engines and energy systems that operate at very high temperatures to achieve better energy efficiency.[1,2] The intermetallic Cr_2Nb phase, with a C-15 complex cubic structure,[3] has a high-melting point (1770°C)[4-5] and relatively low density (7.7 g/cm^2).[6] Results to date indicate that the two-phase Cr_2Nb/Cr(Nb) alloys have excellent strength for structural use at high temperatures (1000-1200°C).[1,2,7,8] However, such alloys suffer from poor toughness and fracture resistance. Current development efforts are focused on improving these properties as well as evaluating the high-temperature oxidation resistance of Cr-Cr_2Nb alloys under relevant metallurgical and environmental conditions. Relatively low oxidation rates over extended periods of time are necessary for deployment of such alloys at the high temperatures envisioned for potential applications.

Previously-reported oxidation results showed that elevated-temperature (900 and 950°C) exposures of Cr-Cr_2Nb alloys containing 6 and 12 % Nb resulted in multilayer scales with an outer layer of chromia and inner products containing niobium.[8] Spallation and indirect evidence of isothermal scale cracking were observed. The alloy with the higher concentration of niobium showed better oxidation resistance in terms of weight gain and scale adherence.[8] This was attributed to its greater volume fraction of the Cr_2Nb-Cr eutectic at the expense of the Cr-rich phase. While parabolic kinetics were observed at 900, 950, and 1000°C, an isothermal exposure temperature of 1100°C led to accelerated reaction of binary Cr-12% Nb manifested in the form of breakaway oxidation.[9] Alloying additions of Al (up to 18%) or Re (2%) did not improve the isothermal oxidation resistance of Cr-12% Nb, nor did the reduction in the level of impurities.[9] Further studies have now been

conducted to evaluate effects of other alloying additions on the isothermal oxidation resistance of Cr-Cr_2Nb alloys in air and form the basis of the present paper. The work has been mainly focused on 6% Nb alloys as these have been shown the most promise in improving room-temperature compressive ductility.[2]

EXPERIMENTAL PROCEDURES

Alloys of Cr-Cr_2Nb were prepared by arc melting and drop casting into water-cooled copper molds. High-purity niobium and chromium metal chips were used as charge materials, and the alloys were melted in a high vacuum (10^{-5} Pa) furnace. Details regarding alloy preparation and processing are described elsewhere.[2,10] Table 1 lists the alloy compositions discussed in this paper. As described below, the element referred to as XM was effective in refining the interconnected eutectic structure and improving mechanical behavior, while XO was beneficial to oxidation resistance. Rectangular specimens (approximately 8 x 8-16 x 1 mm) were cut or machined from as-cast or homogenized (1100°C, 3 days, vacuum) ingot pieces. All major surfaces were mechanically ground with 600-grit SiC abrasive before exposure.

Weight changes due to isothermal oxidation were measured using Cahn 1000 microbalances and a computer-controlled data acquisition system. The specimens were exposed to flowing, preheated, dried air (2 cc/s) at 950 for up to 180 h. At the end of each experiment, the specimens were furnace cooled and visually checked for loss of corrosion products by spallation. Selected specimens were analyzed by scanning electron microscopy (SEM).

RESULTS

Figure 1 compares the weight gain behavior of several 5.6% Nb alloys exposed to air at 950°C. Additions of either Re and Al (CN52) or Fe, Ni, and Al (CN53) had little effect on weight gains relative to the Cr - 6% Nb binary alloy (CN7). On the other hand, XM had a severe detrimental influence: the weight gains and rates for the alloys with 6% XM (CN65 and CN73) were substantially higher than for the XM-free compositions. The XM-containing alloys showed linear kinetics rather than the parabolic behavior associated

Table 1. Nominal compositions of alloys used in this study.

Alloy No.	Concentration (at.%)[a]					
	Nb	Al	Re	XM	XO	Zr
CN-4	12					
CN-7	6					
CN-52[b]	5.6	1.5	4			
CN-53[c]	5.6	1.5				
CN-60	12	2	4	6		
CN-61	12	2	4		4	
CN-65	5.6	1.5		6		0.1
CN-73[d]	5.6	1.5		6		0.1
CN-74	5.6	1.5		6	4	0.1
CN-75	5.6	1.5		6	6	0.1
CN-76	5.6	1.5		6	8	0.1

[a] Balance is Cr.
[b] 0.1% Hf
[c] 2% Fe, 2% Ni, 0.1% Hf
[d] Other ≤ 0.1%

with formation of protective oxide scales. As shown in Fig. 2, XM had a similar, although somewhat less dramatic, effect on the thermogravimetric results for Cr-Cr_2Nb alloys with 12% Nb.

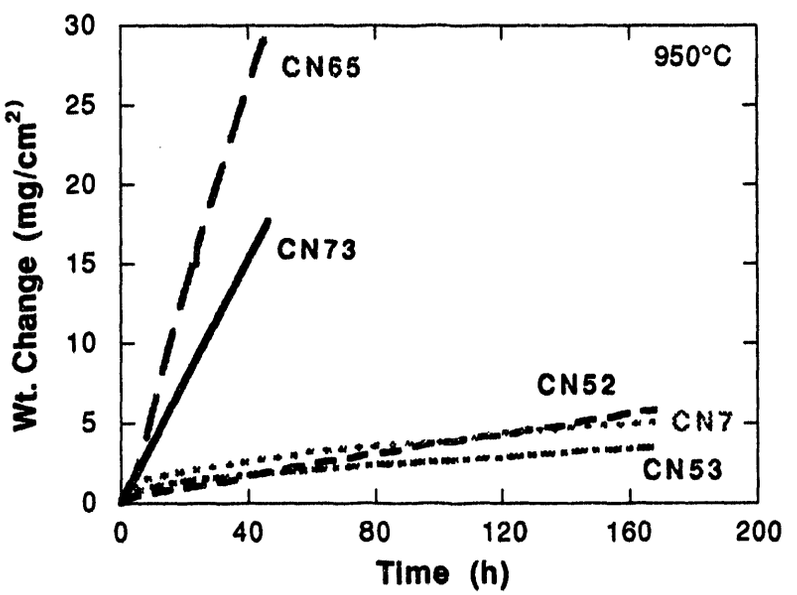

Fig. 1. Weight change versus time for Cr-~6% Nb alloys oxidized in air at 950°C.

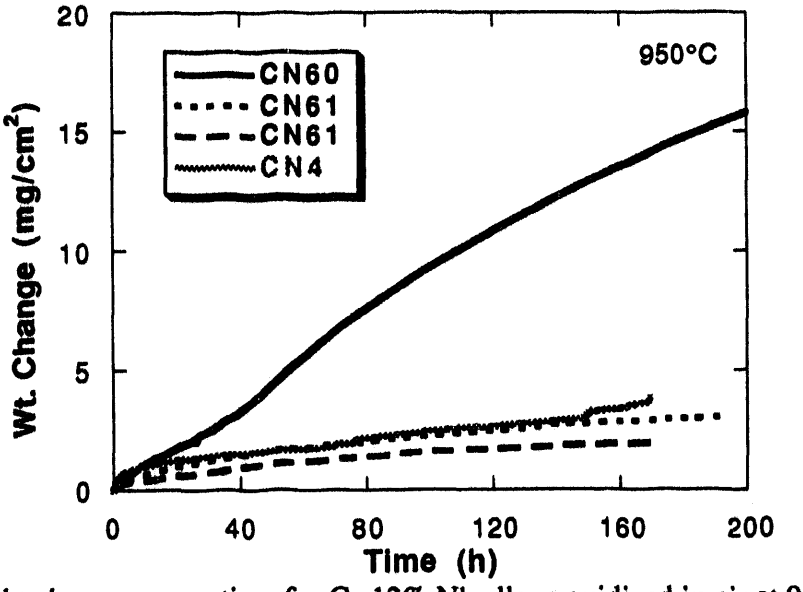

Fig. 2. Weight change versus time for Cr-12% Nb alloys oxidized in air at 950°C. Results from duplicate specimens of CN61 are included.

Figure 2 also indicates that the presence of XO in Cr - 12% Nb (CN61) results in oxidation behavior that is comparable to, or slightly better than, that of the binary composition. Because of this, the combined effect of XM and XO on air oxidation resistance was examined through exposures of alloys CN74, CN75, and CN76 (see Table 1). The results from this series of exposures are shown in Figs. 3 and 4. The data in Fig. 3 indicate a substantial improvement in oxidation behavior when 4 - 8% XO is present in XM-containing alloys. In Fig. 4, the thermogravimetric results for the alloys with XM + XO are compared to those for CN61 and the Cr - 6% and - 12% binary compositions.[8] Alloys CN74, CN75, and CN76 (5.6% Nb) had smaller weight gains and rates than Cr - 6% Nb (CN7) and also compared favorably to Cr - 12% Nb (CN4). The differences in the thermogravimetric results among the three Cr - 5.6% Nb - 6% XM - XO compositions were insignificant (Fig. 4). Oxidation rates of XO-containing alloys appeared to be relatively insensitive to the concentration of this element in the range investigated (4 - 8%). Furthermore, there was essentially no difference between the weight change results for the Cr - 5.6% Nb - 6% XM - XO alloys and that of Cr - 12% Nb - 4% XO (CN61). Indeed, in contrast to the difference in oxidation behavior of CN7 and CN4 (ref. 8 and Fig. 4), the presence of XO appeared to eliminate differences in oxidation resistance observed for the binary 6 and 12% Nb alloys.

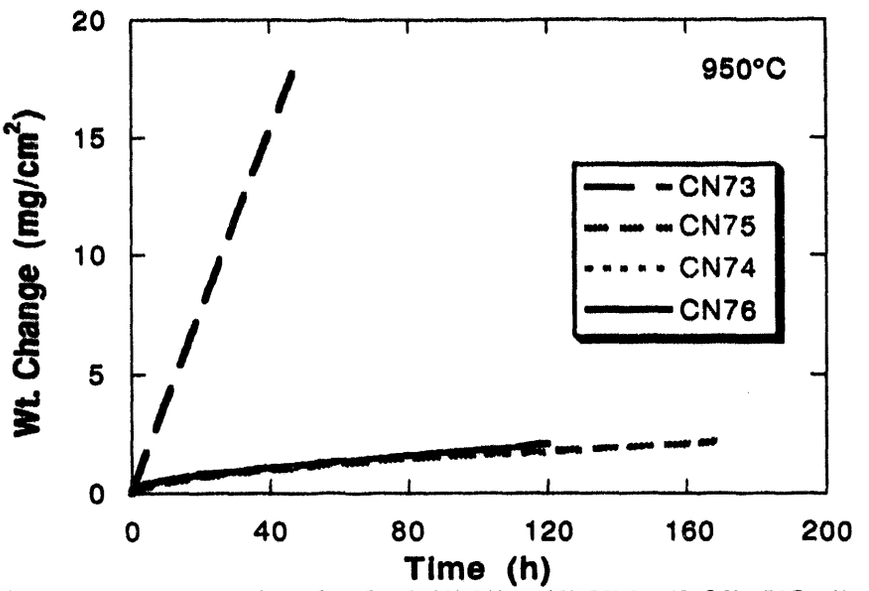

Fig. 3. Weight change versus time for Cr-5.6% Nb - 6% XM - (0-8%) XO alloys oxidized in air at 950°C.

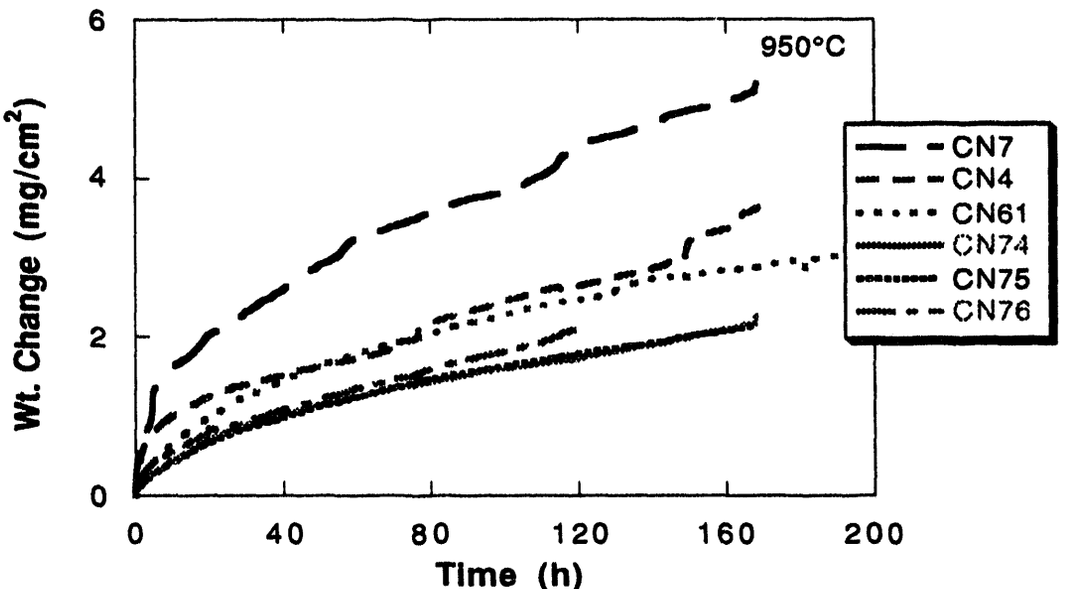

Fig. 4. Weight change versus time for Cr - 5.6% Nb - 6% XM - (4-8%) XO, Cr - 12% Nb - 4% XO, Cr - 6% Nb, and Cr - 12% Nb alloys oxidized in air at 950°C.

In order to ascertain whether significant differences in oxidation behavior could be due to certain microstructural differences, several of the alloys listed in Table 1 were exposed in both the as-cast and homogenized conditions. In isolated cases, an as-cast alloy showed extremely high weight gains. However, the typical differences in isothermal oxidation behavior were small, with the as-cast specimens showing slightly higher weight gains than the homogenized versions of the same composition (Fig. 5). Therefore, in

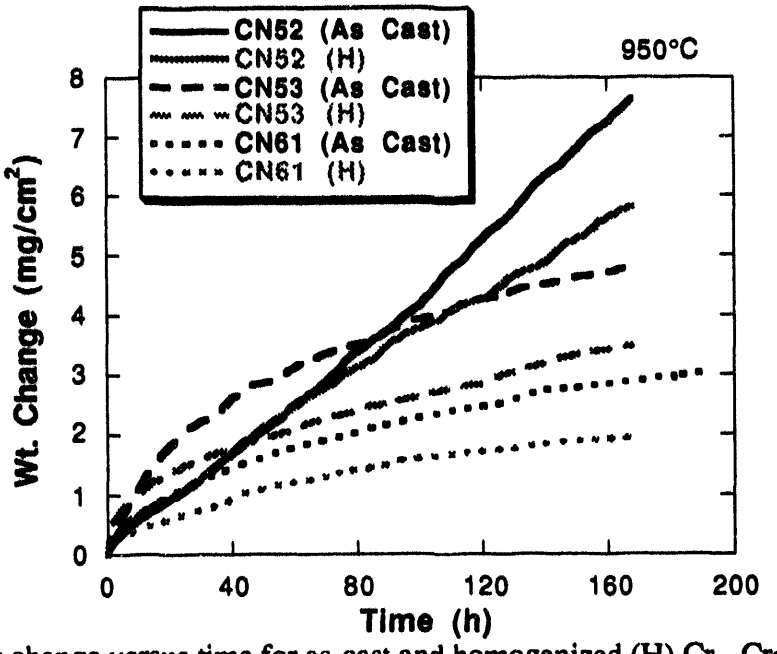

Fig. 5. Weight change versus time for as-cast and homogenized (H) Cr - Cr_2Nb alloys oxidized in air at 950°C.

general, such differences in starting microstructure did not appear to change the relative effects of the observed influences of compositional modifications.

The results of visual examination of specimen surfaces after cooling to room temperature following isothermal exposure at 950°C are given in Table 2. A significant variation in spallation tendency was noted. Alloys with XM suffered extensive spallation, while those with XO showed much less scale loss . An example of a specimen that suffered substantial spallation (CN60, see Table 1) is shown in Fig. 6. Note the scale cracking and multiple layers of surface products.

Table 2. Summary of visual observations of Cr-Cr_2Nb specimens after isothermal exposure to air for 150 to 180 h at 950°C.

Alloy	% Area Showing Some Spallation	Appearance of Scale(s)
CN52	25-50[a]	upper scale gray; lower: green-gray
CN53	<10	gray
CN60	75	gray and dark gray
CN61	<10[a]	gray
CN65	100	many large gray fragments; surface dark gray
CN73	100	many large gray fragments; surface dark gray
CN74	25-50[a]	upper scale gray; lower: green-gray
CN75	<10	gray
CN76	25[a]	upper scale gray; lower: dark and light gray

[a] Duplicate specimens

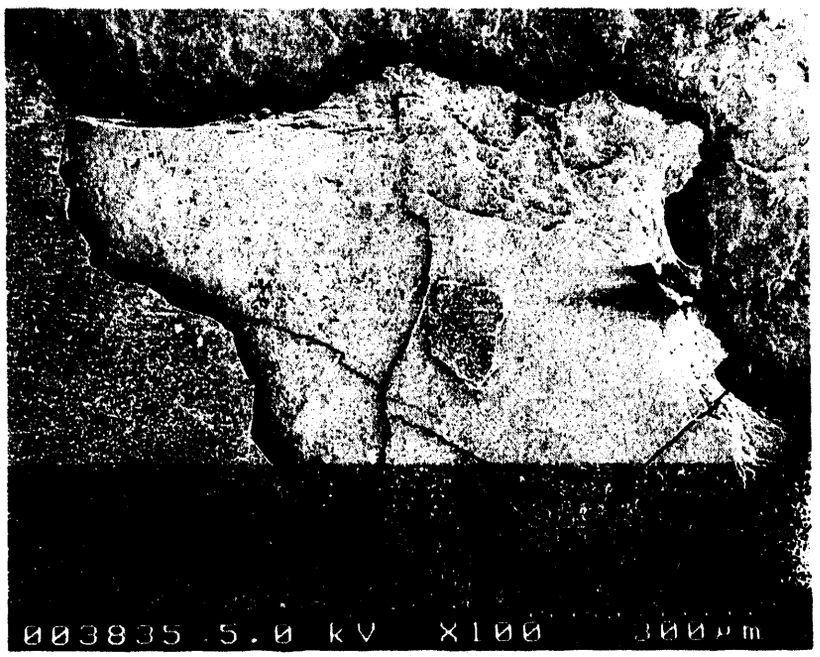

Fig. 6. Scanning electron micrograph of oxidized surface of Cr - 12% Nb - 4% Re - 2% Al - 6% XM after cooling from the isothermal exposure temperature of 950°C.

DISCUSSION

The alloys of the present study are in the hypoeutectic part of the Cr-Cr_2Nb two-phase region. The eutectic (17 at. % Nb) is composed of a Cr_2Nb matrix with a dispersion of Cr-rich material and Cr-rich regions with very fine Cr_2Nb precipitates.[1] It was previously shown that the oxidation of Cr -6 and -12 at. % Nb alloys in air at 950°C led to the formation of multilayer scales with an outer layer of chromia and inner products containing niobium.[8] A porous inner layer preferentially formed on a Cr-rich phase.[8] The alloy with the higher concentration of niobium showed better oxidation resistance in terms of weight gain and scale adherence. Because the increase in niobium concentration from 6 to 12% results in a higher volume fraction of the eutectic mixture, the poorer overall oxidation resistance of the 6% Nb alloy appeared to be related to the greater abundance of the Cr-rich phase.[8]

The presence of the element denoted as XM refines the coarse eutectic structure of Cr-Cr_2Nb and, in so doing, substantially improves the compressive strength and ductility of the alloys.[10] However, the present results clearly indicate that this element has a substantial deleterious effect on the oxidation behavior of Cr - 6 and -12 % Nb alloys (Figs. 1 and 2). The rates of weight gain, and spallation tendencies, of alloys containing 6% XM are significantly greater than those shown by any of the other compositions. For

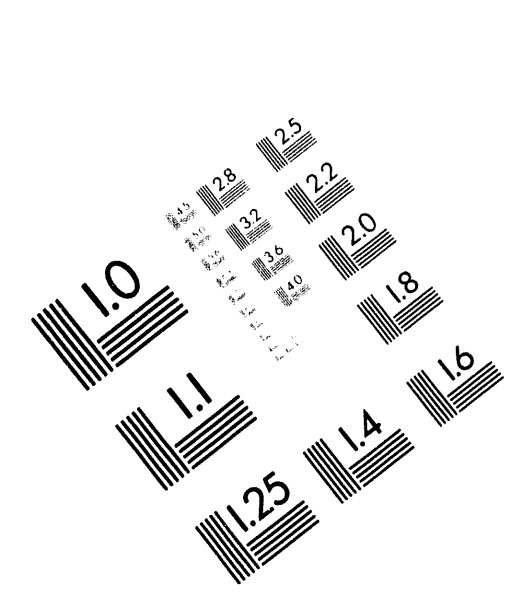

Association for Information and Image Management

1100 Wayne Avenue, Suite 1100
Silver Spring, Maryland 20910

301/587-8202

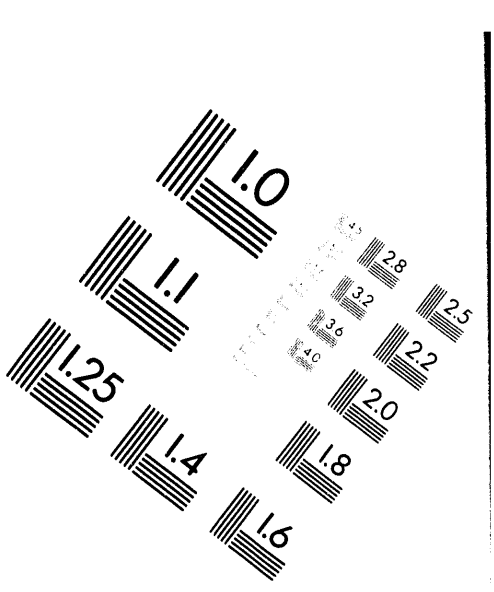

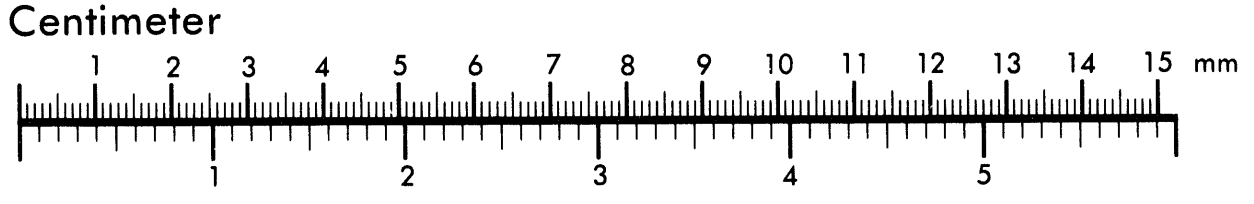

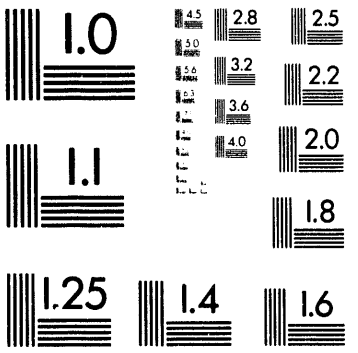

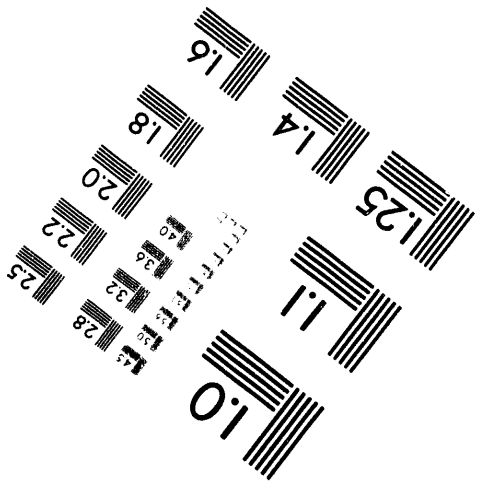

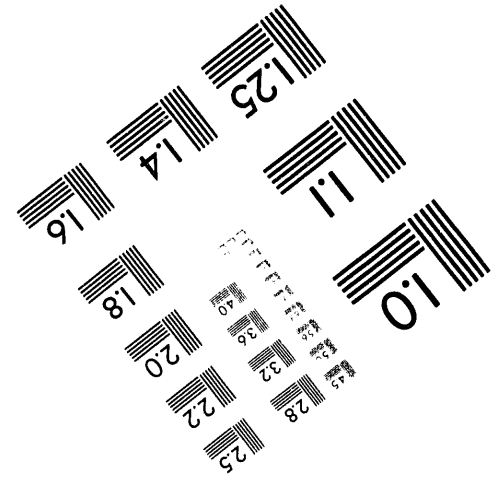

MANUFACTURED TO AIIM STANDARDS
BY APPLIED IMAGE, INC.

2 of 3

5.6% Nb - 6% XM alloys, the oxidation rates were approximately linear (Fig. 1). Indeed, this set of XM-containing alloys appeared more susceptible to air oxidation than the Cr-12% Nb-XM composition (compare Figs. 1 and 2). As such, this dependence on niobium content is consistent with the results of the earlier study of binary 6 and 12% Nb alloys.[8] The conversion of the interconnected Cr_2Nb-phase into a finer distribution (mainly for the 12% Nb alloy)[10] does not appear to be beneficial to oxidation resistance. Any microstructural influence, however, is probably secondary - the rapid weight gains indicate significantly greater reactivity of XM with oxygen such that the overall oxidation resistance of these alloys is substantially reduced.

The marked detrimental influence of XM on the oxidation behavior of Cr-Cr_2Nb can be completely offset by the addition of XO (see Fig. 3). Liu, Horton, and Carmichael have shown that XO strongly partitions to the Cr_2Nb(Cr) phase and stabilizes the eutectic structure.[10] Such a concentration of XO in the eutectic phase can decrease its susceptibility to reaction with oxygen and, when combined with the observed morphology of the Cr_2Nb(Cr), positively affect oxidation resistance. However, it is believed that it is the smaller concentration of XO in the susceptible Cr-rich phase that is actually the cause of improved overall oxidation behavior of the XO-containing alloys. This element has a known beneficial effect for chromia-forming systems, and as the Cr-rich phase is thought to be the more susceptible microstructural component[8] improvement in its oxidation resistance can have a substantial effect on weight gains and spallation resistance.

Corroboration of the role of XO in preferentially improving the oxidation resistance of the Cr-rich regions of Cr-Cr_2Nb alloys awaits microstructural analysis of properly prepared cross sections. However, there are specific results that tend to support such an influence of XO. Figure 4 shows that there is little difference in the isothermal oxidation behavior between XO-containing 6 and 12% Nb alloys (that is, between alloys with different volume fraction ratios of the two phases). This is in contrast to previous findings (described above and in ref. 8) and supports the hypothesis that XO is specifically increasing the oxidation resistance of the Cr-rich phase. If the XO additions acted to preferentially improve the oxidation resistance of the eutectic phase, differences in behavior between 6 and 12% Nb alloys should increase, which is the opposite effect to what is shown by the present data. Furthermore, while there is definite evidence that scale cracking occurs for Cr-6 and -12% Nb alloys during isothermal exposure at 900 and 950°C,[8,9] the discontinuities in the thermogravimetric curves that typically indicate such processes[11] are not observed for the XO-containing alloys (compare the results for CN74,

C75, and CN76 with those for CN4 and CN7). This finding suggests that the presence of this element reduces the susceptibility for isothermal scale cracking normally observed for the binary Cr-Cr_2Nb alloys. As much of the scale cracking and the spallation during subsequent cooldown appeared related to the Cr-rich regions,[8,9] the presence of a small concentration of XO in the Cr-rich phase can therefore significantly improve the oxidation of the alloys by reducing cracking and the resulting accelerated oxide growth and loss of product.

As described above, it was previously reported that 12% Nb alloys were superior in oxidation behavior to the 6% alloys.[8] Subsequent work with other alloys did not reveal any compositional modifications that improved the behavior to the point where they matched or exceeded that of the 12% Nb binary composition.[9] The present results show that, regardless of the presence of XM, the effect of XO is to improve the overall oxidation resistance (in terms of both weight gains and spallation, see Table 2) such that those alloys containing this element show the best behavior of any Cr-Cr_2Nb composition examined to date. As the differences in the isothermal oxidation results among the three Cr - 5.6% Nb - 6% XM - XO compositions are quite small (similar weight gains and rate constants for 4, 6, and 8% XO, Fig. 4), the choice of the appropriate XO level can be based on mechanical properties (or other) considerations.[10]

SUMMARY AND CONCLUSIONS

The effects of several alloying additions on the high-temperature oxidation resistance of Cr-Cr_2Nb were examined on the basis of isothermal exposures to air at 950°C. Additions of either Re and Al or Fe, Ni, and Al had relatively little effect on weight gains relative to the Cr - 6% Nb binary alloy. One alloying element that improved the mechanical behavior of Cr-Cr_2Nb alloys substantially increased the oxidation rates and spallation susceptibilities of Cr - 6 and - 12% Nb alloys. However, the addition of another element completely offset these deleterious effects. The presence of this latter element resulted in the best overall oxidation behavior of all Cr-Cr_2Nb compositions and provides the opportunity to improve the mechanical properties of this alloy system without necessarily compromising oxidation resistance. The effects of this element were manifested as relatively low weight gains, substantially reduced scale cracking and spallation, and elimination of the dependence of oxidation behavior on niobium content (that is, on the relative amounts of the Cr-rich and eutectic phases). Its beneficial influence can be attributed to improvement in the oxidation resistance of the Cr-rich phase, which

otherwise showed preferential susceptibility to degradation upon exposure to high-temperature air.

ACKNOWLEDGMENTS

The authors thank M. Howell for experimental support, A. M. Williams for microscopy, and C. T. Liu, J. R. Keiser, and J. R. DiStefano for their reviews of the manuscript. This research was sponsored by the Fossil Energy Advanced Research and Technology Development (AR&TD) Materials Program, U S. Department of Energy, under contract DE-AC05-84OR21400 with Martin Marietta Energy Systems, Inc.

REFERENCES

1. M. Takeyama and C. T. Liu, "Microstructure and Mechanical Properties of Laves-Phase Alloys Based on Cr_2Nb," *Mater. Sci. Eng.* **A132**, 61, (1991).

2. C. T. Liu, J. A. Horton, and C. A. Carmichael, pp. 297-307, in *Proc. 7th Annual Conf. on Fossil Energy Materials*, ORNL/FMP-93/1, Oak Ridge National Laboratory, July 1993.

3. F. Laves, in *Theory of Alloy Phases*, American Society for Metals, Metals Park, OH, 1956, p. 124.

4. H. J. Goldschmidt and J. A. Brand, J. *Less-Common Met.* **3**, 44 (1961).

5. T. B. Massalski, J. L. Murray, L. H. Bennett, and H. Baker (eds.), *Binary Alloy Phase Diagram*, American Society for Metals, Metals Park, OH, 1986.

6. A. I. Taub and R. L. Fleischer, *Science* **243**, 616 (1989).

7. C. T. Liu, pp. 375-383 in *Proc. 6th Annual Conf. on Fossil Energy Materials*, ORNL/FMP-9211, Oak Ridge National Laboratory, July 1992.

8. P. F. Tortorelli and J. H. DeVan, "The Nature of Scales Grown on Binary Cr-Nb Alloys," pp. 229-236 in *Proc. Symp. on Oxide Films on Metals and Alloys*, B. R. MacDougall, R. S. Alwitt, and T. A. Ramanarayanan (eds.), Proceedings Vol. 92-22, The Electrochemical Society, 1992.

9. P. F. Tortorelli, L. J. Carson, and J. H. DeVan, pp. 309-318 in *Proc. 7th Annual Conf. on Fossil Energy Materials*, ORNL/FMP-93/1, Oak Ridge National Laboratory, July 1993.

10. C. T. Liu, J. A. Horton, and C. A. Carmichael, these proceedings.

11. P. Kofstad, *High Temperature Corrosion*, Elsevier Applied Science, London, 1988.

2.14 Development of Microwave-Heated Diesel Particulate Filters

Mark A. Janney and David P. Stinton
Oak Ridge National Laboratory
Oak Ridge, Tennessee 37831-6087

Overview

The purpose of this research is to help develop microwave-heated diesel engine particulate filter/burner devices. The goal is to develop materials that will perform both as filter and heater in such a device. A Cooperative Research and Development Agreement (CRADA No. ORNL93-0172) between Martin Marietta Energy Systems (MMES) and the Cummins Engine Company is in place that supports this work. The Department of Energy (DOE) CRADA monies come from both the Fossil Energy AR&TD Materials Program and the Energy Efficiency and Renewable Energy - Office of Transportation Technologies (EE-OTT), Heavy Duty Transport Program.

Diesel engines will soon be required (1998) to emit essentially no particulate exhaust into the environment. One of the approaches to prevent such emissions is to trap the particles in a filter, then burn the trapped particles on a regular cycle. An approach that has been proposed by Cummins Engine Co. is to build a system based on a ceramic filter that can be heated with microwaves. We will fabricate such filters and determine how they interact with microwaves to heat and burn the carbon particulates trapped in the filter material.

We propose to develop a ceramic composite structure of SiC-coated ceramic fiber that can be used as a diesel engine particulate filter. For commercial usage a particulate filter must: 1) filter carbon particles from high temperature diesel exhaust gas at an acceptable (low) backpressure; 2) survive thousands of thermal transients caused by regeneration (cleaning) of the filter by oxidizing the collected carbon; (3) be durable and reliable over the life of the filter, which is in excess of 300,000 miles (10,000 hours of operation); and, (4) provide a low overall operating cost which is competitive with other filtering techniques.

SiC-coated ceramic fiber was selected as the filter material because it can be readily heated by microwave energy. Particulate traps must be regenerated by heating the carbon particles to approximately 600°C to oxidize the carbon. Heating by microwaves is expected to provide more uniform heating of the filter and result in a lower cost, more reliable regeneration system. Previous methods of regeneration used diesel-fired burners or electrical resistance heating for regeneration. Uneven heating and use of weak ceramic materials resulted in cracking of the trap and loss of filtration capability. Fiber composites have excellent thermal shock capability. Producing a filter by manufacturing a fiber-reinforced ceramic paper has inherent advantages since it is possible to tailor the filtration characteristics of the ceramic paper while maintaining a strain tolerant material.

The idea of using microwave heating combined with ceramic filters to trap and burn carbon particulate emissions from diesel engines represents a large-scale, near term consumer and industrial application of two technologies, microwave heating and chemical vapor infiltration, developed under the AR&TD materials program. As such, it has the potential to be an excellent example of technology transfer and cooperative research and development between a national laboratory and U.S. industry. This approach represents the front runner in the thinking of one of the nation's foremost diesel manufacturers.

Technical Progress

We propose to investigate the development of materials for diesel particulate filters. We will devote our effort to evaluation of various candidate materials concerning: (1) their interaction with a microwave field - i.e., how they heat; (2) their thermal shock resistance; and, (3) corrosion of the filter caused by interactions with the emissions and the high temperatures required to burn off the residues.

A CRADA between Cummins Engine Company and MMES was signed in August, 1993. Subsequent to the signing, a series of kickoff meetings between Cummins and ORNL personnel were convened. A plan of action was developed involving Cummins corporate headquarters, the FleetGuard Division of Cummins, and ORNL. FleetGuard is developing the filter design based on their expertise and experience in making oil and air filters for large diesel engines. ORNL is developing the process for coating the filter materials with SiC, selecting the type of SiC coating to be used, testing and evaluating the coated papers

regarding corrosion, microwave heating, etc. Cummins corporate is performing evaluation tests on the filters.

During the first six months of this project, major strides have been taken to establish the capability to perform the work and to initiate many of the tasks. A large-scale chemical vapor deposition (CVD) furnace has been built and commissioned. The furnace is six inches in inside diameter with an 24 inch-long central uniform hot zone. Five coating runs have been made so far; these are summarized in Table 1. The SiC deposition conditions were identical in all cases. An average of 2.3 μm of SiC was deposited on the fibers during these runs, based on weight gain of the fiber preforms and knowledge of the starting diameters of the fibers. Three different fiber preforms were coated during each of these runs. Four preforms of woven Nicalon® fiber were coated along with two proprietary samples that were made by FleetGuard, designated Sample #12 and Sample #15. Several of these samples have been forwarded to Cummins, who will have dielectric property measurements made by an independent testing laboratory.

FleetGuard Division of Cummins Corporation has designed and tested a number of different ceramic paper compostions made from several different fibers, including Nicalon® silicon oxy-carbide, Saffil® alumina, Textron SCS6 silicon carbide, and proprietary silicon carbide minifibers. These papers are being fabricated as 4 in. diam by 0.040 in. thick disks. They will be tested for permeability and filtration effectiveness before and after CVD coating, and for their microwave absorption properties.

In addition to the work on the filter materials themselves, work is being done to understand the nature of the heating process for dielectric materials coated with conducting films. All of the work involves measurement of the microwave absorption of a conductive coating on a non-absorbing substrate. The main parameters that are being varied are coating composition, coating thickness (up to 1 μm), and the temperature at which the measurements are made (ambient to as high as 1200°C). There are three elements to the work: (1) SiC-coated ceramic fiber paper; (2) SiC-coated alumina substrates; and (3) gold-coated alumina substrates.

Table 1. CVD Runs Made In New Coating Furnace

Coating Run	Dopant	MTS flow (g/min)	H_2 flow (l/min)	Deposition Temperature	Pressure	Comments
1	None	1.5	3.2	975°C	30 torr	
2	None	1.5	3.2	975°C	30 torr	
(Carbon layer put down before SiC; 100 cc/min propylene, 1 l/min Ar, 30 torr)						
3	Carbon	1.5	3.2	975°C	30 torr	360 ml/min CH_4
4	Boron	1.5	3.2	975°C	30 torr	50 ml/min BCl_3
5	Silicon	1.5	3.2	975°C	30 torr	$SiCl_4$ as Si source

The rationale for the three part approach is as follows. (1) The SiC-coated ceramic fiber paper is the ultimate material of interest for the particulate filter assembly. Its microwave absorption and heating properties are of the most direct importance to the project. We will need to examine the properties of the SiC-coated paper in the as-fabricated state, after heat treatment in air (numerous cycles), and after collection of exhaust particles and subsequent burnout (several cycles). (2) The SiC-coated alumina substrates will give us an opportunity to study the relationship between SiC coating thickness and microwave absorption in a more controlled manner than that afforded by the coated ceramic paper. It will also be easier to evaluate features such as oxidation product formation on such samples. (3) Finally, the gold-coated alumina substrates provide us with a model system to study the microwave absorption properties of thin conducting films on a non-absorbing substrate. A primary advantage of using gold is that its conductivity as a function of temperature is well known. Therefore, the only variable in the study of the microwave absorption of the gold films is thickness. So far, the protocol for making the dielectric properties measurements have been determined by an independent testing laboratory, using samples of gold-coated alumina and SiC-coated ceramic fiber papers supplied by ORNL. In the coming months, samples of alumina-SiC, alumina-gold, and SiC-coated alumina fibers will be tested.

2.15 MATERIALS SUPPORT FOR HITAF

K. Breder and V. J. Tennery

INTRODUCTION

The purpose of this project is to compare structural ceramic materials proposed for use in the air heater of a coal fired high temperature advanced furnace (HITAF) for power generation. The work will provide necessary initial strength and statistical material parameters for design of a prototype system. Two teams are currently funded by Pittsburgh Energy Technology Center (PETC) under the Combustion 2000 program to develop such a system. One team is led by the United Technologies Research Corporation, and consists of UTC Turbo Power and Marine Division, Bechtel, Oak Ridge National Laboratory (ORNL) and a Joint Venture of Physical Sciences Inc. (PSI) Technologies, Reaction Engineering International (REI) and University of North Dakota Energy & Environmental Research Center (UNDEERC); the other team is led by Foster Wheeler Development Corporation, and members are AiResearch Division of AlliedSignal Aerospace Systems & Equipment, Research Cottrell, TRW, General Electric and Bechtel.[1, 2]

DISCUSSION OF CURRENT ACTIVITIES

The following key properties are being evaluated in the present task: fast fracture strength at room temperature, 1100°C, and 1400°C; statistical analysis in the form of a Weibull analysis and necessary fractography; slow crack growth properties evaluated by the dynamic fatigue method; and creep/creep-rupture effects measured through interrupted static fatigue experiments. Initial corrosion experiments are being performed in cooperation with UNDEERC, where ORNL is performing fast fracture measurements of corroded specimens .

Materials

Three materials have been compared. These are β-SiC from Coors Ceramics Company, NT230 siliconized SiC from Saint Gobain Norton and Lanxide Dimox SiC_p/Al_2O_3 from Lanxide Corporation. The manufacturers' data on material properties are summarized in Table 1. β-SiC is sintered silicon carbide with a fine grain structure and high density. NT230 SiC is siliconized silicon carbide and contains free silicon metal (8 vol%) and some residual porosity. The SiC_p/Al_2O_3 which is manufactured by the Lanxide Direct Oxidation process (Dimox) contains 48 vol% SiC_p, 38 vol% Al_2O_3 and 13 vol% Al-alloy, and some residual porosity. The SiC ceramics were tested as machined while the Lanxide Dimox was reoxidized by the manufacturer after machining.

Table 1. Properties of the selected materials.

Coors β-SiC Sintered Silicon Carbide (SiC), Coors Ceramics Company	
99.9% SiC	Density 3.1 g/cm^3
	Thermal Conductivity 110 W/mK
	Thermal Expansion 4.4 x10^{-6} /°C
	Fracture Toughness 3.0 MPam$^{1/2}$
NT 230 Siliconized Silicon Carbide (SiC), Norton Saint Gobain	
8 Vol% Si - metal	Density 3.1 g/cm^3
90 Vol% SiC	Thermal Conductivity 120 W/mK
2 Vol% Pores	Thermal Expansion 4.4 x10^{-6} /°C
	Fracture Toughness 3.0 MPam$^{1/2}$
Lanxide Dimox Aluminum Oxide with Silicon Carbide Particles, Lanxide Corp	
48 Vol% SiC	Density 3.4 g/cm^3
38 Vol% Al_2O_3	Thermal Conductivity 60 W/mK
13 Vol% Al - alloy	Thermal Expansion 6.8x10^{-6} /°C
1 Vol% Pores	Fracture Toughness 4.5 MPam$^{1/2}$

Fast Fracture

The fracture strength of ceramic materials is most commonly measured in four-point flexure.[3] In this test a specimen of 4x3x50 mm is subjected to bending in a fixture providing an inner span of 20 mm and an outer span of 40 mm. The specimen is loaded to fracture while load and deflection are monitored, and the flexure strength is calculated

according to standard beam theory. The flexure method offers the possibility of testing a large number of samples at a reasonable price, and since the load train arrangement is relatively simple, several specimens may be tested simultaneously.

Weibull Analysis

Weibull analysis is the statistical tool most commonly used to analyze fracture data for structural ceramics.[4] Due to the brittle nature of ceramic materials, the fracture strength of a set of specimens may vary as much as 100% from its average strength, necessitating a statistical analysis of the data. The Weibull analysis is a weakest link theory stating that a given volume of a ceramic material under uniform stress will fail from the most severe flaw. The probability of failure is given by:

$$P_f = 1 - \exp\left[- \int V \left(\frac{\sigma_f}{\sigma_0}\right)^m \right], \qquad (1)$$

where

P_f is the failure probability,
V the specimen volume,
σ_f the fracture strength,
m the Weibull modulus, and
σ_0 the Weibull scaling factor.

The Weibull modulus m is used as a design parameter for ceramics and describes the spread in the strength data. The Weibull scaling parameter σ_0 is related to the average strength of the sample. It is desirable that a structural ceramic have a high m and a high σ_0. The Weibull parameters are directly obtained from strength data by, for instance, the maximum likelihood method:[5]

$$\frac{\Sigma[\ln\sigma(\sigma)^m]}{\Sigma(\sigma^m)} - \frac{1}{m} = \frac{\Sigma(\ln\sigma)}{N} \qquad (2)$$

$$\sigma_0 = \left[\frac{\Sigma(\sigma^m)}{N}\right]^{1/m} \qquad (3)$$

where

σ is the fracture strength,

N is the number of specimens, and

m and σ_0 are the Weibull parameters as described above.

Static and Dynamic Fatigue

The term "fatigue" as used for structural ceramics is different from that commonly used for metals. For ceramics the term fatigue is used to describe the decrease in strength due to the combined action of *static* stress and degrading environment. The mechanism which causes this is known as slow crack growth (SCG) and is the growth of small preexisting cracks or voids at stress levels less than those needed to cause catastrophic failure. This happens because the individual atomic bond strength is decreased due to the specific environment. Eventually, a small crack will grow to a size large enough to cause catastrophic failure at the given stress level. In order to predict the lifetime for components in a given environment, the velocity at which cracks grow at a given stress must be known.[6]

A static fatigue experiment is performed by loading a specimen to a given stress in the given environment and recording the time to failure. This type of test can be extremely time consuming (> 1000 h) and several specimens are needed at each condition in order to obtain the required statistics. A common way to accelerate the test is to perform a dynamic fatigue experiment in which the specimens are loaded to failure at several given stressing rates and the fracture strength is recorded as a function of applied stressing rate.[7] If a material is susceptible to SCG, the fracture strength will decrease as a function of decreasing stressing rate, and by applying the following fracture mechanics framework on the measured data, the SCG parameters may be determined. The crack velocity during slow crack growth is often described in a power law form:

$$V = A\left(\frac{K_{appl}}{K_{IC}}\right)^{n} \qquad (4)$$

where

K_{appl} is applied stress intensity,

K_{IC} is the critical stress intensity,

V is the crack growth velocity, and

A and n are materials constants.

Combining this with the Griffith criteria for fast fracture strength:

$$\sigma_i = Y K_{IC} c^{-1/2} \tag{5}$$

where

σ_i is the strength,

c is the crack length, and

Y a specimen geometry and crack shape parameter.

The time to failure under constant applied stress may be obtained:

$$t_f = B \sigma_i^{n-2} \sigma_f^{-n} \tag{6}$$

where

$$B = \frac{2 K_{IC}^2}{(n-2)AY^2}$$ is a material constant,

and

t_f is time to failure

σ_f is fatigue strength

σ_i is fast fracture strength (inert).

In the case of the dynamic fatigue experiment, the equations combine to give

$$t_f = B (n+1) \sigma_{inert}^{n-2} \sigma_f^{-n} \tag{7}$$

and

$$\sigma_{fatigue}^{n+1} = B (n+1) \sigma_i^{n-2} \dot{\sigma} \tag{8}$$

where

$\dot{\sigma}$ is applied stressing rate

and the fatigue parameter n is obtained by plotting $\log\sigma_f$ vs $\log\dot{\sigma}$.

Combining the dynamic fatigue equations with the Weibull statistics we can then estimate the predicted lifetime:

$$\ln t_f = \ln B + \frac{n-2}{m} \ln\ln\left[\frac{1}{1-P_f}\right] + \ln(n+1) + (n-2)\ln\sigma_0 - n \ln \sigma_f . \qquad (9)$$

Hence, it is seen that the estimated time to failure is a function of the slow crack growth parameter n and the Weibull parameters m and σ_0 for the inert strength distribution.

Interrupted static fatigue is a method to supplement the dynamic fatigue data. The specimens are held at a load known to be a certain percentage of the actual fast fracture load at the given environment, and after a given time the test is interrupted and the remaining strength is measured by loading the specimen to failure. In this manner limited information about the tendency for a material to creep is also obtained.

Fractography

The Weibull theory assumes that all failures used to generate the Weibull parameters are similar in nature, i.e., stem from the same type of flaws. This may not always be the case, most notably there will be a difference in flaws stemming from the powder pressing and sintering process and flaws stemming from machining and handling of the components. The purpose of performing careful fractography is to identify the different sources of failure origins, and take that information into account by appropriately censoring the Weibull distribution. Further, fractography is a necessary tool in assessing the SCG behavior. If strength degradation as a function of time is observed, the microscopical investigation can aid in determining the mechanisms for the degradation, whether SCG or other strength degrading mechanisms are operative.

Exposure to Coal Ash

As a first measure of the materials resistance to coal ash corrosion, coupons of the ceramics were exposed in a muffle furnace at UNDEERC. The materials were exposed to two coal ash types; Wyodak and Illinois #6 at 1093°C and 1370°C for 300 h. After exposure the corrosion behavior was evaluated by microscopy at UNDEERC[8], and the coupons were then machined into flexure bars and the residual strength measured at room

temperature at ORNL. The fracture strength and failure mechanisms were then evaluated as a function of exposure environment and exposure temperature.

EXPERIMENTAL RESULTS AND DISCUSSION

Fast fracture as a function of temperature is shown in Fig. 1. The Weibull distributions of the three materials are shown in Figs. 2, 3, and 4 for room temperature, 1100°C, and 1400°C, respectively. The measured strengths as a function of stressing rate are shown in Figs. 5 and 6 for the three materials at 1100°C and 1400°C, respectively.

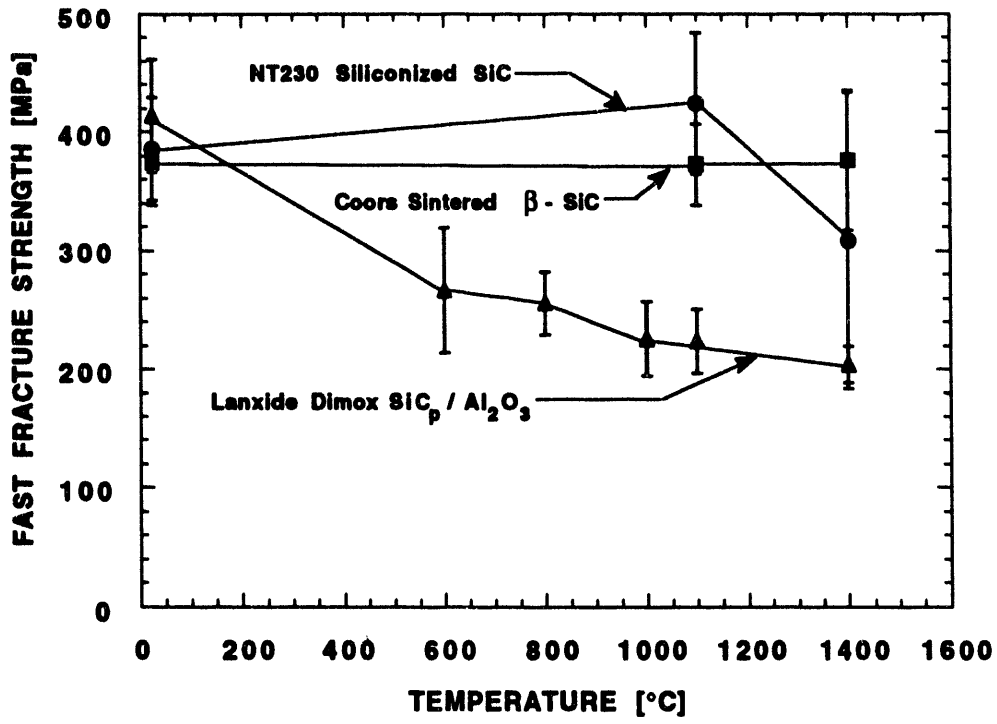

Figure 1. Fast fracture strength as a function of temperature for the three ceramics.

NT230 at 1400°C was the only material-temperature combination which showed any strength degradation over time and the SCG parameter n was calculated to be equal to 18 according to Eq.8. The Lanxide Dimox material could only be tested up to stressing rates of 0.01 MPa/s at 1400°C because at the slower stressing rates creep became so pronounced that the four-point flexure fixtures no longer could accommodate the

specimens. Also at the 0.01 MPa/s stressing rate the creep was measurable, see Fig. 7 for the load deflection curves. The strength values calculated according to beam theory are therefore overestimating the strength of Lanxide Dimox at this condition.

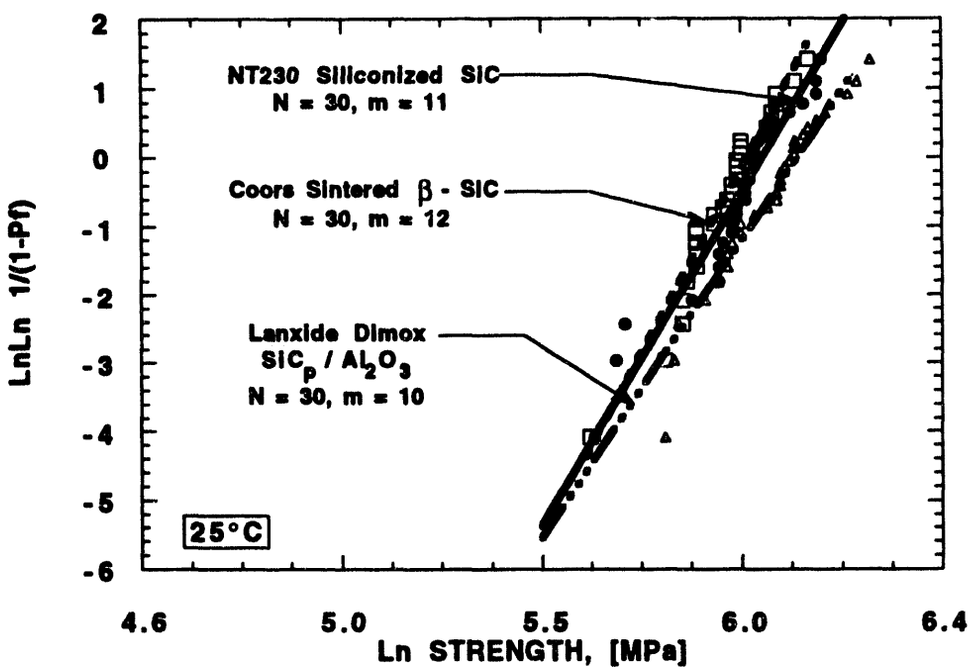

Figure 2. Weibul distribution of the room temperature fast fracture strength for the three ceramics.

The fractography results confirmed the dynamic fatigue results. In general the failure mode for Coors β-SiC was fast fracture from pores in the microstructure, and this did not change as a function of stressing rate or temperature. Lanxide Dimox failed in general from metal rich areas, but at 1400°C at the slower stressing rates, creep became pronounced and the specimens failed due to accumulated creep damage. NT230 was delivered to ORNL in two batches, probably with a slight difference in Si - content. At room temperature and at 1100°C the failure mode for both batches were similar; fast fracture from pores in the microstructure. At 1400°C there was a clear difference between the two batches in the fast fracture test; one batch failing from a combination of pores and metal rich inclusions, the other failing from pores as was observed at the lower

temperatures. At the slower stressing rates where strength degradation was observed, the specimens failed from metal rich areas that had grown in size during the test, and the batch difference became insignificant. A thorough documentation of the fractographic investigation will follow in the final report.

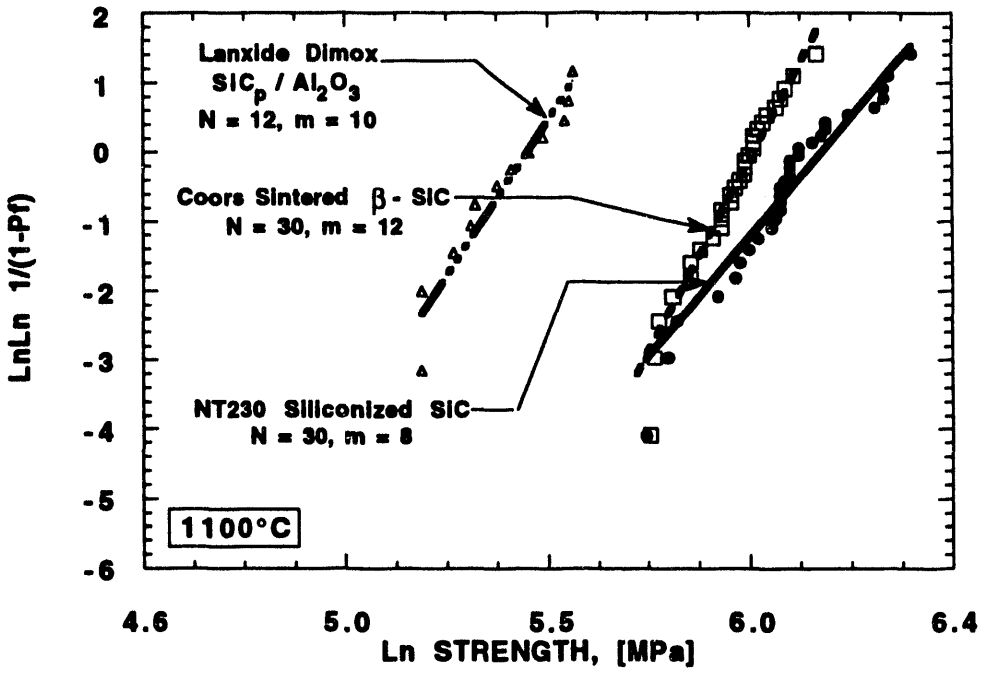

Figure 3. Weibul distribution of the 1100°C fast fracture strength for the three ceramics.

The strength as a function of temperature for the three ceramics under consideration is as expected for these materials. The Coors β-SiC showed no strength reduction at the temperatures under consideration, while the two other materials exhibit a drop in strength at the temperatures where the metal in these materials soften and melt. The Weibull analyses of the three ceramics reveal some important differences. At room temperature both the Weibull modulus and characteristic strength are comparable for the three materials, as can be seen in Fig. 2. At the elevated temperatures, however, it is seen that the Weibull modulus stays relatively unchanged for Lanxide Dimox and Coors β-SiC, while for NT230 a gradual reduction of the Weibull modulus is seen. At 1400°C the Weibull modulus m = 2.8, an unacceptably low value for a structural material. The

reasons for this can be found by investigating the microstructures and by performing careful fractography. The lower Weibull modulus at 1100°C and 1400°C for NT230 is due to the variability in the size of pores in the material and due to the fact that the NT230 was delivered in two batches with slightly different amounts of Si in them. The effect of the Si - content is most pronounced at 1400°C as seen in the fast fracture results. A thorough discussion of these effect will be included in the final report. The dynamic fatigue experiments, shown in Figs. 3 and 4, show that there is no strength reduction with time at 1100°C for any of the ceramics. At 1400°C a pronounced strength reduction is seen for NT230. This strength reduction is due to the subcritical growth of pore-like cracks, often containing metal rich inclusions.

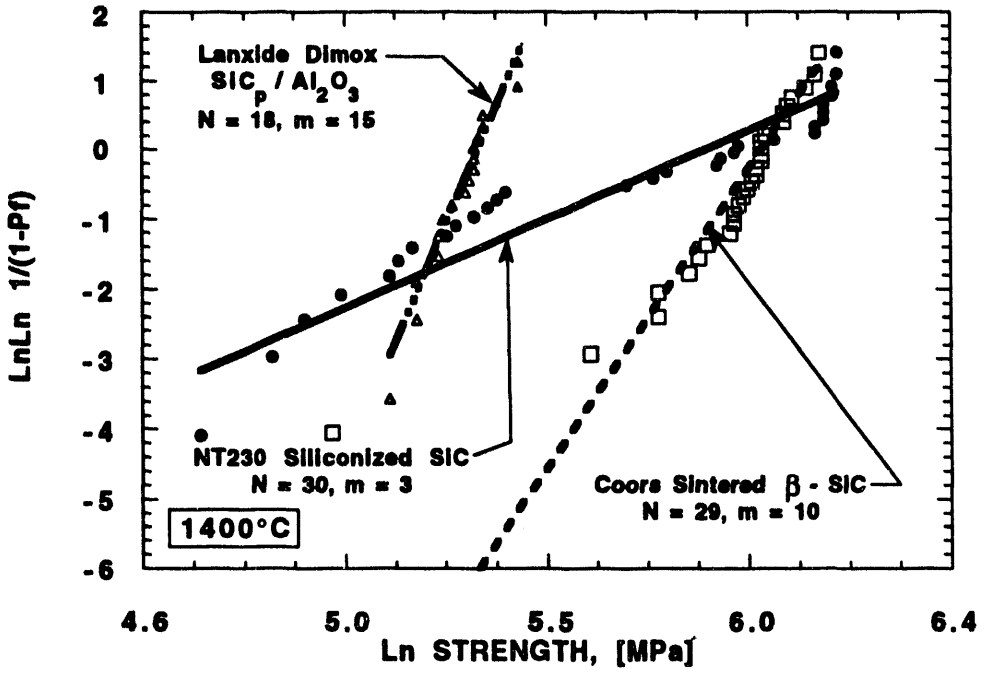

Figure 4. Weibul distribution of the 1400°C fast fracture strength for the three ceramics.

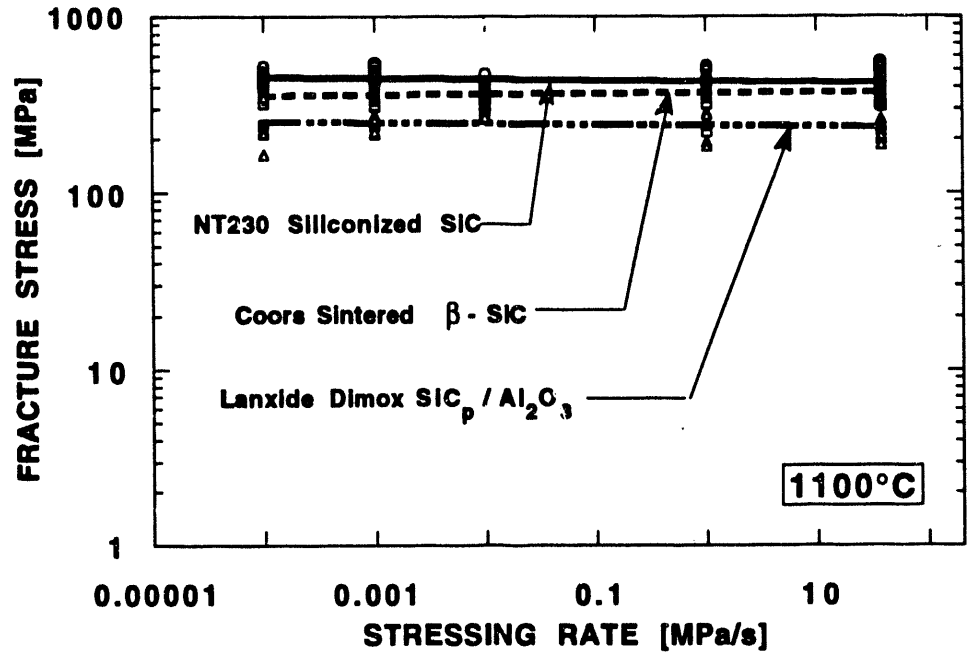

Figure 5. Strength as a function of stressing rate at 1100°C.

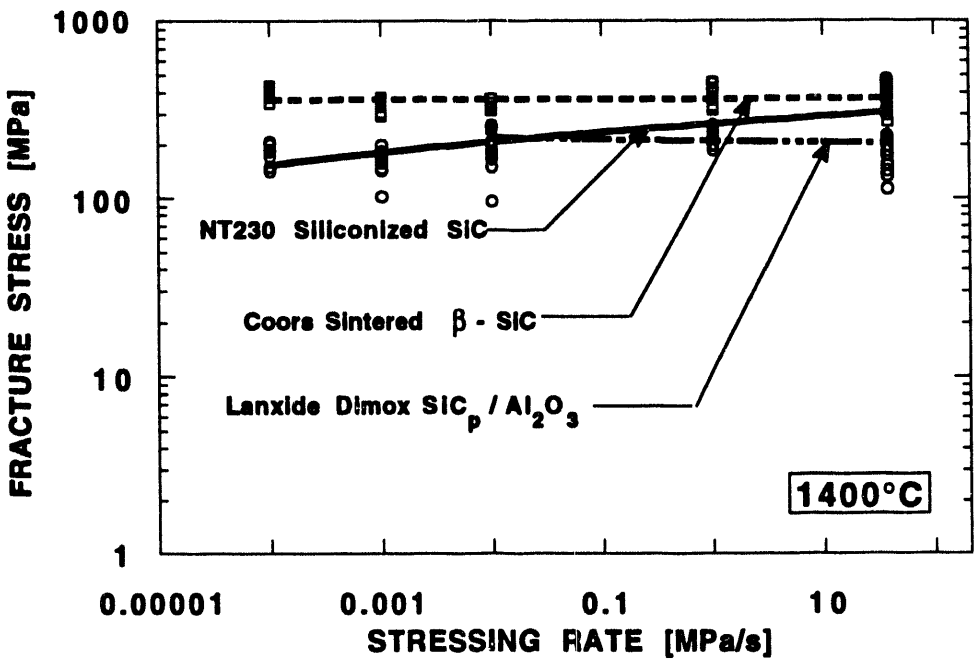

Figure 6. Strength as a function of stressing rate at 1400°C.

As a result of the fractographic investigation, the fast fracture Weibull distribution obtained at 1400°C was censored, resulting in a change in the Weibull modulus from 2.8 to 7.4. This is illustrated in Fig. 8, where the Weibull distributions for NT230 at all the stressing rates at 1400°C are shown. A similar compilation of Weibull graphs is shown in Fig. 9 for NT230 at 1100°C.

By combining the SCG parameters n and B obtained from the dynamic fatigue experiments with the Weibull data obtained at the fast stressing rate, Eq. 9 can be utilized to predict the lifetime of a specimen at a given stress level. This is illustrated in Fig. 10 for NT230 at 1400°C where it can be seen that for the uncensored set of NT230 the lifetime will vary widely from 0 to 28 h, depending on the desired level of certainty of the prediction. Censoring the data, which resulted in better Weibull parameters, will also improve both the lifetime and the uncertainty of the prediction that is made, see Fig. 10.

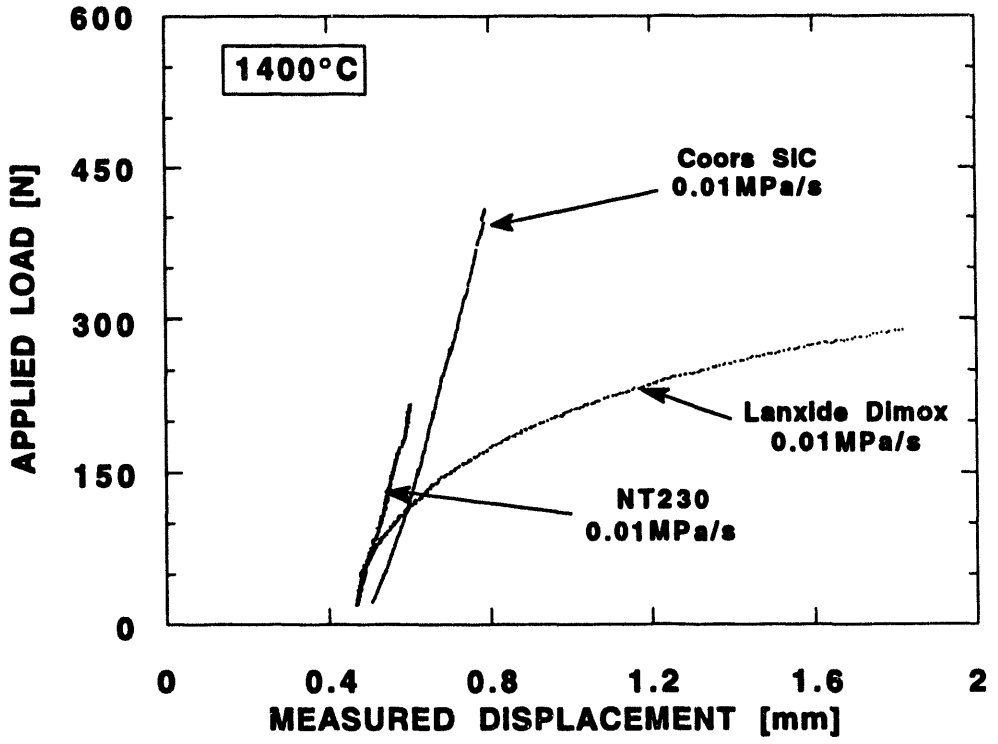

Figure 7. Comparison of the load deflection curves for the three ceramics at 1400°C at a stressing rate of 0.01 MPa/s.

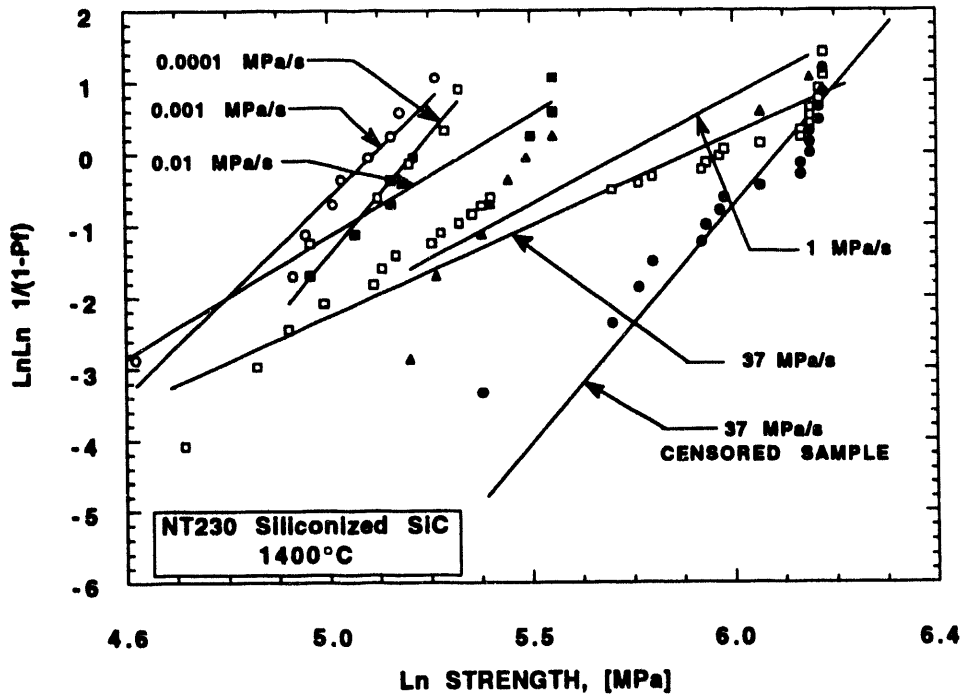

Figure 8. Weibull analysis of the dynamic fatigue data for NT230 at 1400°C.

The materials which were exposed to coal ash at UNDEERC were fractured at room temperature in four point flexure. The resulting fracture strengths are given in Table 2 and illustrated in Fig. 11.

The coal ash exposure experiments show several important things. The present experiments were intended as an initial set of conditions to compare several materials, coal slags and temperatures. By exposing the ceramics to static coal slag in a muffle furnace, significantly different levels of corrosion attack were observed, and reduction in strength values were observed for some of the combinations of ceramics, coal ash and temperature. The subsequent fractography showed that the materials which experienced a strength reduction also had a change in failure mode and that the coal ash in some cases produces severe corrosion pits. The materials which had strengths that were unaffected by the exposure (the two Lanxide grades) failed in a similar manner before and after exposure. A thorough discussion of the coal ash corrosion mechanisms can be found elsewhere[8].

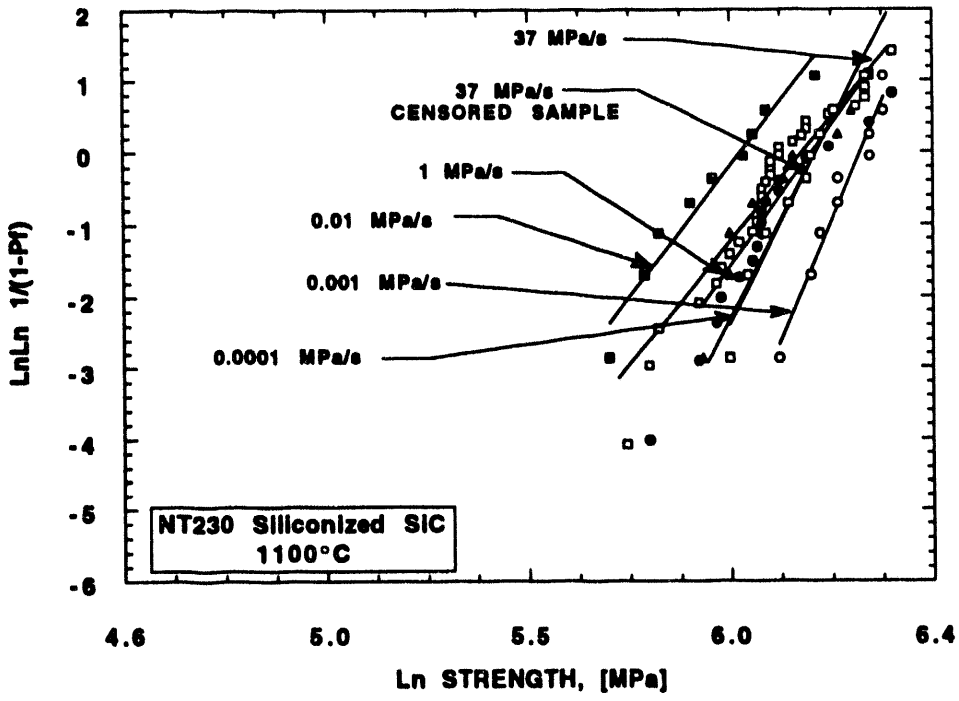

Figure 9. Weibull analysis of the dynamic fatigue data for NT230 at 1100°C.

FUTURE WORK

The results described above indicate that the candidate ceramics have different corrosion behavior under different conditions. Therefore, a continuation and expansion of the coal ash exposure experiments are currently being developed. Previous research[10,11] has shown that the corrosion behavior of ceramics is dependent on the type of coal, the temperature and the active deposition mechanisms for the system in question. The research being planned will expose ceramics to coal ash of different chemistries while simultaneously being mechanically stressed. Parallel research will expose the ceramics to the selected coal ashes and temperatures, and the remaining strength will be measured both at room temperature as above and at the exposure temperature. The temperatures will be chosen to match the expected temperatures in different sections of the ceramic air heaters. The results are expected to provide designers with information on life time predictions for selected combinations of ceramic materials, coal ashes and temperatures,

as well as providing further information on the mechanisms for coal ash corrosion of ceramics.

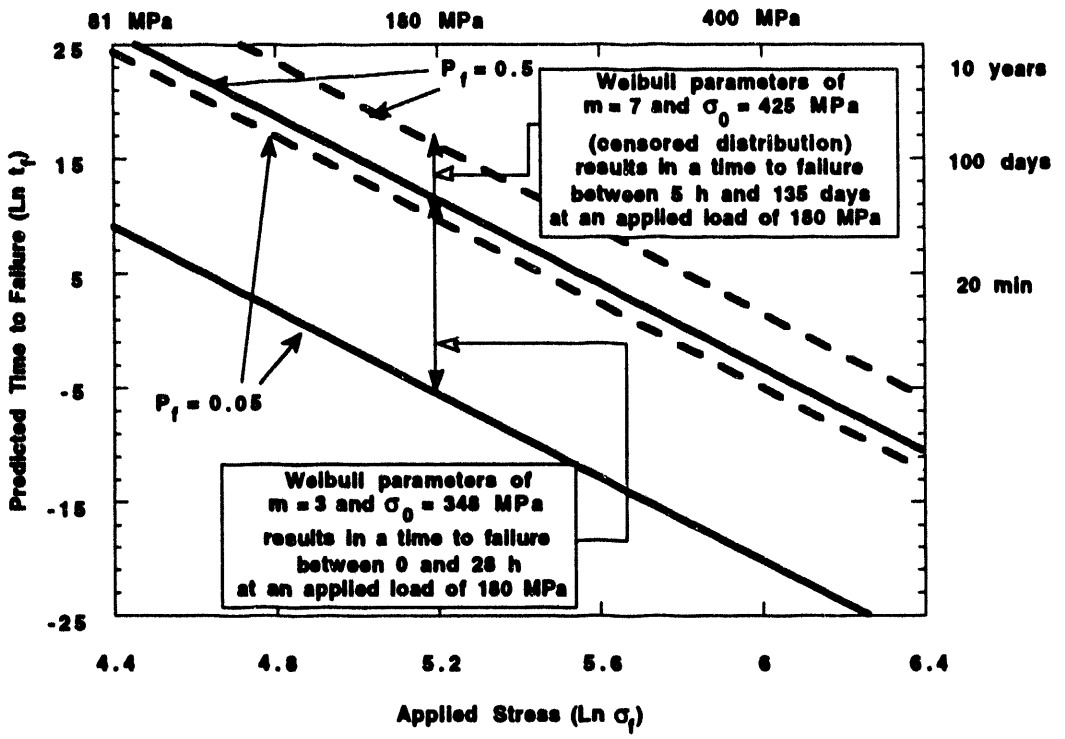

Figure 10. Lifetime prediction for NT230 at 1400°C

Table 2. REMAINING ROOM TEMPERATURE STRENGTH AFTER EXPOSURE OF 300 HOURS AT TWO TEMPERATURES AND TWO COAL ASHES				
W = WYODAK COAL ASH, I6 = ILLINOIS #6 COAL ASH				
NT230				
RT AS RECEIVED	W/1093°C	I6/1093°C	W/1260°C	I6/1260°C
386 MPa	340 MPa	208 MPa	175 MPa	204 MPa
N=30	N=7	N=5	N=6	N=5
m=10.7		m=9.4	m=7.7	m =3.4
LANXIDE DIMOX				
RT AS RECEIVED	W/1093°C	I6/1093°C	W/1260°C	I6/1260°C
414 MPa	365 MPa	352 MPa	364 MPa	388 MPa
N=30	N=6	N=6	N=5	N=6
m=9.6	m=22.5	m=19.0	m=25.2	m=17.9
LANXIDE EXP.				
RT AS RECEIVED	W/1093°C	I6/1093°C		
	343 MPa	287 MPa		
HEXOLOY SA				
RT AS RECEIVED	W/1093°C		W/1260°C	I6/1260°C
400 (HECHT REF. 9)	339 MPa		321 MPa	259 MPa

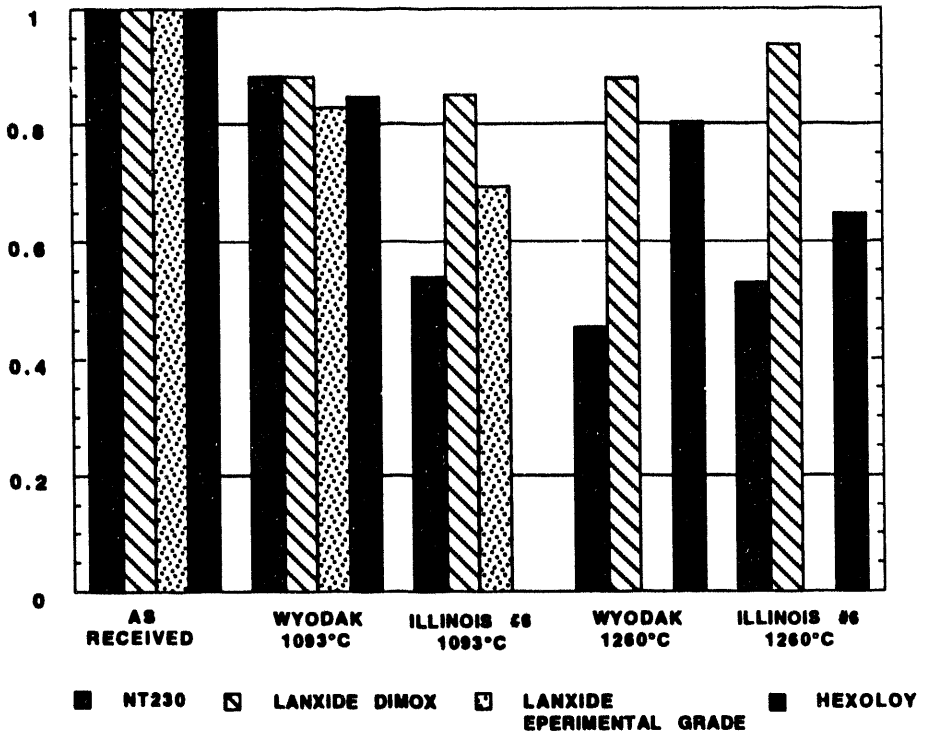

Figure 11. Retained fast fracture flexure strength in percent of the as received strength.

REFERENCES

1. D. J. Seery et al., "Engineering Development of Coal-Fired High -Performance Power Generation Systems," pp 188-195 in Proceedings of the Eighth Annual Coal Preparation, Utilization, and Environmental Control Contractors Conference, U.S. DOE, Pittsburgh Energy Technology Center, Pittsburgh, PA, 1992.

2. J. Shenker, "Development of a High-Performance Coal-Fired Power Generating System with a Pyrolysis Gas and Char-Fired High Temperature Furnace," pp183-187 in Proceedings of the Eighth Annual Coal Preparation, Utilization, and Environmental Control Contractors Conference, U.S. DOE, Pittsburgh Energy Technology Center, Pittsburgh, PA, 1992.

3. ASTM C 1161, "Standard Test Method for Flexural Strength of Advanced Ceramics at Ambient Temperature."

4. W. A. Weibull, "A Statistical Theory of the Strength of Materials," Ingeniørsvetenskapsakademien Handlingar, No. 151, Stockholm, Sweden, 1939.

5. W. Nelson, Applied Life Data Analysis, J. Wiley & Son, New York, NY, 1982.

6. S. M Wiederhorn, "Subcritical Crack Growth in Ceramics'" pp 613-646 in Fracture Mechanics of Ceramics, Vol. 2, R. C. Bradt, D. P. H. Hasselman and F. F. Lange, Eds., Plenum Press, New York, NY, 1974.

7. J. E. Ritter, "Engineering Design and Fatigue Failure of Brittle Materials'" pp 667-687 in Fracture Mechanics of Ceramics, Vol. 4, R. C. Bradt, D. P. H. Hasselman and F. F. Lange, Eds., Plenum Press, New York, NY, 1978.

8. T. M. Strobel, J. H. Hurley, "Coal-Slag Corrosion of SiC-Based Ceramics in a Combustion Environment," to be published in the Proceedings from the Am. Cer. Soc. PAC RIM Meeting, Nov. 1993.

9. N. L. Hecht, S. M. Goodrich, L. Chuck, D. E. McCullum and V. J. Tennery, "Mechanical Properties Characterization of one SiC and two Si_3N_4 Commercially Available Ceramics," Bulletin of the American Ceramic Society, **71** [4] 653-659, 1993.

10. M.K. Ferber and V.J. Tennery, "Evaluation of Tubular Ceramic Heat Exchanger Materials in Basic Coal Ash from Coal-Oil-Mixture Combustion," Ceramic Bulletin, **63** [7] 898 1984.

11. M.K. Ferber and V.J. Tennery, "Evaluation of Tubular Ceramic Heat Exchanger Materials in Acidic Coal Ash from Coal-Oil-Mixture Combustion," Ceramic Bulletin, **62** [2] 236 1983.

3. ENVIRONMENTAL ANALYSIS SUPPORT

R. L. Miller

Activities in environmental analysis support included assistance to the Morgantown and Pittsburgh Energy Technology Centers (METC and PETC) in reviewing and preparing documents required by the National Environmental Policy Act (NEPA) for several projects selected for the Clean Coal Technology (CCT) Program. A key milestone was the completion for PETC of the final Environmental Impact Statement (EIS) for the Healy Clean Coal Project (HCCP) in Healy, Alaska. This work is notable because it is the first site-specific EIS completed for the CCT Program. Another important activity was the preparation for METC of a draft Environmental Assessment (EA) for the Externally Fired Combined Cycle (EFCC) Project in Warren, Pennsylvania. Also, the final EA was completed for the Gasification Product Improvement Facility (GPIF), a proposed project near Morgantown, West Virginia, which is part of METC's R&D Program. In addition, ORNL staff members published a Technical Memorandum entitled "Potential Effects of Clean Coal Technologies on Acid Precipitation, Greenhouse Gases, and Solid Waste Disposal" which documents the findings of three "white papers" prepared for DOE/FE.

3.1 ENVIRONMENTAL SUPPORT TO THE CLEAN COAL TECHNOLOGY PROGRAM

R. L. Miller

Work during this period focused on the completion for DOE's Pittsburgh Energy Technology Center (PETC) of the final Environmental Impact Statement (EIS) for the Healy Clean Coal Project (HCCP). The project, proposed by the Alaska Industrial Development and Export Authority (AIDEA) and selected by DOE in the third solicitation of the Clean Coal Technology (CCT) Program, would be located in Healy, Alaska, about 4 miles north of the nearest border of Denali National Park and Preserve (DNPP). The proposed project is a new 50 megawatt coal-fired power generating facility that would be collocated with an existing 25 megawatt conventional pulverized-coal unit owned and operated by Golden Valley Electric Association. The new facility would feature integration of advanced combustion and flue gas cleanup technologies to reduce emissions of sulfur dioxide (SO_2) and oxides of nitrogen (NO_x).

Impacts to air quality, surface water, groundwater, and ecological and socioeconomic resources from construction and operation of the HCCP were evaluated and results indicate that, for most resource areas, the impacts are not expected to be major. Of primary concern, as predicted by analyses based on computer models, is the degradation of air quality and visibility expected in portions of DNPP because of HCCP operation. Maximum concentrations of air pollutants resulting from the HCCP demonstration are predicted to use up to 40% of the air quality degradation allowed within DNPP. A visible plume from NO_x emissions viewed from the valley containing the DNPP Visitor Access Center is predicted to occur during about 1% of the daytime hours per year.

In response to National Park Service (NPS) concerns about the consequences of potential visibility impacts on DNPP, DOE facilitated negotiations between the project team and NPS which broke an impasse and resulted in a Memorandum of Agreement which was signed in November 1993. The cornerstone of the Agreement is the planned retrofit of the existing unit to reduce emissions of SO_2 and NO_x. The Agreement is a "win-win-win" outcome for the three parties: DOE can demonstrate the new technologies, AIDEA can build a new power plant, and NPS can safeguard the pristine environment of DNPP. Subsequently, DOE released the final EIS in December 1993 and issued a Record of

Decision in March 1994 to provide federal funding support for the construction and operation of the HCCP.

Work also began on the preparation for DOE's Morgantown Energy Technology Center (METC) of a draft Environmental Assessment (EA) for the Externally Fired Combined Cycle (EFCC) Project in Warren, Pennsylvania. Proposed by the Pennsylvania Electric Company (Penelec) and selected by DOE in the fifth solicitation of the CCT Program, the project would be sited at one of the two units at Penelec's Warren Station. The EFCC Project proposes to replace the two existing boilers at Unit 2 with a new "power island" consisting of a staged coal combustor, slag screen, ceramic heat exchanger, an indirectly fired gas turbine, and a heat recovery steam generator. Subsequently, Unit 2 would operate in combined-cycle mode using the new gas turbine and the existing steam turbine simultaneously. The gas turbine would generate 22 megawatts of electricity so that Unit 2 output would increase from the existing 48 megawatts generated by the steam turbine to a total of 70 megawatts. Operation of a conventional flue gas desulfurization dry scrubber as part of the EFCC technology is expected to decrease SO_2 emissions by 90% per kilowatt-hour of electricity generated, and NO_x emissions are anticipated to be 60% less per kilowatt-hour of electricity generated because of the staged combustor. Because the EFCC technology would be more efficient, less carbon dioxide (CO_2) would be emitted to the atmosphere per kilowatt-hour of electricity produced.

Potential resource areas of concern associated with the project include surface water resources, ecological resources, and archaeological resources. In particular, the potential effect of the heated discharge of once-through cooling water from the turbine condensers on aquatic life in the Allegheny River is being evaluated. Also, archaeological investigations have identified significant prehistoric, protohistoric, and historic occupations on the Warren Station site. There has been an ongoing investigation at this site, which is fenced and located east of the proposed project site near the eastern boundary of Warren Station. A cultural resources survey recommended no further investigation of the proposed construction site because it has already been extensively disturbed and graded. However, it is expected that a plan would be developed for dealing with unanticipated finds during construction. Finally, Penelec has committed to installing liners at the active ash disposal area and ash ponds to minimize potential impacts to the groundwater.

In November 1993, ORNL staff members published a Technical Memorandum entitled "Potential Effects of Clean Coal Technologies on Acid Precipitation, Greenhouse Gases, and Solid Waste Disposal" which documents the findings of three "white papers" prepared for DOE/FE. The report found that future nationwide environmental effects of CCTs depend upon which (if any) specific technologies eventually achieve high acceptance in the commercial marketplace. In general, the repowering technologies and a small group of retrofit technologies show the most promise for reducing SO_2 and NO_x emissions (precursors of acid precipitation), CO_2 emissions (a major greenhouse gas), and solid waste. Repowering technologies are those that replace a major portion of an existing facility. These technologies not only reduce emissions substantially but also may provide for the use of a different fuel form, increase facility capacity, extend facility life, and/or improve system efficiency. Retrofit technologies are those that reduce emissions of SO_2 and/or NO_x by modifying existing facilities or their present feedstocks.

Projections of nationwide SO_2 reductions in the year 2010 as a consequence of widespread commercialization of CCTs (compared to projections in the absence of CCTs) range from 29% to 48% for specific repowering technologies; corresponding NO_x reductions range from 14% to 17%. The upper bound for CO_2 reductions in the year 2010 as a result of widespread implementation of CCTs is only enough to reduce global "greenhouse" warming potential by about 1%. However, CO_2 emissions come from such a variety of sources around the globe that no single technological innovation or national policy change could realistically be expected to reduce these emissions by more than a few percent. Particular CCTs can lead to either increases or decreases in the amount of solid waste produced. However, even if decreases are not achieved, much of the solid waste from CCTs would be dry and therefore easier to dispose of than current-generation scrubber sludge.

3.2 ENVIRONMENTAL SUPPORT TO METC R&D PROJECTS

R. L. Kroodsma

During this period, the final Environmental Assessment (EA) for the proposed Gasification Product Improvement Facility (GPIF) at the Fort Martin Power Station (FMPS) was completed for DOE's Morgantown Energy Technology Center (METC). The GPIF would use coal to produce a fuel gas that would be combusted to provide steam for electrical generation in one of the two units at the existing coal-fired FMPS located near Morgantown, West Virginia. The proposed project would develop, demonstrate, and enhance commercialization of an advanced technology for gasification of coal.

The GPIF would include two subsystems that would be constructed in two consecutive phases. Phase I includes the construction and demonstration of a gasifier and the burning of the fuel gas to produce steam for electrical generation by the FMPS. In Phase II, a facility for cleaning the fuel gas from the gasifier would be constructed and demonstrated during continued gasifier operation. High sulfur coal would be burned during Phase II to thoroughly test the gasifier's and hot gas cleanup system's ability to limit sulfur emissions.

Environmental impacts to resource areas resulting from construction and operation of the GPIF were evaluated and results indicate that the impacts are not expected to be major. The GPIF is expected to produce a clean fuel gas while minimizing the emissions of air pollutants. Surface water but no groundwater at the FMPS site would be withdrawn for the GPIF. GPIF consumption of Monongahela River water would represent about 0.34% of the river's low flow and 0.02% of average flow. Groundwater and surface waters receiving drainage from the FMPS ash disposal pile, where GPIF ash would be disposed, should not be impacted by the GPIF because the leachability of contaminants in the GPIF is expected to be less than that in FMPS ash. The proposed GPIF site is already a disturbed area adjacent to the existing FMPS and does not provide important habitat for plants or animals. Socioeconomics would not be appreciably affected because of the small size of the proposed project and its small expected employment of only about 20 to 25 people during construction and operation. Following the completion of the final EA in March 1994, a Finding of No Significant Impact was issued by DOE in March 1994 which

concluded that the proposed project is not a major federal action significantly affecting the quality of the human environment.

3.3 OIL RESEARCH PROGRAM ENVIRONMENTAL SUPPORT

R. L. Miller

INTRODUCTION

The objective of this task is to provide environmental technical assistance to the Department of Energy's Office of Fossil Energy in support of the Oil Research Program. Support includes the preparation of analyses for a Programmatic Environmental Assessment (PEA) and project-specific documentation.

DISCUSSION OF CURRENT ACTIVITIES

There was no substantial activity during the reporting period, since comments on the draft Programmatic Environmental Assessment have not been received.

3.4 ACTION DESCRIPTION MEMORANDUM FOR METC R&D PROGRAM

J. T. Ensminger

INTRODUCTION

The objective of this task is to provide technical and analytical support to the Fossil R&D Program at the DOE Morgantown Energy Technology Center (METC). Specifically, an Action Description Memorandum (ADM) has been prepared that addresses the potential environmental impacts of the overall program. The METC Fossil R&D Program consists of over 300 individual projects that fall into eight program areas. In general, the individual projects are relatively small (median funding level of $1 million), short-term (median duration of about three years), and widely dispersed geographically. The ADM will be the basis for DOE's decision on the appropriate level (Categorical Exclusion, Environmental Assessment or Environmental Impact Statement) of NEPA documentation for the METC Fossil R&D Program.

DISCUSSION OF CURRENT ACTIVITIES

There was no substantial activity during the reporting period, since comments on the draft Action Description Memorandum have not been received.

3.5 SUPPORT TO THE WILSONVILLE COAL LIQUEFACTION R&D FACILITY

N. E. Korte

DISCUSSION OF CURRENT ACTIVITIES

Support to the Wilsonville Coal Liquefaction R&D Facility involved a hydrogeologic site characterization conducted at the former Advanced Coal Liquefaction Research and Development (ACLR&D) facility in Wilsonville, Alabama. The work was conducted by personnel from Oak Ridge National Laboratory's Grand Junction office for the Department of Energy's Pittsburgh Energy Technology Center (PETC). This characterization was performed due to completion of ACLR&D facility operations and planned facility dismantlement. Characterization information was requested by PETC to provide baseline environmental information for use in evaluating needs and in subsequent decision-making for further actions associated with the close-out of facility operations. This hydrogeologic assessment report includes a brief overview of potential risks to the public and the environment.

The hydrogeologic assessment was not routine because of the unusual structural complexity of the subsurface. Bedrock drilling and geophysical surveys demonstrated that both an overturned fold and a strike-slip fault are present beneath the site. Moreover, the site is also underlain by limestone that contains solution cavities. The latter fact was of particular concern because of the enhanced potential for contaminants to migrate both long distances and into beneficial groundwater resources.

Drilling and sampling of shallow boreholes demonstrated the presence of soil contamination under virtually all of the site's formerly operating units. The contamination consists chiefly of petroleum hydrocarbons, including several polynuclear aromatic hydrocarbons (PAHs). Chlorinated solvent contamination was also found in some areas. Of more concern was the fact that chlorinated solvent contamination was found in the groundwater in wells that were completed in the limestone formation underlying the site. As noted above, the limestone is a productive formation with numerous solution cavities that could provide a framework for enhanced transport of the contaminants. A buried drum site at the old hill area of the ACLR&D facility was also identified by this drilling and sampling program. Extensive remediation, conducted by the site owner, has already been completed at the drum site.

Thus, while contamination at the ACLR&D site is extensive, a preliminary review of potential receptors suggests that the site does not pose an immediate threat to human health and the environment. Access to the ACLR&D site is restricted, and its proximity to E.C. Gaston Steam Plant precludes anything other than industrial use. While contamination in the bedrock aquifers is a concern, the available data indicate that there are no water supply wells downgradient of the contamination. Indeed, the nearest water supply wells are clearly upgradient of the site at a distance of 1 to 2 miles.

In addition, remedial options were suggested that might be considered for the former Advanced Coal Liquefaction Research and Development (ACLR&D) site in Wilsonville, Alabama. The applicability of remedial options is complicated by the diverse nature of the contaminants, which include both highly volatile and relatively non-volatile compounds and by the complex nature of the site's hydrogeology. Soils at the site are very fine-grained limiting the use of *in situ* venting and flushing techniques. *Ex situ* volume reduction methods such as soil washing and solvent extraction, are also not well-suited to fine-grained soils. Remediation approaches are also complicated by the fact that site activities have contaminated the limestone aquifer system underlying the site. Solution cavities exist in the limestone. The cavities, in conjunction with the complex folding and faulting that has occurred also limit the applicability of many potential remedial techniques. This review concludes that site excavation, with subsequent removal or on-site treatment, will significantly reduce and may eliminate contaminant ion, but will be subject to much uncertainty with regard to the ultimate depth and cost of excavation and treatment or disposal. An *in-situ* soil reactor concept, otherwise known as deep-soil mixing, is believed to represent the best approach for providing the most cost-effective reduction of contamination. Treatment of contaminated groundwater is not recommended for the fine-grained zones because of the low yield of the aquifer. Treatment of the contaminated limestone system is not possible without a better definition of the flow direction and characteristics of the system.

4. BIOPROCESSING RESEARCH

C. D. Scott

Fundamental bioprocessing research has concentrated on the use of biocatalysts in organic media and on advanced bioreactor systems. Coal conversion research has continued on the biological solubilization of coal using chemically-modified enzymes in organic solvents. Biophotolysis is also being studied for the production of hydrogen.

4.1 FUNDAMENTAL BIOPROCESSING RESEARCH

T. C. Scott

ORNL RESEARCH

Effective reactor modeling, design, and implementation rely upon knowledge of bed expansion and segregation tendencies with particles of varying size and density. In the past year, Mohammad Asif and James Petersen at Washington State University (WSU) have proposed mathematical models to predict both transient and steady-state performance of a liquid fluidized bed of coal. ORNL has provided additional data to our collaborators at WSU and has overseen efforts to demonstrate the predictive capabilities of the mathematical models in terms of predicting steady state bed height, transient pressure fluctuations, and particle-size distributions. We have also initiated experimentation using a tapered fluidized bed to enhance particle fluidization, designed and constructed laboratory scale reactors for coal bioconversion and SO_x/NO_x removal studies, begun project planning for SO_x/NO_x removal, and have continued collaborative efforts with ARCTECH Inc.

Demonstrating the Predictive Capabilities of Mathematical Models for Coal Bioconversion

ORNL has provided additional data to our collaborators at WSU regarding the expansion of large coal particles in liquid fluidized beds. We have also overseen the use of this and previous data to demonstrate the predictive capabilities of the mathematical models in terms of predicting steady state bed heights, transient pressure profiles, and particle-sized distributions in response to varying system parameters. See the next section in this report for a detailed discussion of this work.

Coal Expansion in a Tapered Fluidized-Bed

Previously, we described the design, modeling, and construction of a tapered lower section for our 4 ft experimental column. It was described how this tapered section would allow complete fluidization of a larger size range of coal particles due to the increased superficial velocity at the lower

portions of the column. The tapered section increases in diameter from 1 cm at its base to 2.54 at 30 cm from the bottom, and has pressure taps placed every 5.5 cm along its length. It is hoped that this tapered subsection will alleviate the packing of larger particles that occurred in the straight reactor section. Expansion, pressure profile, and microscopic visualization experiments are underway in this redesigned column using Texas Lignite rather than the Illinois #6 bituminous coal used in previous experiments. Thus, these experiments will test the predictive capabilities of our mathematical model by altering both the reactor geometry, and the particle size and density. Results of these experiments will be reported at a later date.

Construction and Demonstration of Small Scale Reactors for Coal Bioconversion and Flue Gas Removal

Several small scale reactors have been designed, fabricated and tested for possible use in both coal bioconversion and SO_x/NO_x removal studies. These reactors are 1 ft high, 1 in. i.d. jacket glass columns with several alterations to facilitate reactor operation. A 125 ml serum bottle is firmly seated at the top of the reactor for the collection and measurement of reactor off gas. Mesh screens are placed at the column entrance and exit to contain reactor solids (coal particles or biocatalyst beads). Solids may be fluidized by introducing or recycling a feed stream of liquid or gas, or a combination of the two. Several septum controlled and valved ports have been placed in the reactor inlet and exit lines to allow aseptic sampling, feeding or inoculation. The reactor may be loaded anaerobically using "quick disconnect" fittings, by sparging gas through the lines and the reactor, and by introducing media via a pressurized vessel.

Several mock experiments have been undertaken to "shake down" reactor loading and operation prior to the arrival of the microbial populations for use in the specific research programs. A wide size range of coal has been fluidized in water, using both gas and liquid recycle to fluidize the bed and using both Illinois No. 6 and Texas lignite coal as the solid. A mock experiment of coal fluidization with gas production was undertaken using a small charge of Illinois No. 6 coal, *Zymomonas mobilis* (a bacteria that produces ethanol and carbon dioxide from glucose), and liquid media containing both glucose and yeast extract. The reactor demonstrated ease of operation and gas collection when operating in either the gas or liquid recycle mode. Interestingly however, a microbial contaminant either introduced with the liquid inoculum or pre-existing on the unsterilized coal began to thrive in the reactor after the glucose levels fell to zero. This contaminant produced 5 g/L of lactic acid as well as other volatile fatty

acids including acetic acid, butanol, and butyric acid all without a direct carbon source. It may be possible that this contaminant utilized yeast extract as a carbon source, but the yeast extract was initially present only at 5 g/L, and additional carbon must have been incorporated to account for the mass of VFA's produced. We have isolated this contaminant and are conducting additional incubations of this bacteria with coal in order to discern if it is capable of utilizing coal as a carbon source for VFA production.

Initiation of CRADA with Engineering Resources Incorporated (ERI)

Collaborative research with ERI has begun in "Advanced Bioreactors for Gaseous Substrates." ERI will have the lead role in research regarding the bioconversion of coal synthesis gas into liquid fuels, and ORNL will lead in efforts to remove SO_x and NO_x constituents from coal flue gas. Initial discussions between investigators at ERI and ORNL have addressed the utility of presolubilizing the gaseous substrates prior to the introduction to the fermentation reactor, and the feasibility of maintaining an anaerobic environment in these reactors. ORNL has initiated a literature search to investigate how particular bacterial strains have achieved SO_x/NO_x removal in the past, and has begun the acquisition of these strains.

COAL GASIFICATION STUDY WITH ARCTECH

Collaborative research with ARCTECH Inc. has continued regarding the biogasification of low rank coals. The current emphasis is on the conversion of coal derived liquids to both gaseous and liquid products. ORNL has completed fabrication and initial testing of several 1-ft reactors which allow coal bioconversion with either liquid or gas recycle. A non-proprietary microbial consortia from ARCTECH will be tested in proof-of-concept experiments with our reactor systems.

FUTURE WORK

Work will continue in the study of bed expansion in a tapered fluidized bed with coal particles differing in density from the particles used to establish our mathematical models. With this data, we

will attempt to validate the model on both a macroscopic and microscopic scale. Microbial strains for both coal bioconversion and SO_x/NO_x removal will be established and analytical techniques for these projects will be developed.

MATHEMATICAL MODELING OF AN ADVANCED BIOREACTOR FOR COAL SOLUBILIZATION

Introduction

The application of biocatalysts to the solubilization and/or liquefaction of coal enables coal processing at modest temperatures and pressures in a relatively mild chemical environment (Scott *et al.*, 1993). Liquid fluidized bed reactors may be used in such a biocatalytic process due to their efficient mass transport, ease of gas disengagement, and capability to operate in a continuous fashion with high throughput. Unlike conventional fluidization process, the biosolubilization of coal in a fluidized bed reactor exhibits an unique feature, i.e., particles of widely different sizes will be present in the bed as the coal particles are gradually solubilized. That is, as the coal particles solubilize, they will gradually become smaller in diameter. Thus, at some point, the small particles will elute from the bed. In addition, the continuous operation of the solubilization process will require that the coal be replenished in the bed in a continuous fashion. As a result, the mathematical models developed to describe conventional fluidized beds can not be directly applied to such biocatalytic fluidized bed reactors.

In order to achieve the efficient design, assessment, operation, and scaleup of such a reactor, detailed knowledge of bed expansion and segregation tendencies, reactor axial pressure drop, and particle size distribution as a function of axial position and flowrate are required. Particle size distribution is of particularly importance since the specific reactivity of the particles will be a direct function of particle size. Also, to effectively design such a fluidized bed reactor, an accurate prediction of the bed height is mandatory. However, previous studies of particle size distribution within a liquid fluidized bed (Juma and Richardson, 1983; Patwardhan and Tien, 1984) are limited to the distribution of cumulative volume fraction for the fluidization of a binary solid mixture. On the other hand, most of the studies concerning bed heights were either based on the fluidization of mono-sized particles (Chen *et al.*, 1988; Fan *et al.*, 1963) or of a binary solid mixture (Gibilaro *et al.*, 1986).

In our previous work (Asif *et al.*, 1993a-c), a mathematical description of a liquid fluidized bed that is based on the particle mass transport mechanisms of dispersion and convection was developed. This mathematical description is fully predictive in nature. Additionally, we have demonstrated that this model can be used to predict both the transient and steady-state behavior of liquid fluidized beds of coal particles, as observed using differential pressure transducers. However, the direct comparison of predicted and measured particle size distributions, as developed in the bed, and of the height of such beds has not been accomplished. Thus, in this report, the experimentally determined particle size distribution is directly compared with the predicted particle size distribution. This particle size distribution is a function of the axial position and flowrate of liquid through the bed. In addition, comparisons between the predicted and measured bed heights in a fluidized bed containing nonreactive coal particles of wide size distribution are provided.

Model Description

Previously, Asif *et al.* (1993c) followed the approach first developed by Kennedy and Bretton (1966) to develop a particulate transport equation. In this approach, a mass balance is used to account for mass transport by both dispersion and convection. For a particulate system such as that employed in the coal fluidized bed, this mass balance equation can be written as:

$$\frac{\partial C_i}{\partial t} = \frac{\partial}{\partial Z}\left[D_i\left(\frac{\partial C_i}{\partial Z} - \frac{C_i}{\rho}\frac{\partial \rho}{\partial Z}\right) - U_i C_i\right] \qquad (1)$$

where the coal charge is divided into sub-fractions (denoted by subscript "i") based on size, ρ is the bulk density, and C_i is the fractional volumetric concentration of particle species i, D_i its dispersion coefficient, U_i its velocity.

Equation (1) is the governing mass-balance equation for the particle species i present in the fluidized bed. Its solution requires the evaluation of the particle velocity, U_i, and the particle dispersion coefficients, D_i, for each individual particle species. The particle classification velocity, U_i, can be evaluated using the following expression:

$$U_i = Q_0 + \sum_{i=1}^{n_t} U_{t_i} \epsilon^{n_i - 1} C_i - U_{t_i} \epsilon^{n_i - 1} \tag{2}$$

where ϵ is the bed void fraction, n_i is the index of Richardson and Zaki correlation which has been experimentally evaluated in the previous work by Asif *et al.* (1993c), U_{ti} is the particle terminal velocity and Q_0 is the liquid flowrate.

Based on several different sets of experimental data, Asif and Petersen (1993b) proposed a correlation which would allow the evaluation of the particle dispersion coefficient, D_i. Their correlation provides a relationship between the particle dispersion coefficient and relevant particle and fluid properties. This relationship then could be used to calculate the particle dispersion coefficient for each of the particle species present in the bed. However, we found that a better representation of the experimental data was obtained if a single particle dispersion coefficient was evaluated and applied to all particle species. The dispersion coefficient so calculated was based on the harmonic mean particle diameter of the sample mixture. This harmonic mean diameter is calculated using:

$$d_m = \frac{\sum_{i=1}^{n_t} n_i}{\sum_{i=1}^{n_t} \frac{n_i}{d_i}} \tag{3}$$

where n_i is the particle number of species i and d_i is the diameter of this species.

Materials and Methods

Coal expansion experiments were performed by Kaufman and Little at ORNL and have been described in detail in previous reports. Briefly, a glass column of 25.4 mm internal diameter and 1.22 m length was used for carrying out fluidization. A coarse glass frit distributor at the column inlet was used to ensure uniform distribution of liquid across the cross-section of the column. The distributor was preceded by a calming section to dampen the pump-induced flow fluctuations. A disengagement

section followed the test section of the fluidized bed. During the fluidization, 0.5% aqueous solution of the surfactant Tween 80 (polyoxyethylene) was used to avoid particle aggregation. A small quantity of a fluorescent dye was added in the water to carry out *in situ* fluorescence visualization and particle counting. The details of this non-invasive florescence visualization technique and the experimental apparatus have been described by Kaufman and Scott (1993).

Four different fractions of coal were employed in this study. On Fig. 1, the volume fraction of particles in a given size range is provided as a function of particle size for each of these fractions. In all studies, Illinois No. 6 bituminous coal was used.

Results and Discussion

The governing equations [Eq. (1)] were solved using a FORTRAN 77 software package, PDECHEB, developed by Berzin and Dew (1991) on a DEC 3000/400 computer using DEC FORTRAN 77 and double precision arithmetic. To achieve these solutions, each of the coal samples were divided into sub-fractions (from 16 up to 26) and each of these subfractions was defined with a partial differential equation. The resulting set of nonlinear partial differential equations were solved simultaneously. Model predictions of the particle size distribution developed in the bed and of the predicted bed height were obtained and are compared with experimental data.

Particle Size Distribution

At a fluidization velocity of 0.016 cm/s, the model predictions of the number fraction of particles are calculated as a function of particle diameter and bed height. The particle number of individual species per unit bed volume was evaluated from the model prediction of the solid concentration using the following relationship:

$$n_{mi}(z) = \frac{C_i(z)}{\frac{\pi}{6} d_i^3} \tag{4}$$

Then, the number fraction of individual particle species was evaluated as:

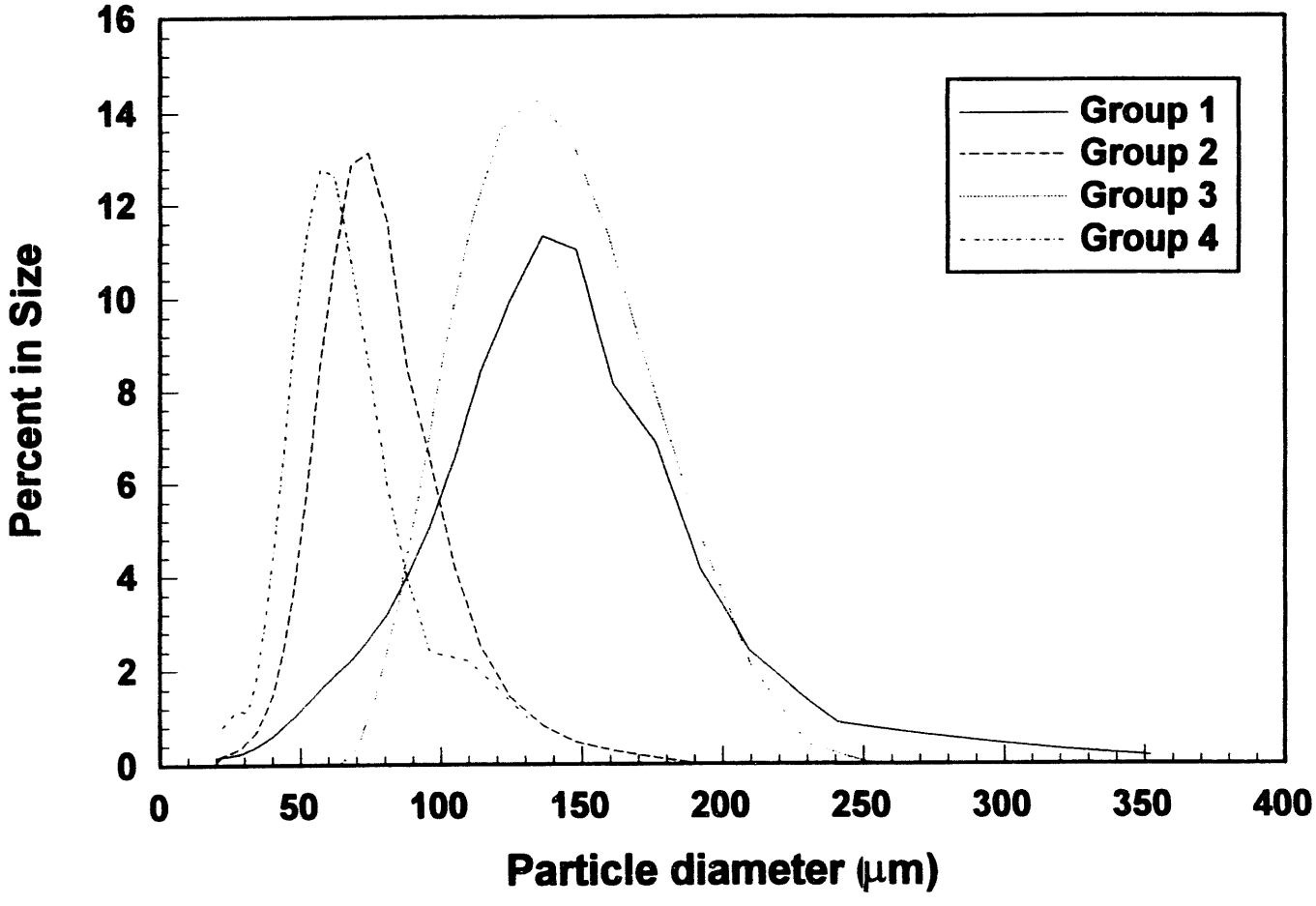

Fig. 1. Size distribution of the various coal samples used in this study.

$$\overline{n_{mi}}(z) = \frac{n_i(z)}{\sum_{i=1}^{N} n_i(z)} \qquad (5)$$

where N is the total number of particle species in the system.

In this case, the solid fraction consisted of a mixture of 80g of group 1 coal and 40g of group 2 coal (refer to Fig. 1 for size distributions of these coal samples). In Fig. 2, the predicted steady state particle size distribution is presented as a function of particle diameter and axial position. For comparison purposes, the corresponding experimental data, obtained using the non-invasive particle distribution visualization technique developed by Kaufman and Scott (1993), as represented by the filled spheres, are also shown.

The predicted particle distribution provides an excellent representation of the experimental data. Both the model predictions and experimental data show that the number fraction of larger particles is higher in the low portion of the bed and progressively decreases towards the upper part of the bed, while the number fraction of smaller particles is higher in the higher bed regions and gradually deceases towards the lower portion of the bed. On the other hand, the number fraction of particles of the intermediate sizes exhibits a maximum in the middle bed regions.

Because 3-D data, such as that shown in Figure 2, is difficult to interpret quantitatively, contour plots of the predicted and experimental profiles are shown in Figure 3. Comparison of these contour plots demonstrates that the model predictions provide a similar overall trend with the experimental data. The only discrepancy is that model predicts a lower number fraction for the particles in the size range of 100-130 μm than was observed experimentally at bed heights from 40 to 60 cm. This could be caused by the experimental error, i.e., the overlays or agglomeration of small particles in this region could result in the erroneous detection of larger particles by the fluorescent visualization technique.

Prediction of Bed Heights

An accurate prediction of the bed height can add important information in the development of the model for a fluidized bed. Also, this issue plays important role in the present context of coal biosolubilization where the movement of the top surface of the fluidized bed will depend on many factors including liquid flowrate, particle segregation, and particle size. In the case where the bed

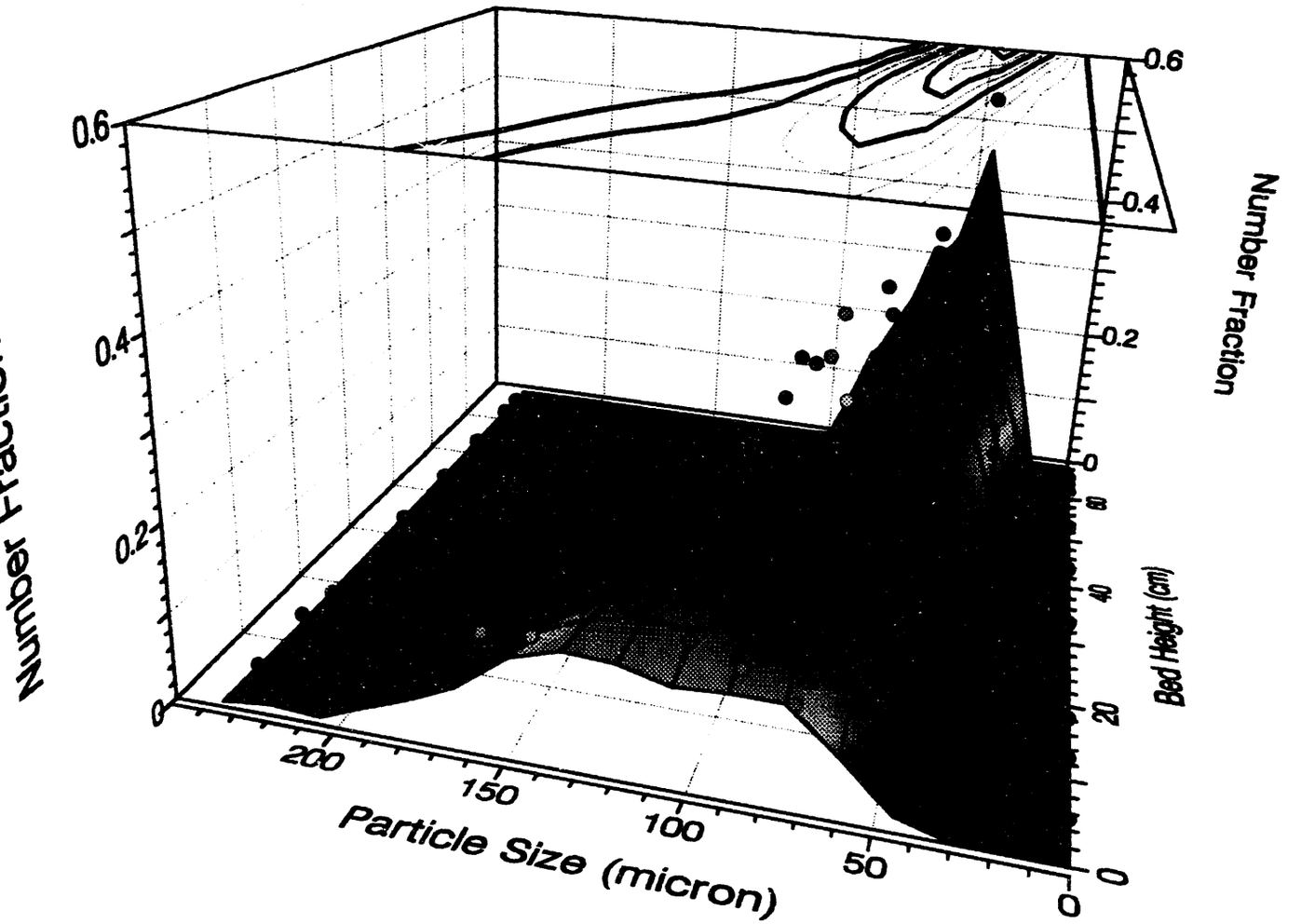

Fig. 2. Particle number fraction at a liquid velocity of 0.016 cm/s as a function of particle diameter and axial position.

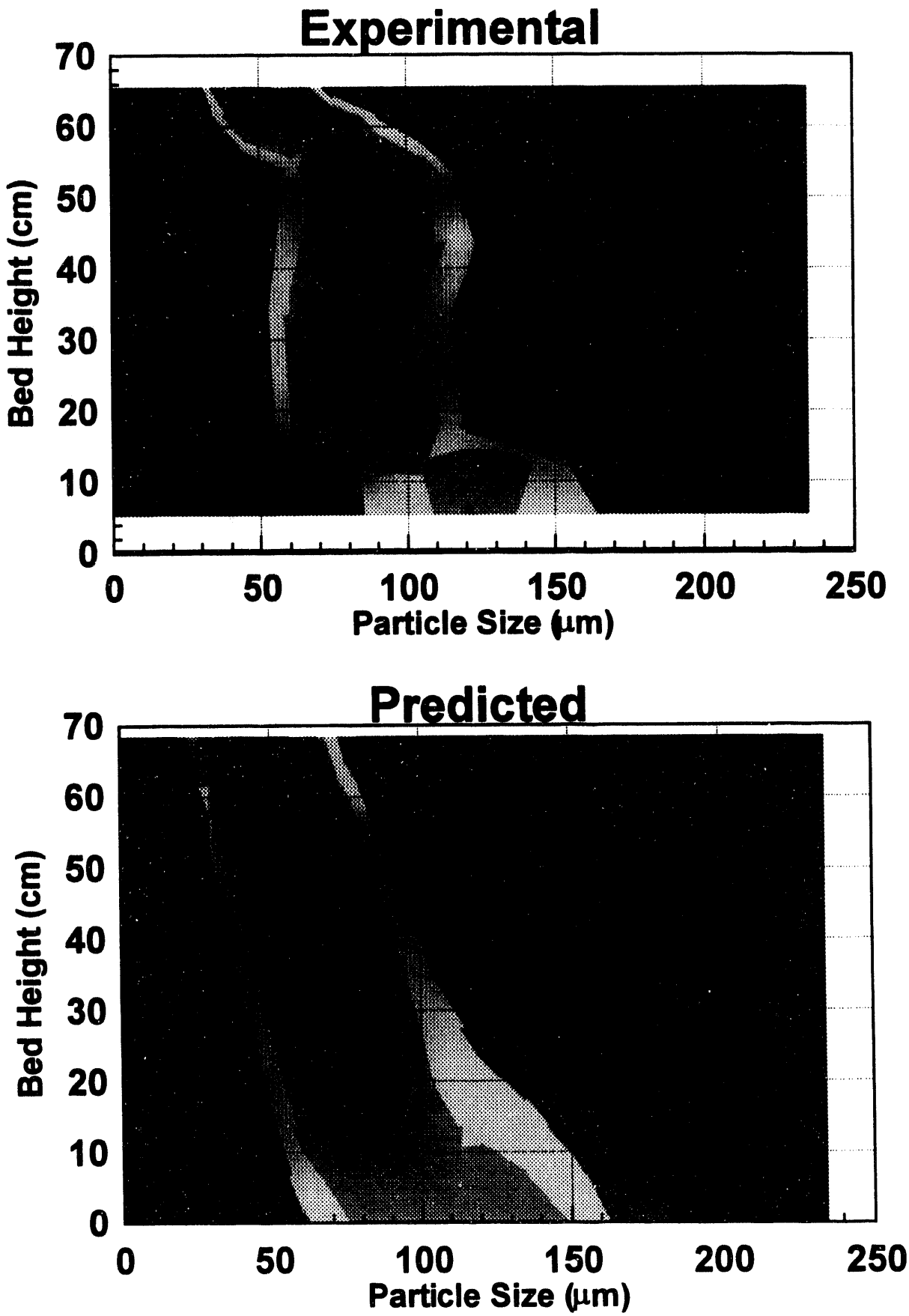

Fig. 3. Contour plots of the 3-D data shown on Fig. 2.

height is a function of time, it is convenient to evaluate the bed heights by the introduction of the following transformation:

$$z = L(t)x \tag{6}$$

where x is the fraction of bed height (0≤x≤1). This will give:

$$\frac{\partial C(z,t)}{\partial z} = \frac{1}{L(t)} \frac{\partial C(x,t)}{\partial x} \tag{7}$$

$$\frac{\partial C(z,t)}{\partial t} = \frac{\partial C(x,t)}{\partial t} - \frac{x}{L(t)} \frac{dL}{dt} \frac{\partial C(x,t)}{\partial x} \tag{8}$$

With the help of this transformation, Eq. (1) can be written as:

$$\frac{\partial C_i}{\partial t} - \frac{x}{L} \frac{dL}{dt} \frac{\partial C_i}{\partial x} = \frac{1}{L^2} \frac{\partial}{\partial x} \left[D_i \left(\frac{\partial C_i}{\partial x} - \frac{1}{\rho} \frac{\partial \rho}{\partial x} C_i \right) - U_i L C_i \right] \tag{9}$$

This is the general mass-balance equation and can be utilized to predict bed heights.

Four different groups of Illinois No. 6 coal with wide range of particle sizes were used in the experiments performed at ORNL. The characteristics of these samples together with both the experimental data and model predictions of bed heights at various flowrates are listed in Table 1. The experimental data are also compared with model predictions in a parity plot shown in Figure 4. The agreement between the experimental data and model prediction is excellent over a wide range of bed heights.

The data of group 3 needs additional explanation. In this case, the experimental system was operated at several different superficial velocities before the bed height data were collected. At the highest of these, the model predicted that some of the particles would elutriate from the bed. Thus, in order to have a more realistic comparison, the model was used to predict the amount of material that would elutriate from he bed during this operation. Then, bed heights were calculated based on the amount of coal that would remain in the bed after this elutriation step was completed.

Table 1. Experimental and predicted bed heights at various flow rates for different samples

Group	Size, μm	Symbol in Figure 4	Flowrate, cm/s	Bed Height, cm	
				Experiment	Prediction
1	106-125 (50 g)	□	0.053	39.3	38.8
			0.034	31.9	30.9
			0.074	53.2	49.6
			0.027	28.5	28.1
			0.079	52.7	52.7
			0.044	35.5	35.0
2	106-125 (80 g)	■	0.071	71.8	77.3
			0.043	56.6	55.8
			0.075	78.5	81.1
			0.032	49.6	48.6
3*	106-150 (100 g)	○	0.023	50.4	48.9
			0.016	44.5	43.4
			0.026	53.2	51.2
			0.019	48.1	45.8
			0.03	55.6	54.3
			0.035	58.6	58.3
			0.041	63.4	63.4
			0.047	66.8	68.8
			0.03	55.6	54.3
			0.054	69.2	70.5
			0.028	54.5	52.7
			0.058	72.8	73.8
			0.031	55.5	55.1
			0.071	85.4	85.5
4	22-132 (100 g)	●	0.0018	34.4	35.0
			0.0037	42.3	41.6
			0.0057	50.3	48.4
			0.0109	68.2	67.2

* Pre-elutriated at 0.054 cm/s for 10 hrs.

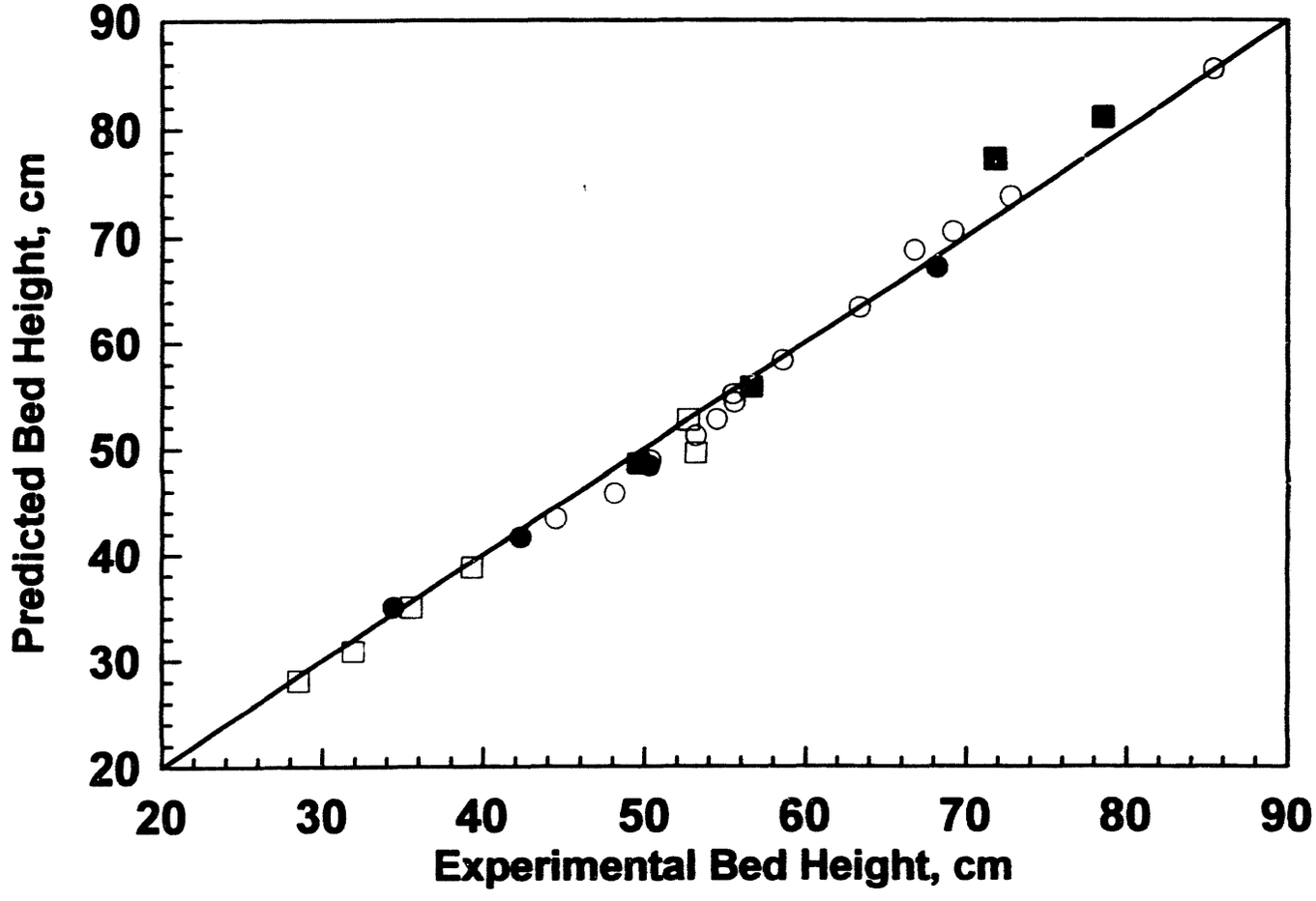

Fig. 4. Parity plot of the predicted versus experimental bed height.

Notation

C_i fractional volumetric concentration of particle species i

d_i particle diameter of species i, mm

d_m particle mean diameter of the sample mixture, mm

D_i dispersion coefficient of particle species i, m^2/s

L height of fluidization bed, m

L_t total column height, m

J_i mass flux of species i in the mixing region of the bed, kg/m^2s

n index of Richardson-Zaki correlation

N total number of particle species

Q_0 liquid flowrate, m^3/s

S surface of the bed system, m^2

U_i velocity of particle species i, m/s

U_s surface movement rate, m/s

U_{ti} terminal velocity of particle species i, m/s

V volume of the fluidized bed, m^3

x fraction of bed height

z distance along the mixing region in the bed, m

Greek letters

ϵ bed voidage

ρ bed bulk density, kg/m^3

References

Asif M., Petersen J.N., Scott T.C., and Cosgrove J.M., 1993a, Hydrodynamic studies of an advanced fluidized-bed for direct coal liquefaction. *Appl. Biochem. Biotech.* **39-40** 535-547.

Asif M. and Petersen J.N., 1993b, Particle dispersion in a binary solid-liquid fluidized bed. *AIChE J.* **39** 1465-1471.

Asif M., Petersen J.N., E.N.Kaufman, J.M.Cosgrove, and T.C.Scott, 1993c, A dynamic model of the hydrodynamics of a liquid fluidized bed of coal particles. (submitted to *Ind.Eng. Chem.Res.*)

Berzin M. and Dew P.M., 1991, Algorithm 690 Chebychev polynomial software for elliptic-hyperbolic systems of PDEs. *ACM Trans. on Mathematical Software* **17** 178-206.

Chen Y.-M, Bavarian F., Fan L.-S, Buttke R.D., and Beaton W.I., 1988, Transients in bed expansion of a three-phase fluidized bed. *AIChE Symp.Series, Fluidization and Fluid Particle Systems-Fundamentals and Applications* **85** 49-56.

Fan L.-T, Schmitz J.A., and Miller E.N., 1963, Dynamics of liquid-solid fluidized bed expansion. 9 149-153.

Gibilaro L.G., Felice R.D., and Waldram S.P., 1986, A predictive model for the equilibrium composition and inversion of binary-solid liquid fluidized beds. **41** 379-387.

Juma A.K.A. and J.F.Richardson, 1983, Segregation and mixing in liquid fluidized beds. *Chem. Engng Sci.* **38** 955-967.

Kaufman E.N. and Scott T.C., 1993, In situ visualization of coal particle distribution in a liquid fluidized bed using fluorescence microscopy. (submitted to *Powder Technology*).

Patwardhan V.S. and Tien Chi, 1984, Distribution of solid particles in liquid fluidized beds. *Can. Chem. Eng.* 62 46-54.

Richardson J.F. and Zaki W.N., 1954, Sedimentation and Fluidization: Part I. *Trans. Instn. Chem. Engrs.* **32** 35-52.

Scott C.D, Scott T.C., and Woodward C.A., 1993, The chemical modification of enzymes to enhance solubilization in organic solvents for interaction with coal. *Fuel* **72** 1695-1700.

BIOLOGICAL CATALYSTS IN ORGANIC MEDIA

C. D. Scott

ORNL Research on Enzymes in Organic Media

The primary effort in this task is the modification of enzymes to increase hydrophobicity and, thus, solubilization in organic solvents while maintaining biocatalytic activity. Research has continued on enzyme modification by reaction with methoxypolyethylene glycol that has been activated with p-nitrophenyl carbonate (PEG-n), and work was started on new approaches in which reductive alkylation was used and in which extremely low concentrations of a surfactant was used. Some additional work has also been carried out on the mutation of organisms that produce hydrogenase to enhance their

tolerance to organic solvents and thus produce enzymes that should be more compatible with the organic solvents.

Organic Liquids

Several organic solvents have been used as the reaction medium in this study. These included relatively polar compounds such as pyridine dimethlysulfoxide (DMSO), and dimethylformamide (DMF), and hydrophobic solvents such as toluene and benzene. All solvents were reagent grade and obtained from Aldridge Chemical Co., J. T. Baker, Inc., Fisher Scientific, or Sigma Chemical Co.

Model Enzymes

This quarter, three proteinaceous compounds were used as the model material for testing chemical modification. Two of these were crude hydrogenase preparations, one isolated from *Proteus vulgaris* at this laboratory and the other from a hyperthermophilic organism, *Pyococcus furiosus*, that was supplied under subcontract by Professor M. W. W. Adams of the University of Georgia. The other was cytochrome c, a heme-containing protein purchased from Sigma Chemical Co.

Enzyme Modification by Reductive Alkylation

The use of PEG-n for enzyme modification continues to be the reference for other modification techniques. The techniques for PEG-n modification have been previously described.[1]

It has been previously shown that the reaction of aliphatic aldehydes with amino groups in proteins in the presence of a reducing agent such as sodium borohydride results in alkylamino protein derivatives which are more resistant to heat inactivation than their unmodified counterparts.[2] This previous research was aimed at enhanced heat tolerance of the enzymes in an aqueous media so relatively low molecular weight aldehydes were used in order to maintain high water solubility. We have now investigated the use of higher-molecular-weight aldehydes for this type of reaction to further increase the hydrophobicity of the enzyme. This required a modification to the original technique since these aldehydes have very low solubility in water.

To test this approach, both cytochrome c and the hydrogenase from *P. vulgaris* were used separately at a concentration of 1 to 15 mg/mL in 10 mL of an aqueous solution containing 20% ethanol and a 0.2 M borate buffer at a pH of 7.5 to 8.5. The ethanol was required to allow the solubility of 10-40 mL/mL of aldehydes such as decyladehyde. The reaction was carried out at 30C for 60 min. Approximately 2 mg of sodium borohydride was added to the reaction mixture at the start of the test and after 30 min.

Heptaldehyde and hexaldehyde (Aldrich Chemical Co.) were used in initial experiments as the modifying agents. Although interactions did occur, further experiments showed that decylaldehyde (Aldrich Chemical Co.) was much more effective at enhancing solubility in organic solvents. (This would be expected since decylaldehyde is much more hydrophobic than the lower-molecular-weight aldehydes.) The reaction solution was then lyophilized and contacted with 10 mL of benzene at ambient conditions for 1 h. Benzene was used since it is very hydrophobic and we have found that it represents the most severe test for solubility of modified enzymes in organic solvents.

Results from the tests with decylaldehyde showed that approximately 0.5 mg/mL of the modified hydrogenase and a comparable amount of modified cytochrome c were solubilized in benzene. The hydrogenase, after recovery from the benzene by drying and solubilization in aqueous buffer, had about 25% of the original activity.

Enzyme Modification by Surfactant Complexation

Proteins can be dispersed in organic solvents by the action of anionic surfactants such as Aerosol OT (AOT) that surround the protein usually contained in a small amount of water. The polar part of the surfactant molecule is oriented toward the protein-water phase while the nonpolar part contacts the organic medium. We have previously shown that large amounts of enzyme can be incorporated into the organic phase by use of a sufficient amount of the surfactant to produce reverse micelles (microdroplets that contain one or more protein molecules). This is actually a dispersion rather than a true solubility, so direct contact with solid surfaces (coal) was shown to be very poor.

It has been suggested by Professor J. Dordick[3] that individual protein molecules may form hydrophobic ion-paired complexes with the surfactant at extremely low surfactant concentrations (less than the critical micelle concentration) and, thus, have an enhanced solubility in the organic. This should result in a modified enzyme somewhat similar to the other techniques that we have tested.

Tests were made using cytochrome c (20 mg/mL) in 7mM phosphate buffer at a pH of 7.0. Approximately 1 mL of the cytochrome c solution was gently agitated with 5 mL of benzene containing 10 or 20 mM AOT at ambient conditions for 1 h. The mixture was then allowed to settle for phase separation and after centrifugation, samples of both liquid phases were scanned by a spectrophotometer over the range of 200 to 600 nm. The spectral peak at 410 nm that is specific for cytochrome was used to quantitate solubility. It was found that a small amount of cytochrome c was solubilized in benzene with the 10mM solution of AOT, but an even larger amount (a total of 0.73 mg in the 5 mL of benzene) was solubilized when 20 mM AOT was used.

A smaller amount of hydrogenase was solubilized under similar operating conditions. The effect of pH was also investigated for this enzyme with essentially no solubilization at a pH of 9.0 and 0.032 mg solubilized at a pH of 7.0. Additional tests will have to be made to establish optimum operating conditions and effects of the modification on enzyme activity.

Enhanced Enzyme Activity by Microbial Mutation

A limited amount of work has continued on the mutation of *P. vulgaris* in contact with DMF or DMSO in order to enhance enzymatic activity in organic media. Mutations are by the classical technique of irradiation with uv light. The organism has been shown to grow in 10% DMF or DMSO and to survive in suspension culture with up to 20% of these organics. Irradiation tests are now being carried out with the microorganisms in 5% agar plates with the low wavelength fraction of a 4-W uv lamp suspended 6 in. above the plate. Under these conditions, all of the organisms are killed with 45 s of irradiation, greater that 90% are killed at 25 s, and about 60% are killed at 10 s. Tests are continuing with 25 s irradiation, with the microorganisms contained in the 5% gel agar that also contains 10% DMSO.

References

1. Scott, T. C., et al., "Progress Report of Fundamental Bioprocessing Research for Coal Applications for the Period April 1, 1993 - June 30, 1993," undocumented ORNL Report (1993).

2. Shatsky, M. A., et al., **Biochim. Biophy. Acta 303**, 298 (1973).

3. Dordick, J., Personal Communications (1993).

OXIDATIVE PROCESSES RELEVANT TO THE CONVERSION OF COAL CATALYZED BY ENZYMES IN ORGANIC SOLVENTS

E. Magner and A. M. Klibanov

In this report, we describe our continued efforts to explore the catalytic potential of heme proteins in nonaqueous solvents. Our investigations during this reporting period have focused on using the oxidizing abilities of catalase's compound I to carry out novel oxidation reactions in such solvents. Compound I is generated by the reaction of bovine liver catalase with *tert*-butyl hydroperoxide (*tert*-BuOOH) (1). The enzyme can be regenerated by reaction with a second molecule of *tert*-BuOOH (2). Here we show

$$E + ROOH \xrightarrow{k_1} EO \text{ (compound I)} + ROH \quad (1)$$

$$EO + ROOH \xrightarrow{k_2} E + ROH + O_2 \quad (2)$$

$$EO + X \xrightarrow{k_3} E + \text{products} + O_2 \quad (3)$$

that compound I of catalase also can be used to oxidize a number of substrates X (3), some of them enantioselectively. We also report on experiments carried out to measure the redox potential of the heme protein cytochrome c in nonaqueous solvents.

A variety of substrates were screened in order to test for their reactivity with compound I of catalase. All reactions were initially carried out in tetrahydrofuran in order to avoid oxidation of the solvent by compound I (see last report). The reaction was carried out using 1 mg ml^{-1} enzyme, 15 mM *tert*-BuOOH, in tetrahydrofuran which contained 2% (v/v) aqueous buffer and 5% (v/v) of the appropriate substrate. Since reaction of substrate X with compound I will increase the production of *tert*-BuOH compared to that produced in the absence of X, the substrates (listed in Table 2) were initially screened by following this increase in the rate using capillary gas chromatography.

Table 2. Rate of production v of *tert*-BuOH in tetrahyrofuran in the presence of different substrates

Substrate X	v/ nmoles $min^{-1}mg^{-1}$
sec-Phenethyl alcohol	>270*
2,4,6-Trimethyl phenol	>150*
2,3-Butanediol	>140*
1,4-Butanediol	>310*
1,3-Butanediol	>190*
N,N-Dimethylaniline	>130*
Benzaldehyde	50
Toluene	50
Styrene	50
1-Octene	50
None	50

* These values represent a lower estimate of the initial rate which was too fast to be measured accurately under the conditions used.

The *sec*-Phenethyl alcohol was examined first to determine the feasibility of its oxidation in an enantioselective manner which would be of preparative interest. When the corresponding ketone, acetophenone, was monitored, no detectable amount of the product was observed. Apart from oxidation to acetophenone, there are two other possible oxidation sites on *sec*-phenethyl alcohol, namely hydroxylation of the methyl or phenyl groups. As these hydroxylation products were not readily available, it was decided to use simpler substrates to test what oxidations can be catalyzed by compound I. Using benzyl alcohol, stoichiometric oxidation to benzaldehyde was observed (relative to the concentration of *tert*-BuOOH), demonstrating that oxidation of an aromatic alcohol by catalase is feasible. Phenol and cresol were also tested as substrates, however both of them were oxidized by *tert*-BuOOH even in the absence of catalase (it should be emphasized that for all of the other substrates, the presence of catalase is required to observe production of *tert*-BuOH). Thus while an enhanced rate of production of *tert*-BuOH is seen in the presence of *sec*-phenethyl alcohol, it was not possible to readily identify the oxidation product.

Attention was then switched to another chiral substrate, 2,3-butanediol. As with *sec*-phenethyl alcohol, each enantiomer of the alcohol, as well as the expected oxidation product (3-hydroxy-2-butanone), is readily available. Tests were made at 30°C and a pH of 7.0 in tetrahydrofuran with 1 mg/ml of catalase and 5% (v/v) butanediol. Production of 3-hydroxy-2-butanone levels off after 200

min under these conditions, yielding an enantioselectivity ratio of 14 in favor of the 2S,3S enantiomer (defined by the ratio of product formed from each enantiomer). With the *meso* form of 2,3-butanediol, production of 3-hydroxy-2-butanone was also observed indicating that the orientation of the second hydroxy group does not affect the rate of the reaction

While the occurrence of enantioselective oxidation of 2,3-butanediol by catalase is encouraging, the rate of the reaction is slow for preparative purposes (12 nmoles min^{-1} mg^{-1}). The reaction was carried out in a number of solvents in order to see if it could be increased. The fastest rate was observed in acetonitrile (Table 3), and this solvent was used in all subsequent experiments.

Table 3. Rate of the enzymatic production v of 3-hydroxy-2-butanone from 2S,3S-butanediol in different solvents

Solvent	v/ nmoles $min^{-1}mg^{-1}$
Acetonitrile	40
Tetrahydrofuran	12
2-Butanone	8
Pyridine	<4
Nitromethane	<4
Ethyl acetate	<4

Raising the concentration of *tert*-BuOOH does not affect the rate of formation of 3-hydroxy-2-butanone. This is consistent with the hypothesis that the reduction of compound I (reaction (2)) by *tert*-BuOOH is relatively slow in comparison to its formation (reaction (1)). Increasing the concentration of catalase from 2 to 25 mg ml^{-1} also increases the rate of production of 3-hydroxy-2-butanone only slightly (from 40 to 56 nmoles $min^{-1}mg^{-1}$). This again demonstrates that the rate-limiting step in the reaction does not involve formation of compound I.

In order to ascertain the generality of our findings, enzymatic oxidation of the R and S enantiomers of 2-octanol and 2-butanol was also examined. Both enantiomers of 2-octanol are oxidized to 2-octanone, with the initial rate of its production being 25 and 12 nmoles $min^{-1}mg^{-1}$ for the R and S enantiomers, respectively. Similarly, with 2-butanol, no significant enantioselectivity was observed, with the rates for the R and S enantiomers being 60 and 80 nmoles $min^{-1}mg^{-1}$, respectively.

These results indicate that in order for *enantioselective* oxidation by catalase to occur, an additional functional group, such as the second hydroxy group in butanediol, must be present. Future work will concentrate on identifying substrates which can be oxidized by catalase both in an enantioselective manner and at a sufficiently fast rate.

In previous reports, we described experiments designed to measure the redox potential of a redox protein in nonaqueous solvents. The bulk of this work was carried out with myoglobin. We attempted to measure its redox potential in nonaqueous solvents by measuring the equilibrium constant for the reaction between myoglobin and a redox dye, tetracyanoquinodimethane (TCNQ). It did not prove feasible to measure the redox potential of myoglobin in

$$Mb(Fe(II)) + TCNQ \text{ <---> } Mb(Fe(III)) + TCNQ^{\cdot-}$$

this manner as reduced mediator was produced when TCNQ was added to a suspension of both the reduced protein and the oxidized protein. Production of $TCNQ^{\cdot-}$ on addition of TCNQ to a suspension of the apoprotein confirmed the existence of an alternative oxidation site on myoglobin.

On switching to cytochrome c, production of reduced mediator was again observed in toluene. However, when the same experiment was carried out in acetonitrile (250 μM cytochrome c(III), 10 mM TCNQ, 0.1 M $LiClO_4$, 25 °C, aerobic conditions), no $TCNQ^{\cdot-}$ was produced. A similar experiment was then carried out with reduced protein (100 μM cytochrome c(II), 1 mM TCNQ, anaerobic conditions); and the production of $TCNQ^{\cdot-}$ was followed with time. No $TCNQ^{\cdot-}$ was produced over 2 d. A similar result was obtained using higher concentrations of the mediator and the protein, 10 and 0.5 mM, respectively. As no $TCNQ^{\cdot-}$ was produced, it is possible that the equilibrium constant for the reaction between cytochrome c(II) and TCNQ is very low and that the reverse reaction, reduction of cytochrome c(III) by $TCNQ^{\cdot-}$, may occur more readily. This possibility is currently being investigated.

DIRECT INTERACTION OF MICROORGANISMS WITH COAL (TEXAS LIGNITE)

K. C. Srivastava

Task 1. Determination of Optimal Conditions for Solubilization and Fermentation

Several experiments were conducted to study the effect of different pHs of the culture medium on attachment of microbial cells to the coal particles and biogasification of Texas lignite. The experiments were carried out in 60-mL vials containing 40 mL 0.2% SNTM (inoculated with 10% of Mic-1 consortium) and 10% Texas lignite (pulverized). The control vials did not contain coal. The initial pH of the medium in both control and experimental vials was adjusted with 1 N HCl or 1 N NaOH to the following pH values: 6.5; 7.0; 7.5; 7.8 (no correction); 8.0; 8.5; and 9.0. Every 7 d, the control and experimental vials were monitored for total gas production, gas composition, COD, protein, and VFA analyses, as well as changes in pH. The samples from the experimental vials were observed for attachment by epifluorescence microscopy (Olympus BH2). At higher solids loadings (10% TxL and higher), even though the pH of the medium was corrected up to 8.5 -9.0, within an hour after the start of the experiment, the pH of the reaction mixture decreased and varied between 6.3 to 7.6. The changes in the pH of the medium affected the attachment of microbes to the TxL particles. The lower and higher pHs did not show significant influence on the attachment. The highest number of attached microbial cells was observed at pH 7.8.

This pH allowed not only the best conditions for highest attachment of microbes (as average number of cells) to the coal particles, but even after shaking the samples for 1 h at 150 rpm, the number of the bacterial cells left on the coal surface was relatively high. These data reconfirm our hypothesis that Mic-1 forms a biofilm on the TxL particle surface. Correction of the initial pH of the medium to 7.8 increases the number of attached bacterial cells to the coal particles.

4.2 ADVANCED BIOREACTOR SYSTEMS FOR GASEOUS SUBSTRATES: CONVERSION OF SYNTHESIS GAS TO LIQUID FUELS AND REMOVAL OF SO_x AND NO_x FROM COAL COMBUSTION GASES

E. N. Kaufman

A Cooperative Research and Development Agreement (CRADA) between the Bioprocessing Research and Development Center at ORNL and Bioengineering Resources, Inc., has been established to study the bioconversion of coal synthesis gas-to-liquid fuels and the biologically mediated removal of SO_x and NO_x from coal flue gases. This review serves as a summary of previous work in this area and outlines our proposed research tasks for this project.

Our large coal reserves may be used to provide precursors for alternative liquid fuels through indirect liquefaction. In such a process, coal is thermochemically converted to synthesis gas consisting mainly of carbon monoxide, hydrogen, and carbon dioxide. Conventional catalytic upgrading of synthesis gas into alcohols or other oxychemicals is subject to several processing problems. Additional constituents in the synthesis gases (e.g., H_2S and CO) are potent poisons to conventional catalysts and must be removed in costly preprocessing procedures. These inorganic catalysts for upgrading also require strict CO/H_2 ratios to maintain a particular product distribution and yield. This may necessitate costly gas recompression and shift reaction conversion procedures. Conventional catalytic conversion is performed at high temperatures and pressures, which increases processing cost and raises safety issues. Finally, product specificity is often poor, resulting in a large product spectrum, decreased yields, and increased separation costs.

Recently isolated and identified bacterial strains capable of utilizing CO as a carbon source and converting CO and H_2 into mixed alcohols offer the potential of performing synthesis gas conversion using biocatalysts.[1] While biocatalytic conversion with such microorganisms is generally slower than that achieved with inorganic catalysts, such methods would offer several advantages over conventional synthesis gas upgrading. Feed-gas components that would poison conventional catalysts do not interfere with the bioconversion in sulfur-tolerant strains of the microorganisms, and enzyme-mediated reactions in biocatalytic conversions are not bound to strict substrate ratios. Thus, synthesis gas preprocessing would be eliminated. Further, many enzymatic reactions are essentially irreversible. This would help eliminate product stability issues that arise in conventional catalytic upgrading.

Finally, biocatalytic reactions may take place at or near ambient temperatures and pressures, reducing both capital and operating expenses.

Clostridium ljundahlii catalyzes the conversion of CO, H_2, and CO_2 into acetate and ethanol.[2] The chemical environment can be modified to either optimize bacterial growth or to favor ethanol production. This microbial strain has been used in a two-CSTR scheme in which growth is favored in the primary reactor, and ethanol production is favored in the secondary reactor.[3] The ethanol production rate in this stepped reactor mode was 250-300 mmol g^{-1} cells d^{-1} with a product concentration of 0.3%.

The most common method of flue gas desulfurization is the use of disposable sorbents, such as limestone. This process results in the production of large quantities of gypsum, which poses additional disposal issues. This process also ignores the removal of the oxides of nitrogen. Promising technologies for simultaneous SO_x and NO_x removal utilize regenerable sorbents as in the copper oxide or NOXSO process. These methods yield concentrated streams of SO_2, H_2S, and NO_2, which must be converted into a useful or disposable product. Microorganisms such as *Desulfovibrio desulfuricans*[4] and *Pseudomonas denitrificans*[5] have been shown to interact with SO_x and NO_x, respectively. However highly efficient and economical bioreactor systems for possible use in flue gas processing have not been demonstrated.

The efficient biocatalytic use of gaseous substrates is constrained by several factors that are often interacting. The solubility of the substrate in the liquid phase is very low. Mass transport of the substrate from the gas phase into the liquid media and to the solid biocatalyst may also be reaction-limiting. High cell density in the reactor is desired for complete and timely substrate conversion, and plug-flow hydrodynamics is desired for these same reasons. These design requirements are often interrelated and self-defeating. Mixing to enhance mass transport erodes plug-flow performance and may affect cell viability. Packed or immobilized biocatalytic systems, while favoring high cell density and plug-flow performance, may be mass transport-limited in their substrate conversion. It is evident that efficient and commercializable liquid fuel production from synthesis gas will require the design of novel gas-phase bioreactors that combine high cell density with high product yield and high rates of substrate flux to the biocatalyst.

This planned research addresses the further investigation of optimal bacterial strains, growth media, and kinetics for the biocatalytic conversion of coal synthesis gas to liquid fuel such as ethanol and the reduction of gaseous flue gas constituents. However, the primary emphasis will be on the

development of advanced bioreactor systems coupled with innovative biocatalytic systems that will provide increased productivity under controlled conditions. This should result in bioprocessing options that have both technical and economic feasibility, thus ensuring early industrial use. Predictive mathematical models will be formulated to accommodate hydrodynamics, mass transport, and conversion kinetics and provide the data base for design and scaleup.

The 3-year research and development effort is divided into five general tasks:

Optimization of Biocatalytic Kinetics - Small laboratory-scale tests will be conducted to identify promising bacterial strains, strain combinations, and optimal media compositions.

Development of Well-Mixed Bioreactors - Most previous investigations have utilized well-mixed reactors, and our efforts will begin at this point. The effects of substrate and system pressure, as well as the effects of mass transport, will be investigated.

Development of Columnar Reactors - The BRDC's experience with columnar reactors utilizing immobilized cells has demonstrated increased productivity with continuous operation and decreased operating costs. Bench-scale experimentation will be performed for both coal synthesis gas conversion and flue gas cleanup. Optimal operating conditions will be established, and hydrodynamics, kinetics, and mass transport phenomena will be investigated to enable reliable process scaleup.

Predictive Mathematical Modeling - Predictive mathematical models have been established to allow reliable scaleup of both ethanol fermentation and coal solubization at the BRDC. Using parameters obtained in bench-scale studies, predictive mathematical models incorporating hydrodynamics, mass transfer, and biochemical kinetics will be established and evaluated.

Industrial Demonstration - At least one of the two bioprocessing applications will be designed and operated at an industrial site to determine true technical and economic feasibility.

References

1. Worden, R. M., A. J. Grethlein, M. K. Jain, and R. Datta, "Production of Butanol and Ethanol from Synthesis Gas via Fermentation," *Fuel*, **70**(5), 615-19 (1991).

2. Vega, J. L., S. Prieto, B. E. Elmore, E. C. Clausen, and J. L. Gaddy, "The Biological Production of Ethanol from Synthesis Gas," *Appl. Biochem. Biotechnol.*, **20**, 781-97 (1989).

3. Klasson, K. T., B. B. Elmore, J. L. Vega, M. D. Ackerson, E. C. Clausen, and J. L. Gaddy, "Biological Production of Liquid and Gaseous Fuels from Synthesis Gas," *Appl. Biochem. Biotechnol.*, **24**, 857-73 (1990).

4. Dasu, B., and K. L. Sublette, "Reduction of Sulfur Dioxide by *Desulfovibrio desulfuricans* in Co-Culture with Fermentative Heterotrophs," *Biotechnol. Bioeng.*, **34**, 405-09 (1989).

5. Apel, W. A., and C. E. Turick, "The Use of Denitrifying Bacteria for the Removal of Nitrogen Oxides from Combustion Gases," *Fuel*, **In Press** (1991).

4.3 BIOLOGICAL CONVERSION OF COAL

C. D. Scott

INTRODUCTION

The feasibility of using biological catalysts for the conversion of coal to useful liquid fuels has been investigated. Biological reagents potentially useful in this application include intact microorganisms in pure or mixed culture and isolated enzymes. The major emphasis has been on the investigation of the use of modified enzymes in organic media to enhance liquefaction/ solubilization of coal.

RESEARCH RESULTS

The liquefaction/solubilization of low rank coal supplied by a coal company was studied and there was some additional work with model compounds.

Biocatalysts

The recent emphasis has been on a continued study of hydrogenase from the thermophilic organism, *Pyrococcus furiosus*, (obtained from Prof. M. W. W. Adams of the University of Georgia) and some additional work with the hydrogenase from the mesophilic organism, *Proteus vulgaris*, a crude enzyme extract prepared in our Laboratory. As previously indicated, it is necessary to use an electron transport mediator such as cytochrome c (obtained from Sigma Chemical Co.) with the hydrogenases for optimum results.

All tests were conducted with dry organic solvents and the enzymes were chemically modified to increase their hydrophobicity and, thus, enhance their solubility in the organic media. Two types of chemical modification were used. The base case was with methoxypolyethylene glycol activated with p-nitrophenyl carbonate (PEG-n), using a technique previously described.[1] A second and newer approach was by reductive alkylation using decyl aldehyde and sodium borohydride in an alcohol-water buffer using a technique described in the recent quarterly report for the AR&TD program entitled "Fundamental Bioprocessing Research for Coal Applications."[2]

Organic Solvents

Various organic solvents have been used as the reaction medium for these enzyme reactions. Although mixed solvents have also been previously used, this quarter only pyridine, toluene, and benzene were used. These solvents essentially cover the range of hydrophobicity of the expected reduction products of coal. All solvents were reagent grade and obtained from Aldridge Chemical Co., J. T. Baker, Inc., or Fisher Scientific.

Tests with the Model Compound

Additional tests were made with the model compound, 1-[4-(2-phenylethyl)benzyl]naphthalene (from TCI America), in order to test the effectiveness of a new chemical modification technique for the enzymes, reductive alkylation. Hydrogenase from *P. vulgaris* and cyctochrome c were modified by this technique as indicated above and solubilized in toluene at a concentration of 0.5-1.0 mg/mL. The model compound was added at a concentration of 0.5 mg/mL. The tests were made in closed shake flasks containing molecular hydrogen in the head space at 30°C for 24 h.

Liquid samples were taken periodically and analyzed by gas chromatography (GC) using operating conditions previously described[3] at which time additional hydrogen was added to the head space. As in past tests, there was a significant decrease in the concentration of the model compound of up to 27% $\pm$ 7% with the enzymes present. Reference tests made without the enzymes resulted in a slight apparent increase in the model compound concentration with a variation of $\pm$ 4%. As indicated by the GC analyses, the same types of reduction products as seen in previous tests were observed in these tests.[3] This was additional conformation of the enzyme enhancement of the reduction process.

Coal Conversion Tests

Some additional tests were made with enzymes that were modified with either PEG-n or reductive alkylation in organic media. The coal used was a Texas lignite that was supplied by the Phillips Coal Company, Richardson, TX (see Table 4 for the proximate and ultimate analysis). The coal was size-reduced to -270+325 mesh and both thermophilic and mesophilic hydrogenases were evaluated in tests made in shake flasks at 30^{o}C under a H_2 atmosphere for 24 to 72 h using 1 to 2

Table 4. Proximate and ultimate analysis of Texas Lignite*

Analysis	Wt%
Proximate (dry)	
Ash	21.9
Volatile Matter	43.0
Fixed Carbon	35.1
Ultimate Analysis (dry)	
Carbon	53.4
Hydrogen	4.7
Nitrogen	1.2
Chlorine	0
Sulfur	1.3
Oxygen	13.5

*Analysis provided by Phillips Coal Company

mg/mL of mixed enzymes (hydrogenase and cytochrome c modified by the PEG-n method). Pyridine and benzene were used in separate tests to determine the effects of polar and nonpolar organic solvents and both mesophilic and thermophilic hydrogenases were used in separate experiments.

As in the past, the enzyme-catalyzed tests always produced a greater increase in the solubilized material (as indicated by an increase in the solution light absorbance) when compared with tests in which the solvent alone was used. After these tests, the reaction solution from the test was analyzed on the GC using the same operating conditions that had been developed for the model compound tests. There was an increase in the number of chromatographic peaks with one major peak (with expected molecular weight of about 250)[3] and several minor peaks.

The lignite used in these tests is of particular interest since there are large reserves available and the material is currently being marketed for energy use. The industrial firm involved also is quite interested in the results of the research.

REFERENCES

1. Scott, T. C., et al., "Progress Report of Fundamental Bioprocessing Research for Coal Applications for the Period April 1, 1993 - June 30, 1993," undocumented ORNL Report (1993).

2. Scott, T. C., et al., "Progress Report of Fundamental Bioprocessing Research for Coal Applications for the Period October 1, 1993 - December 31, 1993," undocumented ORNL Report (1994).

3. Scott, C. D. and Woodward, C. A., "Progress Report of the Biological Coal Conversion Program for the Period July 1 - September 30, 1993," undocumented ORNL report (1993).

4.4 REMOVAL OF HETEROATOMS AND METALS FROM HEAVY OILS BY BIOCONVERSION PROCESSES

C. D. Scott

Biocatalysts, either appropriate microorganisms or isolated enzymes, will be used in an aqueous phase in contact with the heavy oil phase to extract heteroatoms such as sulfur or nitrogen or heavy metals from the oil phase by bioconversion processes. Somewhat similar work on coal processing will be adapted and extended for this application. Bacteria such as *Sulfolobus acidocaldarius* or fungi such as *Paecilomyces* sp. TLi will be investigated for the oxidative removal of organically-bound sulfur and a recently isolated soil bacteria will be studied for the reductive removal of sulfur. Microbial biomass such as that from *Micrococcus luteus* will be investigated for metal removal. At a later time, bacteria that interact with organic nitrogen may also be studied. This type of interaction will be carried out in a bioreactor utilizing a new concept of emulsion-phase contacting in which the aqueous phase is first dispersed in the organic phase and then recoalesced for removal of the contaminants and recycled back to the reactor.

This will be a cooperative research and development program with support and participation by the members of the Petroleum Environmental Research Forum, an industrial consortium of several oil companies. The industrial involvement will be via a CRADA and will include direct participation of industrial R&D staffs as well as joint oversight of the effort. After verification of the bioprocessing concepts on a laboratory-scale, the end-product will be a demonstration of the technology at an industrial site. This should result in rapid transfer of the technology to industry.

The CRADA has been signed and work will begin soon.

4.5 RENEWABLE HYDROGEN PRODUCTION FOR FOSSIL FUEL PROCESSING

E. Greenbaum

SUMMARY

The key goal of this mission-oriented research project is the development of a real-world engineering process for the production of molecular hydrogen (and oxygen) by photosynthetic water splitting. The unicellular algae that we have used for these experiments are known to be particularly rugged and should lend themselves well to the desired process. During the current reporting period we have worked with *Chlamydomonas* cold strain CCMP1619 provided by the algal culture collection of the Bigelow Laboratory for Ocean Sciences, Westboothbay Harbor, Maine. This alga was originally isolated from Lake Bonney, an ice-covered lake in Antarctica.

An important discovery made during the current reporting period is that *Chlamydomonas* cold strain CCMP1619 is capable of producing hydrogen and oxygen in a photosynthetic water splitting reaction. It is also capable of surviving and functioning under harsh conditions and lends itself to our desired process. The data obtained with this alga are contained in Figs. 1 and 2 of the quarterly report. One unusual observation (Fig. 1, 0-3 h) is that at 20°C, *Chlamydomonas* cold strain CCMP1619 has a much higher rate of thermally activated (nonlight-dependent) hydrogen production than its normal wild-type counterpart.

Technical Progress - *Chlamydomonas* Cold Strain CCMP 1619

Background

Photosynthetic algal water splitting for hydrogen and oxygen production is a promising approach to the conversion of sunlight into useful chemical energy. During the current reporting period, we examined temperature effects on hydrogen and oxygen production in two *Chlamydomonas* strains, CCMP1619 and wild type 137c. CCMP1619 was isolated from an ice-covered lake in Antarctica and was grown at 4°C. We have observed that hydrogenase, which catalyzes reduction of protons in hydrogen production, can be induced in both strains. Temperature had a significant effect on the rates of hydrogenase induction and on the kinetics of hydrogen production.

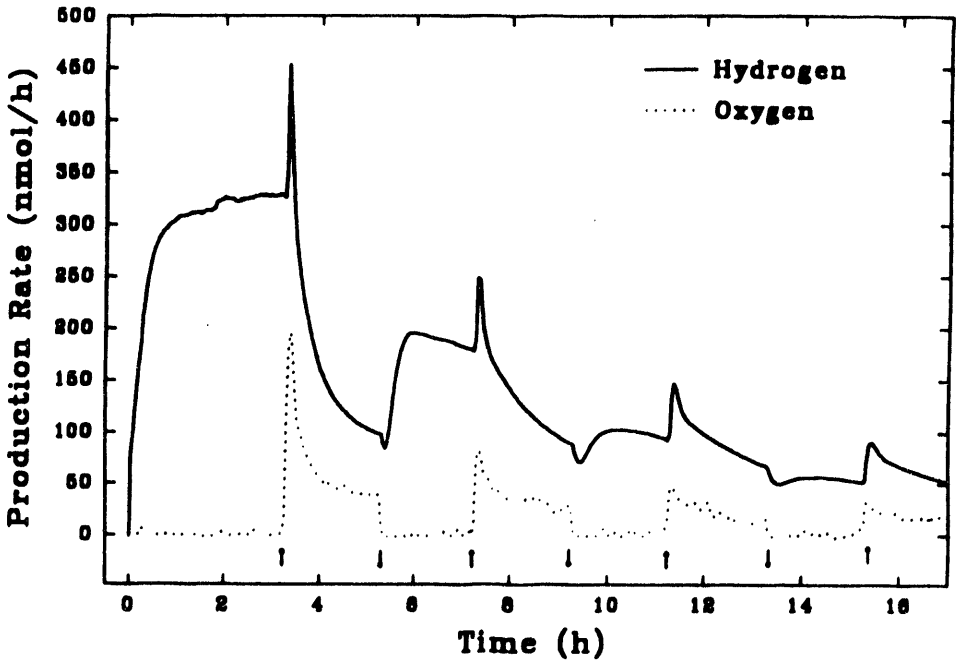

Fig. 1 Production of hydrogen and oxygen by *Chlamydomonas* cold strain CCMP1619 at 20°C under CO_2-free helium atmosphere.

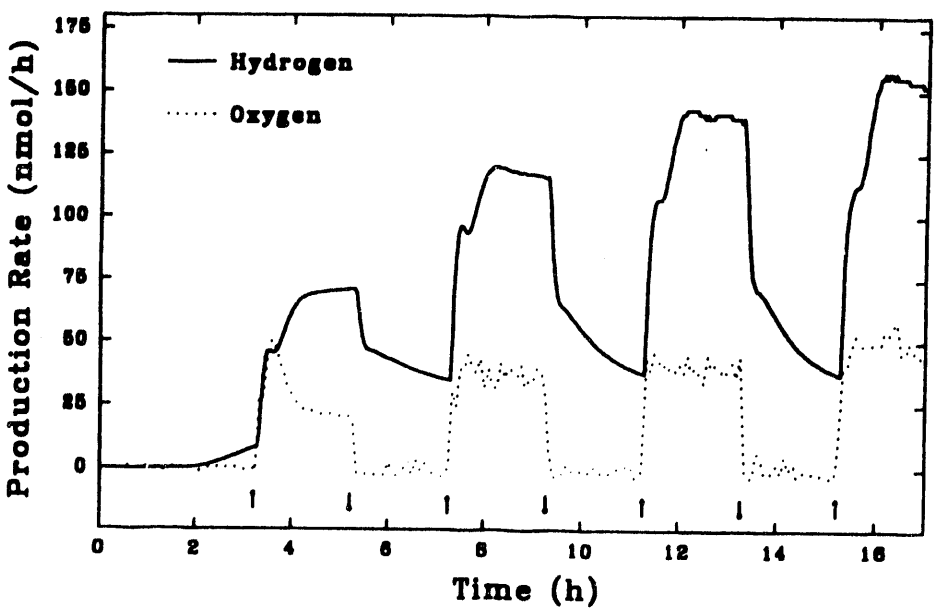

Fig. 2 Production of hydrogen and oxygen by *Chlamydomonas* cold strain CCMP1619 at 4°C under CO_2-free helium atmosphere.

Experimental Technique

Forty mL of alga samples containing 5 μg chl/ml were loaded into a reaction chamber whose temperature was controlled by a temperature-regulated water bath. The hydrogenase enzyme was induced by removing oxygen gas with helium flow through the liquid sample. Production of molecular hydrogen and oxygen were detected with a flow detection system described previously (1). Figs. 1 and 2 illustrate production of hydrogen and oxygen in the CCMP1619 strain at 20 and 4°C, respectively. For the first 3 hours following oxygen removal, the samples were kept in darkness for hydrogenase induction.

Results and Discussion

It is known that hydrogen can be produced via dehydrogenation of carbohydrates. The rate of hydrogen production reflects thermally activated electron-transport and hydrogenase activity. Hydrogen production indicated that the metabolism and hydrogenase induction at 20°C was over 30 times faster than its rate at 4°C and was 6 times faster than that of the wild-type 137c strain at the same temperature (Figure 3). These results demonstrated that CCMP1619 is highly sensitive to "elevated" temperature (at least compared to its natural growth temperature.)

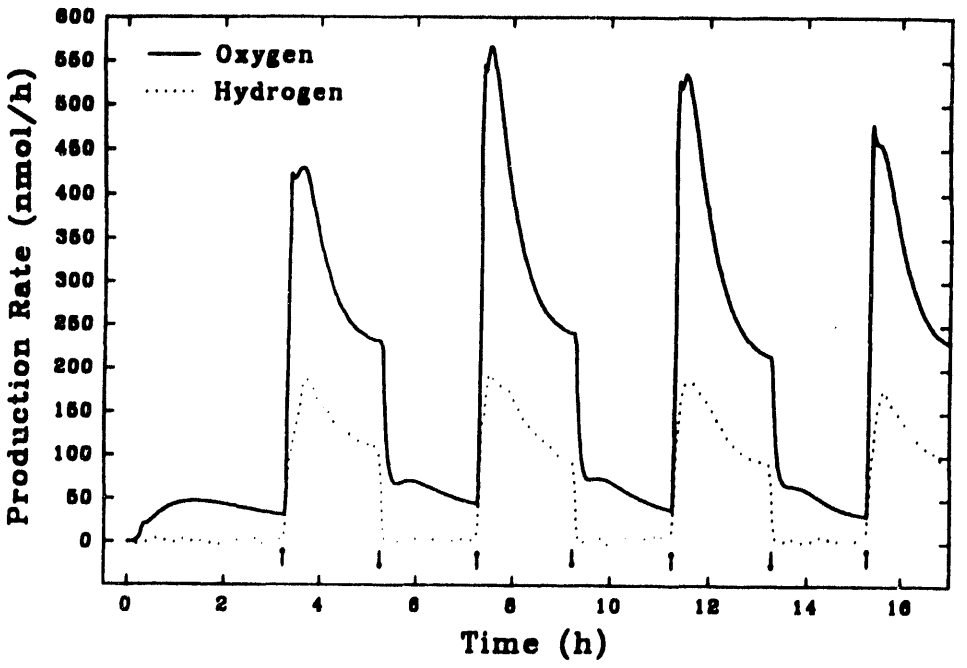

Fig. 3 Production of hydrogen and oxygen by *Chlamydomonas* strain 137c at 20°C under CO_2-free helium atmosphere.

After 3.3 hours of hydrogenase induction, simultaneous production of hydrogen and oxygen by photosynthetic water splitting was observed at both temperatures during periodic 2-hour intervals of actinic illumination (1.5×10^{16} quanta $\cdot s^{-1} \cdot cm^{-2}$). The kinetics of photodependent hydrogen and oxygen production at 20°C (Fig. 1) differ dramatically from those at 4°C (Fig. 2). At 20°C, onset of actinic light (upward arrow) led to a sharp burst of hydrogen followed by a quick and large decrease in hydrogen production. At the end of the first illumination period, the total rate of hydrogen production was even slower than that in the first dark period prior to illumination. When the actinic light was turned off (downward arrow), hydrogen production dropped only for a very short while and then rose quickly again apparently due to onset of "dark" hydrogen production. The dark activation and light inhibition of hydrogen production clearly indicated that light can switch off the "dark" hydrogen pathway. These kinetic characteristics of hydrogen production can also be observed repeatedly in subsequent light-dark cycles. The maximum rate of hydrogen production decreased somewhat in late illumination cycles. The decrease in the maximum rate of hydrogen production demonstrated the instability of the cold strain CCMP1619 at 20°C.

At 4°C, however, photosynthetic water-splitting activity is stable in CCMP1619. In contrast to the kinetics at 20°C, the first onset of actinic illumination at 4°C led to a hydrogen burst followed by a dip, then a continuous increase in the production rate (Fig. 2). This small dip, which occurred soon after the onset of illumination, may result from the light inhibition of "dark" hydrogen production which was apparently limited by the enzymatic activity at 4°C. The increase in photoproduction of hydrogen after this dip is more interesting, since it indicates that some light-dependent physiological process seems to enhance hydrogen production in addition to the induction of hydrogenase that may occur slowly in darkness at 4°C. The maximum rate of hydrogen production increased significantly in the successive illumination cycles (Fig. 2).

At both temperatures, oxygen was produced only in the light periods as expected. The rate of oxygen production reflects the activity of photosynthetic water splitting. The oxygen production curves at the two temperatures (Figs. 1 and 2) show that water-splitting activity of CCMP1619 increased with time at 4°C while it decreased with time at 20°C. This result is consistent with hydrogen production data. It again indicated that the activity of CCMP1619 at 4°C is more stable than that at 20°C. Currently, we have been developing an *in vacuo* hydrogen production system. Cold temperature is desired in such a system where lower water-vapor pressure is required. CCMP1619 may be useful in the development of this new photobiological reactor design.

The wild type *Chlamydomonas reinhardtii* 137c strain responded to temperature change also. Figs. 3 and 4 present its hydrogen and oxygen production curves at two different temperatures. At 20°C, its dark hydrogen induction was apparently faster than that at 4°C. Maximum rate (50 nmol/h) of dark hydrogen production during the first 3.3 hours at 20°C was about 3 times faster than that (16 nmol/h) at 4°C. Upon onset of actinic illumination (upward arrow) at 20°C, both hydrogen and oxygen production quickly rose to their peak rates and then decayed dramatically (to about 50% of maximum production rates).

Similar kinetics have been observed previously in a study with carbon dioxide (CO_2), by Cinco, et al. (2). In that study, the decay of photodependent hydrogen production was mainly explained by the competition with the Calvin cycle for reductant generated from water splitting. In the current work, the samples were constantly purged with CO_2-free helium gas and the Calvin cycle was suppressed due to depletion of CO_2 in the reaction medium. Therefore, the decay of light-activated hydrogen production observed in this study cannot be explained by the competition with the Calvin cycle. There must be something else other than Calvin cycle that is limiting hydrogen production during illumination. Interestingly, very little of such a decay was observed at 4°C (Fig. 4).

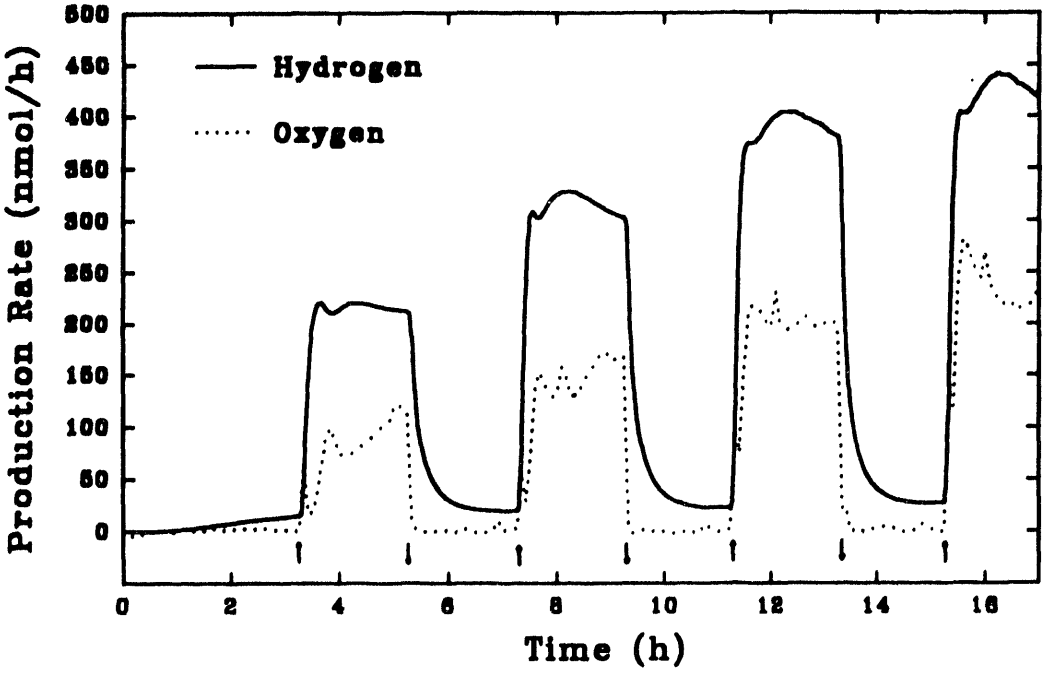

Fig. 4 Production of hydrogen and oxygen by *Chlamydomonas* strain 137c at 4°C under CO_2-free helium atmosphere.

Both hydrogen and oxygen production at 4°C were fairly steady in each illumination period, resulting in nearly square-like curves that were very similar to those of CCMP1619 at the same cold temperature (Fig. 2). This result indicated that the decay of photoactivated hydrogen production can be largely prevented with cold (4°C) temperature. Furthermore, the maximum production rate at 4°C increased in the latter illumination cycles, and they were about 2 times faster than those by CCMP1619 at the same temperature. According to data analysis, the integrated yield of oxygen and hydrogen photoproduction in the latter cycles at 4°C was similar to that at 20°C. Photoevolution of hydrogen and oxygen can be performed well by 137c strain at 4°C.

Conclusion

As a conclusion, *Chlamydomonas* cold strain CCMP1619 is highly sensitive to warm (20°C) temperature, although photoproduction of hydrogen and oxygen by CCMP1619 can be achieved stably at 4°C. Within 3.3 hours at 20°C, its dark hydrogen production can be induced to reach 300 nmol/h, which is 30 times as fast as its rate (about 10 nmol/h) at 4°C and which is 6 times faster than that (50 nmol/h) of strain 137c at 20°C. The hydrogen production can be controlled by light and temperature. Warm temperature stimulates dark hydrogen production, while cold temperature (4°C) can largely prevent decay of hydrogen and oxygen photoproduction in both strains CCMP1619 and 137c.

REFERENCES

1. E. Greenbaum, "Biophotolysis of Water: The Light Saturation Curves," *Photobiochem. Photobiophys.* **8**, 323-332 (1984).

2. R. M. Cinco, J. M. MacInnis, and E. Greenbaum, "The Role of Carbon Dioxide in Light-Activated Hydrogen Production by *Chlamydomonas reinhardtii*," in press, *Photosyn. Res.* (1993)

PUBLICATIONS

1. R. M. Cinco, J. M. MacInnis, and E. Greenbaum, "The Role of Carbon Dioxide in Light-Activated Hydrogen Production by *Chlamydomonas reinhardtii*," in press, *Photosyn. Res.* (1994).

2. J. W. Lee, C. V. Tevault, S. L. Blankinship, R. T. Collins, and E. Greenbaum, "Photosynthetic Water Splitting: *In Situ* Photoprecipitation of Metallocatalysts for Simultaneous Photoevolution of Molecular Hydrogen and Oxygen," in press, *Energy and Fuels* (1994).

5. COAL COMBUSTION RESEARCH

R. L. GRAVES

5.1 ANALYSIS OF FBC DETERMINISTIC CHAOS

C.S. DAW

DISCUSSION OF CURRENT ACTIVITIES

Status Summary

Analysis of fluidized bed data and development of improved analysis algorithms has continued during this reporting period. The onset of chaos in an experimental bubble column and slugging fluidized bed have also been demonstrated and studied extensively. The chaotic instability of the slugging fluidized bed has been used in a closed control loop to greatly inhibit the degree of slugging.

Fluidized Beds

Experimental measurement of voidage and pressure signals from fluidized beds at the University of Tennessee, Morgantown Energy Technology Center, Foster Wheeler Development Corporation, and Babcock and Wilcox Alliance Research Center have continued. Analyses of these data led to the publication of four new papers (1-4). The fourth paper (4) has been accepted for publication in the AIChE Fluidization Symposium Series in 1994.

Pressure measurements from the University of Tennessee and Morgantown have been used to investigate a new potential diagnostic, the characteristic nonlinear signatures of solids agglomeration. It is anticipated that it will be possible to develop characteristic indicators of incipient agglomeration that can be used forwarn operators of impending problems. It may also be possible to implement feedback loop control to eliminate agglomeration based on such indicators.

Experiments at the University of Tennessee with a bubble column (bubbles of air in viscous liquids such as glycerine) have demonstrated conclusively the onset of a period doubling route to chaos as the air flow is increased. There also appear to be intermittent windows of periodic behavior interspersed in the chaotic region. The basic features of the observed dynamics are very similar to the bubble model simulation developed previously with J.S. Halow (5) and seem to confirm its essential

correctness. We anticipate that it should be possible to adjust the model parameters such that the observed behavior is almost exactly mimicked. The general agreement between the bubble experiment and model also seems to confirm that there are many points of similarity between liquid bubbles and bubbles in fluidized beds, because the dynamics of the model were based solely on observations of fluidized beds. A paper is now being written on the bubble experiment for submission to a refereed journal, and a request to present proposal has been submitted to the 1994 AIChE National Meeting in San Francisco.

Fluidized bed experiments with large (Group D) particles at the University of Tennessee indicate that the transition away from slugging with increasing gas flow occurs via an intermittency route to chaos. Also as a part of these experiments, it has been conclusively demonstrated that it is possible to use the chaotic instability of slugging beds to destroy the slugs. The basic idea is to inject a small blast of air at a carefully chosen location and time such that the forming slug is destabilized and collapses. Because the inherent instability of the slugging bed itself is being utilized, the amount of air used to perturb the bed can be extremely small; e.g., less than 1% of the fluidization air.

Using the basic concepts of chaos control theory (see reference 6 for example) it should be possible to define the optimum timing and size of the air pulse for destroying slugs. We are now collaborating with Celso Grebogi and Eric Kostelich at the University of Maryland to define the appropriate methodology. If this concept can be fully demonstrated, it is anticipated that it could have major commercial value in reducing the detrimental effects of slugging in fluidized bed reactors and combustors.

REFERENCES

1. Fuller, T. A., Flynn, T. J., Daw, C. S., and Halow, J. S., "Interpretation of Pilot-Scale, Fluidized-Bed Behavior Using Chaotic Time Series Analysis," 12th International FBC Conference, La Jolla, May 8-13, 1993.

2. Skryzke, D., Nguyen K., and Daw, C. S., "Characterization of Dynamic Behaviors of Fluidized Beds Based on Chaotic Time Series Analysis of Pressure Signals," 12th International FBC Conference, La Jolla, May 8-13, 1993.

3. Daw, C. S. and Halow, J. S., "Evaluation and Control of Fluidization Quality Through Chaotic Time Series Analysis of Pressure-Drop Measurements," Fluid-Particle Processes: Fundamental and Applications, Weimer, A. W., ed, AIChE Symposium Series No. 296, Vol. 89, 1993.

4. Halow, J .S. and Daw, C. S., "Characterizing Fluidized Bed Behavior by Decomposition of Chaotic Phase Trajectories," AIChE National Meeting, September, 1993.

5. Daw, C. S. and Halow, J. S., "Modeling Deterministic Chaos in Gas-Fluidized Beds," Fluidized Processes: Theory and Practice, Weimer, A. W., ed, AIChE Symposium Series No. 289, Vol. 88, 1992.

6. Shinbrot, T., Ditto, W., Grebogi, C., Ott, E., Spano, M., and Yorke, J. A., "Using the Sensitive Dependence of Chaos (the 'Butterfly Effect') to Direct Trajectories in an Experimental Chaotic System," Phys. Rev. Lett. 68, May 11, 1992, p 2863.

5. COAL COMBUSTION RESEARCH

R. L. GRAVES

5.2 TECHNICAL SUPPORT TO PETC-USAID COLLABORATIVE COAL PROJECTS

R. P. KRISHNAN

BACKGROUND

The Oak Ridge National Laboratory (ORNL) is providing technical assistance to PETC in the implementation of collaborative coal projects in India under a cooperative agreement between the U.S. Agency for International Development (USAID), and the Government of India (GOI).

In May 1983, the GOI and the USAID initiated the Alternative Energy Resources Development (AERD) Project with a coal conversion component comprising of six collaborative coal projects.

(1) Evaluation of freeboard performance in a fluidized bed combustor (FBC)

(2) Scale-up of an atmospheric fluidized bed combustion boiler

(3) Rheology, stability, and combustion of coal-water slurries

(4) Beneficiation of fine coals in dense media cyclones

(5) Hot gas cleanup and separation

(6) Cold gas cleanup and separation

The PETC, USDOE under a Participation Agency Service Agreement (PASA) had the management responsibility for implementing the collaborative coal projects. In the FBC projects, ORNL and Bharat Heavy Electricals Ltd. (BHEL), Trichy, India, were designated as the lead institutions for the collaborative efforts.

The successful completion of the above coal projects in June 1987 led to a strong interest by the participants in the AERD coal conversion projects to continue the involvement of USAID and the USDOE/PETC in the following coal projects under the AERD, Phase 2 coal conversion activities.

(1) Development of Pollution Control Strategies for Abatement of NO_x and SO_2 Emissions from Coal-Fired Power Plants

(2) Slagging Combustor Development for High-Ash Indian Coals

(3) Characterization of Indian Coals for Combustion and Gasification

(4) Residual Life Assessment and Life Extension of Coal-Fired Power Plants

(5) Environmental and Natural Resource Analysis of Coal Cycle

Projects 1 through 4 were implemented by BHEL, Trichy, in collaboration with ORNL, PETC, and the Tennessee Valley Authority (TVA). Environmental Analysis of Coal Cycle (Project 5), was carried out by the Tata Energy Research Institute (TERI), New Delhi. Technical assistance was provided by ORNL, PETC, and the Environmental Protection Agency (EPRI) in the screening, selection and adaption of the air/water quality prediction models.

The AERD Phase 2 projects, with the exception of the Fuels Evaluation Test Facility (FETF), was completed in June 1992, when the official agreement between USAID and the Government of India (GOI) on the AERD project ended. The accomplishments in the completed projects were reported in the ORNL Fossil Energy Semi-Annual Report, April 1992 - September 1992. PETC and ORNL continued to proivde technical assistance from the U.S. on an "as needed" basis to BHEL during the erection of the FETF.

Under another cooperative agreement between USAID, New Delhi and GOI, the Energy Management Consultancy and Training Project (EMCAT) was initiated in June 1991. The purpose of EMCAT is to introduce technology, financing, and management innovations in the Indian energy supply and end-use sectors. The supply side comonent is administered by the Power Finance Corporation (PFC).

Under EMCAT, a cooperative agreement between USAID, New Delhi, and PETC, was signed in April 1993 for a model demonstration on condition assessment and remaining life estimation of coal-fired power plant at a utility site in India. PETC and PFC have the joint management responsibility for this project. ORNL, the Tennessee Valley Authority (TVA), specialty contractors/consultants to TVA, and the Electric Power Research Institute (EPRI) will perform the condition assessment model demonstration at the Indian utility site. From the Indian side, the BHEL, the National Thermal Power Corporation (NTPC) and the Damodar Valley Corporation (DVC) will provide the technical and logistic support. The study will be performed in teh DVC Unit 2, 140 MW(e) coal-fired station at Chandrapura in the State of Bihar, India. The plant was commissioned in October 1964 and is equipped with a Combustion Engineering (CE) boiler and a General Electric steam turbine. Burns and Roe, USA was the architect and engineering contractor. The condition assessment will be carried out by the Tennessee Valley Authority with technical support from equipment vendors and speciality service contractors from

the United States. The on-site demonstration will expose the Indian collaborating institutions on state-of-the-art power plant condition assessment techniques and procedures so that they can effectively plan, manage, and execute future assessments. Training of Indian engineers in the TVA plants will be provided on the equipment and the diagnostic monitoring techniques prior to the actual demonstration in the DVC plant.

DISCUSSION OF CURRENT ACTIVITIES

Fuels Evaluation Test Facility

Erection of the FETF was completed in December 1993. On January 24, 1994, the FETF was inaugurated by Dr. S. W. Chun, Director, PETC. A site visit was made by ORNL March 3-5, 1994. Commissioning of the individual equipment (fans, coal feeders, oil burners, pumps and air preheater) including insulation and leak tests on all the pipe lines have been completed. External cladding for the pipe lines were being installed and preparations for the drying of the furnace refractory with oil firing were in progress. The schedule for the first coal fire and shakedown was prepared during the site visit. Mr. Scott Smouse from PETC will travel to Trichy in April 1994 to participate in the coal fire stabilization tests. Testing of Indian coals and data gathering will begin in June 1994. The FETF is the first pulverized coal test facility in India and will simulate a commercial boiler with respect to firing pattern, temperature residence time, flue gas composition, and velocity. Continuous flue gas monitoring for SO_2, NO_x, CO, O_2, total hydrocarbons, particulates and flyash resistivity will be possible in the FETF.

DVC Power Plant Condition Assessment

On August 1993, a team (USAID, NTPC, BHEL, PFC, PETC and ORNL) visit to the DVC Chandrapura Thermal Power Station (CTPS) was arranged by PFC to gather the technical information on the DVC plant. CTPS is located in Bokaro in the State of Bihar, about 300 miles north of Calcutta on the Calcutta-New Delhi rail link. DVC was established in 1948. The history and development of DVC is similar to that of TVA in the United States. DVC is modeled after TVA, and several DVC staff have visited and/or have been trained at TVA during the formative years of DVC. Mr. S. P. Guha, Chief Engineer, CTPS was our host. The plant staff was very cooperative and lead the team on a detailed

walkdown tour of the facility. The tour covered the entire plant and included the coal crushing and pulverizing operations, the boiler and turbine areas, the feedwater and condenser system, the electrostatic precipitators, and the instrumentation and control room. Video tapes were prepared during the tour to assist with communications with TVA and the United States technical experts who will be responsible for the actual life assessment of the plant. Prior to the site visit, two questionnaires, one prepared by NTPC and BHEL jointly, and one prepared by TVA, Chattanooga, were sent to DVC. Details on the plant design and equipment including sectional drawings, the plant operating history, the frequency of forced outages, maintenance practices, fuel supply and fuel quality, feedwater analaysis, and other pertinent operational data were requested in these questionnaires. The data are now being reviewed by TVA, ORNL, NTPC, and BHEL. The total installed capacity of CTPS is 780-MW consisting of three 140-MW units (Units, 1, 2, and 3) and three 120-MW units (Units 4, 5, and 6). Units 1, 2, and 3 are of imported design (Combustion Engineering/General Electric, USA) whereas Units 4, 5, and 6 are indigenous (Associated Babcock Ltd./Bharat Heavy Electricals Ltd., India). Units 1, 2, and 3 were commissioned between October 1964 and July 1968. Unit 2 has been identified for the life extension demonstration study. The general features of the plant are provided in Table 1. Although, the units are designed for 140 MW(e) output, the present capability is only 105 to 115 MW(e). Except for a brief period during the early stages of plant commissioning, none of the units have been run for an extended period at their full rated capacity. Surprisingly, the number of tube failures that have occurred in the boilers to date are well below the average rate of failure for units with similar service life. DVC staff has provided a detailed list of the problems experienced in the plant. The major concerns appear to be frequent breakdown of the coal pulverizing system, flame instability, and isolated incidents of boiler explosion, all of which are related to poor coal quality. Other major concerns are breakdown of the high pressure feedwater heaters, repeated bearing failure in the feedwater pumps, blade failure in the low pressure turbine, and excessive vibration of the high pressure turbine bearings. Problems in the coal crushing, sizing, and feeding are, by far, the main causes for the low plant load factors. The feed coal contains excessive amount of extraneous material (rocks and shale) and is of non-uniform size. The coal is also low in heating value. A combustion performance evaluation of the Unit 2 boiler during the November-December 1993 time frame was recommended by the team. The intent of this exercise was to fix the combustion related problems early on in the life assessment program, so that the unit can be operated at its full rated capacity, prior to the shutdown for conducting the life assessment.

Table 1. Equipment and plant parameters for Units 1 through 3 of the DVC Plant

Equipment	Description
Steam generators	Combustion Engineering (CE), USA, tangentially fired, national circulation type. Capacity: 960,000 lbs/h; steam condition 1995 psi/1000°F/1000°F
Turbines	General Electric (GE), USA, horizontal tandem compound reheat-turbine; steam condition: 1800 psi/1000°F/1000°F Number of Stages: 26 RPM: 3000
Generator:	General Electric, USA, Double pole, 50 cycles/s 15000 volts, 165 MVA, Power factor 0.85, Hydrogen cooled
Primary crusher	Hammer Hill, Pettibane Mulliken Co., USA, Capacity 500 tons/h
Coal mills	5 Numbers in each unit, CE Raymond Bowl Mill of suction type, crushing capacity 19 tons/h; four mills are required for full-load operation and one mill is spare
Burners	20 Numbers, tilting tangential type; oil support for flame stabilization at low load
Air preheater	CE-Lungstrom, regenerative heater
Boiler feed pumps	Worthington (France) for Units 1 and 2 and Ingersoll Rand, USA, for Unit 3; three pumps for each unit: Capacity: 1240 gallons per pump Head: 5800 ft Motor: HP 2300
Induced draft fan	Buffalo Forge, USA, two per unit Capacity: 7759m^3/min at 25 cms water column Motor: HP 1000 RPM: 1000 Flow control: Inlet and hydraulic speed control
Forced draft fan	Buffalor Forge, USA, two per unit Capacity: 5635m^3/min at 25 cms water column Motor: HP 450 RPM: 1000 Flow control: Inlet vanes and outlet dampers
Feedwater heaters	Alco Products, Worthington Corporation, USA; two high-pressure heaters and four low-pressure heaters
Ash-handling equipment	Allen-Sherman Hoff Co., USA, flyash by vacuum and bottom ash as slurry by hydroejection
Electrostatic precipitators	Joy Manufacturing Co., USA, (Units 1 and 2) and Research Cottrell, USA, (Unit 3). Units 1 and 2 ESPs have been replaced recently with Flakt India Ltd. ESPs
Combustion controls	Control, Bailey Meters, USA, Pneumatic
Plant Operational parameters	Coal consumption: 80 tons/h in each unit Plant heat rate (design): 8098 BTU/kWh Design Coal: Fixed carbon 34.9%; Ash 40%; Moisture 6%; Volatile matter 19.1%; Heating value Hardgrove Grindability Index: 55 Specific coal consumption: 0.7444 Kg/kWh Specific oil consumption: 33-36 ml/kWh
Excess air	18% at full load

A seven member team of engineers from BHEL, NTPC, DVC and PFC visited TVA during October-November 1993, for four weeks to obtain "hands-on" training on the turbine-generator condition assessment. The major portion of the training was conducted at the TVA Widows Creeks Plant during the outage. Site visits to other TVA plants and the machine shop facilities in Muscle Schoals, Alabama, were also organized for the team.

In November-December 1993, TVA led a team for an on-site assessment of the plant during operation. Unit 2, which is designed for a power output of 140 MW(e), was operating 105 MW(e). The loss in capacity, as mentioned earlier is primarily due to the poor coal quality. The "as-fired" coal has an ash content of about 46% and a volatile matter of 12%. The "design coal" is 36% ash and 14% volatile on a moisture free basis. Furthermore, the "as-fired" coal has an excessive quantity of rocks and shale even though a fair amount of the extraneous matter is manually handpicked on the conveyor belts feeding the coal bunkers. Other factors that are contributing to the lower plant capacity are lack of proper instrumentation and control, frequent breakdown of the critical equipment (coal pulverizers, coal feeders, feedwater heaters), air ingress in the furnance, excessive leakage of air from the air preheater, low windbox pressure, and overloading of the induced draft fan. TVA recommended that some of these problems be fixed and that a performance test be carried using a batch of de-shaled coal in order to establish the maximum power output that can be achieved in the present system. Accordingly, the test was conducted by BHEL and NTPC in January 1994. However, the power output did not improve and the test results were reviewed by TVA and ORNL in February-March 1994. Several inconsistencies have been noted in the test data. The general consensus now is that the capacity of the coal mills is inadequate for the degraded coal and not enough coal is being fed to the boiler to achieve the design output. To correct this situation, some of the major equipment may need modification and/or replacement. TVA has agreed to prepare a bid specification package which would focus on both the equipment and operational parameters for DVC to implement in order to recover the lost capacity.

Discussions pertaining to the workscope and requirements for the condition assessment were completed by TVA and ORNL during the visit to CTPS, PFC, BHEL and NTPC facilities in February 17-March 4, 1994. The team consisted of R. P. Krishnan (ORNL), Laney H. Bisbee (Structural Integrity Associates), B. W. Roberts (TVA), P. S. Chang (TVA), H. G. Best (TVA), and R. S. Love (TVA), and Dr. R. Viswanathan, Electrical Power Research Institute (EPRI). Following travel between the USA and India, the conduct of business began on February 21, 1994, in Hyderabad, India.

The Bharat Heavy Electricals Limited (BHEL) Corporate Research and Development Division is located in Hyderabad. While this organization provides R&D support to the entire BHEL product line,

the emphasis is on turbines, generators, transformers, and transmission. The following BHEL key personnel were involved in the discussions: L. Nagarajan, J. P. N. Sastry, S. K. Bhave, P. V. Sastry, K. M. Chowdary, P. K. Sinha, K. Rajendran, and K. V. Muthukrishnan.

Upon our arrival on the morning of February 21, a video and slide presentation was given on the BHEL product line and the corporate R&D Division. A tour of the following facilities and laboratories was then given:

- Insulation/High Voltage
- Aerodynamics and Flow Modeling for Rotating Equipment
- Non-Destructive Examination
- Tribology
- Experimental Stress Analysis
- Metallurgy
- Mechanical Testing
- Simulated Component Testing

The team then reviewed the objectives of the trip and the support required from the BHEL Hyderabad facility. Discussions on the workscopes prepared by the U.S. team for the turbine, generator, boiler, and piping were held with the corporate R&D staff. It was agreed that during the DVC CTPS demonstration in July-August 1994, the BHEL Hyderabad unit will support the turbine and generator assessments in the areas of metallurgy, NDE, stress analysis, and fracture mechanics evaluations.

The team departed Hyderabad on the evening of February 22, 1994 and spent the night in Calcutta. On the morning of February 23, 1994, a visit was made to the headquarters of the Damodar Valley Corporation (DVC) in Calcutta. In addition to the U.S. team, participants in the meetings at DVC headquarters were: Major General Sharad Gupta, Chairman, DVC, N. N. Sur, P. K. Chakraborty, B. Batabyal, and T. N. L. Agarwal.

The workscopes for the turbine, generator, boiler, and piping were briefly discussed. Attention was then focussed on the outage schedule windows which were compatible with TVA's domestic obligations. The two possibilities were July 25-August 19, 1994 and the January-February 1995 time frame. The earlier date has the potential heat and monsoon problem, and the later date extends the completion goal of the project. Major General Gupta was of the strong opinion that the earlier date should be adopted. This was agreed to by all parties with the intent to establish pre-shutdown and shutdown dates during the visit to CTPS.

The duration of the stay in Calcutta was cut short because of a local strike which had been called for the following day. The team departed by train from Calcutta and arrived around midnight.

In addition to the U.S. team, participants at the meetings at CTPS included PFC, DVC, CTPS staff, BHEL, and NTPC. A list of attendees is contained in Appendix A. On the morning of February 24, 1994, the team toured the power plant, including the coal preparation facilities. In the afternoon, a meeting of the entire group was held to define the objectives of the team while at CTPS. Afterwards, the group divided into teams which focussed on specific issues. The following teams were represented:

- Turbine-Generator
- Boiler
- Piping
- Balance of Plant (BOP)
- Non-Destructive Examination (NDE), and
- Capacity/Plant Performance

The same format of group meeting by teams was followed in the morning and afternoon work sessions on subsequent work days (February 25-26, 1994). The hot walkdown of the piping was completed during the visit to CTPS. Appendix A contains most of the significant results from the meetings at CTPS. The following is a brief summary of some of the decisions reached:

1. The plant indicated the need for 20 days prior to commencement of assessment activities for cooldown, disassembly, scaffolding, etc. Accordingly, the following timetable was established:
   - June 28, 1994; Collection of preshutdown information.
   - July 5, 1994; Shutdown.
   - July 25, 1994; Commencement of condition assessment activities by TVA, DVC, BHEL, and NTPC teams.
   - August 19, 1994; Completion of condition assessment with recommendations on issues requiring attention during the present outage. Essentially all U.S. team presence onsite will be completed on or prior to this date.

- Restart date for plant not established.
- December 12, 1994; Initial draft of condition assessment report jointly prepared by TVA, DVC, BHEL, and NTPC teams.

2. All organizations involved in the condition assessment identified the number of people comprising their teams as contained in Appendix A. The U.S. team will contain 14-18 participants.

3. No agreement was reached on specific "balance of plant" systems to be included in the assessment. The TVA contract with DOE allocated about 10 percent of total funding for this activity and all systems cannot be included at this funding level. Mr. Dingra from PFC expressed a strong preference for "Instrumentation and Controls". The U.S. team expressed a preference for those components directly affecting the capacity/performance issue (coal feeder, pulverizer, exhauster, air heater, induced draft fan). The finalization remains to be negotiated.

4. While details of the testing were different, the capacity/performance tests run in December 1993 and January 1994 indicate very similar results in power output. Peter Chang believes there is simply an inability to feed enough coal to achieve design power with the "degraded" coal available. He agreed to prepare a specification addressing the recovery of lost capacity within the next two months. This specification could be used in a bid package to equipment suppliers in an attempt to regain the lost capacity.

5. No piping isometric, orthogonal, or individual spoolpiece drawings were available at the plant. Gibbs and Hill consulting engineering firm in New York, NY designed the piping and Mannesmann in Germany supplied the piping material. A "best effort" was made to establish dimensional layout on the piping. Hanger settings and nameplate information, where legible, were obtained during the hot walkdown. An effort will be made to obtain additional information from Gibbs and Hill and from Mannesmann.

On February 22, 1994, Peter Chang was accompanied by a representative from BHEL, for a visit to the boiler facility at Trichy and discussions on the performance/capacity issues with the Trichy staff members. He rejoined the TVA team in Delhi on the morning of March 1, 1994. On February 27, 1994, the other TVA team members were toured through the Damodar River region and the coal fields near the CTPS site. The entire condition assessment team, still onsite, had lunch with the DVC Chairman Major General Gupta and the CTPS Chief Engineer Mr. Agarwal. Accomplishments during the time at the plant were reviewed

as well as plans for the assessment activities in the July-August period. The team then departed by car for Dhanbad and traveled by overnight train to Delhi.

The team visited the NTPC research and development center in New Delhi. Dr. R. Viswanathan, EPRI joined in the site visit. The NTPC R&D Center has testing facilities and state-of-the-art equipment to cater to the needs of all the NTPC power stations. The center provides technical support to the NTPC plants in boiler operations, preventive maintenance, non destructive examination, water chemistry, pollution control, ash disposal and utilization, and controls and instrumentation. NTPC will provide equipment and manpower support in these areas during the DVC condition assessment.

The last two days of the U.S. team visit were spent on wrap-up meetings with PFC and the EMCAT project steering committee in the PFC offices. The workscope and schedules were discussed and finalized. It was agreed that TVA and ORNL will look into the possibility of leasing the equipment that are not available at BHEL or NTPC and which are required for the condition assessment in August 94. Procurement action for these equipment will be initiated by BHEL and/or NTPC in the coming months. TVA will provide the specifications for the equipment.

The training program for the boiler and NDE engineers from India in the TVA plants was reviewed. The tentative date for the training was set for April 10-May 20, 1994. ORNL and TVA agreed to send PFC a detailed itinerary on the training program. TVA indicated that at least two coal-fired plants will be available during this window for conducting the hands-on training.

Appendix A

Table 1. Turbine Assessment Work Scope

Major Component	Subcomponent	Assessment Scope	Component Status Required for Assessment	Assessment Duration (h)
High Pressure Turbine	Outer Cylinder (UH and LH)	Insulation	None	2
		Bolting:	Bolts removed and clean	
		-stretch		4
		-NDE		4
		Gland Areas:	Cylinder removed	
		-cracks		2
		-water erosion		2
		Horizontal Joint:	Cylinder removed	
		-water erosion		1
	Inner Cylinder (UH and LH)	Opening clearances	Upper half inner cylinder removed	8
		Bolting:	Bolts removed and cleaned	
		-stretch		4
		-NDE		4
		Gland Areas	Cylinder removed	
		-cracks		2
		-water erosion		2
		Diaphragms & Nozzle Block	Diaphragms and nozzle removed and cleaned	
		-NDT		4
		-area checks		12
		Horizontal Joint:		
		-water erosion	Cylinder removed and cleaned	1
		NDT of Cylinder (includes replicas)		8
			Cylinder removed and cleaned	
	Rotor (HP-RH)	Rotating Blade Inspection	Rotor removed and cleaned	4
		Rotor NDT (includes replicas)	Rotor removed and cleaned	16
		Rotor Boresonic	Rotor removed and cleaned	32
		Rotor Run-out	Rotor removed and cleaned	8

Major Component	Subcomponent	Assessment Scope	Component Status Required for Assessment	Assessment Duration (h)
High Pressure Turbine (contd.)	Front Standard	Clearances	Front standard opened	8
		Oil pump	Front standard opened	1
		Control devices	Front standard opened	2
		Safety devices	Front standard opened	2
		Number 1 bearing and thrust bearing	Front standard opened	
		Movement	Front standard opened	2
	Control Valves	Clearances	Valves opened and cleaned	4
		Stem run-out	Valves opened and cleaned	4
		NDT (includes replicas)	Valves opened and cleaned	8
	Main Stop Valves	Clearances	Valves opened and cleaned	4
		Stem run-out	Valves opened and cleaned	4
		NDT (including replicas)	Valves opened and cleaned	8
Reheat Turbine	Outer Cylinder (UH and LH)	Insulation	None	2
		Bolting:	Bolts removed and cleaned	
		-stretch		4
		-NDE		4
		Gland Areas:	Cylinder removed	
		-cracks		2
		-water erosion		2
		Horizontal Joint:	Cylinder removed	
		-water erosion		1

Major Component	Subcomponent	Assessment Scope	Component Status Required for Assessment	Assessment Duration (h)
Reheat Turbine (contd.)	Inner Cylinder (UH and LH)	Opening Clearances	Upper halfinner cylinder removed	8
		Bolting:	Bolts removed and cleaned	4
		-stretch		4
		-NDE		2
		Gland Areas	Cylinder removed	4
		-cracks		1
		-water erosion		1
		Diaphragms	Diaphragms removed and cleaned	8
		-NDT		
		-area checks		
		Horizontal Joint:	Cylinder removed and cleaned	
		-water erosion		16
		NDT of Cylinder (includes replicas)	Cylinder removed and cleaned	12
	#2 Bearing Pedestal	Clearances	Pedestal opened	8
		Movement	Pedestal opened	1
		#2 Bearing	Pedestal opened	2
	Intercept Valves	Clearances	Valves opened and cleaned	4
		Stem run-out	Valves opened and cleaned	4
		NDT (includes replicas)	Valves opened and cleaned	8
	Reheat Stop Valves	Clearances	Valves opened and cleaned	4
		Stem run-out	Valves opened and cleaned	4
		NDT (includes replicas)	Valves opened and cleaned	8

Major Component	Subcomponent	Assessment Scope	Component Status Required for Assessment	Assessment Duration (h)
Low Pressure Turbine	Exhaust Hood and Cross-over	Insulation	None	2
		Bolting:	Bolts removed and cleaned	
		-stretch		4
		-NDE		4
		Gland Areas:	Cylinder removed	
		-cracks		2
		-water erosion		2
		Diaphragms	Cylinder removed	
		-NDT		1
		-area checks		
		Horizontal Joint:		
		-water erosion		
	Inner Cylinder (UH and LH)	Opening Clearances	Upper Halfinner cylinder removed	8
		Bolting:	Bolts removed and cleaned	
		-stretch		4
		-NDE		4
		Gland Areas	Cylinder removed	
		-cracks		2
		-water erosion		2
		Diaphragms	Diaphragms removed and cleaned	
		-NDT		4
		-Area Checks		12
		Horizontal Joint:	Cylinder removed and cleaned	
		-water erosion		1
		NDT of cylinder (includes replicas)	Cylinder removed and cleaned	8
		Area check diaphragms and nozzle	Diaphragms and nozzle removed and cleaned	12

Major Component	Subcomponent	Assessment Scope	Component Status Required for Assessment	Assessment Duration (h)
Low Pressure Turbine (contd.)	Rotor	Rotating Blade Inspection	Rotor removed and cleaned	4
		Rotor NDT (includes replicas)	Rotor removed and cleaned	16
		Rotor Boresonic	Rotor removed and cleaned	32
		Rotor run-out	Rotor removed and cleaned	8
	#3 Bearing Pedestal	Clearances	Pedestal opened	8
		Movement	Pedestal opened	1
		#3 Bearing	Pedestal opened	2
	Turning Gear	Clearances	Gear disassembled	4

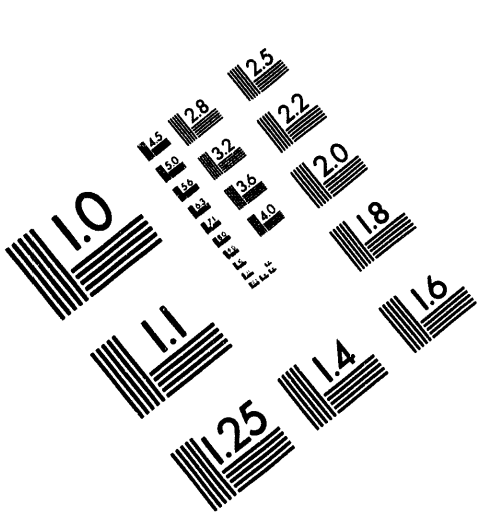

Association for Information and Image Management

1100 Wayne Avenue, Suite 1100
Silver Spring, Maryland 20910

301/587-8202

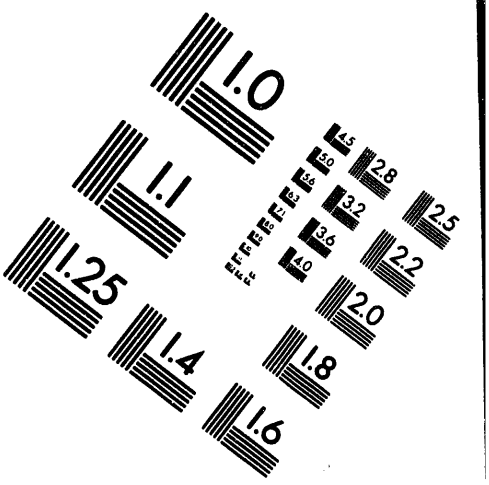

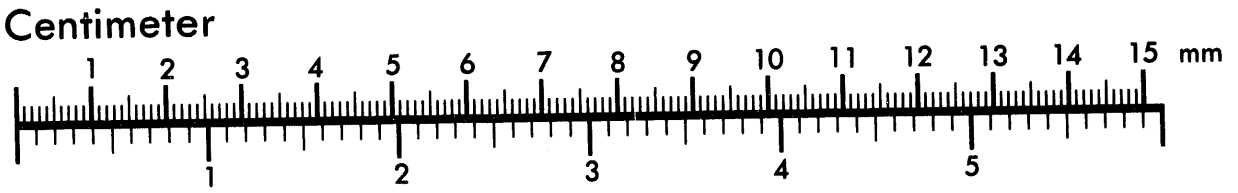

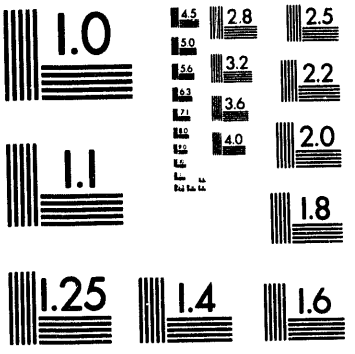

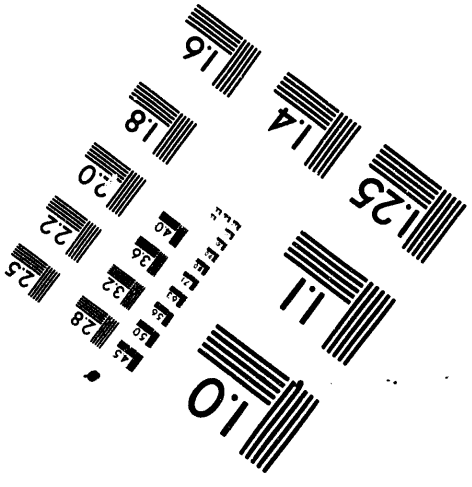

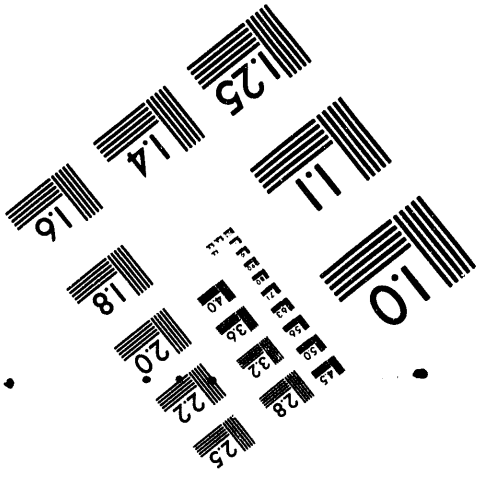

3 of 3

Table 2. Generator Component Assessment Work Scope

Major Component	Sub Component	Assessment Scope	Component Status Required for Assessment	Assessment Duration (h)
Stator Winding	End Winding Bracing	Ties, Blocking, Support Braces, Winding Movement, Distortion	Inner, outer end shields removed. Generator Field (Rotor) removed.	6
	Cooling Vent Slots	Check for evidence of bar vibration, excessive radial clearance in slots, etc.	Inner, outer end shields removed. Generator field (rotor) removed.	3
	End winding Insulation	Insulation girth cracks, Corona damage	Inner, outer end shields removed. Generator field (rotor) removed.	4
	Electrical Testing	Dielectric absorption (PI) testing, each phase at 2500 VDC	Inner, outer end shields removed. Generator field (rotor) removed.	1
		Dielectric absorption (PI) testing, each phase at 10,000 VDC	Inner, outer end shields removed. Generator field (rotor) removed.	1
		DC step high voltage testing	Inner, outer end shields removed. Generator field (rotor) removed.	1.5
		Insulation high voltage proof testing	Inner, outer end shields removed. Generator field (rotor) removed.	2
		Winding resistance, Kelvin bridge testing	Inner, outer end shields removed. Generator field (rotor) removed.	1
		Power factor testing	Inner, outer end shields removed. Generator field (rotor) removed.	2.5
		Capacitance Measurement of each winding.	Inner, outer end shields removed. Generator field (rotor) removed.	1

Major Component	Sub Component	Assessment Scope	Component Status Required for Assessment	Assessment Duration (h)
		All generator RTD's, Megger check at 100 VDC.	Inner, outer end shields removed. Generator field (rotor) removed.	1
Stator Winding (contd.)	Electrical Testing (contd.)	Generator RTD's. Resistance measurements.	Inner, outer end shields removed. Generator field (rotor) removed.	3
Stator Iron	Iron Laminations	EL-CID testing	Inner, outer end shields removed. Generator field (rotor) removed.	8
	Cooling Vent Passages	Boroscope check of vent slots	Inner, outer end shields removed. Generator field (rotor) removed.	6
	Fretting, Rust.	Visual inspection of iron	Inner, outer end shields removed. Generator field (rotor) removed.	2
	Iron Loosemess	Thru-bolt torque testing	Inner, outer end shields removed. Generator field (rotor) removed.	8
	Wedges	Random hammer tapping check	Inner, outer end shields removed. Generator field (rotor) removed.	2
		Electronic wedge mapping	Inner, outer end shields removed. Generator field (rotor) removed.	8
		Wedged migration	Inner, outer end shields removed. Generator field (rotor) removed.	1
		Greasing indications	Inner, outer end shields removed. Generator field (rotor) removed.	2
Gen. Field	Forging	Borosonic inspection	Rotor removed from generator.	12
		Wedge check, shifting, heating	Rotor removed from generator.	4

Major Component	Sub Component	Assessment Scope	Component Status Required for Assessment	Assessment Duration (h)
		Cooling vent inspection with boroscope	Rotor removed from generator	4
	Retaining Rings	Visual inspection	Rotor removed from generator	3
Gen. Field (contd.)	Retaining Rings	Zyglo inspection	Rotor removed from generator	6
	Balance Weights	Check for tightness, map location	Rotor removed from generator	3
	Electrical Testing	Megger test, 10 minute PI, 250VDC	Brush rigging removed. Safety precautions	1
		AC impedance test	Brush rigging removed. Safety precautions	2
		Kelvin bridge testing	Brush rigging removed. Safety precautions	1
	Fan Assembly	Check bolts for tightness	End bells removed from generator	2
	End Windings	Visual inspection, boroscope inspection	Rotor removed from generator.	2
	End Bracing	Visual inspection, boroscope inspection	Rotor removed from generator	2
	Collector Rings	Visual inspection. Even wear check	Brush rigging removed. Exciter assembly removal preferred	2
		Runout testing	Brush rigging removed. Exciter assembly removal preferred	6
	Journals	Visual inspection	Exciter assembly removed	1
		Runout check	Exciter removed	6

Major Component	Sub Component	Assessment Scope	Component Status Required for Assessment	Assessment Duration (h)
Hydrogen Coolers	Entire Assembly	Pressure	Hydrogen cooler removal	8
	Tube Sheets	Visual inspection	Hydrogen cooler removal	3
Hydrogen Coolers (contd.)		Pressure test	Hydrogen cooler removal	6
	Cover Assembly	Visual inspection. Gasket condition, corrosion, etc.	Hydrogen cooler removal	4
Pressure Testing of Gen. Enclosure	Entire Assembly	Air pressure test, helium trace gas. Check for leaks around endbells, valves, leak detectors, etc.	Generator fully closed. Purged of H2.	24
Gen. Stator Side Bushing Box	Bushing Seals	Visual condition	Generator purged. Safety procedures invoked.	1
	Enclosure	Environmental condition. Oil/water accumulation?	Generator purged. Safety procedures invoked.	1
	Bushing Porcelain	Check for cracking, chipping, oil film	Generator purged. Safety procedures invoked.	1
	Bushing Terminals	If insulated: fraying, signs of heating	Generator purged. Safety procedures invoked.	1
		If exposed bolted terminals: check for magnetic bolts, loose bolts, heating.	Generator purged. Safety procedures invoked.	1

Major Component	Sub Component	Assessment Scope	Component Status Required for Assessment	Assessment Duration (h)
Gen. Bushing Bus Enclosure	Bus Work Condition	Check for magnetic bolts; heating, oil film, corrosion, rust oxide, etc.	Generator purged. Safety procedures invoked.	1
	Enclosure Environment AL Condition	Presence of oil/water, overall appearance	Generator purged. Safety procedures invoked.	1
Generator Bushing Bus Enclosure (contd.)	Flexible Bus Straps	Fraying, breakage, corrosion	Generator purged. Safety procedures invoked.	1
	Gen. Bushings Condition	Porcelain chipping, breakage, oil film, etc.	Generator purged. Safety procedures invoked.	1
Exciter Field Rheostat & Control Cabinet	Gen. Bushings Electrical Testing	Power factor testing.		4
Emerg. Lube Oil & Turning Gear Motors	Emergency Backup Battery Condition, Capacity	Batter condition. Specific gravity measurements. Cell voltages. Float voltage level. Equalize voltage check. Cell plate state.	Access to battery room	10
	Lube Oil DC Motor Condition	Megger motor, 10 minute PI test, visual check	Motor isolation from primary voltage source	3
	Turning Gear DC. Motor Condition	Megger motor, 10 minute PI test, visual check.	Motor isolation from primary voltage source	3

Major Component	Sub Component	Assessment Scope	Component Status Required for Assessment	Assessment Duration (h)
Auxillary Electrical Protective Circuits	Gen. CT CKT	Electrical megger & turns ration test	Current transformer circuit isolation	6
		CT terminals conditions	Current Transformer circuit isolation	6
	Gen. PT CKT	Electrical megger test	Potential transformer circuit isolation	4
Auxillary Electrical Protective Circuits (contd.)	Gen. Reactor XFMR	Electrical megger test	Reactor isolation from neutral Y generator circuit	2
	Gen. Lightning Arrestors	Electrical power factor testing. Visual condition	Lightning arrestor circuit isolation	2
	Gen. Field Ground Relay Circuit Checkout	Verify proper field ground relay operation, setting. Verify operation of auxiliary relay operation megger back toward field to verify cable run integrity.	Circuit isolation. Safety procedures invoked.	8

Table 3. Equipment List for Turbine/Generator Inspection

U.S. Supplied:	India Supplied:
Automated ELCID	All Standard Generator Test Equipment.
Electronic Wedge Mapping	MEGGER
Power Factor Test Device	Hi - POT
Steam Path Audit Tools	ETC
Diaphragm Roundness Tool	

Table 4. Turbine/Generator Manpower List

	Turbine	Generator
PFC	-	1
BHEL	3	6
NTPC	2	1
TVA	2	1

Note: (1) Support by DVC will be required for moving equipment and electrical hook-ups.
(2) Assessment activity from July 25-August 19, 1994

Table 5. Boiler Assessment Work Scope

Component	Section	Assessment Scope	Duration (h)	Plant Support Required
Waterwalls	Walls	UT 5 elevations	16	Scaffold, grind 790 pts.
		UT condition driven pts.	8	Grind 650 pts.
		UT lower slope	4	Scaffold, grind 258 pts.
		Visual inspection	16	Clean
		Metallurgical samples		Remove, replace 3 each
		Visual cold side corrosion	4	Remove, replace insulation
	Platens	UT 3 elevations	8	Scaffold, grind 240 pts.
		UT wall penetrations optional	4	Grind 100 pts.
		Visual inspection	4	Clean
		Video ID inspection	16	Cut 16 tubes
		Metallurgical samples		Remove, replace 1 each
Steam Cooled Walls	Walls	Visual inspection	8	Clean, some scaffold
		PT/MT bifurcates	4	Access, clean, 4 pts.
		UT condition driven pts.	8	Grind 500 points
Reheater	Pendant	Visual inspection	8	Scaffold, clean
	Pendant Int. R.H.	UT 3 elevations	4	Grind 441 pts.
		UT for oxide scale thickness	4	Grind 441 pts.
		Metallurgical sample		Remove, replace 1 sample
Attemperator	Attemp.	Visual/video attemperator	4	Cut, replace access
Economizer	Horiz.	Visual inspection	4	Remove, replace shields
		UT for tube thickness all bends	8	Grind 384 pts.
		Visual/video for ID pits (Pittings)	4	Cut 4 tubes
	Walls	UT condition driven pts.	8	Grind 360 pts.

Component	Section	Assessment Scope	Duration (h)	Plant Support Required
Horizontal Superheater	Horiz.	Visual inspection	4	Remove, replace shields
		UT for tube thickness all bends	4	Grinding 300 pts.
		Metallurgical sample		Remove, replace 1 sample
Pendant	Pendant	Visual inspection	8	Scaffold, clean
	Platen	PT/MT dissimilar metal welds	8	Clean 50 welds
		UT. for tube thickness	4	Grind 480 pts.
Platen Superheater		UT for oxide scale	4	Grind 480 pts.
		UT condition driven pts.	4	Grind 500 pts.
		Metallurgical samples		Remove, replace 3 samples
	Attemp.	Visual/video attemporator	4	Cut, replace access
High-Temp Headers	-	PT/MT 10% of tube stub welds	24	Access, remove insulation, Clean
	HSH Outlet RH Inlet	PT/MT 20% of tube stub welds	24	Access, remove insulation, clean
	All	Visual OD, diametric check	16	Access, remove insulation, clean
		Video ID for cracking	16	Cut 3 tube stubs/header
		Check location, sag, twist	8	Access
		PT/MT saddle welds	8	Access, remove insulation, clean
	RH Outlet	Replica		1 at Girth weld, 1 near girth weld (HAZ) 2 at HAZ near tube stubs
		UT Shear Wave		end caps
	RH/HSH Outlet Header	Visual ID, partition plates, alloy analysis	4	Remove drum internals remove handhole caps
Low Temp Headers	Steam Drum	PT/MT girth welds	4	Remove insulation, clean

Component	Section	Assessment Scope	Duration (h)	Plant Support Required
Low Temp Headers (contd.)	Econ. Inlet	Visual OD/video ID for cracking	4	Remove insulation, cut 3 tube stubs
		PT/MT inlet saddle weld	4	Remove insulation, clean
		PT/MT 20% header stub welds	4	Remove insulation, clean
	Econ. Outlet	PT/MT outlet nozzle weld	2	Clean, remove insulation/if applicable
		Visual OD	2	Clean, remove insulation
		PT/MT 10% header stub welds	4	Clean, remove insulation if applicable

Table 6. Non-Destructive Examination NDE Work Scope

Chandrapura Unit 2 - NDE Group.

Principal Investigations: L. Bisbee, Structural Integrity (MET : NDE)
K. M. Chowdary, BHEL-Hyderabad (MET).
P. S. Subrahmanyam, BHEL-Tricky (NDE)

Objective: To identify the procedures, personnel, equipment, plant support, drawings, material specifications required to perform the condition assessment on Unit 2 CTPS.

Major Component: Turbine/Generator Work Scope form Turbine/Generator Group

Subcomponent	NDE Method	Surface Prep	Equipment	Equip. Avail.
Bolting	WFMT, PT	Brush	MT. machine, coils, PT	BHEL-H
Cylinders	WFMT	Grind Brush	MT. yoke	BHEL-H
Diaphragms	WFMT	Sand Blast	MT. machine, coils	BHEL-H
Nozzle Block	WFMT	Sand Blast	MT. machine, coils	BHEL-H
Valves:Bowl:Seat	WFMT, PT	Brush, N.A.	MT. yoke PT consumables	BHEL-H BHEL-H
Blading:Airfoil	WFMT	Sand Blast	MT machine, coils	BHEL-H
Lugs	PT	Sand Blast	PT consumables	BHEL-H
L&T Edges	ECT	Sand Blast	ECT:Probes	SI/TVA (BHEL-H)
Tenons	UT	Sand Blast	Manual/Auto UT	SI/TVA (BHEL-H)
Bearings	UT	N/A	Manual UT	BHEL-H

Chandrapura Unit 2 - NDE Group (continued)

Major Component : Turbine/Generator

Subcomponent	NDE Method	Surface Prep.	Equipment	Equip. Available
Rotors:Periphery	WFMT	Sand Blast	MT machine:coils	BHEL-H
Bore	Visual	Honed (BHEL)	Borescope	BHEL-H
Bore	MT	Honed (BHEL)	Borescope:MT machine	BHEL-H
Bore	UT (1)	Honed (BHEL)	Automated UT	WEST DYN
Bore	UT (2)	Honed (BHEL)	Manual UT w/focusing	SI:BHEL-H
Bore	UT (3)	Honed (BHEL)	Manual UT	BHEL-H
Retaining Ring	Hardness	N/A	Hardness tester	BHEL-H
Magnetic/Non	UT (1)	N/A	Automated UT	WEST DYN
Magnetic	UT (2)	N/A	Manual scanner:UT	SI
	UT (3)	N/A	Manual UT	BHEL-H
Metallurgical	Harness	N/A	Hardness Tester (Microdur)	BHEL-H
Evaluations	Alloy Identification	Ground	Texas Nuclear	BHEL-H
	Replication	N/A	Microscope	SI
	Replication	N/A	Consumables	SI
	Replication	N/A	Basic Equip.	BHEL-H

Equipment Required From USA

1. ECT (Eddy Current) for blading.
2. Boresonic equipment:automated or focused with digital data system.
3. Ultrasonic system for retaining rings.
4. Blading tenon inspection system.
5. Portable microscope.
6. Replication consumables (flapper wheels, acetate, tape, diamond paste)

Chandrapura Unit 2 - NDE Group (continued)

Major Component : Turbine/Generator.

Required Component Data:			Data to be Provided by
Rotor:	Number of stages, number of blades per stage, rotor length, bore diameter		DVC Plant/Turbine Group
Blades:	Lashing Lug or Wire		DVC Plant/Turbine Group
	Tenon/Shroud Type		DVC Plant/Turbine Group
	Attachment Type		DVC Plant/Turbine Group
Bolting:	Number of bolts		DVC Plant/Turbine Group
	Size of bolts		DVC Plant/Turbine Group
Retaining Ring:	Dimensions		DVC Plant/Turbine Group
	Material		DVC Plant/Turbine Group
	Geometry		DVC Plant/Turbine Group
Compilation of all turbine/generator NDE procedures			BHEL-H
Proposed List of Inspectors with Qualifications:			
Alloy Analysis	1 Person	BHEL-H	
Replication	2 Persons	BHEL-H	NTPC:Observers 3
NDT	4 Persons	BHEL-H	
Dimensional	2 Persons	BHEL-H	
Bore	2-4 Persons	BHEL-H	
BHEL Total	11 Minimum		NTPC Total : 3

Chandrapura Unit 2 - NDE Group

Major Component : Boiler

Workscope of Boiler NDE Group

Subcomponent	NDE Method	Surface Prep	Equipment	Equip. Avail.
Tubing	UTT	Sand Blast/Grind	Digital Logger (3)	TVA/SI
	Video Probe	Cut Tubes	Video-Probe	TVA/SI
	UT-oxide	Sand Blast/Grind	Testpro/Lifecode	SI
	PT/MT	Sand Blast	MT Yoke, PT	BHEL-T
Hi-Temp Headers	WFMT/PT	Sand Blast	MT Yoke, PT	BHEL-T
	Diameter	Sand Blast	Micrometers	BHEL-T
	Video-Probe	Cut Tubes	Video-Probe	TVA/SI
	Alloy Analysis	Grind	Tekas Nuclear	BHEL-H
	Replication	N/A	Replication	BHEL-T
	UT	Sand Blast	UT Shear Wave	BHEL-T
Steam Drum	Alloy Analysis	Grind	Texas Nuclear	BHEL-H
	WFMT/PT	Grind/Brush	MT Yoke, PT	BHEL-T
Economizer Header	WFMT/PT	Sand Blast	MT Yoke, PT	BHEL-T
	Alloy Analysis	Grind	Texus Nuclear	BHEL-H
	Video Probe	Cut Tubes	Video Probe	TVA/SI

Equipment to be procured/leased from USA

1. D-Meter with data logger (3 required)
2. Video probe system.
3. Oxide thickness UT system.
4. Consumables

Chandrapura Unit 2 - NDE Group.

Major Component : Boiler (continued)

Required Component Data:

Tubing : Dimensions, Material

Headers : Dimensions, Material

Proposed List of NDE Inspectors with Qualifications:

Alloy Analysis 1 (Same as Turbine)

Replication 2

NDT3 (UT/MT/PT)
BHEL Total : 5 NTPC Total : 2

Chandrapura Unit 2 - NDE Group

Major Component : High Energy Piping Workscope Assumed

Subcomponent	NDE Method	Surface Prep	Equipment	Equip. Avail.
Main Steam:Hot Reheat	WFMT	Sand Blast	MT Yoke	BHEL-T
Hanger Lugs	WFMT	Sand Blast	MT Yoke	BHEL-T
Welds	UT	Sand Blast	UT Shear	BHEL-T
	Replication	N/A	Replication	BHEL-T
	Digital UT Imaging	N/A	Scanner:Testpro	SI

Will do five girth welds per piping system plus header outlet weld.

Equipment to be procured/leased

1. Digital UT imaging with manual pipe scanner.

2. Consumables.

Required Data:
Piping Sizes
Piping Dimensions
High Stress Locations
Piping Materials.

Proposed List of Inspectors:
WFMT2 (1 NTPC, 1 BHEL-T)
UT Shear 2 Level II (1 NTPC, 1 BHEL-T)
Replication (Covered By Boiler Group)
BHEL Total : 2
NTPC Total : 2

NDE Group - DVC Requirements:

Facilities - Office space for data evaluation, computers, and microscope, preferably air conditioned for the computers.

Plant Support
Personnel: - In addition to the plant support for scaffolding sandblasting, grinding and insulation removal, the NDE teams will require the following.

Turbine+NDE Team	: 1 Electrician 3 Unskilled Workers
Boiler NDE Team	: 1 Electrician 5 Unskilled
Piping NDE Team	: 1 Electrician 3 Unskilled

Lighting & Power : Lighting must be supplied in the penthouse, and numerous power points must be supplied in the penthouse and at the locations of turbine component inspections. In addition, lighting and power must be supplied at the following piping locations:

- Main Steam WYE
- Hot Reheat WYE
- Main Steam Stop Valves
- Hot Reheat Intercept Valves
- Steam Chest (Main Steam Control Valves)
- Plant Must Supply 2, 110-220V Transformers.

All scaffolding, sandblasting, grinding, tube cutting, insulation removal, and cleaning is identified in the specific workscopes for the turbine, bowl, and piping. However, the penthouse must be cleaned of ash prior to the start of inspections.

Facilities - Storage space for a large column of NDE equipment must be supplied. The space should be a minimum of 5 × 5 meters in size. This space must be locked, no personnel will work in this area.

Chandrapura Unit 2

Recommended NDE Equipment by Component: (for BHEL/NTPC Procurement).

Turbine/Generator:

1. Boresonic System, Westdyne	$150,000
2. Retaining Ring UT System, Westdyne	$50,000
3. Tenon UT System, Manual	$10,000
4. ECT of Blade Edges, Probes	$3,000

Boiler:

1. UT Oxide/Lifecode	$50,000
2. Video-Probe System	$35,000
3. D-Meter : Data Logger	$5,000

Piping:

1. Manual Pipe Scanner, UT Imaging	$20,000

Metallurgy:

1. Portable Microscope	$15,000
2. Consumables	$3,500

Chandrapura TPS - Hot Walkdown of Unit 2 Main Steam and Hot Reheat Piping

The hot walkdown was conducted by Kothanda Raman (BHEL) and Bob Love (TVA) with assistance from J. P. Singh (DVC). Due to the absence of any drawings or specifications being provided for this walkdown, field measurements were taken and data collected from hanger Nameplates. At the same time visual inspections of hangers and components were made to determine the general condition of the hangers on the two systems. The hot position was recorded and will be combined with the cold walkdown data (in July-August 1994) to complete the stress analysis.

From the hot walkdown inspection both hanger systems appear to be in an acceptable condition with few hangers outside their range (i.e. bottomed out or topped out).

The plan of action is as follows:

(1) Submit suspect high stress areas to DVC before leaving the plant to facilitate insulation removal for NDE inspection. TVA/BHEL observed that marking indicated in the drawings are high stressed points and require NDE Inspection.

(2) Immediately upon return to USA TVA will contact the Burns and Roe (Architect Engineers) and the piping supplier to determine if specifications and drawings are available.

(3) After cold walk down in August 1994, data that are collected will be combined with hot walk down data. The stress analysis will be completed based on the "best data" collected to estimate the expected life of the system and condition of the piping system.

List of Attendees at the DVC Plant

1. R. P. Krishnan, ORNL
2. L. H. Bisbee, Structural Integrity
3. Peter S. Chang, TVA
4. H. G. (Jerry) Best, TVA
5. R. S. (Bob) Love, TVA
6. Blaine W. Roberts, TVA
7. K. M. Chowdary, BHEL
8. U. K. Das, BHEL
9. K. R. Bhardwaj, BHEL
10. R. Easwaran, BHEL
11. K. Rajendran, BHEL
12. P. S. Subramanian, BHEL
13. V. Raja, NTPC
14. P. K. Chakraborty, DVC, Nodal Officer
15. P. S. Dhingre, PFC
16. John Zachariah, BHEL
17. V. Kothandaraman, BHEL
18. Nagapati Hedge, NTPC (R&D)
19. D. D. N. Verman, NTPC (R&D)
20. P. K. Dev, NTPC (Engg.)
21. H. K. Sandhir, NRPC (Opn. Services)
22. S. S. Prasad (Maint. Planning Cell), DVC, CTPS
23. A. Biswas (Maint. Planning Cell) DVC, CTPS
24. P. P. Singh (Boiler & Auxiliaries), DVC, CTPS
25. A. K. Sarkar (Boiler & Auxiliaries), DVC, CTPS
26. S. D. Roy (Coal Mills), DVC, CTPS
27. R. K. Gupta (Turbine Auxiliaries), DVC, CTPS
28. G. K. Upadhyay (Turbine Generator), DVC, CTPS
29. J. P. Singh (Turbine Generator), DVC, CTPS
30. T. Singh (Coal Handling Plant), DVC, CTPS
31. S. Jha (Coal Handling Plant), DVC, CTPS
32. A. Niranjan (Cooling Towers), DVC, CTPS
33. G. P. Singh (Cooling Towers), DVC, CTPS
34. S. N. Shukla (Operations), DVC, CTPS
35. M. K. Majumder (Operations), DVC, CTPS

5.3 MILD GASIFICATION PRODUCT CHARACTERIZATION

C. S. DAW, R. L. GRAVES, A. L. COMPERE

BACKGROUND

From previous studies it is known that mild gasification of coal produces liquids that are potentially useable as diesel fuel or diesel fuel diluents [1,2]. However, the yield and quality of these liquids as well as the degree of upgrading required can vary substantially with the process severity (i.e., the degree of devolatili-zation). Char is similar in that the degree of devolatilization directly affects its combustion properties. The economic viability of any mild-gasification process is thus determined by tradeoffs among product yield, upgrading costs, and end-use requirements.

PROJECT DESCRIPTION

The purpose of this investigation is to develop basic characterization data for the liquid and char products of mild gasification. Such data are needed to evaluate key relationships among process conditions, product yield, and product end-use value. Of particular interest is the suitability of the liquid (with minimal upgrading) as diesel fuel and the suitability of the char as boiler fuel, although non-fuel uses of these products are also considered.

Representative samples of mild-gasification liquids and chars are being obtained from industrial groups involved in the development of candidate processes. These samples are subjected to a variety of characterization tests including:

-- chemical and physical analyses of the char and liquids;

-- combustion testing of the liquids in a diesel engine; and

-- combustion testing of the chars in laboratory reactors.

In general, ORNL is tasked to carry out the more detailed, unconventional laboratory characterizations such as proton NMR (nuclear magnetic resonance), FTIR (Fourier transform infra-red) spectroscopy, and neutron activation. Standard laboratory assays are carried out either by ORNL or major mild gasification teams. The use of the liquids as engine fuels, with either blending or mild upgrading, is still of interest so those evaluations have been continued. Although there are several high-value products that can be derived from the char, its use as fuel remains a potentially large market.

In addition, it is anticipated that char combustion will supply a major fraction of process heat in commercial mild-gasification processes. Hence a basic understanding of the char combustion properties is important.

DISCUSSION OF CURRENT ACTIVITIES

A final report summarizing the results of high pressure char characterization tests and PFB performance simulations based on the resulting characterization parameters was completed and issued to the DOE project manager. The chars evaluated in this phase of the project were one UCC (CTC) char and two IGT chars.

Additional char combustion characterization work was initiated under an R&D subcontract with with Babcock and Wilcox for four new char samples obtained from Maumee Research. The char samples were reportedly representative of process derived fuel made from the Shell/SGI (ENCOAL) process. The parent coals were Sarpy Creek, Knife River, Buckskin, and Usibelli coals, respectively. The current tests are being conducted at atmospheric pressure in the B&W/EPRI Fuels Characterization Facility. Problems with leaks in the combustion reactor have delayed completion of the characterization tests. It is anticipated that the tests will be completed by June, 1994.

Progress

Based on the data in Table 1, there has been considerable progress in decreasing the amount of residual aromatics in coal-derived liquids. With the exception of the Knife River sample, all of the aromatic/aliphatic ratios are below 0.15. The Sarpy Creek sample had particularly low aromatic/aliphatic ratios.

In running the scans, a peculiarity of these fuels was noticed. The Knife River, and to a lesser extent, the Usibelli sample, appear to have a significant aliphatic carbon - carbon double bond content.

Table 1. Aromatic and aliphatic content of coal derived liquids

Fuel source	Aromatic	Aliphatic	Ratio
Buckskin	19.6	160.7	0.122
Knife River	40.8	139.1	0.294
Sarpy Creek	10.7	173.4	0.062
Usibelli	18.5	144.3	0.128

Simulated distillation curves for the four coal-derived liquids are shown in Table 2. As a group, these materials are somewhat higher boiling than are conventional diesel fuels; final boiling points are above that of the n-C_{46} alkane used as a standard. These distillation characteristics are strongly influenced by the method used to condense and collect the liquids and may not be entirely inherent to the mild gasification process conditions.

Table 2. Simulated distillation of coal derived liquids

% Off	Sample			
	Buckskin °C	Knife River, °C	Sarpy Creek, °C	Usibelli, °C
IBP	170	166	173	171
5	191	83	201	193
10	210	193	223	214
15	224	209	241	232
20	239	218	256	248
25	252	231	271	263
30	266	241	289	279
35	283	254	306	299
40	300	267	324	316
45	317	285	342	336
50	336	305	357	355
55	353	326	373	374
60	369	349	387	391
65	385	370	399	409
70	401	388	414	427
75	418	408	429	441
80	434	429	443	453
85	451	448	457	467
90	472	472	478	483
95	503	507	510	513
FBP	561	566	569	589

REFERENCES

1. Graves, R. L., and Fox, E. C., Diesel Fuels From Minimally Processed Coal Liquids - Exploratory Investigations, *Proc. 19th IECEC Meeting, San Francisco, August 1984.*

2. Moore, H., Fuel Oil for Heavy Oil Engines, The Trans. of the Fuel Conference, World Power Conference, Vol. III, Percy Lund, Humphries & Co. Ltd., London 1928.

6. FOSSIL FUELS SUPPLIES MODELING AND RESEARCH

6.1. STRATEGIC PETROLEUM RESERVE PLANNING AND MODELING

P. N. Leiby and Donald W. Jones

INTRODUCTION

The Strategic Petroleum Reserve (SPR) is a government-owned stockpile of crude oil intended to serve as a buffer against possible oil market disruptions. The overall purpose of this project is to develop and apply improved models for SPR long-run planning. Current project efforts emphasize developing new modeling tools to explicitly and flexibly portray oil market uncertainty and SPR planning risk.

DISCUSSION OF CURRENT ACTIVITIES

Recent efforts have completed a risk-based SPR planning model, called DIS-Risk. The DIS-Risk Model is a risk-analysis oriented implementation of the DIS-SPR model used in the 1990 DOE/Interagency SPR Size Study (DOE90).[1] It allows the reproduction of DOE90 study results, while permitting extensions and the analysis of specific, risk-related outcomes. For example, the risk analysis approach allows reports on the expected frequency of disruptions and SPR use, and on the probability of SPR exhaustion. It also displays the probability distribution of SPR economic benefits. The analyst or decision-maker may weigh expected net economic benefits (the decision criterion of the DOE90 study) against other performance measures such as the reduction in the probability of large losses.

The model structure and performance has been documented in Leiby and Jones [1993].[2] This report summarizes the DIS-Risk model equations and confirms its consistency with the DOE90 Size Study methodology. It also reports on experiments with the model to evaluate its sensitivity to important parameters, and to explore its ability to address questions of interest.

Model experiments indicate that the Net Present Value (NPV) of *social* benefits from the SPR increase rapidly as the assumed riskiness of the world oil market increases. However, under all sets of assumptions considered, the SPR net *government* revenue is still negative. That is, stockpiling costs exceed discounted expected sales revenues. This is consistent with the notion that strategic oil stockpiles are not profitable from a purely private

perspective, even under assumptions implying a high risk of disruptions. Thus, the motivation for the SPR must be its external benefits to the economy as a whole, i.e., its ability to moderate oil price spikes.

Much of the uncertainty in SPR planning concerns the likelihood of oil market disruptions. The simple examination of 90% confidence intervals around the expected value of SPR benefits highlights the asymmetry of outcomes. The worst that the U.S. could do by expanding the reserve (and, conversely, the best that it could do by a planned program size reduction) is limited to the difference between the current price of oil and its discounted price at the presumed salvage date. However, the confidence intervals suggest that the realized (not expected average) benefits of larger reserves *could* be substantial, should adverse events occur. This risk-related information may be of use if decision makers are concerned with limiting exposure to extreme losses during disruptions.

REFERENCES

1. U.S. Department of Energy, Interagency Working Group 1990. Strategic Petroleum Reserve: Analysis of Size Options, DOE/IE-0016, February.

2. Leiby, Paul N. and Donald W. Jones 1993. "DIS-Risk Model for SPR Analysis: Model Documentation and Benchmarking Results," December 15.

INTERNAL DISTRIBUTION

K. Breder
T. D. Burchell
P. T. Carlson (2)
N. C. Cole
A. L. Compere
D. F. Craig
C. S. Daw
J. H. DeVan
J. T. Ensminger
D. E. Fain
W. Fulkerson
G. M. Goodwin
R. L. Graves
E. Greenbaum
J. A. Horton
M. A. Janney
R. R. Judkins (6)
E. N. Kaufman
N. E. Korte
R. P. Krishnan
R. L. Kroodsma
P. N. Leiby
C. T. Liu
P. J. Maziasz
C. G. McKamey
R. L. Miller
G. E. Roettger
C. D. Scott
T. C. Scott
V. K. Sikka
D. P. Stinton
R. W. Swindeman
V. J. Tennery
P. F. Tortorelli
S. Viswanathan
Central Research Library (2)
Document Reference Section
Laboratory Records Department (2)
Laboratory Records, ORNL - RC
M&C Records Office (2)
ORNL Patent Section

EXTERNAL DISTRIBUTION

M. Green
ABB LUMMUS CREST
1515 Broad St.
Bloomfield, NJ 07003

S. C. Weiner
AIR PRODUCTS AND CHEMICALS
7201 Hamilton Blvd., P.O. Box 538
Allentown, PA 18105

W. A. Ellingson
ARGONNE NATIONAL LABORATORY
9700 S. Cass Avenue
Argonne, IL 60565-4838

I. G. Wright
BATTELLE COLUMBUS LABORATORIES
505 King Avenue
Columbus, OH 43201

J. M. Chilton
BETHLEHEM STEEL CORPORATION
Homer Research Laboratories
Bethlehem, PA 18016

G. Twizell
BRITISH GAS plc
Westfield Development Centre
Cardenden
Fife, Scotland KY5OHP

Tom Butcher
BROOKHAVEN NATIONAL LABORATORY
Bldg. 475
Upton, NY 11973

R. A. Wolfe
COAL TECHNOLOGY CORP.
103 Thomas Rd.
Bristol, VA 24201

R. E. Wright
COAL TECHNOLOGY CORP.
103 Thomas Rd.
Bristol, VA 24201

F. P. Burke
CONSOL, INC.
R&D Department
4000 Brownsville Road
Library, PA 15129-9566

D. Nichols
CONSOL, INC.
R&D Department
4000 Brownsville Road
Library, PA 15129-9566

J. K. Weddell
DUPONT FIBERS
Experimental Station, E302
Wilmington, DE 19880-0302

C. A. Lundgren
DUPONT FIBERS
Experimental Station, E302
Wilmington, DE 19880-0302

W.D. Hewett
DUPONT FIBERS
Pencader Plant, CMC
P.O. Box 6100
Newark, DC 19714

S. B. Alpert
ELECTRIC POWER RESEARCH INSTITUTE
P.O. Box 10412
3412 Hillview Avenue
Palo Alto, CA 94303

D. M. Golden
ELECTRIC POWER RESEARCH INSTITUTE
P.O. Box 10412
3412 Hillview Avenue
Palo Alto, CA 94303

J. Stringer
ELECTRIC POWER RESEARCH INSTITUTE
P.O. Box 10412
3412 Hillview Avenue
Palo Alto, CA 94303

Y.C.L. Susan Wu
ERC, INCORPORATED
P. O. Box 417
Tullahoma, TN 37388

M. L. Gorbaty
EXXON RESEARCH & ENGINEERING CO.
Route 22 East, Clinton TWP
Annadale, NJ 08801

Heidrun Barnert-Wiemer
FORSCHUNGS ZENTRUM JÜLICH GmbH
Institute for Chemical Technology
Postfach 1913
D-5170 Jülich, Germany

Martin Novack
GENERAL APPLIED SCIENCE LABS
77 Raynor Ave.
Ronkonkoma, NY 11779

P. A. Lowe
INTECH, INC.
11316 Roven Drive
Potomac, MD 20854-3126

R. L. Phen
JET PROPULSION LABORATORY
4800 Oak Grove Drive - MS 79-21
Pasadena, CA 91020

M. H. Van de Voorde
JOINT RESEARCH CENTRE OF THE EUROPEAN COMMUNITIES
Westerduinweg 3, P.O. Box 2
1755 ZG Petten, The Netherlands

S. T. Viscontini
MOBIL RESEARCH & DEVELOPMENT CORPORATION
Engineering Department
P. O. Box 1026
Princeton, NJ 08540

J. P. Gyekenyesi
NASA LEWIS RESEARCH CENTER
21000 Brookpark Road (MS 6-1)
Cleveland, OH 44135

S. R. Levine
NASA LEWIS RESEARCH CENTER
21000 Brookpark Road
Cleveland, OH 44135

S. J. Dapkunas
NATIONAL INSTITUTE OF STANDARDS AND TECHNOLOGY
Materials Building, A259
Gaithersburg, MD 20899

S. Hirano
NEW ENERGY AND INDUSTRIAL TECHNOLOGY DEV. ORGANIZATION
Sunshine 60 bldg., P.O. Box 1151
Higashi-Ikeburkuro, Toshima-Ku
Tokyo, 170 Japan

T. Fukumizu
NEW ENERGY AND INDUSTRIAL TECHNOLOGY DEV. ORGANIZATION
1800 K Street, NW, Suite 924
Washington, DC 20006

Aksel Olsen
RISOE NATIONAL LABORATORY
P.O. Box 49
Roskilde 4000, Denmark

S. McNulty
SHELADIA, INC.
Suite 100, 15825 Shady Grove Rd.
Rockville, MD 20850

C. M. Huang
TENNESSEE VALLEY AUTHORITY
Research & Development
MR 3A
Chattanooga, TN 37402-2801

Harry Cheung
UNION CARBIDE INDUSTRIAL GASES, INC.
Linde Division
P.O. Box 44, 175 East Park Drive
Tonawanda, NY 14151

Gilbert Kirsch
UNIVERSITE DE METZ
Laboratoire de Chimie Organique
Faculty des Sciences
Ile du Saulcy 57
Metz, France

K. N. Strafford
UNIVERSITY OF SOUTH AUSTRALIA
Department of Metallurgy
The Levels SA 5095, Australia

K. Fuhrmann
VEBA OEL
P. O. Box 45
4650 Gelsenkirchen-Buer
Germany

D. H. Archer
WESTINGHOUSE ELECTRIC CORP.
114 Kentzel Road
Pittsburgh, PA 15237-2816

D. L. Keairns
WESTINGHOUSE SCIENCE AND TECHNOLOGY CENTER
1310 Beulah Road
Pittsburgh, PA 15235

W. A. Brown
DEPARTMENT OF ENERGY
Morgantown Energy Technology Center
P. O. Box 880
Collins Ferry Road
Morgantown, WV 25506

Leonard Graham
DEPARTMENT OF ENERGY
Morgantown Energy Technology Center
P.O. Box 880
Morgantown, WV 26505

J. S. Halow
DEPARTMENT OF ENERGY
Morgantown Energy Technology Center
P.O. Box 880
Morgantown, WV 26505

J. S. Wilson
DEPARTMENT OF ENERGY
Morgantown Energy Technology Center
P.O. Box 880
Morgantown, WV 26505

Deputy Assistant Manager for Energy Research and Development
DEPARTMENT OF ENERGY
Oak Ridge Operations Office
P.O. Box 2008
Oak Ridge, TN 37831-6269

J. W. Cooke
DEPARTMENT OF ENERGY
Oak Ridge Operations Office
P.O. Box 2008
Oak Ridge, TN 37831-6269

E. E. Hoffman
DEPARTMENT OF ENERGY
Oak Ridge Operations Office
P.O. Box 2008
Oak Ridge, TN 37831-6269

D. J. Beecy
DEPARTMENT OF ENERGY
Office of Technical Coordination
FE-72, B-119
19901 Germantown Road
Germantown, MD 20845

R. J. Braitsch
DEPARTMENT OF ENERGY
Office of Fossil Energy, FE-13
1000 Independence Avenue
Washington, DC 20545

J. P. Carr
DEPARTMENT OF ENERGY
Office of Fossil Energy
FE-72, B-127 GTN
Washington, DC 20585

F.M. Glaser
DEPARTMENT OF ENERGY
Office of Fossil Energy, FE-14
1000 Independence Avenue
Washington, DC 20545

Arthur Hartstein
DEPARTMENT OF ENERGY
Office of Fossil Energy
FE-33, D-122/GTN
Washington, D.C. 20585

D. S. Jewett
DEPARTMENT OF ENERGY
Fossil Energy
FE-222, 713/ROSS
Washington, D.C. 20545

P. C. Scott
DEPARTMENT OF ENERGY
Office of Advanced Research
FE-72, B-125
1000 Independence Avenue
Washington, DC 20545

T. B. Simpson
DEPARTMENT OF ENERGY
Office of Fossil Energy, FE-231
1000 Independence Avenue
Washington, DC 20545

M. I. Singer
DEPARTMENT OF ENERGY
Office of Deputy Assistant Secretary
FE-70, 4G-052
1000 Independence Avenue
Washington, DC 20545

H. G. Borgstrom
DEPARTMENT OF ENERGY
Office of Planning
and Financial Management
Petroleum Reserves
FE-43
1000 Independence Avenue, SW
Washington, DC 20585

A. L. Baldwin
DEPARTMENT OF ENERGY
Pittsburgh Energy Technology Center
P.O. Box 10940
Pittsburgh, PA 15236

S. W. Chun
DEPARTMENT OF ENERGY
Pittsburgh Energy Technology Center
P.O. Box 10940
Pittsburgh, PA 15236

Earl Evans
DEPARTMENT OF ENERGY
Pittsburgh Energy Technology Center
P.O. Box 10940
Pittsburgh, PA 15236

W. C. Peters
DEPARTMENT OF ENERGY
Pittsburgh Energy Technology Center
P.O. Box 10940
Pittsburgh, PA 15236

Shelby Rogers
DEPARTMENT OF ENERGY
Pittsburgh Energy Technology Center
P.O. Box 10940
Pittsburgh, PA 15236

R. Santore
DEPARTMENT OF ENERGY
Pittsburgh Energy Technology Center
P.O. Box 10940
Pittsburgh, PA 15236

C. A. Smith
DEPARTMENT OF ENERGY
Pittsburgh Energy Technology Center
P.O. Box 10940
Pittsburgh, PA 15236

T. M. Torkos
DEPARTMENT OF ENERGY
Pittsburgh Energy Technology Center
P.O. Box 10940
Pittsburgh, PA 15236

DEPARTMENT OF ENERGY
Office of Scientific and Technical
Information
P. O. Box 62
Oak Ridge, TN 37831
For distribution by microfiche as shown in
DOE/TIC-4500, Distribution Category:
UC-114 (Coal Based Materials and
Components)

DATE FILMED

8/19/94

END